

Experimental study on vesiculation and formation of
groundmass microlites induced by decompression:
Constraints on processes related to magma ascent at
Unzen volcano

Von der Naturwissenschaftlichen Fakultät
der Gottfried Wilhelm Leibniz Universität Hannover
zur Erlangung des Grades
Doktorin der Naturwissenschaften
Dr. rer. nat.

genehmigte Dissertation
von
Dipl.-Geow. Sarah Bettina Cichy
geboren am 08.08.1981 in Hannover

2011

Referent: Prof. Dr. François Holtz
Korreferent: Prof. Dr. Marcus Nowak
Tag der Promotion: 28. Juni 2011

Erklärung zur Dissertation

gemäß §6(1) der Promotionsordnung der Naturwissenschaftlichen Fakultät der
Gottfried Wilhelm Leibniz Universität Hannover

für die Promotion zum Dr. rer. nat

Hierdurch erkläre ich, dass die Dissertation mit dem Titel

**“Experimental study on vesiculation and formation of groundmass microlites
induced by decompression: Constraints on processes related to magma ascent at
Unzen volcano“**

selbstständig verfasst und alle benutzten Hilfsmittel und Quellen sowie
gegebenenfalls die zu Hilfeleistung herangezogene Institutionen vollständig
angegeben wurden.

Die Dissertation wurde nicht schon als Masterarbeit, Diplomarbeit oder andere
Prüfungsarbeit verwendet.

Hannover, den 15. April 2011

Sarah Bettina Cichy

Acknowledgements

I would like to thank...

Prof. Dr. François Holtz & Dr. Roman Botcharnikov for giving me the opportunity to work on this project, for their extraordinary support, motivation & guidance, for many discussions and for their patience & continuous ambition to educate the best scientist out of me that I could possibly be.

Prof. Dr. Harald Behrens for his support on FTIR spectroscopy and discussions.

Otto Diedrich for his prompt and perfect sample preparations.

The former and current **workshop team** (especially: **Willi Hurkuck, Bettina Aichinger, Ullrich Kroll** and **Marcus Köhler**) for their technical support and advice concerning the high pressure devices.

The **microprobe team** (**Jürgen Koepke, Wanja Dziony** and **Eric Wolff**) for their support and expenditure of time.

Dr. Karl-Ingo Friese for putting so much effort into reprogramming his 3D software *YaDiV* to suit my mineralogical needs and for his friendly patience explaining mathematical computer details to me.

Prof. Dr. Marcus Nowak for his cooperation and vital discussions. Him and the workshop team of the University Tübingen for constructing and providing the new decompression valve.

Prof. Dr. Jürgen Koepke for giving me the opportunity to work on other projects not related to my PhD project, widen my scientific horizon bit by bit.

Roger-Michael Klatt for the SEM introduction and his confidence to let me use the SEM on my own.

The **TOMCAT team** (**Federica Marone, Julie Fife** and **Kevin Mader**) at Swiss Light Source, Paul-Scherrer-Institute, Switzerland for their technical support.

Dr. Stefan Dultz for sharing his beam time at TOMCAT, SLS at PSI, measuring some of my samples.

H. Sato for ongoing discussions and professional support.

M. Wilson, M. Mangan, D. Laporte and **A. Toramaru** for their constructive comments and helpful suggestions on my Journal of Petrology paper.

S. Noguchi and **M. Higgins** for their helpful correspondence concerning the calculation of bubble/microlite number densities.

Deutsche Forschungsgemeinschaft DFG and **EU** for financial support (ICDP Schwerpunktprogramm, DFG project Ho 1337/16; EU SLS 20090928).

All members and guests of the Institute for Mineralogy, Leibniz University Hannover for the continuous support and discussions, fun and laughter.

Abstract

This experimental study focuses on revealing of magma ascent conditions (e.g. decompression rate, volatile composition, P-T path) related to the 1991-1995 eruption of Unzen Volcano, Japan by investigating in degassing and crystallization processes. Fluid-saturated phase stability and isothermal decompression experiments were performed using a synthetic analogue to the rhyodacitic Unzen groundmass composition. For decompression experiments at 850 and 930°C, we distinguished between high pressure decompression (HPD; 300 to 50 MPa) and low pressure decompression (down to surface pressures of 0.1 MPa). Finally, the experimental end products were compared to natural Unzen dome and conduit samples.

The natural mineral assembly of plagioclase, amphibole, pyroxenes and oxides were reproduced in decompression and phase stability experiments. Bubble number densities (BNDs) follow a heterogeneous nucleation trend at decompression rates ≥ 0.01 MPa/s, resulting in decreasing BND values with decreasing decompression rates. While at lower decompression rates (< 0.01 MPa/s), the BND values of decompression experiments including plagioclase microlites do not follow the above mentioned trend anymore. Their relatively high BNDs are indicating dominant bubble nucleation. Furthermore, there was no significant variation of the plagioclase microlite number density (MND_{pl}) value observed as a function of the decompression rate, indicating overall dominant microlite nucleation during decompression. Decompression-induced MND values are dependent on the initial value at isobaric starting conditions. Anyway, our MND_{pl} values for HPD and LPD experiments range from $10^{5.4}$ mm^{-3} to $10^{5.7}$ mm^{-3} and from $10^{5.7}$ mm^{-3} to $10^{6.4}$ mm^{-3} , respectively. Natural large plagioclase microlites were best experimentally reproduced in water-bearing HPD experiments at 850°C with decompression rates ≤ 0.0005 MPa/s, reaching up to maximum sizes of 200-250 μm .

In general, two main observations were made: (1) the large sizes and skeletal shapes of natural Unzen plagioclase microlites can be experimentally reproduced when its nucleation and growth occurs during decompression only and (2) amphibole microlites are not stable at pressure below ~ 100 MPa and at temperatures above 900°C. Based on the textural and chemical analyses of experimental run products (mineral phases and residual glasses), the average magma ascent rate of Unzen magmas in the pressure range of > 200 to 0.1 MPa is estimated to be ~ 30 -50 m/h, presumable following a non-isothermal decompression path ($< 900^\circ\text{C}$).

Keywords: crystallization, vesiculation, magma ascent

Zusammenfassung

Die Magmaaufstiegsbedingungen (z.B. Druckentlastungsrate, Volatilzusammensetzung, P-T-Pfad) der 1991-1995 Eruption des Unzen-Vulkans (Japan) werden in dieser experimentellen Studie unter Berücksichtigung der Entgasungs- und Kristallisationsprozesse untersucht. Mittels eines synthetisierten Rhyodazits analog zur Grundmassenzusammensetzung des Unzen-Vulkans wurden fluidgesättigte Phasenstabilitäts- und isothermale Druckentlastungsexperimente durchgeführt. Die Druckentlastungsexperimente wurden in Hochdruck- (HDE; 300 bis 50 MPa) und Niederdruckentlastungsexperimente (NDE; bis zu Oberflächendrücken von 0.1 MPa) unterschieden und wurden bei 850°C und 930°C durchgeführt. Abschließend wurden die chemischen und strukturellen Ergebnisse der experimentellen Endprodukte mit den natürlichen Dom- und Schlotproben verglichen.

Die natürliche Mineralparagenese von Plagioklas, Amphibol, Pyroxen und Oxidmineralen wurde in Druckentlastungs- und Phasenstabilitätsexperimenten nachgebildet. Bei schnellen Druckentlastungsraten (≥ 0.01 MPa/s) folgen die Blasenanzahldichten (BAD) einem heterogenen Nukleationstrend, welcher durch die Abnahme von BAD mit abnehmenden Druckentlastungsraten charakterisiert wird. Im Gegensatz dazu folgen die BAD bei langsamerer Druckentlastung (< 0.01 MPa/s) nicht mehr diesem oben genannten Trend, speziell in Experimenten mit Plagioklasmikrolithen. Deren relativ erhöhte BAD-Werte weisen auf eine Dominanz der Blasenbildung hin. Es konnte keine signifikante Variation der Plagioklasmikrolithenanzahldichte (MAD_{Pl}) in Abhängigkeit der Druckentlastungsrate beobachtet werden, welches auf eine allgemeine Dominanz des Mikrolithenwachstums während der Druckentlastung schließen lässt. Unsere druckinduzierten MAD-Werte zeigen eine Abhängigkeit vom Ausgangsmaterial bei isobaren Bedingungen auf. Jedenfalls variieren unsere MAD_{Pl} -Werte der HDE- und NDE-Experimente von $10^{5.4}$ mm⁻³ bis $10^{5.7}$ mm⁻³ bzw. von $10^{5.7}$ mm⁻³ bis $10^{6.4}$ mm⁻³. Die Reproduzierbarkeit der natürlichen, lang gewachsenen Plagioklasmikrolithe (mit Längen von bis zu 200-250 μ m) wurde am besten in wassergesättigten HDE-Experimenten bei 850°C und einer Druckentlastungsrate von ≤ 0.0005 MPa/s erzielt.

Aus den experimentellen Untersuchungen konnten zwei wichtige Schlussfolgerungen gezogen werden: (1) das skelettartige Wachstum und die Längen der natürlichen Plagioklasmikrolithe des Unzens können experimentell reproduziert werden, wenn deren Keimbildung und Wachstum nur während der Druckentlastung stattfindet und (2) sind Amphibolmikrolithe instabil bei Drücken unter ~ 100 MPa und bei Temperaturen über 900°C. Basierend auf strukturellen und chemischen Analysen der experimentellen Endprodukte (Mineralphasen und Restschmelze) wird eine Magmaaufstiegsrate von ~ 30 -50 m/h im Druckbereich von > 200 bis 0.1 MPa für die Unzen-Eruption angenommen, wobei der Druckentlastungspfad vermutlich nicht isotherm verlief ($< 900^\circ\text{C}$).

Schlagerwörter: Kristallisation, Blasenbildung, Magmaaufstieg

TABLE OF CONTENTS

Chapter	Page
1. INTRODUCTION _____	1
1.1 1991-1995 Mt. Unzen eruption, Japan _____	1
1.2 Decompression-related dynamic processes _____	6
2. Phase stability experiments _____	8
3. Decompression experiments (set-I to set-VI) _____	26
3.1 High pressure decompression (HPD) _____	27
3.1.1 HPD at low-temperature (850 °C; set-I) – modified after Journal of Petrology paper Cichy et al. (2011) _____	27
3.1.2 HPD at high-temperature (930 °C; set-II) _____	60
3.2 Low pressure decompression (LPD) _____	69
3.2.1 LPD: from 50 to 0.1 MPa at high- and low-temperature (set-III and set-IV) _____	70
3.2.2 LPD: from 200 to 0.1 MPa at low-temperature (set-V) _____	80
3.3 Comparison of three different decompression methods: continuous, multi-step and single-step decompression (set-VI) _____	88
3.4 3D segmentation and visualization of textures from decompression experiments _____	99
4. Discussion _____	112
5. Conclusion _____	127
6. References _____	128
7. Appendix _____	137
7.1 Tables _____	137
7.2 Figures _____	153
<i>Lebenslauf – Curriculum Vitae</i> _____	162

1. INTRODUCTION

1.1 1991-1995 Mt. Unzen eruption, Japan

Mt. Unzen is situated on the Shimabara Peninsula of Kyushu Island, Japan. The volcano is located in the volcanotectonic “Unzen graben”, approximately 70 km west of the volcanic front of SW Japan, where the Philippine Sea Plate is subducting beneath the southwestern part of Japan, see Fig. 1.1.

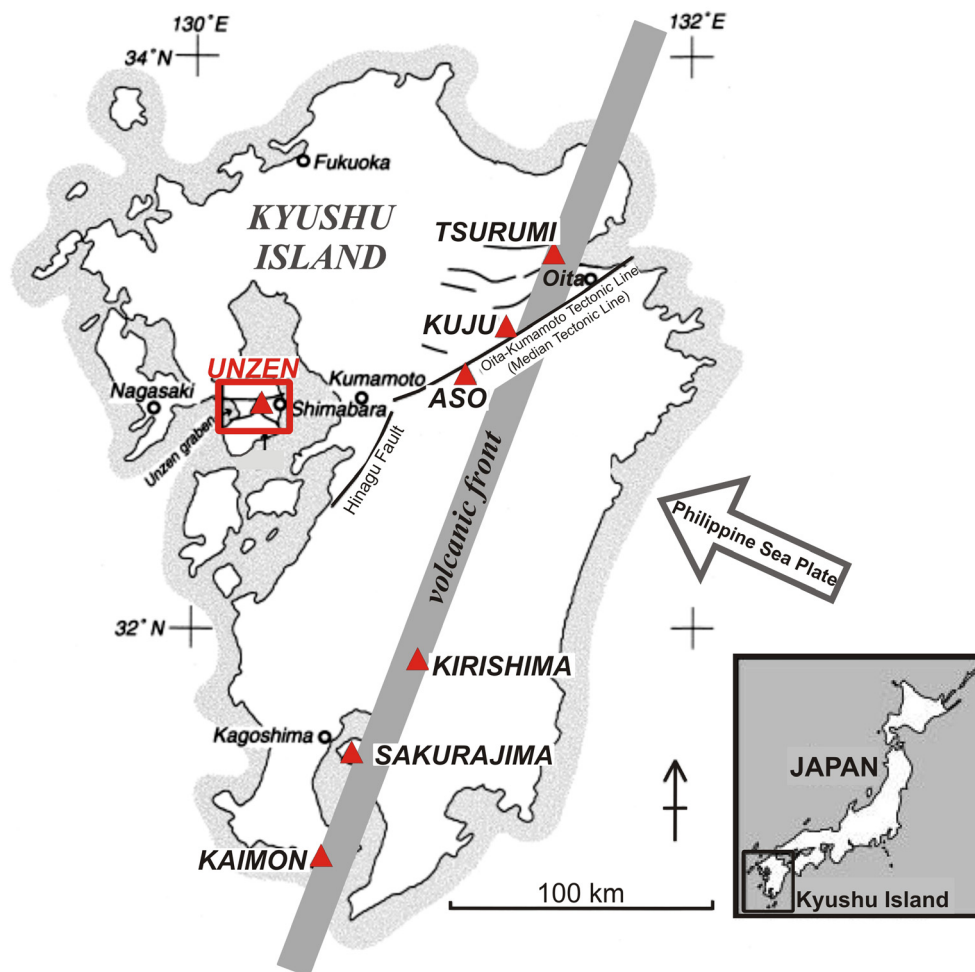


Fig. 1.1. Location map of Kyushu Island and Unzen volcano, Japan modified after Hoshizumi *et al.* (1999). Grey arrow shows the relative moving direction of the Philippine Sea Plate after Seno (1977). Red triangles indicate active volcanoes, Unzen volcano is indicated by red triangle in red square.

Unzen volcano offers a unique opportunity to interpret magmatic textures and volcanic processes because its latest eruption in 1991-1995 was well-observed and well-documented before, during and after the eruption as its occurrence was announced by seismic activity (e.g. Nakada & Fuji, 1993; Nakada *et al.*, 1999). In the framework of an

international project, a drilling was conducted in 2004 to reach the so-called conduit zone at depth (USDP-4; e.g. Nakada & Eichelberger, 2004; Hoshizumi *et al.*, 2005), see Figs. 1.2 and 1.3. Therefore, samples have been not only collected at the surface (e.g., Nakada *et al.*, 1999) but also at depth (ICDP drilling, Nakada *et al.*, 2005).

The 1991-1995 Unzen eruption occurred as a result of mixing between andesitic and rhyolitic magmas in deep magma chambers followed by an ascent of mixed dacitic magma from depth (Venezky & Rutherford, 1999; Holtz *et al.*, 2005), see Fig. 1.4. It has to be noted that enclave studies of Browne *et al.* (2006) conclude a mingling of basaltic and dacitic magmas during magma recharge events. Petrological and experimental studies indicate that before the eruption the mixed dacitic magma was stored at a minimum pressure of about 160 MPa and temperatures from 870 to 930°C, while it contained about 6 wt% H₂O (Venezky & Rutherford, 1999; Holtz *et al.*, 2005). The maximum pressure of the magma chamber is considered to be less than 300–400 MPa based on the geophysical data (maximum storage depth of about 11 km, Nishi *et al.*, 1999) and on the H₂O content of the melt inclusions in phenocrysts (up to 7–8 wt.% H₂O; Nishimura *et al.*, 2005; Holtz *et al.*, 2005). Botcharnikov *et al.* (2008) estimated 0.02 wt% of sulphur and 0.05 wt% of chlorine for the mixed magma, while additional 0.09 wt% of CO₂ are meant to be present (estimated after Ohba *et al.*, 2008).

During the eruption, a lava dome, composed of several lava lobes, was formed on the top of the volcano, producing numerous pyroclastic flows (e.g. Nakada & Motomura). The dome rocks consist of vesicular dacites with plagioclase, hornblende, biotite and quartz as main phenocrysts which are presumably originated from silicic rocks at depth (e.g. Nakada & Motomura, 1999; Holtz *et al.*, 2005). The groundmass is interpreted to be representative of the melt after magma mixing and it is composed of matrix glass, plagioclase, pargasite, pyroxene, Fe-Ti oxides and apatite microlites (e.g. Nakada & Motomura, 1999, Sato *et al.*, 1999). Since the vesiculation and crystallization of Unzen groundmass mainly occurred during magma ascent, the textures and phase compositions of the groundmass in the dome lavas may provide constraints on processes of magma degassing and crystallization (Noguchi *et al.*, 2008).

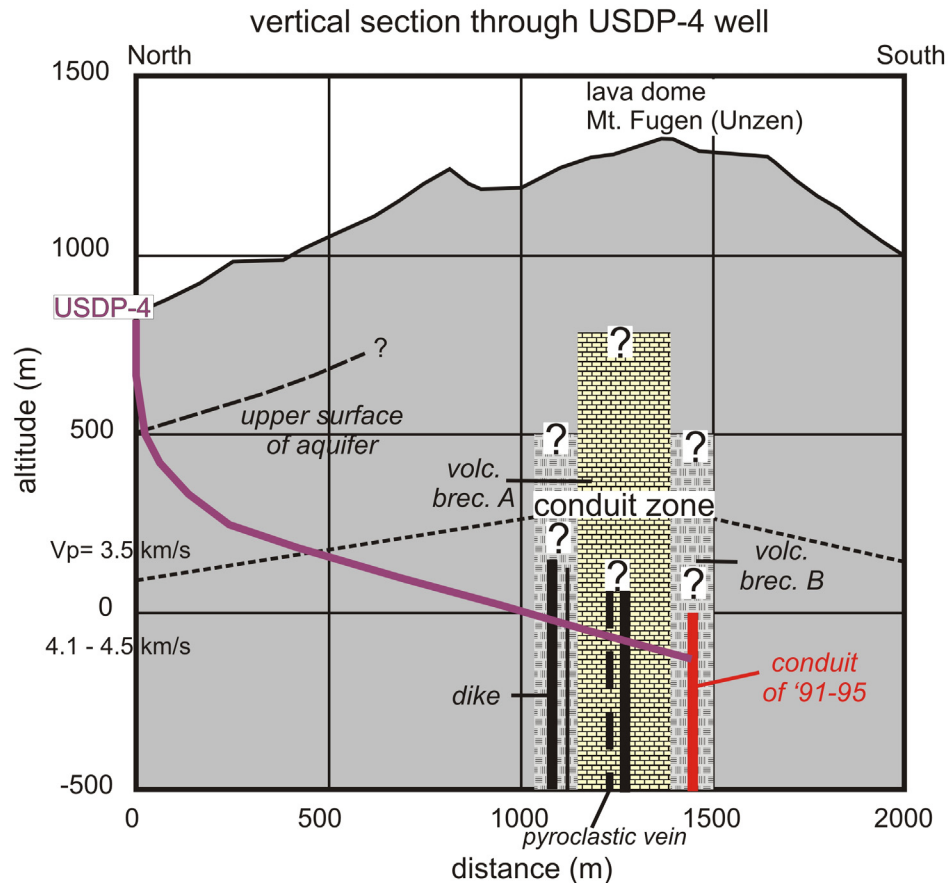


Fig. 1.2. Vertical section through the USDP-4 well (purple color; modified after Nakada *et al.*, 2005). A lava dike that is considered to be the conduit of the 1991-1995 eruption was located at the deepest part of the well, indicated in red color.

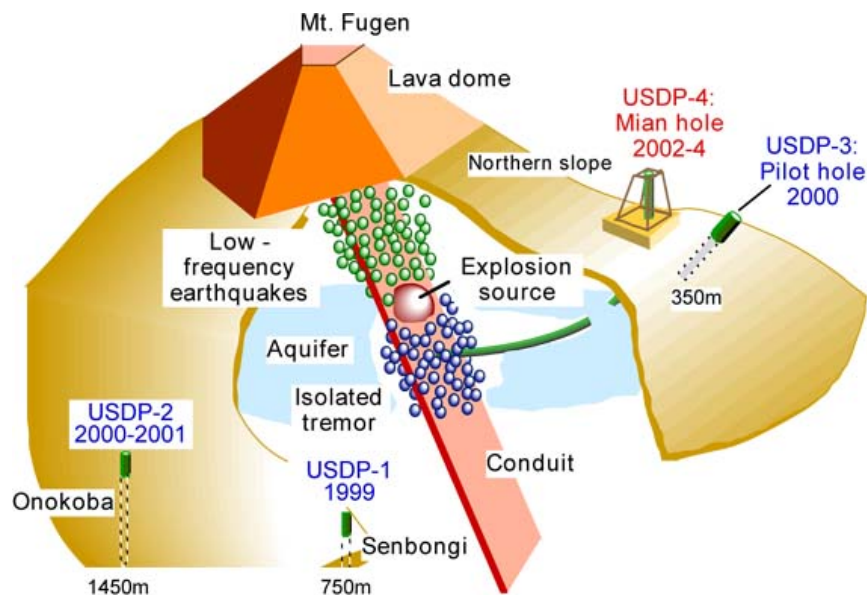


Fig. 1.3. Three-dimensional image of conduit drilling (image courtesy of the Unzen Scientific Drilling Project). Shown inside the volcano are the drilling trajectory of conduit drilling (USDP-4) and plate-shaped conduit (dike) together with earthquake hypocenters, water table and explosion source (e.g. Nakada & Eichelberger, 2004).

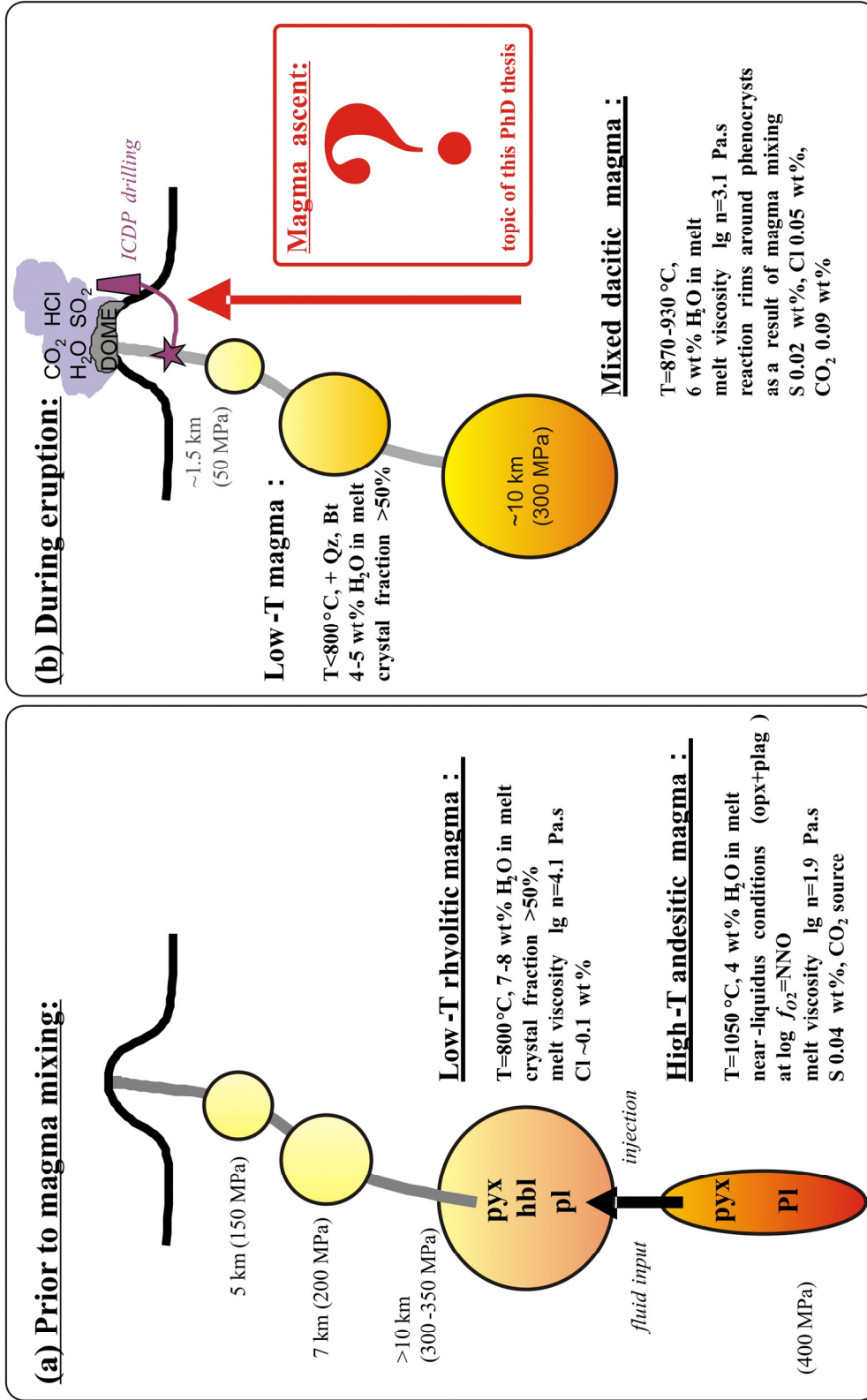


Fig. 1.4. Illustration of literature data available on the pre-eruptive condition of 1991-1995 Unzen eruption after Hess & Dingwell (1996), Venezky & Rutherford (1999), Holtz *et al.* (2005), Nishimura *et al.* (2008), Botcharnikov *et al.* (2008), Ohba *et al.* (2008) and Vetere *et al.* (2008). Red box including question mark is representing the topic of this PhD thesis (sketch not at scale). Findings of Browne *et al.* (2008) are not shown for simplicity.

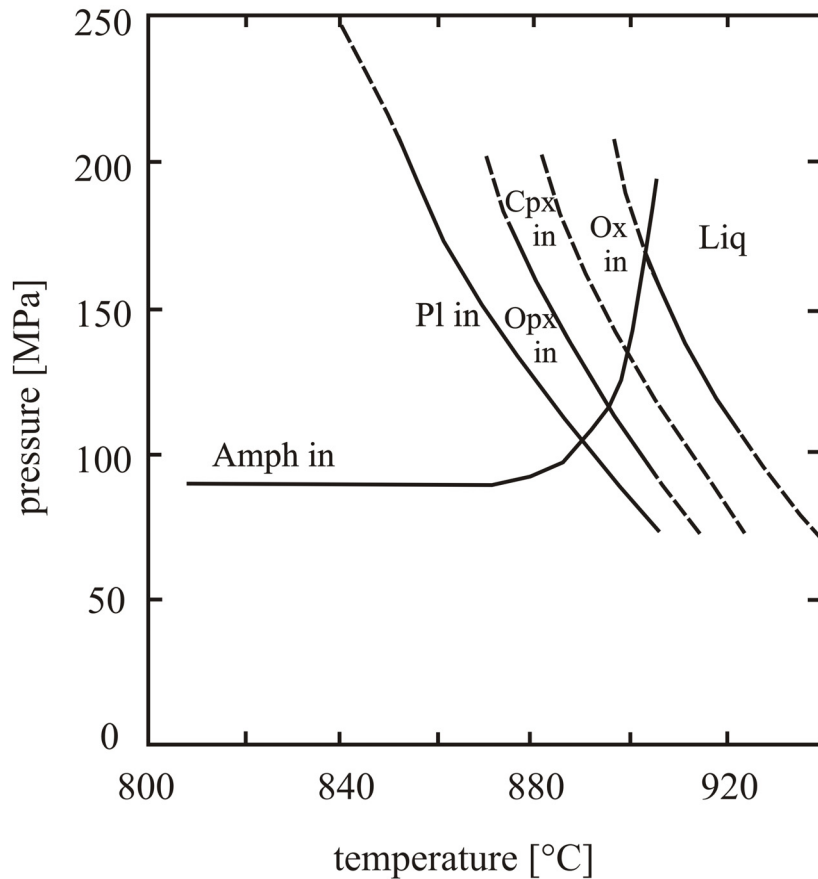


Fig. 1.5. Schematic phase diagram for water-saturated rhyodacitic magma, corresponding to groundmass of Unzen based on a compilation of experimental data from Rutherford & Hill (1993), Sato *et al.* (1999), Holtz *et al.* (2005) and Larsen (2005).

The phase diagram in the pressure (P) – temperature (T) field for water-saturated ($X^{\text{fl}}\text{H}_2\text{O}=1.0$) rhyodacitic groundmass composition is shown in Fig. 1.5, based on the available literature data relevant to Unzen rhyodacitic system (e.g. Rutherford & Hill, 1993; Sato *et al.*, 1999; Holtz *et al.*, 2005; Larsen, 2005). At a given temperature, the stability fields of minerals expand with decreasing pressure due to exsolution of dissolved water from the melt. On the other hand, some minerals such as amphibole belong to high-pressure mineral phase assemblage and are not stable at pressures below 80-100 MPa. Consequently, an isothermal magma ascent to the surface should result in a continuous change in the mineral assemblage, in the compositions and textures of groundmass microlites as well as in the vesicularity of erupted rocks. Similar variations are expected at water-undersaturated conditions in presence of a $\text{H}_2\text{O}-\text{CO}_2$ -bearing fluid. However, a P-T phase diagram for the $\text{H}_2\text{O}+\text{CO}_2$ -bearing Unzen rhyodacitic system at given mole fraction of water in the fluid phase ($X^{\text{fl}}\text{H}_2\text{O}$) is not available from literature data.

However, the interpretation of the textures of Unzen rhyodacitic groundmass observed at depth and at the surface requires quantitative data on growth kinetics of

microlites resulting from slow decompression and related volatile degassing. Most available data (see above) are not applicable for the example of Unzen. Even experimental datasets from rhyodacitic or rhyolitic examples (e.g. Martel & Schmidt, 2003) are difficult to apply to Unzen because the phase stability of minerals such as plagioclase and amphibole are strongly dependent on small compositional variations. For example, although the bulk compositions of Mt. St. Helens, Redoubt and Unzen are very similar (63.4 to 65.2 wt% SiO₂), the stability field of Unzen amphibole is extended to lower pressures when compared to Mt. St. Helens and Redoubt (difference up to 60 MPa at same temperature and $a_{\text{H}_2\text{O}}$, Sato *et al.*, 1999; Holtz *et al.*, 2005). Amphibole belongs to the microlite assemblage at Unzen and, clearly, decompression-induced crystallization (or dissolution) experiments with the groundmass composition of Unzen need to be conducted to interpret and compare the natural textures at depth and at the surface.

1.2 Decompression-related dynamic processes

Magma ascent rate can control the eruption style (e.g., Hurwitz & Navon, 1994; Sparks *et al.*, 1998) and groundmass textures of erupted rocks (e.g., crystal and vesicle sizes and number densities) may preserve important information about the decompression path and processes related to the magma ascent within the conduit. Decompression in ascending magmas leads to (homogeneous or heterogeneous) nucleation and growth of gas bubbles (mainly H₂O, CO₂, SO₂, H₂S and HCl) and of microlites as a result of exsolution of volatiles from the melt into bubbles increasing the magma liquidus temperatures and therefore enabling extensive groundmass crystallization. There have been several studies to quantify nucleation and growth rates of both microlites and bubbles as a function of decompression or cooling rate (e.g. for microlites, Cashman & Marsh, 1988; Marsh, 1988, 1998; Higgins, 2000, 2002, 2006; Hammer & Rutherford, 2002; e.g. for bubbles Simakin *et al.*, 1999; Mourtada-Bonnefoi & Laporte, 1999, 2002; Gardner & Denis, 2004; Toramaru, 2006; Gardner, 2007). In addition to decompression rate, these studies emphasize the role of melt viscosity, of nucleation and undercooling on number and size of bubbles and microlites. However, in order to interpret quantitatively parameters such as textures and compositions of magmatic phases and to evaluate the dynamics of a magmatic system, the processes of magma degassing and crystallization need to be simulated

experimentally. Considering that each natural magmatic system has its own characteristics before ascent, the available data can not be extrapolated to interpret quantitatively parameters such as BND and MND (bubble number density and microlite number density) to evaluate the dynamics of magmatic system (e.g., ascent rate).

Most previous works focused so far either on bubble nucleation and growth or on microlite nucleation and growth as a result of decompression (see review of Hammer, 2008). Only little attention has been given to the characterization of experimental samples in which bubbles and microlites nucleate and grow simultaneously (e.g., Simakin *et al.*, 1999). In this PhD study, it is aimed to experimentally simulate the magma ascent from magma chamber to shallow levels or to surface pressures during the 1991-1995 Unzen eruption and to correlate chemical compositions and textural features of the experimental products with natural Unzen groundmass samples collected from the dome and from drill cores provided by literature data. Therefore, several sets of isothermal decompression experiments for high pressures (300 to 50 MPa) and for lower pressures (final pressure of 0.1 MPa) at two different temperatures (850°C and 930°C) were performed, varying the decompression rates from 20 to 0.0001 MPa/s and using two fluid-saturated series: (a) H₂O and (b) H₂O+CO₂. Additionally phase stability experiments were conducted at different P-T-X^{H₂O} conditions to improve and complete the interpretation of the experimental decompression datasets. The results will provide a unique opportunity to compare data obtained experimentally with information from natural samples collected at the surface (e.g., Nakada *et al.*, 1999) and at depth (ICDP drilling, Nakada *et al.*, 2005). The experimental results on kinetics of decompression-induced nucleation and growth of bubbles and microlites are used to interpret textures of erupted products and to constrain processes occurring in magmatic conduit during the last Unzen eruption.

2. PHASE STABILITY EXPERIMENTS

Up to this point, no adequate literature data on mineral phase stabilities have been published that are covering the investigated rhyodacitic groundmass composition of the 1991-1995 Unzen eruption, especially data at water activities lower than 1.0 are lacking. In order to facilitate and support the interpretation of the isothermal decompression experiments (*chapter 3*), phase stability experiments were performed at different P-T- $X^{\text{fl}}\text{H}_2\text{O}$ (pressure, temperature and mole fraction of water in the fluid, respectively) conditions, using a synthetic analogue of the natural bulk groundmass composition of the 1991-1995 erupted Unzen magma (Sato *et al.*, 1999, 2005; Botcharnikov *et al.*, 2004; see Table 2.1). The aim of this experimental approach is the determination of the stability fields of the major microlite mineral phases observed in natural Unzen rocks such as amphiboles, plagioclases, pyroxenes and Fe-Ti oxides (e.g. Nakada & Motomura, 1999; Venezky & Rutherford, 1999), as a function of the parameters described above.

Table 2.1. Chemical composition of groundmass glasses (dry; in wt%) from natural Unzen analysis (1) and used as starting materials for experimental studies (2), (3) and (4).

#	Groundmass compositions	SiO ₂	TiO ₂	Al ₂ O ₃	FeO _{total}	MnO	MgO	CaO	Na ₂ O	K ₂ O	Total
(1)	natural Unzen groundmass glass (Nakada & Motomura, 1999)	68.14	0.57	15.08	3.78	0.09	1.80	4.10	3.51	2.78	99.85
(2)	experimental study of Sato <i>et al.</i> (1999) on Unzen 1991-1995 groundmass separate	68.24	0.53	14.95	4.05	0.09	1.91	3.86	3.48	2.85	99.86
(3)	This experimental study (rhyodacitic groundmass composition as a starting glass)	69.95	0.50	14.21	3.57	0.12	1.44	4.05	3.16	2.75	99.75
(4)	experimental study of Venezky & Rutherford (1999) on Unzen bulk rock composition (=crushed bomb from June 11 th , 1991 Unzen eruption; U-2 Pdr), chemical composition taken from Nakada & Fuji (1993)	64.74	0.66	16.21	4.62	0.07	2.28	4.93	3.93	2.40	99.84

Starting material and experimental methods

A mixture of oxides (SiO₂, TiO₂, Al₂O₃, Fe₂O₃, MnO and MgO) and carbonates (CaCO₃, Na₂CO₃ and K₂CO₃) was ground in a rotary mortar. The mixed powder was melted for 2

hours in platinum crucible at 1600°C, 1 atm in air ($\log f_{O_2} = -0.68$). Afterwards, the melt was quenched to glass by placing the crucible into a water bath. To improve the homogeneity of the batch, the glass was ground again in the agate mortar and melted again for 0.5 hour, using same P-T-conditions as described above.

For capsule preparation, 50 mg of the synthesized powdered silicate glass were loaded in 18 to 25 mm long Au or Au₈₀Pd₂₀ capsules with a outer diameter of 3.2 mm. Additionally, 10 wt% of fluids were added to the dry glass, containing of certain proportions of liquid H₂O and solid Ag₂C₂O₄ (CO₂ source), which resulted in fluid-saturated samples with mole fractions of water ($X^f_{H_2O}$) between 1.0 and ~ 0.1 . The capsules were welded shut by arc welding. After the experimental runs, $X^f_{H_2O}$ was measured after opening the capsule using a conventional weight-loss method (e.g. Ebadi & Johannes, 1991). Therefore, capsules were weighted after the runs and cooled by putting them into liquid nitrogen to freeze H₂O in the fluid phase. Frozen capsules were pierced with a steel needle and warmed up to room temperature. By subsequent weighting, the mass of CO₂ in the fluid was determined. The capsules were then placed into an oven at 110°C for 2-3 minutes and weighted to determine the mass of evaporated H₂O. It has to be noted that the technique to determine the mass of free CO₂ in the capsule does not discriminate between CO₂ and N₂. An entrapment of atmospheric nitrogen in the experimental charge during loading the capsules was estimated to be negligible (0.5 to 4.0 mol%, Tamic *et al.*, 2001). As main source of errors of the mole fractions of H₂O in the fluid we considered the uncertainty in the weighing of the capsule before and after piercing. Additional uncertainty induced by atmospheric nitrogen was taken in account (0.007 mol% for H₂O and 0.02 mol% for CO₂; Tamic *et al.*, 2001). In capsules, where weight-loss procedure of determining of fluid composition failed, mole fractions of H₂O and CO₂ in the fluid were calculated by mass-balance, using initial amounts of loaded volatiles and rock powder and measured concentrations of volatiles in run product glasses. Nevertheless, our determined mole fractions of water are probably still afflicted with relatively high errors due to difficulties in fluid measurements.

Phase equilibrium experiments were conducted in cold sealed pressure vessels or in internally heated pressure vessels, depending on the P-T conditions (see next sections). Temperatures ranged from 1000 to 800°C and pressures ranged from 300 to 50 MPa. The experimental annealing duration varied between a minimum of four days to a maximum of 14 days before quenching.

Cold seal pressure vessel (CSPV)

Externally heated cold seal pressure vessels (CSPV) were used for experiments at lower temperatures ($\leq 850^\circ\text{C}$). The vessels are made of an alloy containing mainly nickel and were pressurized with water (Fig. 2.1), allowing a maximum pressure of 500 MPa. The temperature variations were less than 5°C , while the accuracy in temperature was estimated to be $\pm 10^\circ\text{C}$. Pressure was measured with pressure transducer calibrated against a strain gauge manometer. The accuracy of pressure measurements were 1 MPa and pressure variations during the experiments were less than ± 5 MPa. Inside the CSPV, the redox conditions were buffered by the reaction of water with a solid oxygen buffer (added as a mixture of Ni and NiO powders, i.e. NNO buffer). An effective in-diffusion of H_2 through the walls of Au capsules fixed the hydrogen fugacity (f_{H_2}) in the capsules and controlled the redox conditions in the systems via the reaction of $\text{H}_2 + \frac{1}{2} \text{O}_2 = \text{H}_2\text{O}$. Hence, in the H_2O -saturated systems, the redox conditions were close to NNO buffer while in the $\text{H}_2\text{O}+\text{CO}_2$ -bearing systems, the fugacity of f_{O_2} is expected to be about 0.5 log units lower. The cold autoclave, including the capsules, was inserted into the pre-heated external furnace to reduce the time of the heating process at the start of the experiment. The experiments were quenched by removing the autoclave from the furnace and cooling it with compressed air, while keeping the final pressure constant. The quench rate was approximately 150°C per minute at the beginning of the cooling and was sufficient to avoid quench effects in rhyodacitic magma (e.g. Chevychelov *et al.*, 2008).

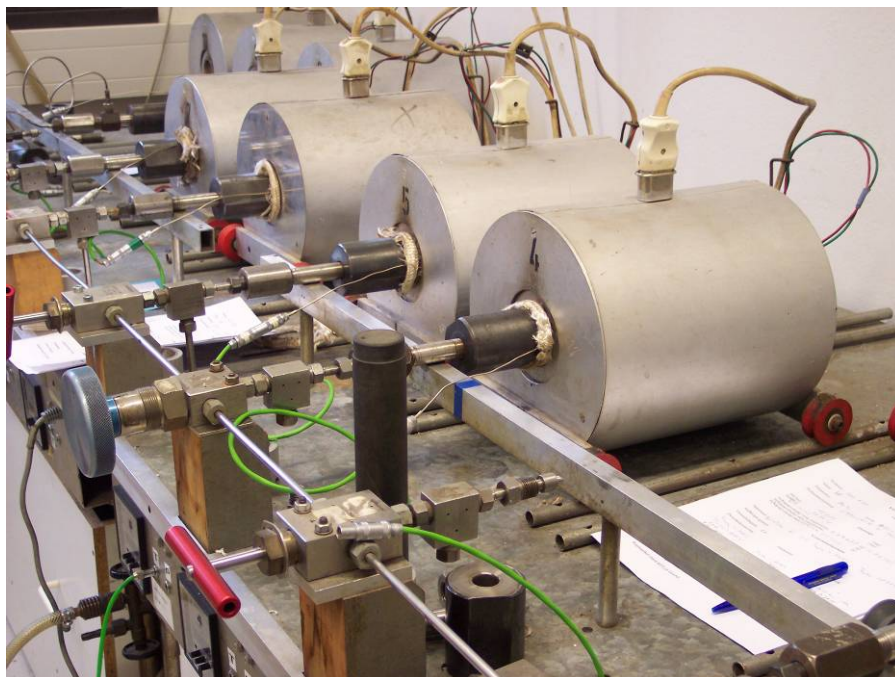


Fig. 2.1. Photo of externally heated pressure vessels (CSPV) at the high-pressure laboratory of the Institute for Mineralogy, Leibniz University Hannover, Germany.

Internally heated pressure vessels (IHPV)

Isobaric and decompression experiments at temperatures higher than 850°C were conducted in internally heated pressure vessels (IHPV; see Fig. 2.2). The general characteristics of IHPVs were already explained by Holloway (1971) and further details can be also found in Berndt *et al.* (2002). The pressure vessel consists of several components; (a) an autoclave, (b) an intensifier, (c) a pre-pressure pump and (d) a switchboard. The autoclave is made of tool-steel cylinder surrounded by water-cooled copper-tube windings, where a resistance furnace is inserted from the top and a sample holder is inserted from the bottom; both are fixed onto closure heads sealing the vessel.

Argon (Ar) is the pressurizing gas and maximum pressures of 500 MPa and maximum temperatures of 1250°C can be reached. Additionally, it is possible to adjust the oxygen fugacity (fO_2) to reducing conditions in the experimental system by adding hydrogen (H_2) to the argon pressure medium. Furthermore, in each individual capsule is the prevailing oxygen fugacity dependent on the water activity (a_{H_2O}). Here, fO_2 is controlled by the equilibrium reaction of water dissociation ($H_2 + 1/2 O_2 = H_2O$) inside the capsules. Water activities for every run were calculated using activity coefficients after Aranovich & Newton (1999) and molar volumes of pure H_2O after Pitzer & Sterner (1994). The fO_2 was calculated for each experiment as $\log fO_{2,capsule} = \log fO_{2,vessel} + 2\log(a_{H_2O})$ (see also Botcharnikov *et al.*, 2008) and correlated to the NNO buffer regression data of O'Neill (1987).

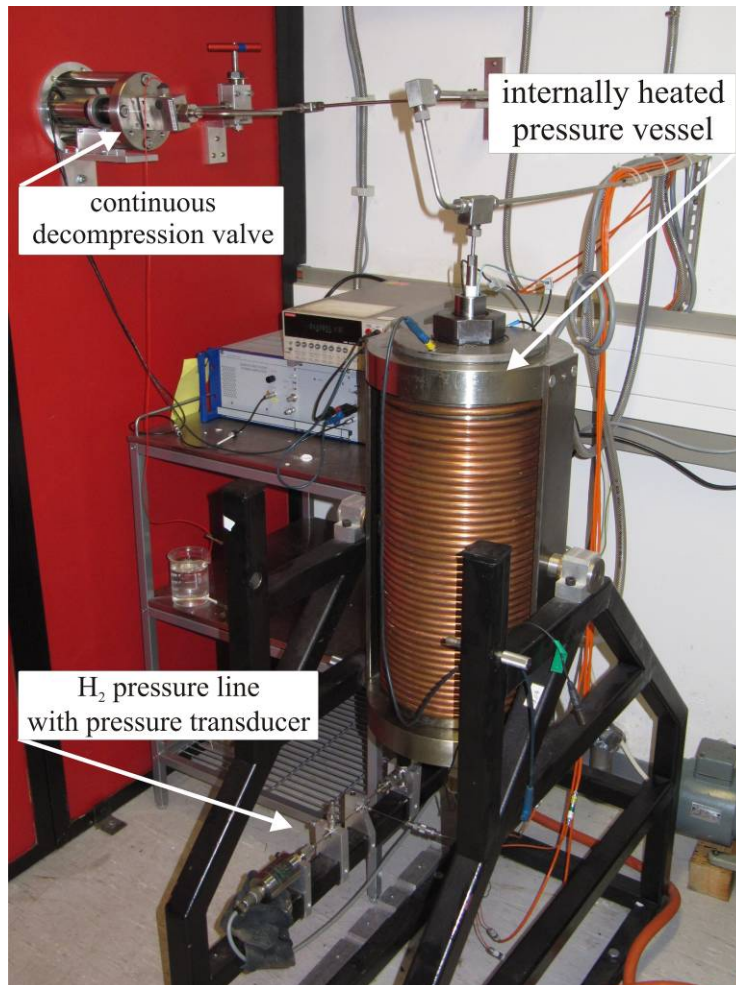


Fig. 2.2. Picture of a the internally heated pressure vessel (IHPV) at the laboratory of the Institute for Mineralogy, Leibniz University Hannover, Germany, with H₂-line at the bottom and a new developed decompression valve on top.

Oxygen fugacity values for each experiment are reported in *Appendix* Table A.1. In case of experiments with reduced f_{O_2} , the vessel is only pressurized until a certain pre-pressure at room temperature, so final pressures are reached by the heating process itself (heating rate of 30°C/min) while decoupling the autoclave from the intensifier (no pressure automatic in use). This shall prevent the loss of hydrogen in the system, which would result in more oxidizing conditions. Pressure transducers, having an accuracy of $\pm 1\%$, are installed for the autoclave and the intensifier, and are connected to displays in the switchboard. The H₂ partial pressure can be detected during the experimental run with the help of a so-called Shaw-membrane (Shaw, 1963). It consists of a platinum (Pt) tube which is welded shut on one side, then filled with corundum (Al₂O₃) powder and a one-hole ceramic capillary. To seal the membrane a steel capillary, fixed in a steel plug, is soldered to the Pt tube. Hydrogen diffuses through the wall of the Pt tube in the hot zone of the experiment, while Argon molecules are too big. Through osmosis an equilibrium between

the outside pressure (inside the autoclave) and the inside pressure (inside the membrane including the steel capillary) of hydrogen will be enabled. At the end of the steel capillary, outside the IHPV, a pressure transducer detects the actual H₂ partial pressure inside the autoclave (Berndt *et al.*, 2002).

The rapid-quench (RQ) sample holder used at Hannover was described by Berndt *et al.* (2002) and consists of four S-type thermocouples (Pt-Pt₉₀Rh₁₀), a H₂-membrane and a Pt quench wire (0.5 mm thickness). The upper and the lower most thermocouples (distance ca. 25 mm) are connected to the *EUROTHERM* program controller, which enables the precise adjustment of the temperatures created by the two molybdenum wire (thickness 0.5 mm) windings of the furnace. The two middle thermocouples measure the sample temperatures. Up to five samples are being packed into a basket (maximum length 30 mm), hanging inside the ceramic falling tube while being connected through a ceramic ring to the quench wire (0.3 mm thickness). After a successful experimental run, capsules are rapidly quenched (150 °C/sec) by melting of the quench wire which results in immediate falling of the capsule (basket) into the cold zone of the sample holder (Berndt *et al.*, 2002).

Analytical methods

Electron microprobe analysis (EMPA)

Major element composition of solid experimental products, composed of minerals and glass, were analyzed with a *Cameca SX-100* microprobe using 15 kV as the acceleration voltage. Glass analyses were conducted with 4 nA beam current, a defocused electron beam (5-10 µm diameter), and peak counting times of 4 sec for Na and K and 8 sec for the other elements. Mineral phases were analyzed using a 15 nA beam current and a focused electron beam. Multiple measurements (minimum 3) were made for each phase to reduce possible analytical errors and to check the homogeneity.

Fourier transform infrared spectroscopy (FTIR)

Fourier transform infrared spectroscopy (FTIR) was used to estimate concentrations of dissolved water and carbon dioxide in the experimental glasses, using a *Bruker IFS88 FTIR* spectrometer with a connected *IRscopeII* microscope. For NIR (near infra-red) analysis we used a tungsten light source, a CaF₂-beam splitter and a MCT-detector. The spectral resolution was 4 cm⁻¹. One hundred scans per background and per sample were collected. The analyzed area was 80 x 80 µm. For MIR (mid infra-red) analysis we used a global light source, a KBr-beam splitter and a MCT-detector. The spectral resolution was 2

2. PHASE STABILITY EXPERIMENTS

cm⁻¹. Fifty scans per background and per sample were collected. The analyzed area was 80 x 80 μm. The concentrations of molecular water and water dissolved as OH⁻ were calculated from the heights of the peaks at 5200 cm⁻¹ and 4500 cm⁻¹, respectively, and the concentration of carbon dioxide (CO₂) was calculated from the heights of the peak at 2350 cm⁻¹, using a tangential baseline correction. The extinction coefficients of water species in the glasses for the calculation of water concentration in the glasses were estimated using an empirical calibration of Ohlhorst *et al.* (2001) and they varied from 1.34 to 1.97 l/mol*cm for the 5200 cm⁻¹ peak and from 1.13 to 1.67 l/mol*cm for the 4500 cm⁻¹ peak, using the straight line (TT) baseline correction method. Since the compositions of glasses were close to rhyolites, glass densities were calculated applying the empirical calibration after Withers & Behrens (1999): density (in g/L) = 2390 – 17.0 * wt% H₂O. Sample thicknesses were determined with a *Mitutoyo* digital micrometer (precision of ± 2 μm). The glass thicknesses were chosen rather small, varying between 70 and 100 μm, to avoid noises induced by bubbles and microlites. The low sample thickness results in relatively low absorption from which a possible error of about 20 % in peak heights can be assumed. Care was taken to choose areas without or with small amount of bubbles and crystals. However, since they contain minerals and since bubbles could not be completely avoided, the uncertainty of the calculated water concentration is high (± 20 relative %) and the data can only be used to discuss qualitatively the relative variations of water concentrations. In some samples water and carbon dioxide concentrations were not determined by NIR and MIR, respectively, because doubly polished slices of good quality could not be prepared (cavities were still filled with fixation glue resulting in large disturbances in the absorption spectra). The average values (and standard deviations) of NIR and MIR measurements repeated at different locations on higher quality samples and are shown in *Appendix Table A.2*.

RESULTS

Phase stabilities

The experimental products consist of glass and mineral phases ± vesicles. It was able to distinguish chemically between the following mineral phases: orthopyroxene (Opx), clinopyroxene (Cpx), amphibole (Amph), plagioclase (Pl), quartz (Qtz) and Fe-Ti oxides (Ox, mainly ilmenite), see *Appendix Table A.1*. While the mineral phases Ox, Opx and Cpx were observed in nearly all of the end products of the phase stability experiments,

Amph, Pl and Qtz showed characteristic dependences on the P-T- $X^{\text{fl}}\text{H}_2\text{O}$ conditions, which will be described in detail in the following.

Phase stabilities at given pressures

Fig. 2.3 a-d show phase stability diagrams (T- $X^{\text{fl}}\text{H}_2\text{O}$) at constant pressures ranging from 300 to 50 MPa. At 300 MPa, Amph is only stable at low temperatures (less than $\sim 875^\circ\text{C}$) and at higher mole fractions of water ($X^{\text{fl}}\text{H}_2\text{O} > 0.5$), see orange fields in Fig. 2.3a. Pl minerals are present at all investigated temperatures (1000-800°C) assumed that the mole fraction of water is less than 0.5. Pl is present at all $X^{\text{fl}}\text{H}_2\text{O}$ if the temperatures are less than $\sim 830^\circ\text{C}$. At 200 MPa, the stability fields of Amph and Pl are nearly similar to those at 300 MPa, compare Figs. 2.3a and 2.3b. Compared to 300 MPa, the stability line of Pl (dashed green line) is only slightly shifted to higher mole fractions of water at 200 MPa (at given temperatures). The Amph stability line (dashed orange line) is shifted slightly to lower temperatures with decreasing pressure from $\sim 870^\circ\text{C}$ at 300 MPa to $\sim 850^\circ\text{C}$ at 200 MPa at high $X^{\text{fl}}\text{H}_2\text{O}$ (> 0.5). At pressures of 300 and 200 MPa, liquidus conditions (grey colored fields in Fig. 2.3a and 2.3b) were determined in experiments at 1000°C and with the two highest conducted mole fractions of water ($X^{\text{fl}}\text{H}_2\text{O} > 0.8$). At lower pressures, no experiments were run at 1000°C .

At 100 MPa (Fig. 2.3c) and at temperatures $\leq 950^\circ\text{C}$, Pl crystallized at all mole fractions of water. At this condition, the stability field of Amph is restricted to $T \leq 800^\circ\text{C}$ and $X^{\text{fl}}\text{H}_2\text{O} > 0.8$, see orange line and field in Fig. 2.3c. The phase stability diagram at 50 MPa and at temperatures of $\leq 950^\circ\text{C}$ (Fig. 2.3d) is very similar to that at 100 MPa with one exception: Amph is not stable at the investigated conditions.

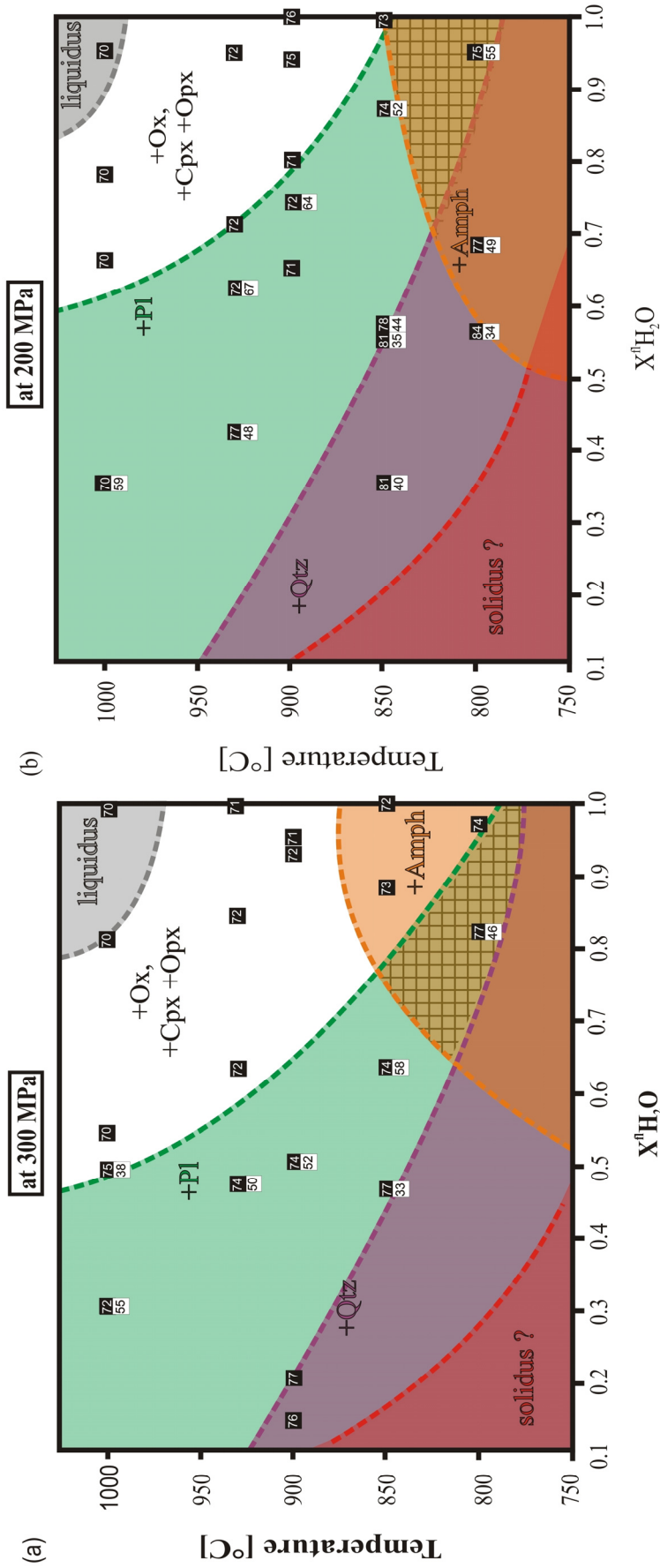


Fig. 2.3 a-b. Phase stability diagrams at constant pressures of 300 MPa (a) and 200 MPa (b) as a function of the mole fraction of water ($X^{\text{H}_2\text{O}}$; x-axis) and on the temperature (y-axis). Dashed lines represent the stability lines for the corresponding mineral phases. While, their positive occurrences are highlighted by the corresponding colored fields (Pl: green color; Amph: orange color; Qtz: purple color; Ox: Cpx and Opx: white color), which are to some degree overlapping. The solidus is marked by red and the liquidus by grey colors. The black boxes represent individual experiments and the SiO_2 content of the residual melt (normalized to 100 wt%) is given by the white numbers (in wt%), while the black boxes below indicate the determined average An content of crystallized plagioclase minerals (in mol%). The checked fields represent the experimental conditions under which the mineral assemblage observed in natural Unzen groundmass (Nakada & Motomura, 1999; Venzky & Rutherford, 1999) is stable.

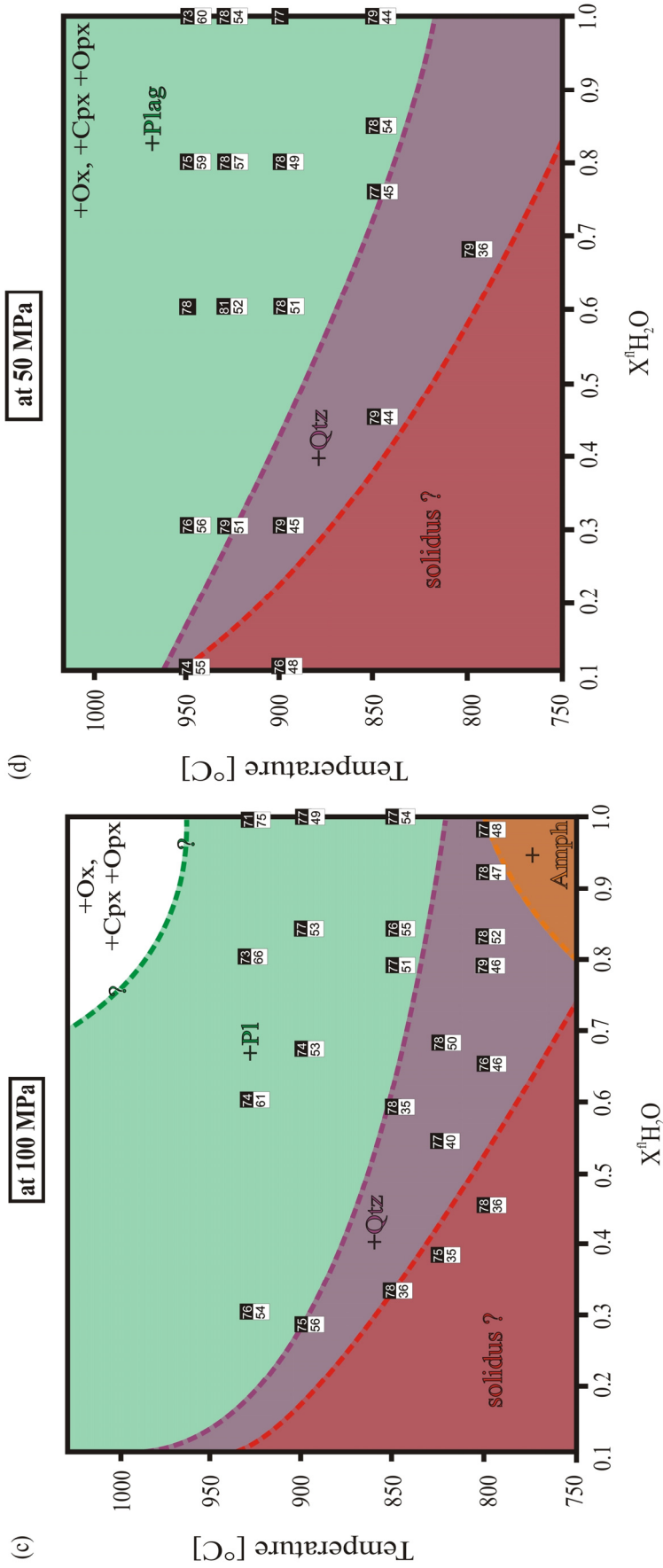


Fig. 2.3 c-d. Phase stability diagrams at constant pressures of 100 MPa (c) and 50 MPa (d) as a function of the mole fraction of water ($X^{\text{H}_2\text{O}}$; x-axis) and on the temperature (y-axis). Dashed lines represent the stability lines for the corresponding mineral phases. For detailed symbol explanations see figure caption 2.3. a-b.

2. PHASE STABILITY EXPERIMENTS

Phase stability at constant temperatures

Phase stability diagrams (P- $X^{\text{fl}}\text{H}_2\text{O}$) at constant temperatures ranging from 850 to 930°C are plotted in Fig. 2.4 a-c. At 850°C (Fig. 2.4a), Amph is only stable at pressure ≥ 200 MPa and at mole fractions of water higher ~ 0.7 . Pl is stable at all conditions except at pressures ≥ 200 MPa and at mole fractions of water ≥ 0.8 . At higher temperatures of 900 and 930°C (Figs. 2.4 b-c, respectively), amphibole is not stable anymore, while the stability lines of Pl (green dashed lines) shift to lower $X^{\text{fl}}\text{H}_2\text{O}$ values and to slightly lower pressures (minimum P of ~ 150 MPa at 930°C) with increasing temperatures from 900 to 930°C. At 930 °C (Fig. 2.4c) and 300 MPa, Pl is only stable at $X^{\text{fl}}\text{H}_2\text{O} < 0.55$.

Two overall trends can be observed from the given SiO_2 contents of the residual melts (white numbers in black boxes) and from the determined anorthite (An) contents of crystallized Pl (black numbers in white boxes) in all presented phase diagrams (Figs. 2.3 a-d and 2.4 a-c). First, the SiO_2 content of the residual melts increases with decreasing P-T- $X^{\text{fl}}\text{H}_2\text{O}$ conditions, while secondly the An content of crystallized plagioclases decreases simultaneously with decreasing P-T- $X^{\text{fl}}\text{H}_2\text{O}$ conditions.

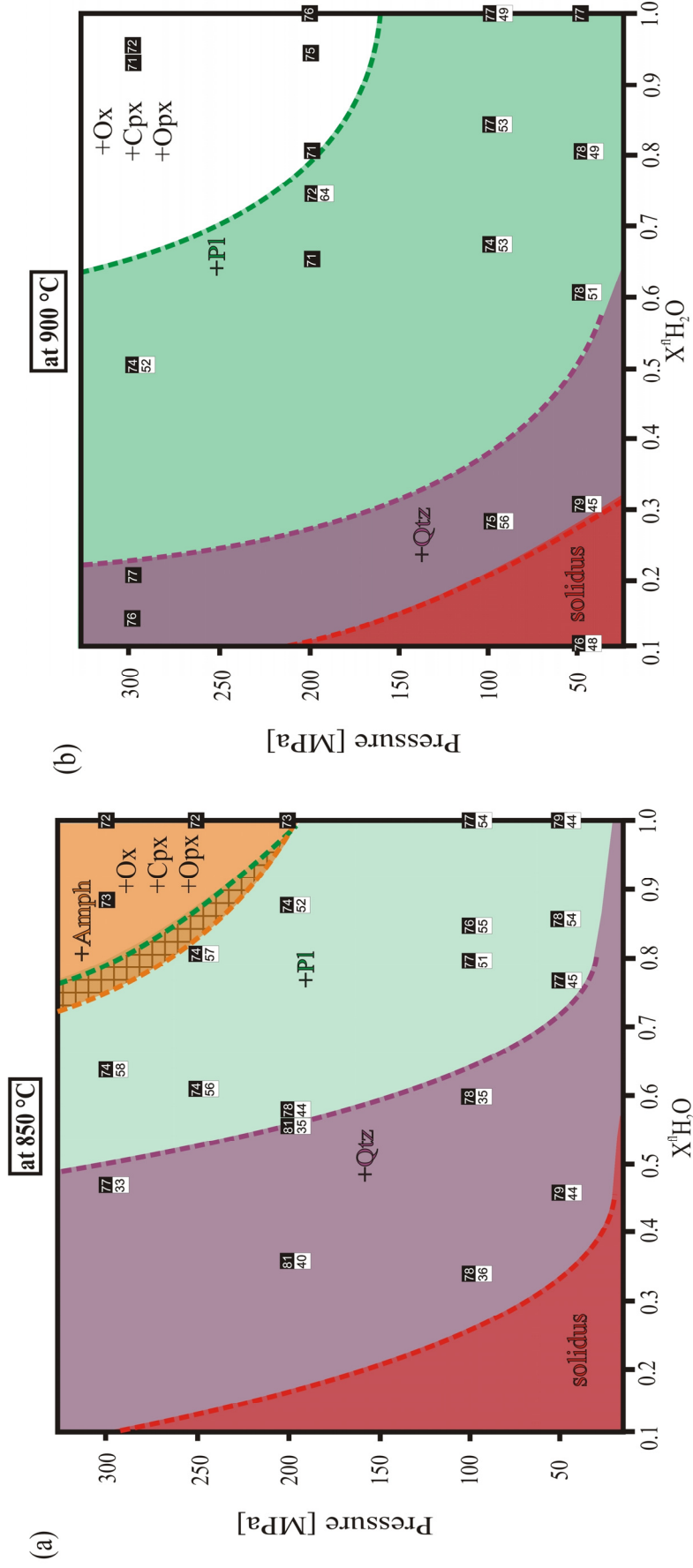


Fig. 2.4 a-b. Phase stability diagrams at constant temperatures of 850°C (a) and of 900°C (b) in dependences on the mole fraction of water ($X^{\text{H}_2\text{O}}$; x-axis) and on the pressure (y-axis). Dashed lines represent the stability lines for the corresponding mineral phases. For detailed symbol explanations see figure caption 2.3. a-b.

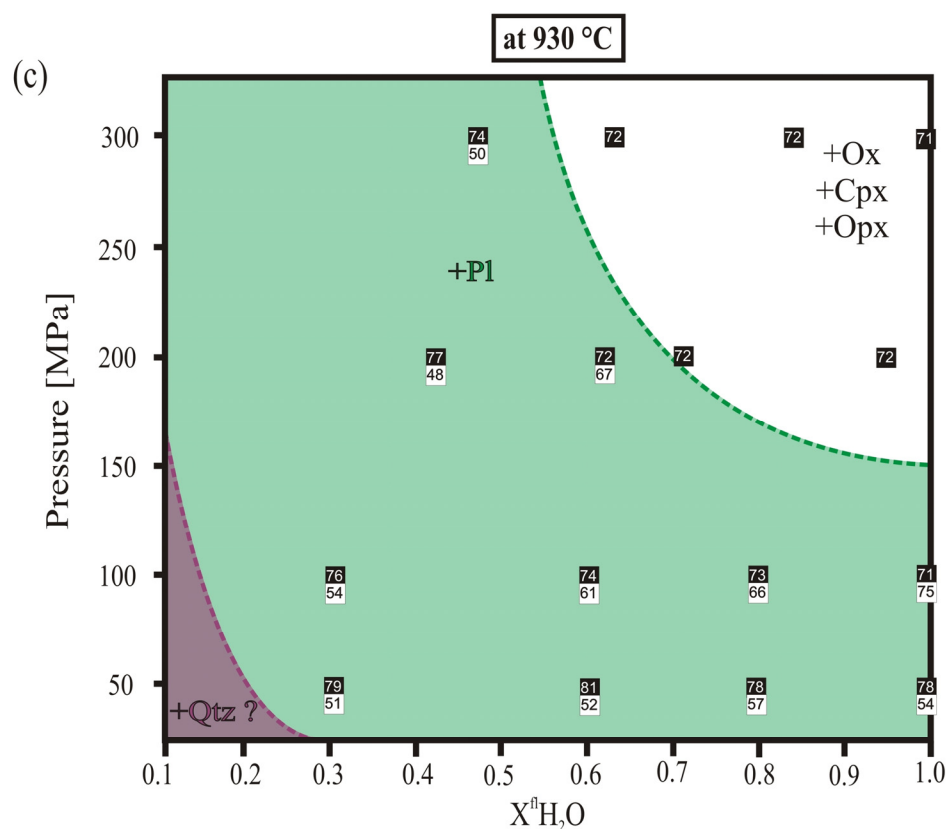


Fig. 2.4 (c) Phase stability diagrams at constant temperatures of 930°C in dependences on the mole fraction of water ($X^{\text{H}_2\text{O}}$; x-axis) and on the pressure (y-axis). Dashed lines represent the stability lines for the corresponding mineral phases. For detailed symbol explanations see figure caption 2.3. a-b.

DISCUSSION

The mineral assemblage (Pl, Amph, Opx, Cpx, Ox and Qtz) crystallized in our phase stability experiments is consistent with those of other (experimental) studies (e.g. Rutherford & Hill, 1993; Sato *et al.*, 1999; Holtz *et al.*, 2005 and Larsen, 2005; see also Fig. 3.2 in *chapter 3.1.1.*) which can be related to our rhyodacitic system, although those studies were performed for water-saturated ($X^{\text{H}_2\text{O}}=1.0$) systems only. Major differences can be found in the individual mineral stability fields, which are obviously sensitive to the investigated P-T- $X^{\text{H}_2\text{O}}$ conditions and the chemical composition of the used starting materials, especially for Amph minerals. The compilation of water-saturated literature data, see Fig. 2.5b, suggests that Amph is either stable down to pressures of 40-50 MPa (Sato *et al.*, 1999; dashed lines) at temperatures below $\sim 850^\circ\text{C}$, or only stable down to pressure of 60-80 MPa at temperatures below $\sim 860^\circ\text{C}$ (Venzky & Rutherford, 1999; solid lines). While our experimental study show that at these water-saturated conditions

($X^{\text{fl}}\text{H}_2\text{O}=1.0$, see Fig. 2.5a) Amph is not stable at temperatures above $\sim 880^\circ\text{C}$ at all investigated pressures (≤ 300 MPa) and that Amph stability was not observed at pressure below ~ 100 MPa. Our determined Amph stability field is narrower than those determined by Sato *et al.* (1999) and Venezky & Rutherford (1999), which could be explained by the slightly differing starting compositions, see Table 2.1. As there are already major discrepancies between the literature data (compare dashed and solid lines in Fig. 2.5b), especially when looking at their liquidus conditions at high temperatures, it can be assumed that this rhyodacitic groundmass system is very sensitive to minor changes in chemical composition leading to variable phase stability fields.

The observed trends of increasing silica content and of decreasing anorthite content with decreasing P-T- $X^{\text{fl}}\text{H}_2\text{O}$ conditions are in agreement with former studies on crystallization processes (e.g. Holtz *et al.*, 2005; Larsen, 2005). Additionally, it is known that the volatile component H_2O has a major influence on the liquidus temperature of silicate melts (e.g. Johannes & Holtz, 1996). As the mole fraction of water ($X^{\text{fl}}\text{H}_2\text{O}$) in the system decreases, the increase of the liquidus temperature results in an increase of the mineral proportion in the system. This crystallization of mineral phases (here: mainly plagioclase) from the melt is accompanied by the enrichment of the residual melt in SiO_2 leading to the crystallization of quartz at conditions of oversaturation.

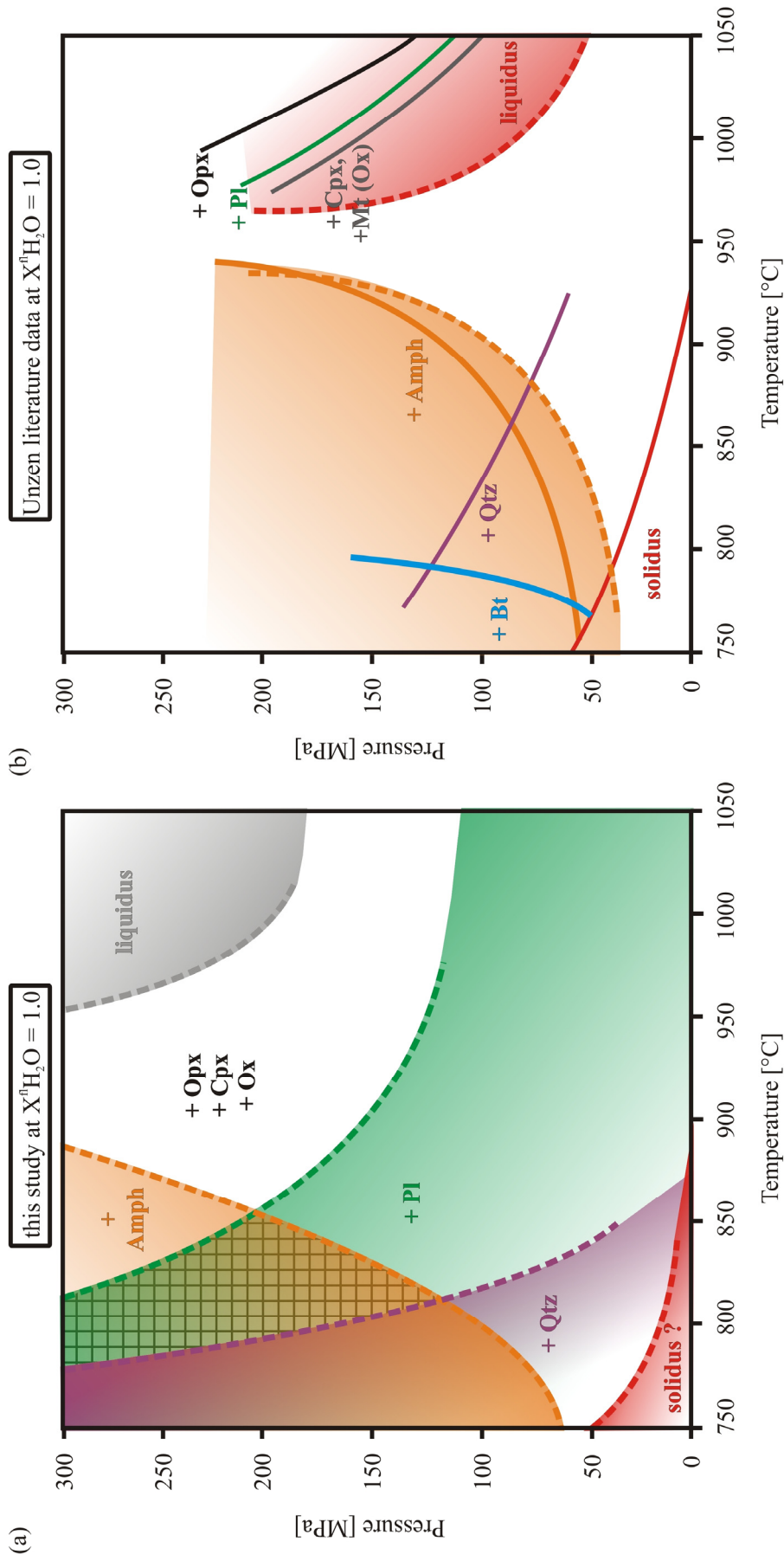


Fig. 2.5 a-b. Phase stability diagram of Unzen groundmass composition at water-saturated conditions ($X^nH_2O=1.0$): (a) results of our study and (b) compilation of literature data from Sato *et al.* (1999) dashed lines and from Venezky & Rutherford (1999) solid lines. The chemical composition of the starting materials of our study, of that of Sato *et al.* (1999) and that of Venezky & Rutherford (1999) can be found in Table 2.1. Abbreviations: Pl=plagioclase, Amph=amphibole, Opx=orthopyroxene, Cpx=clinopyroxene, Qtz=quartz, Bt=biotite, Mt=magnetite, Ox=oxide. The checked field in (a) represents the conditions under which the mineral assemblage observed in natural Unzen groundmass (Nakada & Motomura, 1999; Venezky & Rutherford, 1999) is stable.

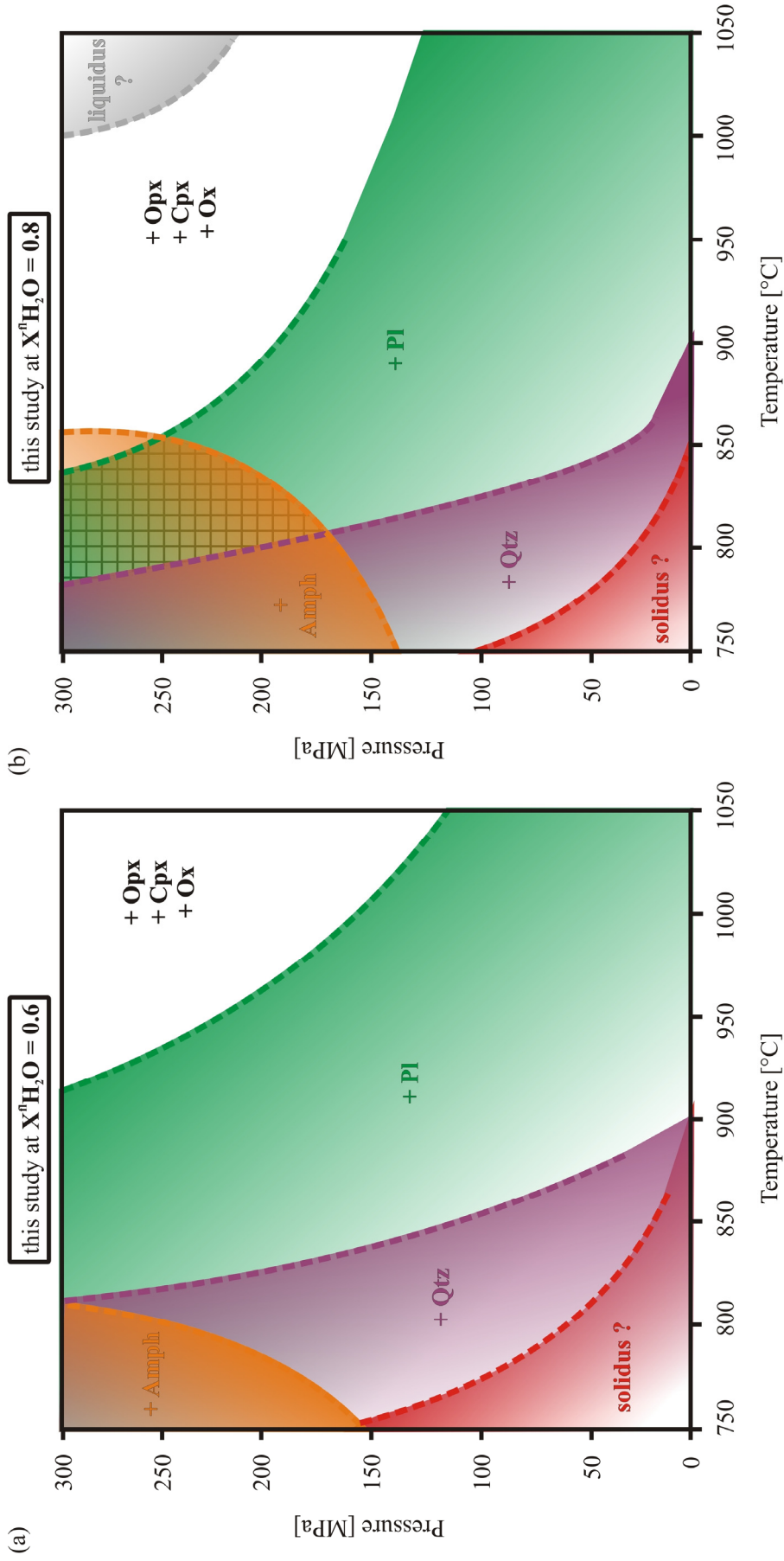


Fig. 2.6 a-b. Results on phase stabilities of Unzen groundmass composition at fluid-saturated conditions of this study at (a) $X^{\text{fl}}\text{H}_2\text{O}=0.6$ and (b) $X^{\text{fl}}\text{H}_2\text{O}=0.8$. Abbreviations and symbol explanations see figure caption 2.3 a-b.

2. PHASE STABILITY EXPERIMENTS

In Figs. 2.3 a-b, 2.4a, 2.5a and 2.6 a-b, the checkered areas represent the P-T-X^{H₂O} conditions under which the natural Unzen groundmass mineral assemblage was experimentally reproduced. These conditions vary between pressures of 300-100 MPa, mole fractions of water of 1.0 - 0.65 and temperatures $\leq \sim 870^\circ\text{C}$. As magma storage conditions of the mixed magma were suggested by earlier (analytical and experimental) studies to lie within the pressure range of minimum 160 MPa (Venezky & Rutherford, 1999) to a maximum of 300-400 MPa (Nishi *et al.*, 1995) and having a temperature range of $900 \pm 30^\circ\text{C}$ (Venezky & Rutherford, 1999), it can be assumed that the Amph phenocrysts in the mixed magma were not in equilibrium with the silicate melt after mixing. Consequently, natural Amph microlites must have crystallized only during the subsequent magma ascent while crossing the Amph stability field emphasized in this study.

Petrological studies of the natural Unzen dome samples distinguished between hornblende phenocrysts and groundmass pargasites (e.g. Nakada & Motomura, 1999; Sato *et al.*, 1999). Natural hornblende phenocrysts have usually lower Al₂O₃ contents and slightly lower Mg numbers (Mg#) when compared to natural groundmass pargasites, see Fig. 2.7. Our crystallized Amph microlites produced during phase stability experiments (green circles plotted in Fig. 2.7) have Al₂O₃ contents ranging from ~ 7 -10 wt% and Mg# of 0.60 to 0.73, which are close to natural phenocryst hornblende compositions determined by Nakada & Motomura (1999) and also similar to some natural groundmass pargasites determined by Sato *et al.* (1999), having also Al₂O₃ contents of less than the usual minimum value of 10 wt%.

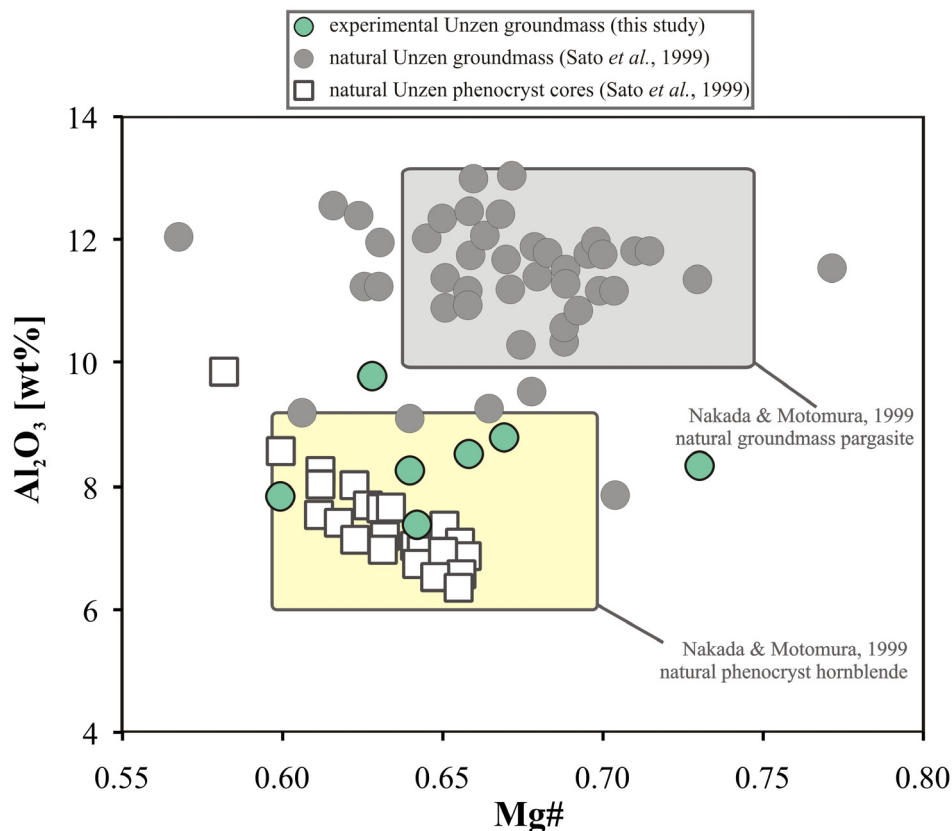


Fig. 2.7. Al_2O_3 , vs. Mg\# ($= \text{Mg}/[\text{Mg}+\text{Fe}]$) of amphiboles determined for natural Unzen dome samples and for our experimentally reproduced microlites. Natural phenocryst cores and groundmass pargasites given by Sato *et al.* (1999) are plotted by empty squares and by grey-filled circles, respectively. Compositional ranges by Nakada & Motomura (1999) of natural groundmass pargasites and natural phenocryst hornblende are indicated by the grey-shaded square and by the yellow square, respectively. Our experimentally reproduced Amph microlites are plotted as green circles.

CONCLUSION

The mineral assemblage observed in natural erupted rocks was successfully reproduced by our phase stability experiments, providing details on the magma storage conditions prior to the 1991-1995 Unzen eruption as well as on the magma ascent dynamics.

As Amph microlites are preserved in natural surface rocks but are not in equilibrium at pressures below ~ 80 MPa in the rhyodacitic Unzen groundmass system, two conclusions can be made: (1) the mixed Unzen magma must have crossed $\text{P-T-X}^{\text{fl}}\text{H}_2\text{O}$ conditions that allow the crystallization of Amph microlites (and the overgrowth of Amph phenocrysts) during ascent and (2) the decompression rate of the rising magma from depth to surface pressures had to be fast enough so that Amph crystals did not dissolve entirely during the magma ascending process below their stability field.

3. DECOMPRESSION EXPERIMENTS

Isothermal magma decompression was simulated at 850°C (in CSPVs) and at 930°C (in IHPVs), which covers the range of estimated Unzen magma storage temperatures at depth (870-930°C; Venezky & Rutherford, 1999; Holtz *et al.*, 2005). Furthermore, two main approaches were used for decompression: high pressure decompression (HPD; *chapter 3.1*) and low pressure decompression (LPD; *chapter 3.2*). For the HPD approach, a starting pressure of 300 MPa was used, which is closely corresponding to magma mixing and storage conditions at Mt. Unzen prior to the 1991-1995 eruption. In this case, decompression was conducted until a final pressure of 50 MPa, corresponding to the pressure at depth that was targeted during the Unzen Scientific Drilling Project (~1.5 km; Nakada *et al.*, 2005, see also *chapter 1.1*). In LPD experiments, we wanted to simulate the final stage of magma ascent until surface pressures of 0.1 MPa.

Since natural magmas contain not only water but also other dissolved volatiles (mainly CO₂, SO₂ and HCl) and magma degassing is accompanied by a release of multi-component fluids, two series of HPD experiments were conducted: one using only water as a volatile component (H₂O-bearing) and the other one using a water and carbon dioxide (H₂O+CO₂-bearing) fluid mixture. While in LPD experiments, only the H₂O-bearing system was investigated as it is assumed that CO₂ is completely exsolved from the melt at these low pressures (e.g. Fogel & Rutherford, 1990; Behrens *et al.*, 2004; Liu *et al.*, 2005). Multiple decompression rates were investigated and were performed either as a single continuous pressure release or as a multi-step decrease in pressure, depending on the used pressure vessel and the decompression rate. The overall conducted decompression rates ranged from 20 to 0.0001 MPa/s, corresponding to ascent velocities of 2400 km/h to ~10 m/h.

This experimental approach can represent natural conditions during magma ascent in volcanic conduits (e.g. Hammer & Rutherford, 2002; Couch *et al.*, 2003), however it must be noted that in natural systems the actual ascent rates and temperatures might not be constant along the ascent path (e.g. Noguchi *et al.*, 2008a; Nakada & Motomura, 1999). After the experiments, the quenched samples have been analyzed for compositional and textural changes and compared with natural rocks from Unzen.

3.1. High pressure decomposition (HPD)

The main focus in HPD experiments is the magma ascent from a starting pressure of 300 MPa to a final pressure of 50 MPa at both investigated temperatures of 850°C (set-I; *chapter 3.1.1*) and 930°C (set-II; *chapter 3.1.2*), see Fig. 3.1. Two fluid-saturated systems are investigated: H₂O-bearing system ($X^{\text{fl}}\text{H}_2\text{O}=1.0$) and H₂O+CO₂-bearing system ($X^{\text{fl}}\text{H}_2\text{O}=0.6$).

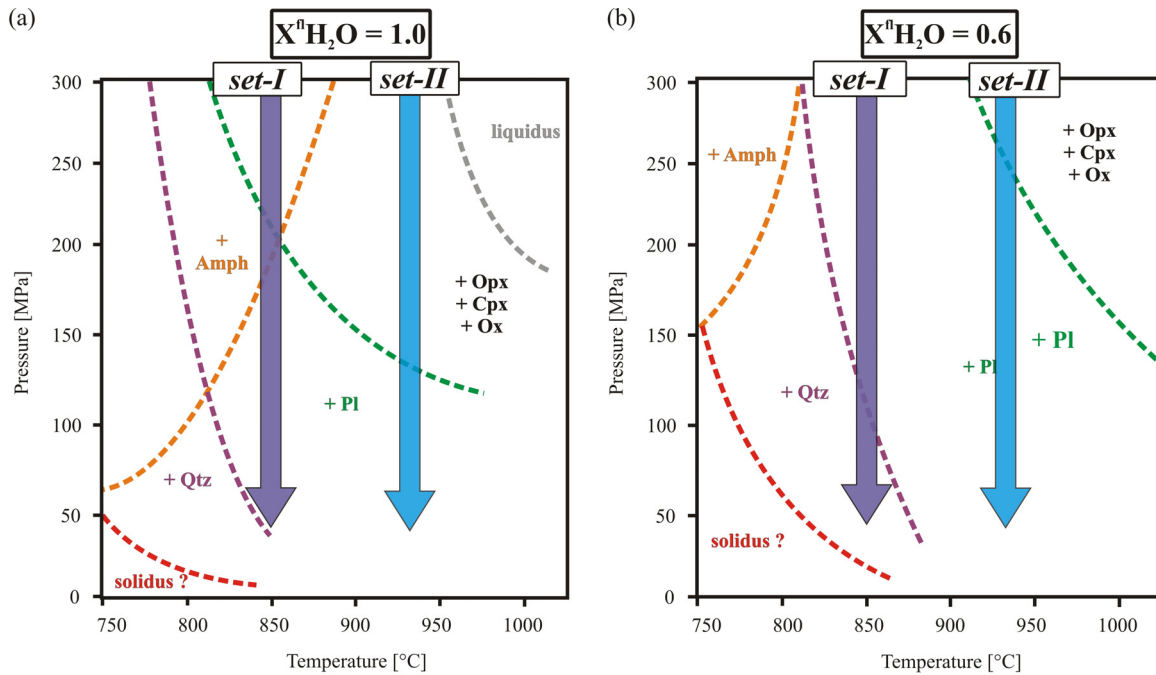


Fig. 3.1. Schematic phase diagram for fluid-saturated rhyodacitic magma, derived from this study *chapter 2* (phase stability experiments). The purple and blue arrows show the isothermal decompression paths of HPD set-I and set-II, starting from 300 MPa down to final 50 MPa at temperatures of 850°C and 930°C, respectively.

3.1.1. HPD at low-temperature (850 °C; set-I) – modified after *Journal of Petrology* paper Cichy et al. (2011)

Vesiculation and Microlite Crystallization Induced by Decompression: A Case Study of the 1991-95 Mt Unzen Eruption (Japan)

SARAH B. CICHY*, ROMAN E. BOTCHARNIKOV, FRANÇOIS HOLTZ AND HARALD BEHRENS
 INSTITUT FUER MINERALOGIE, LEIBNIZ UNIVERSITAET HANNOVER, CALLINSTR. 3, D-30167 HANNOVER, GERMANY

ABSTRACT

Isothermal decompression experiments were performed to simulate magma ascent at Unzen volcano from depths of magma storage to shallow level, corresponding to pressure decrease from 300 to 50 MPa. A partially crystallized synthetic rhyodacitic magma (representing equilibrium conditions at 850°C and 300 MPa) was used as a starting material with a composition identical to the groundmass composition of Unzen rocks erupted in 1991-1995. Decompression rates were varied from 0.0002 to 20 MPa/s. The experiments were fluid-saturated, either containing only water as a fluid component (H₂O-bearing) or containing a water and carbon dioxide mixture (H₂O+CO₂; initial mole fraction of H₂O in the fluid ~ 0.6).

The experimental products of the H₂O-bearing experiments consist of amphibole, pyroxenes, oxides and glass. Plagioclase microlites only nucleated and grew in experiments with the two lowest decompression rates of 0.0005 and 0.0002 MPa/s. The length of those plagioclases reaches up to 200-250 μm which is consistent with the size of plagioclase microlites observed in natural samples. The experimental products of the H₂O+CO₂-bearing system are composed of pyroxenes, oxides, glass and plagioclase. Plagioclase microlites in the H₂O+CO₂-system were already present in the starting assemblage and grew to a maximum size of ~80 μm.

Equilibrium concentrations of water in the residual glasses at final pressure of 50 MPa are reached at decompression rates ≤ 1 MPa/s for the H₂O+CO₂-bearing system and ≤ 0.1 MPa/s for the H₂O-bearing system. The bubble number density (BND) values range from 10^{3.7} mm⁻³ to 10^{5.6} mm⁻³ in the H₂O-bearing system and from 10^{4.6} mm⁻³ to 10^{6.4} mm⁻³ in the H₂O+CO₂-bearing system. In both systems, BND values decrease with decreasing decompression rate from 20 to 0.01 MPa/s, and increase with decreasing decompression rates < 0.01 MPa/s, which is interpreted to reflect a predominant bubble growth and bubble nucleation, respectively.

The onset of crystallization, observed from changes in the chemical composition of the residual melt, occurs at decompression rates < 0.1 MPa/s. At the lowest decompression rate (0.0002 MPa/s) the chemical composition of the residual melt in the H₂O+CO₂-bearing system becomes similar to the natural matrix glass composition. There is no significant variation of the microlite number density (MND) value as a function of the decompression rate. The MND values for plagioclases-only range from 10^{5.4} mm⁻³ to 10^{5.7} mm⁻³, whereas the MND values for the other phases range from 10^{5.3} mm⁻³ to 10^{5.9} mm⁻³.

Our experimental MND_{Pl} values are in the range of those from natural samples (10^5 - 10^6 mm^{-3}).

We show that the size of microlites nucleating and crystallizing during decompression (plagioclase in our experimental dataset) are useful to constrain magma ascent rates at the onset of the crystallization of the corresponding phase. Based on the size of plagioclase microlites and on the composition of residual melts, the average magma ascent rates of Unzen magmas in the pressure range of 200 to 50 MPa is estimated to be 10 to 50 m/h.

KEY WORDS: *crystallization; decompression experiments; magma ascent; Unzen volcano; vesiculation*

INTRODUCTION

Crystallization of a silicate melt during eruption is mainly caused by decompression-induced volatile loss. The most abundant volatile in magmas is H₂O, followed by CO₂, SO₂, H₂S and HCl. As the magma ascends, the exsolution of volatiles from the melt into bubbles increases the magma liquidus temperatures and therefore enables extensive groundmass crystallization. Vesicle and mineral nucleation and growth in the melt are significantly influenced by magma decompression rate (e.g. Rutherford & Hill, 1993; Geschwind & Rutherford, 1995; Simakin *et al.*, 1999, 2000; Hammer & Rutherford, 2002; Couch *et al.*, 2003; Martel & Schmidt, 2003; Browne & Gardner, 2006). Hence, magma ascent rate can control the eruption style (e.g. Sparks, 1978; Hurwitz & Navon, 1994), and groundmass textures of erupted rocks (e.g., crystal and vesicle sizes and number densities) may preserve important information about the decompression path and processes related to the magma ascent within the conduit. However, in order to interpret quantitatively parameters such as textures and compositions of magmatic phases and to evaluate the dynamics of a magmatic system, the processes of magma degassing and crystallization need to be simulated experimentally.

Up to now, most previous works focused either on bubble nucleation and growth or on microlite nucleation and growth as a result of decompression (see review of Hammer, 2008). Little attention has been given to the characterization of experimental samples in which bubbles and microlites nucleate and grow simultaneously. In this study we present the results of decompression experiments aimed at understanding bubble and microlite nucleation and growth in the magma ascending from magma chamber to shallow levels during the 1991-1995 eruption of Unzen volcano, Japan. These processes are simulated under controlled temperature and decompression rate. The results provide a unique

opportunity to compare data obtained experimentally with information from natural samples collected at the surface (e.g., Nakada *et al.*, 1999) and at depth (ICDP drilling, Nakada *et al.*, 2005). The experimental results on kinetics of decompression-induced nucleation and growth of bubbles and microlites are used to interpret textures of erupted products and to constrain processes occurring in magmatic conduit during the last Unzen eruption.

Magmatic system of Unzen volcano

The 1991-1995 eruption of Unzen volcano occurred as a result of mixing between andesitic and rhyolitic magmas in deep magma chambers followed by an ascent of mixed dacitic magma from depth (Venezky & Rutherford, 1999; Holtz *et al.*, 2005). Petrological and experimental studies indicate that before the eruption the mixed dacitic magma was stored at a minimum pressure of about 160 MPa, temperature from 870 to 930°C and it contained about 6 wt% H₂O (Venezky & Rutherford, 1999). The maximum pressure of the magma chamber is considered to be less than 300–400 MPa based on the geophysical data (maximum storage depth of about 11 km, Nishi *et al.*, 1995) and on the H₂O content of the melt inclusions in phenocrysts (up to 7–8 wt.% H₂O; Holtz *et al.*, 2005; Nishimura *et al.*, 2005).

During the eruption, a lava dome, composed of several lava lobes, was formed on the top of the volcano, producing numerous pyroclastic flows. The dome rocks consist of dacites with plagioclase, hornblende, biotite and quartz as main phenocrysts which are presumably originated from silicic rocks at depth (e.g. Nakada & Motomura, 1999). The groundmass is interpreted to be representative of the melt after magma mixing and it is composed of matrix glass, and microlites of plagioclase, pargasite, pyroxene, Fe-Ti oxides and apatite (Nakada & Motomura, 1999). Since the vesiculation and crystallization of Unzen groundmass mainly occurred during magma ascent, the textures and phase compositions of the groundmass in the dome lavas may provide constraints on processes of magma degassing and crystallization (Noguchi *et al.*, 2008a,b).

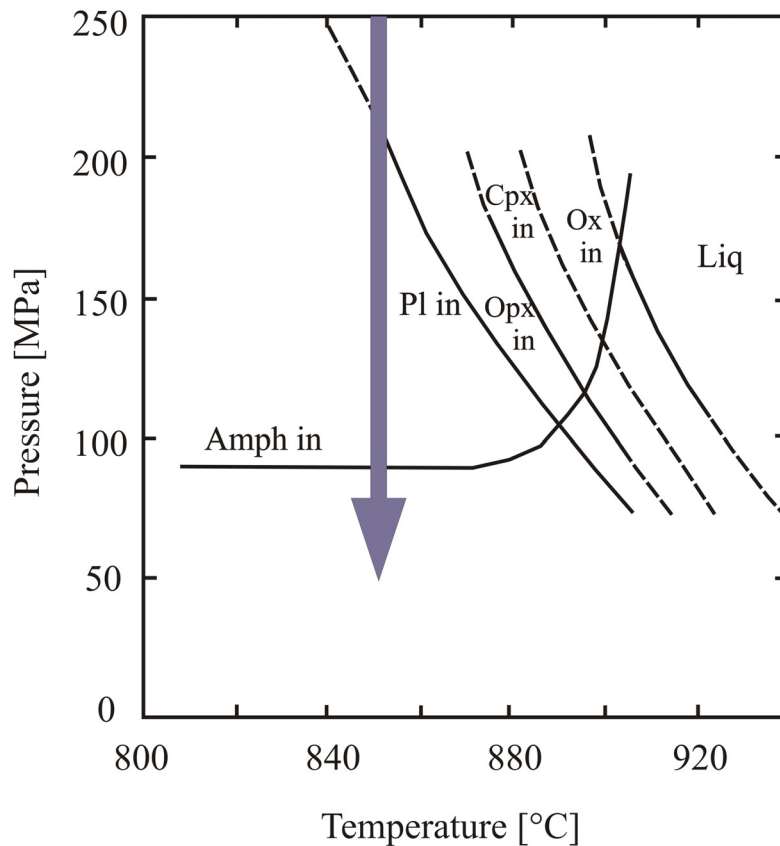


Fig. 3.2. Schematic phase diagram for water-saturated rhyodacitic magma, corresponding to groundmass of Unzen based on a compilation of experimental data from Rutherford & Hill (1993), Sato *et al.* (1999), Holtz *et al.* (2005) and Larsen (2005). The purple arrow shows the isothermal decompression path which is simulated in this study

The phase diagram in the pressure (P) – temperature (T) field for water-saturated rhyodacitic groundmass composition is shown in Fig. 3.2, based on the available literature data relevant to Unzen rhyodacitic system. At a given temperature, the stability fields of minerals expand with decreasing pressure due to exsolution of dissolved water from the melt. On the other hand, some minerals such as amphibole belong to high-pressure mineral phase assemblage and are not stable at pressures below 80-100 MPa. Consequently, an isothermal magma ascent to the surface should result in a change of the mineral assemblage and in a continuous variation of the composition, of the texture of groundmass microlites as well as of the vesicularity of erupted rocks. Similar variations are expected at water-undersaturated conditions in presence of a H₂O-CO₂-bearing fluid. However, a P-T phase diagram for the H₂O+CO₂-bearing Unzen rhyodacitic system at given mole fraction of water in the fluid phase ($X^{\text{fl}}\text{H}_2\text{O}$) is not available from literature data.

EXPERIMENTAL AND ANALYTICAL APPROACHES

Experimental strategy

Magma decompression was simulated at different decompression rates. After annealing at pressure of 300 MPa, corresponding to the depths of magma storage and mixing, the fluid-bearing magmas were isothermally decompressed to 50 MPa which is equivalent to the pressure at the final depth of ICDP drilling (Nakada *et al.*, 2005). Since natural magmas contain not only water but also other dissolved volatiles and magma degassing is accompanied by a release of multi-component fluids, two different fluid-bearing magmas, one containing only H₂O and the other saturated with a H₂O+CO₂ fluid, were investigated. The decompression experiments were performed either as a single continuous pressure release for fast decompressions or as a multi-step decrease in pressure. This approach can represent natural conditions during magma ascent in volcanic conduits (e.g. Hammer & Rutherford, 2002; Couch *et al.*, 2003), however it must be noted that in natural systems the actual ascent rates and temperatures might be not constant along the ascent path (e.g. Noguchi *et al.*, 2008a; Nakada & Motomura, 1999). After the experiments, the quenched samples have been analyzed for compositional and textural changes and compared with natural rocks from Unzen.

Starting material

A synthetic analogue of a rhyodacitic silicate melt was used as a starting material (Table 2.1 and 3.1). This composition, already investigated in several studies related to Unzen volcano (Sato *et al.*, 1999, 2005; Botcharnikov *et al.*, 2004), corresponds to the bulk groundmass of the 1991-1995 erupted magma. Hence, the decompression experiments are focused on the evolution of the rhyodacitic melt formed after magma mixing. This approach minimizes the possible effects of phenocrysts on nucleation and growth processes of bubbles and microlites.

Table 3.1. Experimental conditions and composition of residual melts for HPD set-1.

sample	X H ₂ O	Decompression rate [MPa/s] (method)	Decompression duration/steps	SiO ₂	TiO ₂	Al ₂ O ₃	FeO	MnO	CaO	Na ₂ O	K ₂ O	total [wt%]	H ₂ O _{glass} [wt%] ⁺
<i>Chemical composition of synthetic rhyodacitic starting glass</i>													
DA11	1	isobaric at 300 MPa		70.13	0.50	14.25	3.58	0.12	4.06	3.17	2.76		
				71.67 (0.36)	0.38 (0.06)	15.23 (0.04)	2.88 (0.27)	0.10 (0.12)	0.62 (0.10)	3.46 (0.18)	2.85 (0.12)	91.57 (0.26)	6.45 (0.32)
DA19	1	20 (continuous)	duration 13 sec	72.67 (0.20)	0.43 (0.08)	14.69 (0.21)	2.58 (0.24)	0.01 (0.08)	0.63 (0.09)	3.22 (0.22)	2.93 (0.30)	91.40 (0.74)	6.54 (0.35)
DA22	1	1 (continuous)	duration 4:10 min	72.01 (0.38)	0.37 (0.02)	14.61 (0.05)	2.67 (0.24)	0.02 (0.08)	0.65 (0.04)	3.37 (0.11)	3.02 (0.09)	96.31 (0.93)	3.41 (0.30)
DA13*	1	0.1 (continuous)	duration 41:10 min	72.33 (0.78)	0.43 (0.06)	14.75 (0.33)	2.56 (0.28)	0.05 (0.15)	0.59 (0.08)	3.36 (0.16)	2.79 (0.15)	96.11 (0.48)	2.05 (0.26)
DA64*	1	0.01 (multi-step)	steps: 31 MPa / 1 h	72.49 (0.53)	0.41 (0.08)	14.59 (0.20)	2.62 (0.31)	0.00 (0.08)	0.46 (0.11)	3.15 (0.22)	3.05 (0.12)	95.67 (0.58)	1.61 (0.27)
DA50	1	0.001 (multi-step)	steps: 40 MPa / 12 h	71.76 (0.28)	0.39 (0.02)	15.10 (0.07)	2.73 (0.16)	0.00 (0.03)	0.43 (0.05)	3.25 (0.19)	3.06 (0.07)	98.47 (0.69)	--
DA54**	1	0.0005 (multi-step)	steps: 20.4 MPa / 12 h	72.71 (0.31)	0.33 (0.04)	14.68 (0.23)	2.39 (0.21)	0.00 (0.07)	0.46 (0.10)	2.88 (0.17)	3.02 (0.24)	94.10 (0.63)	--
DA28**	1	0.0002 (multi-step)	steps: 8.4 MPa / 12 h	74.20 (1.15)	0.32 (0.04)	13.93 (0.55)	2.25 (0.34)	0.01 (0.06)	0.32 (0.08)	2.26 (0.30)	3.40 (0.16)	97.30 (0.66)	2.92 (0.40)
DA44	1	isobaric at 50 MPa		78.84 (0.12)	0.33 (0.07)	10.93 (0.06)	1.45 (0.14)	0.03 (0.09)	0.19 (0.04)	1.20 (0.05)	4.20 (0.11)	98.77 (0.50)	1.25 (0.20)
DA12	0.6	isobaric at 300 MPa		74.03 (0.35)	0.38 (0.02)	14.11 (0.28)	2.09 (0.12)	0.11 (0.03)	0.47 (0.10)	2.53 (0.38)	3.23 (0.15)	93.98 (0.48)	3.86 (0.41)
DA20	0.6	20 (continuous)	duration 13 sec	74.65 (0.47)	0.41 (0.10)	13.78 (0.29)	2.09 (0.22)	0.02 (0.04)	0.44 (0.09)	2.78 (0.25)	3.04 (0.11)	95.62 (0.91)	--
DA23	0.6	1 (continuous)	duration 4:10 min	73.91 (0.41)	0.34 (0.04)	14.10 (0.20)	2.14 (0.21)	0.05 (0.05)	0.45 (0.10)	2.69 (0.20)	3.16 (0.23)	95.56 (0.30)	1.43 (0.22)
DA14*	0.6	0.1 (continuous)	duration 41:10 min	73.38 (0.52)	0.40 (0.04)	14.27 (0.26)	2.37 (0.30)	0.01 (0.10)	0.46 (0.14)	2.82 (0.34)	3.13 (0.25)	97.01 (1.03)	1.39 (0.27)
DA65*	0.6	0.01 (multi-step)	steps: 31 MPa / 1 h	74.97 (0.71)	0.42 (0.08)	13.24 (0.33)	2.19 (0.33)	0.02 (0.08)	0.31 (0.11)	2.12 (0.24)	3.48 (0.15)	97.34 (0.61)	1.04 (0.23)
DA51	0.6	0.001 (multi-step)	steps: 40 MPa / 12 h	77.25 (0.67)	0.32 (0.03)	11.99 (0.09)	1.85 (0.18)	0.04 (0.15)	0.21 (0.00)	1.42 (0.21)	3.03 (0.30)	97.72 (0.42)	--
DA29	0.6	0.0002 (multi-step)	steps: 8.4 MPa / 12 h	79.07 (0.32)	0.30 (0.04)	11.46 (0.13)	1.52 (0.14)	0.03 (0.06)	0.19 (0.05)	1.16 (0.09)	3.51 (0.12)	96.65 (1.26)	1.60 (0.27)
DA46	0.6	isobaric at 50 MPa		79.07 (0.28)	0.27 (0.04)	10.94 (0.04)	1.30 (0.12)	0.04 (0.08)	0.13 (0.00)	0.88 (0.02)	4.63 (0.06)	98.77 (0.55)	1.10 (0.13)
<i>Initial and final pressure of decompression experiments after 7 day of annealing at 850°C were 300 and 50 MPa, respectively.</i>													
<i>Note: Numbers in parentheses show the standard deviation (1σ) of replicated analyses</i>													
<i>+ : errors in parentheses for FTIR derived H₂O contents are calculated by error propagation, but are likely to have relatively higher (~20%) uncertainties, e.g. due to the low sample thickness</i>													
<i>X H₂O: mole fraction of water prior to decompression</i>													
<i>--: values were not (successfully) determined by FTIR spectroscopy</i>													
<i>*: the experiment was duplicated at the same condition, analyses of water content and glass are average values</i>													
<i>** : 3 experiments were conducted at the same condition. In all experiments large PI microlites were observed. The glass analysis was determined for 1 experiment</i>													

Table 3.2. Experimental conditions and results of textural analysis for HPD set-I.

sample	X H ₂ O	Decompression rate [MPa/s]	log BND [mm ⁻³]	log MND _{OP} [mm ⁻³]	log MND _{PLAG} [mm ⁻³]	average plag aspect ratio	maximal Pl aspect ratio	maximal Pl length [μm]	mass fraction crystallized [wt%]
DA11	1	isobaric at 300 MPa	3.68 (0.01)	5.37 (0.26)	n.p.	n.p.	n.p.	n.p.	3.23 (0.1)
DA19	1	20 (continuous)	5.64 (0.21)	5.67 (0.04)	n.p.	n.p.	n.p.	n.p.	5.91 (0.3)
DA22	1	1 (continuous)	4.72 (0.28)	5.62 (0.11)	n.p.	n.p.	n.p.	n.p.	8.87 (0.1)
DA13*	1	0.1 (continuous)	4.21 (0.05)	5.82 (0.06)	n.p.	n.p.	n.p.	n.p.	1.17 (0.2)
DA64*	1	0.01 (multi-step)	3.70 (0.03)	5.76 (0.14)	n.p.	n.p.	n.p.	n.p.	9.71 (0.1)
DA50	1	0.001 (multi-step)	4.08 (0.07)	5.91 (0.04)	n.p.	n.p.	n.p.	n.p.	9.99 (0.1)
DA54*	1	0.0005 (multi-step)	4.44 (0.41)	5.70 (0.13)	5.46 (0.11)	n.d.	17.34	99.49	8.78 (0.2)
DA28**	1	0.0002 (multi-step)	4.66 (0.22)	5.73 (0.16)	5.67 (0.09)	n.d.	18.54	292.32	18.99 (0.2)
DA44	1	isobaric at 50 MPa	4.08 (0.04)	5.65 (0.34)	5.97 (0.08)	2.17	12.77	29.01	34.37 (0.1)
DA12	0.6	isobaric at 300 MPa	4.61 (0.02)	5.80 (0.14)	5.90 (0.02)	2.04	29.90	31.31	n.d.
DA20	0.6	20 (continuous)	6.38 (0.12)	5.69 (0.19)	5.52 (0.01)	2.18	16.03	15.01	n.d.
DA23	0.6	1 (continuous)	5.50 (0.23)	5.39 (0.19)	5.64 (0.07)	2.40	23.00	15.45	n.d.
DA14*	0.6	0.1 (continuous)	4.89 (0.34)	5.72 (0.08)	5.72 (0.10)	1.80	14.02	24.53	n.d.
DA65*	0.6	0.01 (multi-step)	4.57 (0.20)	5.39 (0.13)	5.62 (0.09)	2.47	25.03	33.72	n.d.
DA51	0.6	0.001 (multi-step)	5.01 (0.28)	5.30 (0.12)	5.58 (0.06)	1.94	17.69	37.98	n.d.
DA29	0.6	0.0002 (multi-step)	5.29 (0.39)	5.40 (0.18)	5.42 (0.10)	2.03	20.96	87.41	n.d.
DA46	0.6	isobaric at 50 MPa	4.73 (0.16)	6.04 (0.06)	6.43 (0.10)	2.38	15.60	18.44	n.d.

MND_{OP}: microcline number density calculated for other microcline phases incl. pyroxenes, amphiboles and oxides
MND_{PLAG}: microcline number density for plagioclase microclines only
 Note: Numbers in parentheses show the standard deviation (1σ) of replicated analyses
 X H₂O: mole fraction of water prior to decompression
 *: the experiment was duplicated at the same condition, analyses of BND, MND, Pl lengths and aspect ratio as well as glass are average values
 **: 3 experiments were conducted at the same condition. In all experiments large Pl microclines were observed. The glass analyses, BND and MND values were determined for 1 experiment
 n.p.: no plagioclase (Pl) microclines crystallized
 n.d.: not detected / determined

For the preparation of the starting material, a mixture of oxides (SiO_2 , TiO_2 , Al_2O_3 , Fe_2O_3 , MnO and MgO) and carbonates (CaCO_3 , Na_2CO_3 and K_2CO_3) was ground in a rotary mortar. The mixed powder was melted for 2 hours in platinum crucible at 1600°C , 1 atm in air ($\log f_{\text{O}_2} = -0.68$). Afterwards, the melt was quenched to glass by placing the crucible into a water bath. To improve the homogeneity of the batch, the glass was ground again in the agate mortar and melted again for 0.5 hour (see same P-T conditions as above). Finally, the glass was crushed and two fractions of $< 100 \mu\text{m}$ and $100\text{-}200 \mu\text{m}$ were mixed in a volume ratio of $\sim 1:1$ to minimize the free volume in the experimental capsules and to reduce the incorporation of atmospheric nitrogen into the charge.

Experimental methods

Two series of decompression experiments were conducted: one using only water as a volatile component (H_2O -bearing) and the other one using a water and carbon dioxide ($\text{H}_2\text{O}+\text{CO}_2$ -bearing) fluid mixture. In the first experimental series, 50 mg of the powdered silicate glass and 5 mg of H_2O were loaded in 20 to 25 mm long gold capsules with a diameter of 3.2 mm. In the second experimental series, 3.8 mg of H_2O and 7 mg of $\text{Ag}_2\text{C}_2\text{O}_4$ (CO_2 source) were added to 50 mg of the glass. In both experimental series the rhyodacitic melt was saturated with H_2O - or $\text{H}_2\text{O}+\text{CO}_2$ -bearing fluid phase at 300 MPa, resulting in final fluid composition with mole fraction of water in the fluid phase ($X^{\text{fl}}\text{H}_2\text{O}$) equal to 1 and about 0.6, respectively. $X^{\text{fl}}\text{H}_2\text{O}$ was measured after opening the capsule using a conventional weight-loss method. The capsules were welded shut by arc welding.

Experiments were performed in externally heated cold seal pressure vessels (CSPV) made of an alloy containing mainly nickel. The vessels were pressurized with water. The temperature was controlled with an external Ni-CrNi thermocouple (vessels were calibrated for temperature). The temperature variations were less than 5°C , while the accuracy in temperature was estimated to be $\pm 10^\circ\text{C}$. Pressure was measured with pressure transducer calibrated against a strain gauge manometer. The accuracy of pressure measurements were 1 MPa and pressure variations during the experiments were less than ± 5 MPa. Inside the CSPV, the redox conditions were buffered by the reaction of water with a solid oxygen buffer (added as a mixture of Ni and NiO powders, i.e. NNO buffer). An effective in-diffusion of H_2 through the walls of gold capsules fixed the hydrogen fugacity (f_{H_2}) in the capsules and controlled the redox conditions in the systems via the reaction of $\text{H}_2 + \frac{1}{2} \text{O}_2 = \text{H}_2\text{O}$. Hence, in the H_2O -saturated systems, the redox conditions were close to NNO buffer while in the $\text{H}_2\text{O}+\text{CO}_2$ -bearing systems, the fugacity of f_{O_2} is expected to be

about 0.5 log units lower. It should be also noted that the proportions of H₂O and CO₂ in the fluid changed during decompression due to different dependences of water and carbon dioxide solubilities on pressure and because of higher diffusivity of H₂O in silicate melts (e.g., Behrens & Zhang, 2001; Baker *et al.*, 2005). This could presumably result in a small increase in fO_2 mainly due to increasing fugacity of H₂O in the fluid phase on pressure release.

The pairs of H₂O- and H₂O+CO₂-bearing capsules were annealed for 7 days at 850 °C (maximum temperature to conduct experiments in CSPVs) and 300 MPa before the decompression, allowing initial equilibration in the systems at conditions that closely correspond to magma storage conditions at Unzen. One series of experiments was quenched isobarically after 7 days, producing reference samples equilibrated at 300 MPa. Isobaric series were obtained in the same way at 50 MPa, representing the final equilibrium reference material for the decompression experiments. After equilibration at 300 MPa, the capsule pairs were decompressed manually by reducing the pressure in the autoclaves either continuously (decompression rates ≥ 0.1 MPa/s) or at regular steps (see Table 3.1) down to 50 MPa (multi-step decompression, decompression rates ≤ 0.1 MPa/s). The average decompression rates varied in the range from 0.0002 to 20 MPa/s (Table 3.1). The experiments were quenched by removing the autoclave from the furnace and by cooling it with compressed air, while keeping the final pressure constant. The quench rate was approximately 150°C per min at the beginning of the cooling and was sufficient to avoid quench effects on crystallization and presumably on vesiculation in rhyodacitic magma. Several replicate runs were conducted to check the reproducibility of the experimental approach (Table 3.1).

Analytical methods

Major element composition of solid experimental products

The chemical compositions of the experimental products, composed of minerals and glass, were analyzed with a *Cameca SX-100* microprobe using 15 kV as the acceleration voltage. Glass analyses were conducted with 5-10 nA beam current, a defocused electron beam (5-10 μm diameter), and peak counting times of 4 sec for Na and K and 8 sec for the other elements. Mineral phases were analyzed using a 15 nA beam current and a focused electron beam, and peak counting times of 5 sec for Na and K and 10 sec for the other elements. Multiple measurements (minimum 3) were made for each phase to reduce possible analytical errors and to check the homogeneity. For some crystals ($> 5 \mu\text{m}$),

profiles were measured through individual grains to determine changes in chemical compositions from rim to core of the mineral.

Determination of H₂O content of the glasses

Fourier transform infrared spectroscopy (FTIR) was used to estimate concentration of dissolved water in the experimental glasses, using a *Bruker IFS88* FTIR spectrometer with a connected *IRscopeII* microscope. For NIR (near infra-red) analysis we used a tungsten light source, a CaF₂-beam splitter and a MCT-detector. The spectral resolution was 4 cm⁻¹. One hundred scans per background and per sample were collected. The analyzed area was 80 x 80 μm. The concentrations of molecular water and water dissolved as OH were calculated from the heights of the peaks at 5200 cm⁻¹ and 4500 cm⁻¹, respectively, using a tangential baseline correction. Due to crystallization during decompression, the compositions of the quenched melts (glasses) were different, presumably influencing the extinction coefficients of water species in the glasses. The extinction coefficients used for the calculation of water concentration in the glasses depend on the glass composition and were estimated using an empirical calibration of Ohlhorst *et al.* (2001). They vary from 1.41 to 1.75 l/mol*cm for the 5200 cm⁻¹ peak and from 1.19 to 1.48 l/mol*cm for the 4500 cm⁻¹ peak. Since the compositions of glasses were close to rhyolites, glass densities were calculated applying the empirical calibration after Withers & Behrens (1999): density (in g/L) = 2390 – 17.0 * wt% H₂O. Sample thicknesses were determined with a *Mitutoyo* digital micrometer (precision of ± 2 μm). The thicknesses varied between 60 and 70 μm. Care was taken to choose areas without or with small amount of bubbles. However, since the samples contain minerals (especially those of the H₂O+CO₂-bearing system) and since bubbles could not be completely avoided, the uncertainty of the calculated water concentration is high (± 20 relative %) and the data can only be used to discuss qualitatively the relative variations of water concentrations. The average values of water concentration (and standard deviations) of NIR measurements repeated at different locations on higher quality samples are shown in Table 3.1. For some samples, (DA50 and DA51) water concentrations could not be determined by NIR because doubly polished slices of good quality could not be prepared (cavities were still filled with fixation glue resulting in large disturbances in the absorption spectra).

The determination of carbon dioxide concentrations in glasses by FTIR was not possible because the CO₂ concentrations were too low and because the absorption bands of

3. DECOMPRESSION EXPERIMENTS

molecular CO₂ were superimposed with bands due to the presence of crystalline phases in the mid infra-red (MIR) spectra.

Image and texture analysis

Back-scattered electron (BSE) images of the experimental samples were obtained with a scanning electron microscope (SEM) *FEI QUANTA 200*. The picture sizes range from minimum 30 x 26 µm to maximum 1500 x 1125 µm. These images were used to identify the textures and to quantify the textural characteristics of the experimental products, applying the public computer program *ImageJ* (<http://rsb.info.nih.gov/ij>). The image analysis provided information about total area, average size, area fraction, as well as about the width and length of each particle. The detection limit for the particle size is dependent on the magnification and the resolution of the digitalized BSE pictures. For the characterization of the run products, at least three BSE-pictures at different magnifications were analyzed for each sample to ensure that particles of all sizes are included and to minimize the truncation effect (e.g. Armienti, 2008). At the highest magnification (5000 x), the *ImageJ* program allowed detection of particles with a minimum diameter of 0.2 µm. It must be noted that some voids in experimental samples were filled with epoxy and abrasive materials during sample preparation, making the automatic processing by *ImageJ* difficult. In order to minimize this effect, all bubbles in the images were outlined and colored black manually to obtain better contrast between bubbles and the other phases before processing by *ImageJ*.

The geometric information obtained by *ImageJ* analysis was used to determine textural characteristics such as bubble and crystal size distributions (BSD and CSD, respectively) as well as bubble and microlite number densities (BND and MND, respectively). The BSD and CSD values were determined following the methods of Higgins (2000, 2002, 2006a,b) using the *CSDcorrections1.3.8* software (<http://www.dsa.uqac.ca/~mhiggins/csdcorrections.html>).

The bubble or crystal size distribution in a rock is the number of bubbles or crystals per unit volume within a series of defined size intervals. The population density n is defined as the number of crystals in a given size class per unit volume, where N is the total number of bubbles or crystals of size less than R , and R is some characteristic crystal size (Marsh, 1988):

$$n = \frac{dN}{dR} \quad (1).$$

For the determination of bubble and microlite number density, we followed the method of Noguchi *et al.* (2008a). The calculation procedure includes a 3D-correction as an important contribution. We obtained data on the crystal (or bubble) numbers from the *CSDcorrections* software (see above): The bubble or crystal number (N) of each given size interval is represented by the multiplication of the population density (n) with the bin width (see Higgins, 2006b). Therefore, the integration of crystal numbers N (number of microlites/bubbles of a given size interval) for the observed range of microlite/bubble sizes (R^*) is defined as the microlite number density (MND) and as the bubble number density (BND), respectively, per unit volume of the magma:

$$MND = \int_0^{R^*} NdR \quad (2).$$

According to the requirements of the *CSDcorrections* program, an aspect ratio and a roundness factor have to be fixed for BSD and BND calculation. An aspect ratio of 1.0 : 1.1 : 1.2 (short axis : intermediate axis : long axis) and a roundness factor of 0.7 (roundness factor varies from 0 for rectangular parallelepipeds to 1 for triaxial ellipsoids/spheres, see Higgins, 2006 a,b) were used for BSD and BND analyses. The value chosen for the aspect ratio assumes that bubbles are subspherical and the roundness factor is given by *ImageJ* analysis.

For the CSD and MND determination, we have separated plagioclase microlites from all other microlite phases (Opx, Cpx, Amph, oxides). For Pl microlites, an aspect ratio of 1.0 : 2.0 : 5.0 (also corresponding to that used by Noguchi *et al.* 2008a) and a roundness factor of 0.0 were used. Due to the difficulties in distinguishing between pyroxenes and amphiboles in BSE pictures, both phases were treated as a one phase. For all other phases other than Pl (OP), we considered an averaged aspect ratio of 1.0 : 1.5 : 3.0 and a roundness factor of 0.0. The roundness factor was obtained from the *ImageJ* analysis of the samples whereas the aspect ratios were estimated manually by measuring size characteristics of a number of microlites in each sample. Although the maximum aspect ratios (=major/minor) of Pl microlites may reach up to ca. 30 (Table 3.2), the average aspect ratios do not significantly differ from sample to sample for all decompression experiments.

RESULTS

Phase assemblages and compositions in water-saturated experiments

The experimental products consist of glass, microlites and vesicles (Fig. 3.3). The vesicularity ranges from almost zero to nearly thirty percent. The solid experimental products of the H₂O-bearing system (in the following text, “H₂O-bearing” refers to experiments at H₂O-saturated conditions) obtained at isobaric conditions of 300 MPa are composed of glass, amphibole (Amph) and oxides (Ox, mainly ilmenite) as well as of minor clinopyroxene (Cpx) and orthopyroxene (Opx). The products of the H₂O-bearing isobaric experiment at 50 MPa are composed of glass, plagioclase (Pl), Ox, Cpx and minor amounts of Opx (see compositions in *Appendix* Tables A.5). Thus, the mineral assemblages observed at 300 MPa and 50 MPa are consistent with the phase diagram in Fig. 3.2 (note absence of Amph at 50 MPa and of Pl at 300 MPa).

In the H₂O-bearing decompression experiments, the same assemblage as in the isobaric 300 MPa experiment is observed, except for decompression rates lower than 0.0005 MPa/s (runs DA54 and DA28, *Appendix* Table A.5). In these experiments large Pl microlites are found (e.g. Fig. 3.3g). Considering that Pl microlites are present as an equilibrium phase at 50 MPa and not at 300 MPa (isobaric experiments), the large Pl microlites are expected to nucleate and grow during decompression from 300 to 50 MPa. The large Pl microlites obtained at decompression rates ≤ 0.0005 MPa/s have an average An content of An₅₀₋₅₄. The rims of the plagioclase are slightly more Ab-rich than the cores (difference of 1-2 mol% An). It can be noted that the An-contents of the experimental Pl are in the range of natural Pl microlites from Unzen dome rocks (52-69 mol%: Noguchi *et al.*, 2008a) and from the samples drilled from the conduit (40-70 mol%: Noguchi *et al.*, 2008b).

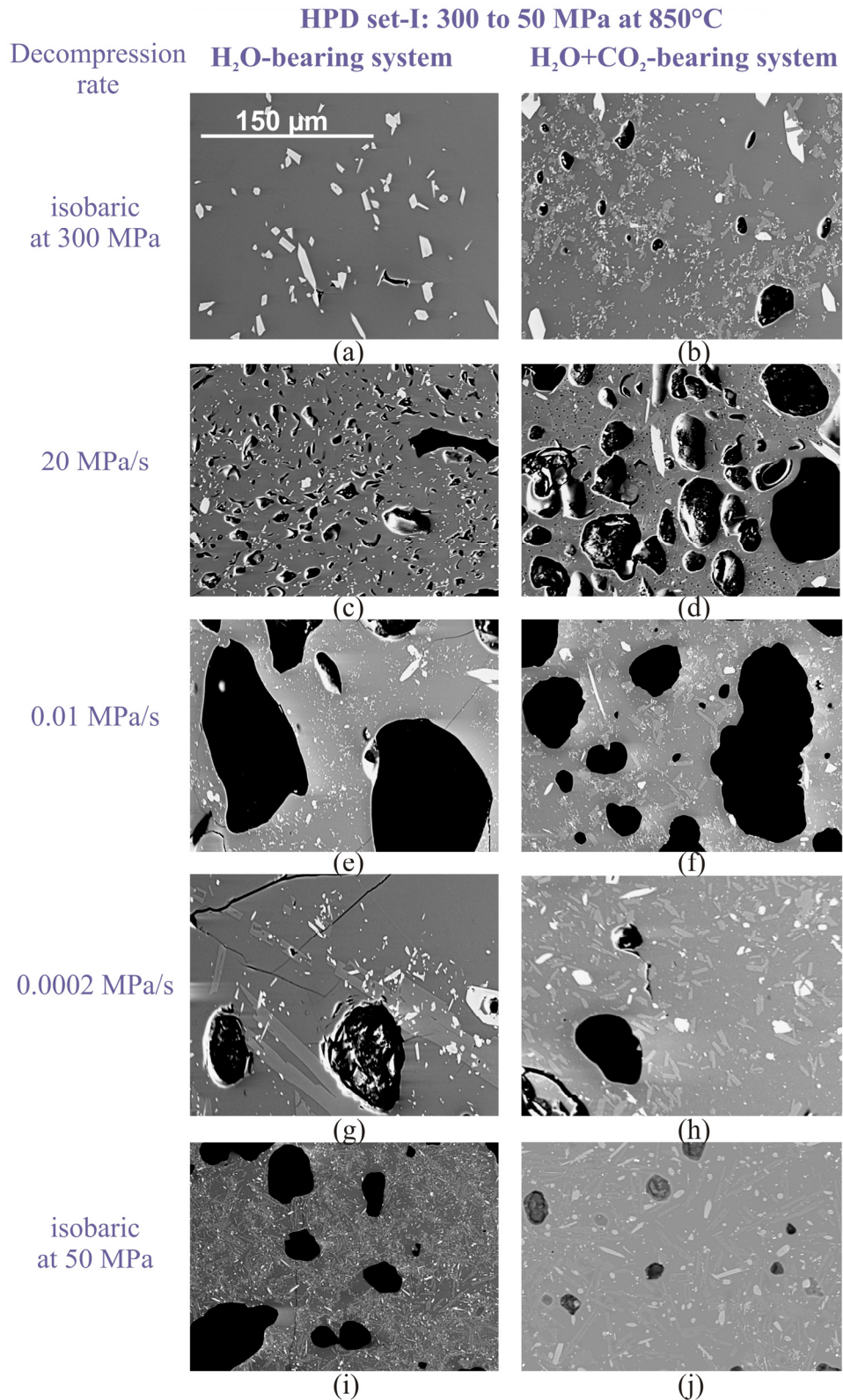


Fig. 3.3 a-j. BSE pictures of the products of isobaric and decompression experiments. Black bodies are bubbles; light grey particles represent microlites such as Cpx, Opx, Amph, Pl and oxides. Note the large plagioclase (Pl) crystals at a decompression rate of 0.0002 MPa/s in the H₂O-bearing system (Fig 3.3g; light grey color).

3. DECOMPRESSION EXPERIMENTS

Water-saturated amphibole stability experiments performed by Sato *et al.* (1999) for Unzen groundmass composition showed that amphiboles are only stable at pressures higher than 50 MPa for experimental temperature of 850°C. Therefore, at equilibrium conditions Amph microlites should not be stable at the final experimental pressure of 50 MPa. However, Amph microlites were detected in nearly all our decompression experiments of the H₂O-bearing system. In some of those experiments it was possible to observe a reaction rim around Amph. Although the rims are not found around all Amph minerals, the size of the rim tends to increase with decreasing decompression rate in agreement with other experimental studies (see e.g. Browne & Gardner, 2006). The maximum width up to 4 µm was measured at a decompression rate of 0.0002 MPa/s. It is emphasized that the rim size can only be interpreted qualitatively because it is dependent on the cut-section of the minerals. When possible, the compositions of Amph cores and rims were analyzed and the Mg# [$\text{Mg}/(\text{Fe}_{\text{tot}} + \text{Mg})$, moles] of the rims is systematically lower than that of the cores, e.g., $\text{Mg\#}_{\text{core}} = 0.59\text{-}0.70$ and $\text{Mg\#}_{\text{rim}} = 0.57\text{-}0.64$ for low decompression rates.

Phase assemblages and compositions in the H₂O+CO₂-bearing system

All experimental products of the H₂O+CO₂-bearing system obtained in isobaric runs at 300 MPa and at 50 MPa contain glass, Ox, Opx, Pl and Cpx. The same assemblage was found in the decompression experiments (see compositions in *Appendix* Tables A.5). Amph was found only as a minor phase in one experiment with decompression rate of 0.01 MPa/s. In a duplicate experiment (DA65*, *Appendix* Table A.5.2), Amph was not observed, indicating that the conditions with $X^{\text{fl}}\text{H}_2\text{O} = 0.6$ are close to that of the stability limit for Amph. In contrast to the H₂O-bearing system, Pl microlites are already part of the mineral assemblage in the H₂O+CO₂-bearing system at 300 MPa and are present in all decompression experiments. In the H₂O+CO₂-bearing system, the An content of Pl cores varies from An₅₃ to An₅₉. The An content of Pl in isobaric experiments at 300 MPa is An₅₈ and this composition is also observed for experiments with decompression rates varying from 0.1 to 0.0002 MPa/s. The An content of the Pl from experiments with decompression rates of 20 and 1 MPa/s is slightly lower (An₅₃ to An₅₆) which may be due to a slightly lower water activity (an $X^{\text{fl}}\text{H}_2\text{O}$ of exactly 0.6 is difficult to realize experimentally). The An content of Pl in isobaric experiments at 50 MPa is An₄₄.

Melt compositions

The chemical analyses of the residual melts are listed in Table 3.1 and plotted in Fig. 3.4. The chemical composition of the glasses in the H₂O+CO₂-bearing system remains nearly constant for experiments at decompression rate ≥ 0.1 MPa/s. At lower decompression rate, the SiO₂ and K₂O contents in residual glasses increase with decreasing decompression, while Al₂O₃, FeO, MgO and CaO contents of glasses decrease with decreasing decompression rate. The chemical composition of the glasses in the H₂O-bearing system remains nearly constant for experiments at decompression rate of 20 to 0.001 MPa/s while with the beginning of Pl crystallization the compositions change, following similar trends as described for the H₂O+CO₂-bearing system. The concentration of MgO in glasses from H₂O-bearing system starts to decrease at decompression rates < 0.1 MPa/s. The experimental data are compared with the compositional range of natural matrix glasses in Fig. 3.4 (grey fields). In the H₂O-bearing system, only MgO concentrations in glasses obtained from very low decompression rates overlap with natural matrix glasses. In contrast, the concentrations of all major oxides overlap with natural compositions in the H₂O+CO₂-bearing system at low decompression rates. In the H₂O-bearing system, concentration profiles in the residual melts in the vicinity of large Pl microlites show that Al₂O₃ and CaO contents are decreasing while the SiO₂ content is increasing with the distance from Pl microlites.

3. DECOMPRESSION EXPERIMENTS

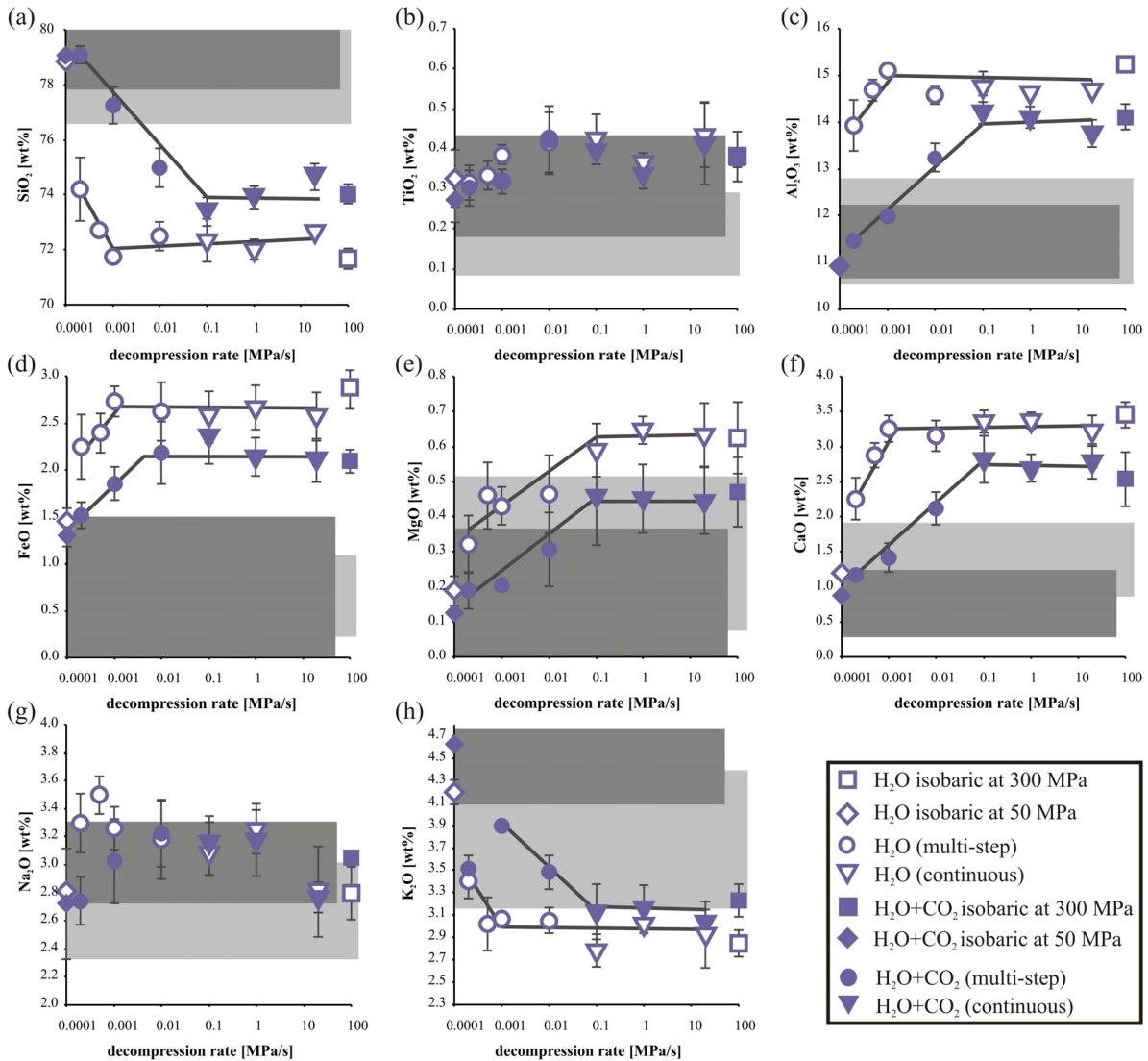


Fig. 3.4. Normalized chemical compositions of the experimental residual melts as a function of the decompression rate. The dark grey shaded areas show the chemical composition range of the erupted natural groundmass glass in erupted rocks (Nakada & Motomura, 1999) and the light grey shaded areas show the estimated chemical composition range of groundmass glass composition in the conduit rocks (Noguchi *et al.*, 2008b) of the 1991-1995 Unzen eruption. Error bars show standard deviation (1σ) of replicate analyses.

The data of NIR spectroscopy and the totals of microprobe analyses indicate that the water content of melts decreases with decreasing decompression rate, becoming similar to the expected water solubility at 50 MPa for the lowest decompression rates (Fig. 3.5). Equilibrium concentrations of water are reached at a decompression rate of 1 MPa/s for $\text{H}_2\text{O}+\text{CO}_2$ -bearing system and at 0.1 MPa/s for the H_2O -bearing system. The H_2O content of the experiment DA28 in the H_2O -bearing system with the slowest decompression (0.0002 MPa/s) is slightly higher than that expected for 50 MPa. However, this experimental product contains large plagioclase microlites (in contrast to all other samples) which may affect the quality of the NIR determination.

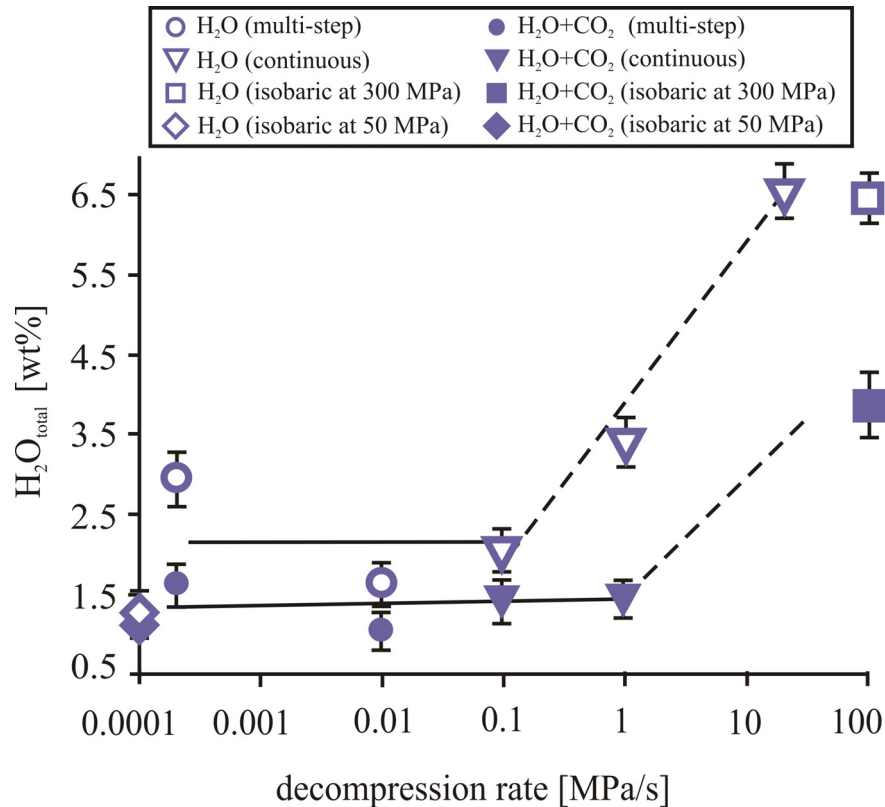


Fig. 3.5. H₂O-contents of the residual glasses (in wt%; determined by NIR) of the H₂O-bearing system and of the H₂O+CO₂-bearing system as a function of the decompression rate. Circles are multi-step decompression experiments and triangles are continuous decompression experiments. Error bars show standard deviation (1σ) of replicate analyses.

Textures

Bubbles

The BSD in the samples shows concave-up size distribution curves, as illustrated in Fig. 3.6. There is no systematic variation of the BSD as a function of the decompression rate. The BND values of the H₂O+CO₂-bearing system are slightly higher (0.9-1.2 log units) when compared to values of the H₂O-bearing system. Two distinct trends can be observed in both systems. First, the BND values decrease with decreasing decompression rate at high rates (20 to 0.01 MPa/s) ranging from $10^{6.4} \text{ mm}^{-3}$ to $10^{4.6} \text{ mm}^{-3}$ in the H₂O+CO₂-bearing system and from $10^{5.6} \text{ mm}^{-3}$ to $10^{3.7} \text{ mm}^{-3}$ in the H₂O-bearing system (Table 3.2, Fig. 3.7). Secondly, BND values increase again at decompression rates lower than 0.01 MPa/s. Whereas, the BND value in the H₂O+CO₂-bearing system at 0.0002 MPa/s is similar to that in the equilibrium experiment at 50 MPa, the BND value in the H₂O-bearing system is 0.6 log units higher than that in the isobaric experiment at final pressure.

3. DECOMPRESSION EXPERIMENTS

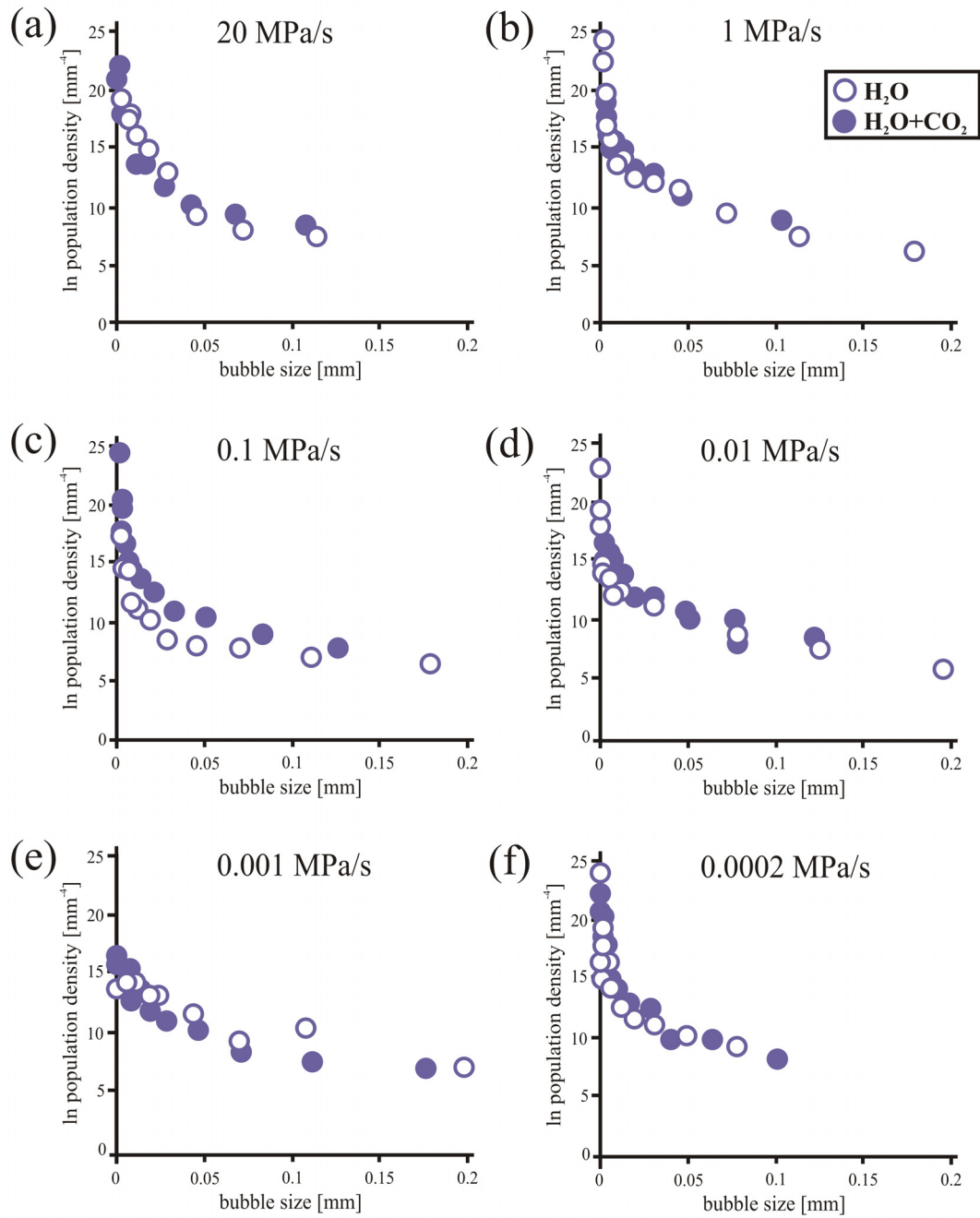


Fig. 3.6 a-f. Bubble size distribution, calculated following the method of Higgins (2000), in samples after decompression experiments.

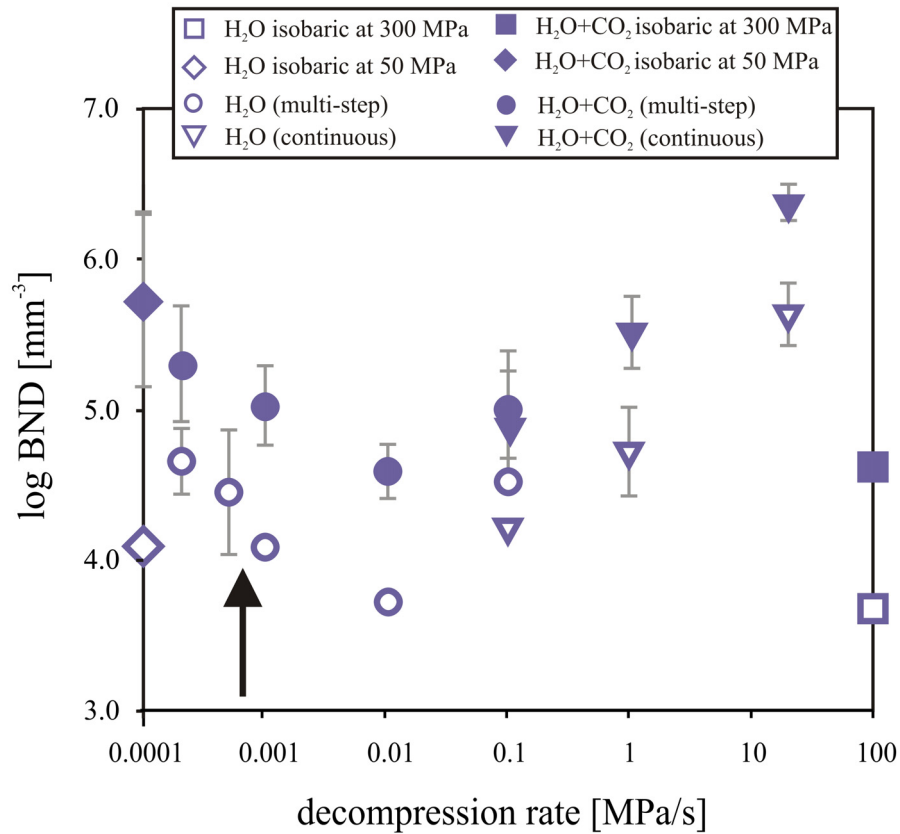


Fig. 3.7. Bubble number density (BND) as a function of the decompression rate for the H₂O-bearing system (empty symbols) and the H₂O+CO₂-bearing system (filled symbols). Circles are multi-step decompression experiments and triangles are continuous decompression experiments. The black arrow indicates the onset of plagioclase crystallization in the H₂O-bearing system. Error bars show standard deviation (1σ) of replicate analyses.

Microlites

The CSD in the samples shows concave-up size distribution curves (Fig. 3.8) and there is no systematic variation of the CSD as a function of the decompression rate. In most cases, the population density of crystals at sizes < 0.01 mm is slightly higher in the H₂O+CO₂-bearing system when compared to the H₂O-bearing systems for plagioclases as well as for the other phases. At the lowest decompression rate (0.0002 MPa/s; see Fig. 3.8f), the size of Pl microlites in the H₂O-bearing system is significantly larger than that in the H₂O+CO₂-bearing system.

3. DECOMPRESSION EXPERIMENTS

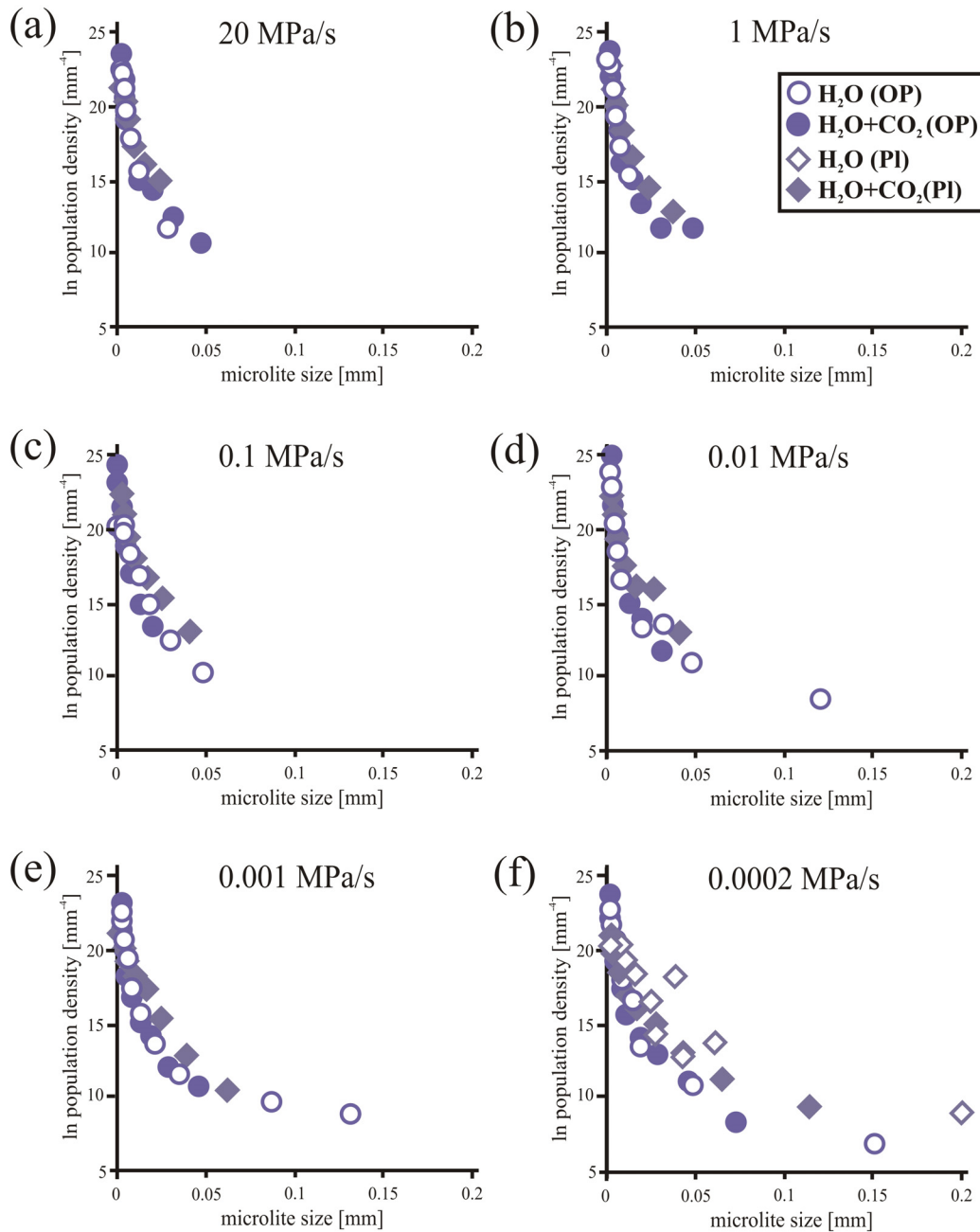


Fig. 3.8 a-f. Crystal size distribution, calculated following the method of Higgins (2000), for plagioclases (PI) and other phases (OP) in samples after decompression experiments.

In the $\text{H}_2\text{O}+\text{CO}_2$ -bearing system, the MND_{PI} values show no detectable dependence on decompression rate and vary in the range from $10^{5.4} \text{ mm}^{-3}$ to $10^{5.7} \text{ mm}^{-3}$. In the H_2O -bearing system, plagioclase microlites only nucleated and grew at decompression rates $\leq 0.0005 \text{ MPa/s}$, having MND_{PI} values of $10^{5.4} \text{ mm}^{-3}$ to $10^{5.7} \text{ mm}^{-3}$ (Fig. 3.9a). The MND_{PI} values determined at the lowest decompression rate (0.0002 MPa/s) are 0.3 log units higher in the H_2O -bearing system when compared with the experiment in the $\text{H}_2\text{O}+\text{CO}_2$ -bearing system at the same conditions. The MNDs for other phases (MND_{OP}) range from $10^{5.3} \text{ mm}^{-3}$ to $10^{5.9} \text{ mm}^{-3}$ in both systems, also showing no distinct change with changing

decompression rate (Fig. 3.9b). The MND_{OP} values obtained in the H_2O -bearing system are in most cases ~ 0.3 log units higher than those in the H_2O+CO_2 -bearing system.

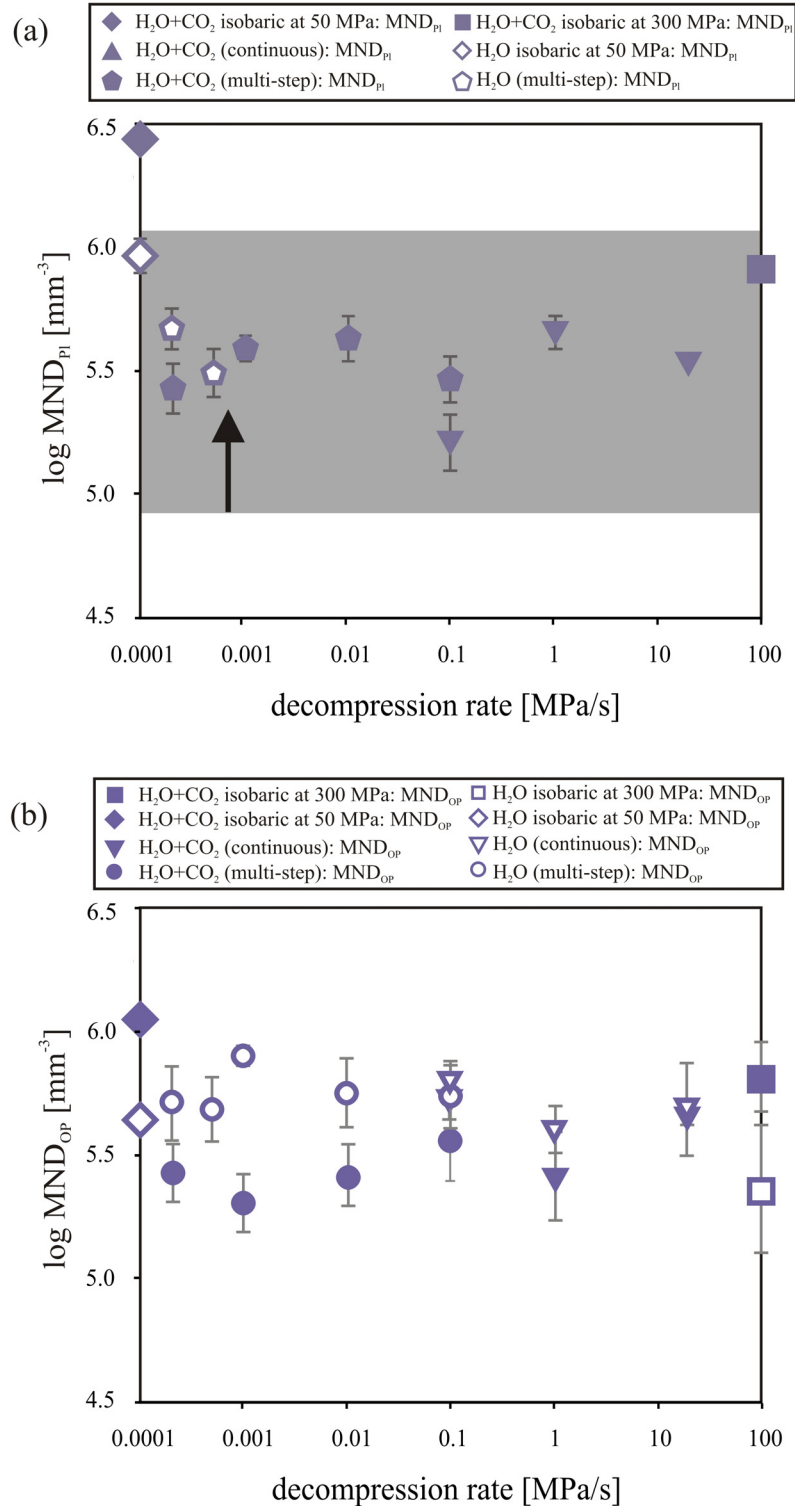


Fig. 3.9. Microlite number density (MND) as a function of the decompression rate for the H_2O -bearing system (empty symbols) and the H_2O+CO_2 -bearing system (filled symbols). (a) MND for plagioclases only (MND_{PI}) and (b) MND for all other phases (MND_{OP}) such as amphiboles, pyroxenes and oxides. Circles are multi-step decompression experiments and triangles are continuous decompression experiments. The black arrow indicates the onset of plagioclase (Pl) crystallization in the H_2O -bearing system. The grey shaded area show the MND_{PI} of natural dome samples (Noguchi *et al.*, 2008a). Error bars show standard deviation (1σ) of replicate analyses.

3. DECOMPRESSION EXPERIMENTS

The maximum length of Pl microlites in the H₂O+CO₂-bearing system increases (Fig. 3.10), whereas the maximum aspect ratios of Pl microlites in the H₂O+CO₂-bearing system show no variation with decompression rate (Table 3.2). In the H₂O-bearing system, Pl microlites crystallized only at two decompression rates (0.0005 and 0.0002 MPa/s). These experiments were duplicated and large Pl microlites were reproduced reaching up to 50-150 μm in length at 0.0005 MPa/s and up to 200-250 μm in length at 0.0002 MPa/s (Table 3.2, Fig. 3.10). Plagioclase microlites of these runs show a skeletal appearance and are often observed in close contact to bubbles.

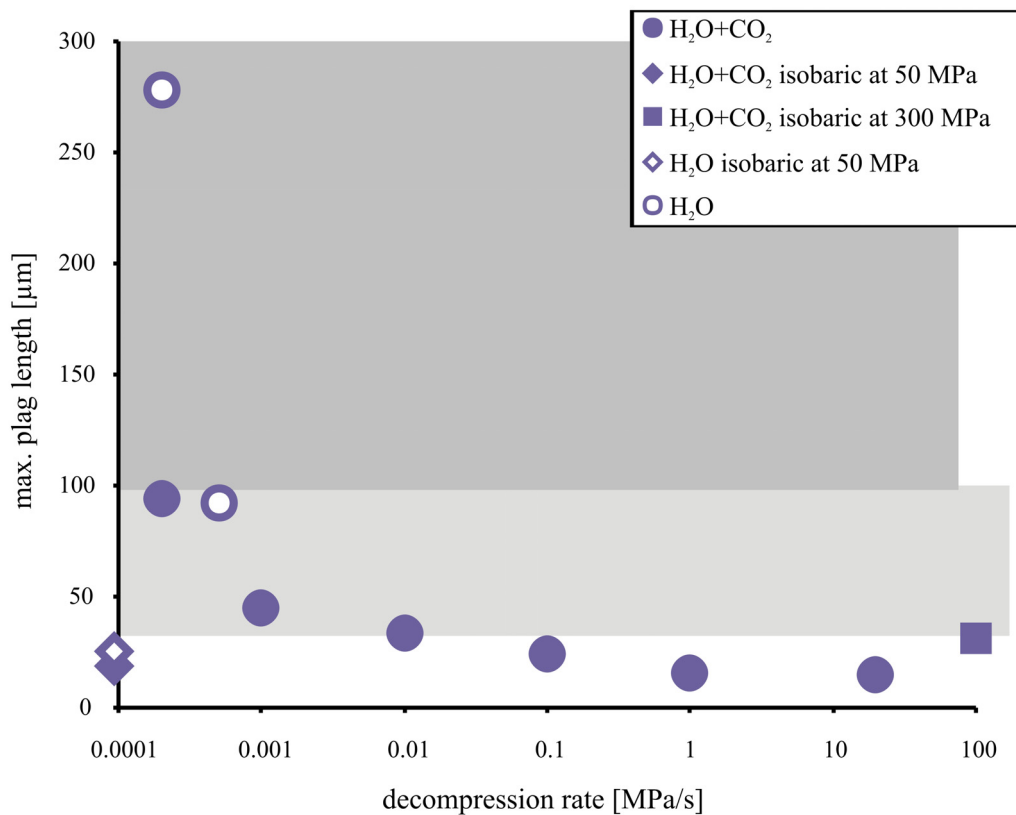


Fig. 3.10. Maximum Pl length as a function of the decompression rate. Dark grey shaded area represents the range of Pl microlite lengths of Unzen natural dome samples after Noguchi *et al.* (2008a). Pl microlites in core samples are smaller (<100 μm) (indicated by the light grey shaded area), except one sample (C14-1-1) where Pl microlites reach up to 300 μm in length (see Noguchi *et al.*, 2008a,b; Goto *et al.*, 2008).

DISCUSSION

Dynamics of vesiculation

Equilibrium distribution of volatiles in melt and fluid

The analysis of water contents in the residual glasses gives information on the onset of bubble formation processes, including nucleation, growth and coalescence of bubbles in the samples. Although water concentrations are determined with a large error due to influences of small bubbles and mineral phases, the plot of dissolved water in glasses as a function of pressure (Figs. 3.5 and 3.11) clearly shows that no significant amount of water is exsolved at the decompression rate of 20 MPa/s and that equilibrium water concentrations are reached at decompression rates < 0.1 MPa/s in the H₂O-bearing system. In a rhyolitic melt with a composition similar to our residual melts, Mangan & Sisson (2000) observed that, at 900°C, some water already degassed at 8.5 MPa/s. They also suggested that equilibrium conditions were not yet reached at the decompression rate of 0.003 MPa/s, which differs from our results (also plotted in Fig. 3.11). However, Mangan & Sisson (2000) simulated crystal-free homogeneous bubble nucleation processes in slightly more viscous rhyolitic melts (higher SiO₂ content) which may considerably affect the kinetics of degassing. Another explanation for the observed difference can be that the fluid exsolution processes might have been dramatically enhanced by the presence of microlites. For instance, Hurwitz & Navon (1994) showed that Fe-Ti oxides, biotite etc. can act as bubble nucleation sites. A review of Rutherford (2008), based on decompression experiments in rhyolitic systems (Hurwith & Navon 1994; Gardner *et al.*, 1999; Mangan & Sisson 2000; Gardner & Denis 2004; Baker *et al.*, 2006; Gardner 2007b), shows that there is a transition from non-equilibrium to near-equilibrium water release from the melt at decompression rates of 0.025 to 0.25 MPa/s. At faster decompression rates (≥ 0.25 MPa/s), at which the diffusion of water out of the melt into the bubbles is too slow, the melt becomes water-supersaturated and the fluid-melt equilibrium cannot be reached.

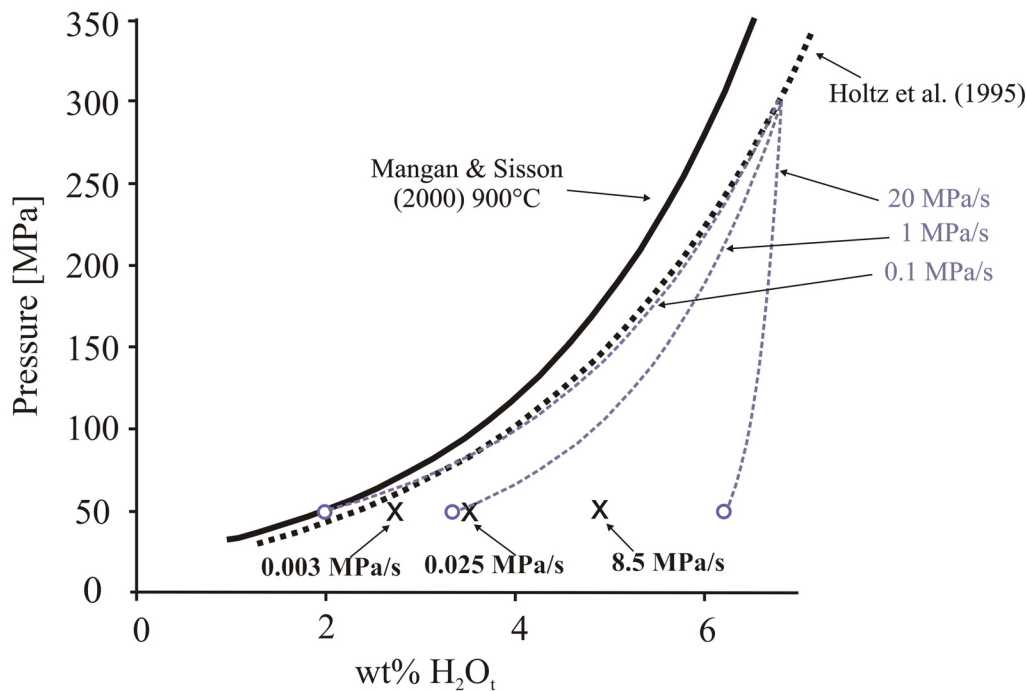


Fig. 3.11. Dissolved H_2O contents (in wt%) of the glasses obtained from decompression experiments. Empty purple circles are decompression experiments at 850°C in the H_2O -bearing system ($X^{\text{H}_2\text{O}}=1$). The solid curve illustrates the equilibrium water contents from solubility experiments for a rhyolitic magma at 900°C (from Mangan & Sisson, 2000), the black dotted curve shows the water solubility for haplogranitic melts (from Holtz *et al.*, 1995). Crosses are experiments from Mangan & Sisson (2000) at decompression rates of 0.003, 0.025 and 8.5 MPa/s.

Bubble growth vs. bubble nucleation

The relatively high BND values in the $\text{H}_2\text{O}+\text{CO}_2$ -bearing system (compared to the H_2O -bearing system) may result from two generations of bubbles (one with diameters $> 20\mu\text{m}$ and a second with diameters $< 5\mu\text{m}$), which can be observed in BSE pictures (e.g. Fig. 3.3d) and in the BSD diagram (Fig. 3.6a). In contrast, in the H_2O -bearing system, only one bubble generation of intermediate sizes can be found (e.g. Fig. 3.3c and 3.6a). The two generations of bubbles in the $\text{H}_2\text{O}+\text{CO}_2$ -bearing system point to a possible delay in nucleation of CO_2 -rich bubbles due to the lower diffusion rate of CO_2 in silicate melts compared to that of H_2O (Baker *et al.*, 2005).

In general, it can be expected that as water exsolves from the melt, the melt-vapor surface tension increases, lowering the bubble nucleation rate and therefore bubble growths outweighs nucleation in the system (Mangan & Sisson, 2005). It is confirmed in our experiments at high decompression rates, in which the BND decreases with decreasing H_2O content of the melt as decompression rates decrease from 20 to 0.01 MPa/s. This observation indicates that bubble growth is the dominant process occurring at these

decompression rates (Gardner, 2007a,b). In contrast, at lower decompression rates (0.01 to 0.0002 MPa/s) an increase in BND is observed.

Our results on bubble formation are consistent with previous experimental studies (e.g. Toramaru 1995, 2006; Mourtada-Bonnefoi & Laporte, 2004; Cluzel *et al.*, 2008) showing that the main parameter controlling BNDs in magmas is indeed the decompression rate: BND values decrease with decreasing decompression rates from 20 to 0.01 MPa/s (see Fig 3.7). In addition, the BND values determined in this study are within the BND range obtained from other studies investigating heterogeneous bubble nucleation in rhyolitic compositions (H₂O-bearing system at decompression rates ≥ 0.01 MPa/s; Fig. 3.12). The BNDs of our H₂O+CO₂-bearing system follow the same trend but are shifted to higher BNDs by ~ 0.6 log units. It is worth noting that the BND values determined at decompression rates lower than 0.01 MPa/s do not follow the heterogeneous bubble nucleation trend indicated by the black arrow in Fig. 3.12. The increase in BND with decreasing decompression rate in the range 0.01 – 0.0002 MPa/s is interpreted as an indication that bubble nucleation processes start to dominate over bubble growth processes. This observation was not reported in previous studies and may be explained by the absence of experiments with decompression rates lower than 0.02-0.01 MPa/s.

Significance of BND in the starting material

One important parameter controlling the BND values in the decompression experiments is the bubble distribution in the starting material (isobaric experiments). The BND in the starting material is dependent (1) on sample preparation (e.g., size of the glass powder fractions used as a starting material, i.e., initial heterogeneity) and (2) on the annealing period prior to decompression. As a result of Ostwald ripening, the BND decreases with increasing annealing time (Lautze *et al.*, 2010). Thus, the BND values determined in our decompression experiments after 7-day annealing at 300 MPa can not be directly transferred to interpret natural conditions (the residence time in the magma chamber prior to an eruption is presumably longer than 7 days). However, based on our observations obtained in both the H₂O-bearing and the H₂O+CO₂-bearing systems, it is evident that the effect of decompression rate on the BND trends is nearly identical for all samples, independently on the bubble distribution in the starting material (compare open and black symbols in Fig. 3.7). In this particular example, the difference in BND is due to the difference in volatile composition of the bulk system. Thus, even if relevant quantitative

3. DECOMPRESSION EXPERIMENTS

data can be slightly affected by the initial heterogeneity of the sample, the dataset can be used to predict qualitatively the evolution of BNDs as a function of decompression rates.

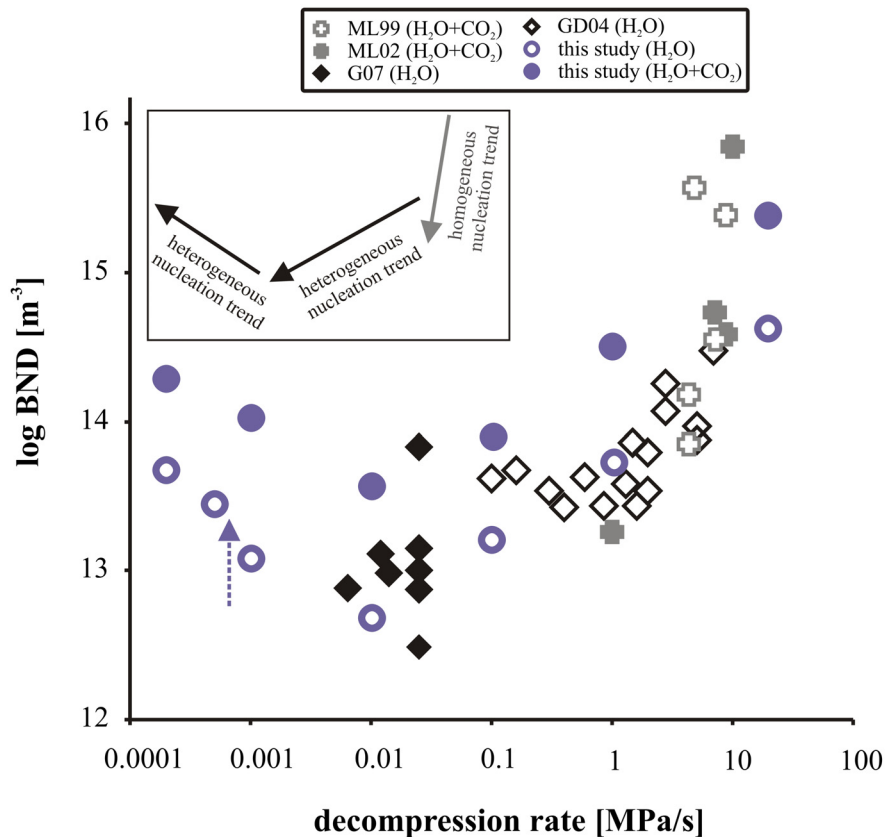


Fig. 3.12. Compiled experimental data of the BND as a function of the decompression rate. In the legend, ML99 refers to data from Mourtada-Bonnefoi & Laporte (1999; $T = 800^{\circ}\text{C}$, $P_{\text{start}} = 285\text{-}200\text{ MPa}$, $P_{\text{final}} = 198\text{-}51\text{ MPa}$) and ML02 from Mourtada-Bonnefoi & Laporte (2002; $T = 1000^{\circ}\text{C}$, $P_{\text{start}} = 295\text{-}200\text{ MPa}$, $P_{\text{final}} = 179\text{-}51\text{ MPa}$) characterized by the occurrence of a homogeneous nucleation of bubbles. GD04 refers to data on heterogeneous bubble nucleation from Gardner & Denis (2004; $T = 800^{\circ}\text{C}$, $P_{\text{start}} = 175\text{-}125\text{ MPa}$, $P_{\text{final}} = 145\text{-}80\text{ MPa}$) and G07 from Gardner *et al.* (2007b; $T = 725\text{-}875^{\circ}\text{C}$, $P_{\text{start}} = 100\text{ MPa}$, $P_{\text{final}} = 60\text{-}20\text{ MPa}$). The inlet shows the 3 distinct bubble nucleation trends.

Despite the fact that the determined BND values can not be directly applied to natural case studies (see above), it is interesting to note that some of the data generated in this study are very close (same order of magnitude) to the BND determined in natural rocks. The experimental data obtained in this study are compared with the calculated BND values of natural samples from several Plinian eruptions of different volcanoes in Fig. 3.13 (compiled by Toramaru, 2006). The experimental samples from the runs at the highest decompression rate (20 MPa/s) are very close to the general trend reported by Toramaru (2006). The deviation of the experimental data from the observed vesicularity trend of Plinian eruptions has its maximum at 0.01 MPa/s (see Fig. 3.13b).

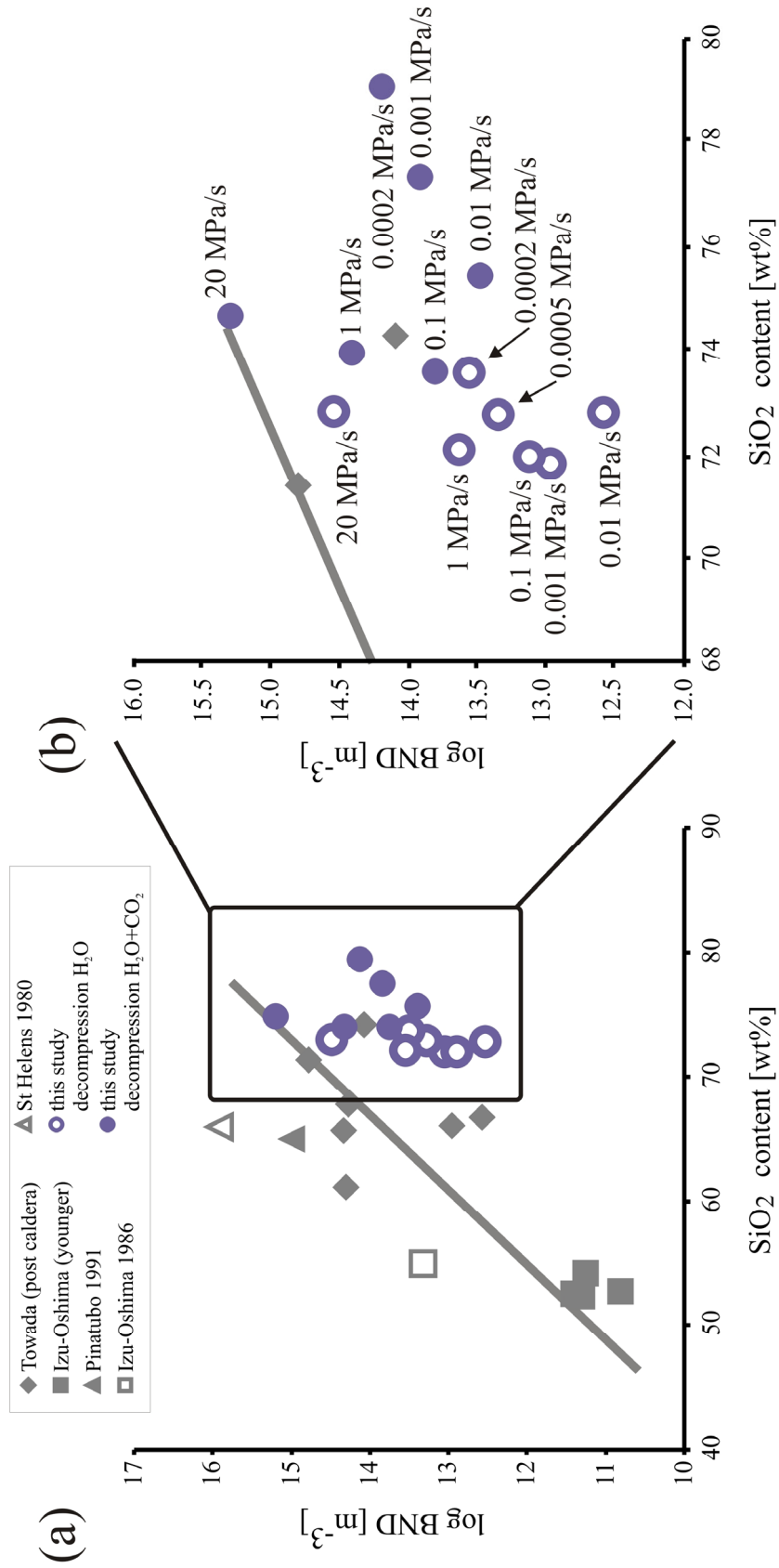


Fig. 3.13. Log BND vs. SiO₂-content of bulk rock for Plinian eruptions, modified after Toramaru (2006). The grey trend line is from Toramaru (2006) and does not account for the data obtained in this study (in purple color).

Dynamics of magma crystallization

Crystallization processes occurring during decompression can best be detected by a shift in the chemical composition of the residual melts. In the H₂O+CO₂-bearing system, the decrease of the MgO, FeO, CaO and Al₂O₃ contents and the simultaneous increase of the SiO₂ and K₂O content at decompression rates lower than 0.1 MPa/s are clearly related to the crystallization of Pl and MgO-bearing phases such as Cpx and/or Opx. In the H₂O-bearing system, the decrease of the MgO content of residual melts at decompression rates lower than 0.1 MPa/s indicates the crystallization of mafic minerals. The changes in Al₂O₃, CaO and SiO₂ contents at decompression rates of 0.0002 and 0.0005 MPa/s are attributed to the crystallization of the large Pl microlites. The delay of the decompression-induced nucleation and growth of microlites, occurring at decompression rates lower than 0.1 MPa/s, relative to the onset of magma degassing (compare Fig. 3.4 and Fig. 3.5) can be explained by the low diffusivity of major elements in silicate liquid when compared with the diffusivity of volatiles. Moreover, the local oversaturation of the melt with respect to a mineral phase (so-called undercooling of the system) may result in rapid and non-equilibrium growth of microlites. In particular, the appearance of Pl in H₂O-bearing experiments only at low decompression rates and the fact that Pl microlites are characterized by irregular skeletal shapes can be explained by kinetic effects (an undercooling of ~ 100°C or less is necessary to explain the skeletal shape of Pl; Lofgren, 1974; Muncill & Lasaga, 1987, 1988). The chemical heterogeneity of the glasses surrounding the Pl microlites also shows that equilibrium conditions are not reached during decompression.

The determined logMND_{Pl} and logMND_{OP} values for experimental samples range from 5.4-5.7 and 5.3-5.9, respectively, and do not show any clear dependence on the decompression rate within the experimental and analytical uncertainties. This indicates that, within the analytical uncertainty, no significant nucleation did. The absence of nucleation and growth is possible at fast decompression, but we clearly observed rims around amphiboles in the H₂O-bearing system and thin rims around plagioclase in the H₂O+CO₂-bearing system at decompression rates ≤ 0.01 MPa/s. Thus, at least crystal overgrowth processes occurred in the slow decompression experiments, as confirmed by the larger microlite sizes at decompression rates ≤ 0.001 MPa/s in the CSD plots (Fig. 3.8e and f). However, the analysis of the MND using our method does not show any significant effect of this overgrowth on logMND_{Pl} (H₂O+CO₂-bearing system) and on logMND_{OP}. The

$\log MND_{PI}$ of experiments in which PI nucleation clearly occurred (H_2O -bearing system) is not significantly different from that in the H_2O+CO_2 -bearing system.

The results of isobaric experiments at 300 and 50 MPa (Table 3.1) can be used to calculate the proportion of minerals which are expected to crystallize with decreasing pressure. Such mineral proportions as a result of equilibrium crystallization can be calculated in terms of mass fraction of crystallized material (ϕ) as a function of pressure, assuming K_2O concentration in the residual melt as a crystallization index (K is a strongly incompatible element during magma differentiation):

$$\phi = 1 - \left[\frac{\left(\frac{cK_2O_{start}}{cK_2O_{exp}} - DK_2O \right)}{(1 - DK_2O)} \right] \quad (3),$$

where K_2O_{start} is K_2O concentration in the starting glass, K_2O_{exp} is the concentration of K_2O in the experimental glasses, D is a partition coefficient of K_2O between mineral phases and melt, ϕ is the mass fraction of residual liquid. For this approach we assumed that the partition coefficient is close to 0.0001 (Rollinson, 1993; this value may be a minimum estimation assuming that plagioclase contain some K_2O). The results show that very small mineral proportions are expected for Unzen water-saturated groundmass composition at $850^\circ C$ (less than ~ 5 wt %) and that ~ 35 wt% crystals should present at 50 MPa (isobaric equilibrium experiments). Using equation (4), the calculated crystal contents are in the range of 5-10 wt% for all decompression experiments in the H_2O -bearing system which is identical within error to the equilibrium value at 300 MPa. The only experiment differing significantly from the initial crystal content was performed with the slowest decompression (0.0002 MPa/s) with a calculated crystal fraction of ~ 19 wt%. Thus, even in this experiment the equilibrium crystal fraction at 50 MPa was not reached (Table 3.2).

Effect of degassing and crystallization: Implications for magma ascent dynamics at Unzen

Decompression range from 50 MPa to surface pressure

The fact that the compositions of natural matrix glasses from the dome samples are similar to the estimated composition of the groundmass glass of the conduit for most major elements (see Fig. 3.4) could indicate that no significant crystallization processes did occur during the last stage of magma ascent at Unzen. Such a conclusion is in agreement with our results on MND. Our MND values ($MND_{PI} = 10^{5.4}-10^{5.7} \text{ mm}^{-3}$) are in the same range as

3. DECOMPRESSION EXPERIMENTS

those of natural dome samples ($MND_{Pl} = 10^5 - 10^6 \text{ mm}^{-3}$; Noguchi *et al.*, 2008a; Toramaru *et al.*, 2008). On the other hand, observation contrasts with experimental results of Martel & Schmidt (2003), who investigated in the nucleation processes in dacitic magma at low pressures. They observed that at high pressure decompression (from 150 to 50 MPa) crystal growth is a dominating process while at low pressure decompression (from 50 to 15 MPa) crystal nucleation is more favorable. Hence, further decompression experiments conducted at lower pressures are needed to better interpret the dome textures and to evaluate the actual magma ascent rates in the low pressure range (e.g. using MND rate-meter from Toramaru *et al.*, 2008). Moreover, although MND values have been determined for the conduit samples (Noguchi *et al.*, 2008b), which are similar to the dome data set, these data should be used with caution since these rocks have undergone a different thermal history after the eruption.

Decompression range from 300 MPa to 50 MPa

Based on the obtained compositional and textural data we can estimate the velocity of magmas ascend from depths with pressures of 300 to shallow levels with pressure of 50 MPa during Unzen eruption. The two main observations which are useful for the estimation of the magma ascent rate are (1) the chemical composition of natural matrix glasses which can be well reproduced in the experiments performed in $\text{H}_2\text{O} + \text{CO}_2$ -bearing system at decompression rate of 0.0002 MPa/s (Fig. 3.4) and (2) the natural Pl microlite lengths which can be reproduced in the H_2O -bearing system at the same decompression rate (Fig. 3.10). Considering that the second observation is crucial, the agreement between experimental data and natural observation is expected to be reached best at decompression rates lower than 0.0005 MPa/s which corresponds to approximately 50 m/h. If the water activity is only slightly lower than 1.0 in the ascending system, the natural glass compositions observed in the dome can only be reproduced at decompression rates lower than 0.0001 MPa/s (Fig. 3.4) corresponding to $\sim 10 - 12$ m/h. The exact determination of the water activity in the ascending magmas close to the surface (~ 50 MPa) is difficult. Considering that the estimated ascent rates are lower than 50 m/h, volatile exsolution must have occurred at conditions close-to-equilibrium in the pressure range 300-50 MPa, which is typical for effusive non-violent eruptions (e.g. Hurwitz & Navon, 1994), as observed at Unzen. Assuming that the released volatiles are, at least in part, escaping from the magmatic system (open system degassing; e.g., Turner *et al.*, 1983; Gerlach, 1986) melts would be almost free of CO_2 at low pressure. On the other hand, the model of Ohba *et al.*

(2008) assumes that CO₂-H₂O-bearing fluids were continuously ascending in the Unzen conduit, which would maintain a relatively low water activity in the ascending magmas (the water activity would be mainly controlled by the percolation of CO₂-H₂O-bearing fluids). Thus, if the percolation of such fluids were “buffering” the water activity in the conduit, an ascent rate of ~ 50 m/h is more realistic than a value of ~ 10 m/h. In any case, these values are in general agreement with estimations from petrology by Nakada & Motomura (1999; 12-30 m/hour), from textural analysis by Noguchi *et al.* (2008a; 29-274 m/h in the pressure range 70-100 MPa) and from water exsolution rates by Toramaru *et al.* (2008; 50-245 m/h), while data from electrical resistivity structure measurements by Kagiya *et al.* (1999) lead to lower estimated ascent rates (~0.8 m/h).

CONCLUSION

Decompression experiments using a rhyodacitic composition show that the size of natural microlites can be only reproduced experimentally if the nucleation occurs during the decompression path. For example, in the investigated system, plagioclase is not present as equilibrium phase at 300 MPa but crystallizes during decompression because the stability field of this mineral is dependent on pressure and water activity. Once nucleation has proceeded, the degree of undercooling (as well as diffusivity of cations in the melts), which is dependent on the decompression rate, is expected to be the main parameter influencing mineral growth kinetics (mineral size). Thus, the size and shape of microlites can be used to constrain ascent rates at the onset of the crystallization of the corresponding phase. In the case of Unzen magmas, assuming that water activity is close to 1, the size of plagioclases is compatible with magma ascent rates of ~ 30-50 m/h at depths corresponding to ~ 200 to 50 MPa.

In our decompression experiments, using a partially crystallized starting material containing bubbles, a transition from non-equilibrium to near-equilibrium water release from the Unzen rhyolitic melt is observed at decompression rates between 1 and 0.1 MPa/s (at water-saturated conditions). At the investigated pressures, the dominant exsolution process is the result of bubble growth at relatively high decompression rates, which may be explained by increasing melt-vapor surface tension with ongoing degassing. However, at low decompression rates (< 0.01 MPa/s), heterogeneous bubble nucleation may become a dominant process which could be facilitated by the beginning of crystallization of microlites (overgrowth of preexisting crystals).

3.1.2. HPD experiments at high-temperature (930 °C; set-II)

Starting material

The starting material (glass powder) was generated as already explained in *chapter 2* and in *chapter 3.1.1*. But instead of annealing each capsule pair individually (one H₂O-saturated and the other H₂O+CO₂-saturated) before the decompression run, first a large homogeneous capsule (3.5-4.0 cm long and an inner diameter of 4.0 mm) was synthesized for 4 days at the starting P-T conditions (300 MPa, 930°C) in the IHPV under reducing conditions (Ar-H₂ gas mixture; ~NNO+0.95 for H₂O-bearing system and ~NNO-7.11 for H₂O+CO₂-bearing system) with final rapid quench. Then small cylinders with a total length of about 5 mm were cut from the big synthesis capsules. The synthesized and fluid-saturated glass cylinders were individually inserted into new capsules, which were again welded shut. After another short annealing time (2-4 hours) at same starting P-T conditions, isothermal continuous decompression (details see text below) was initialized until final pressure of 50 MPa with subsequent rapid quench. Decompression rates varied between 0.1 and 0.0002 MPa/s, see Table. 3.3.

Continuous decompression method

The decompression experiments at high-temperature (930°C) were conducted in IHPVs, using a new developed decompression valve that has been constructed by the team of Prof. Dr. Nowak (University Tübingen, Germany), which allows a continuous pressure release even at very low decompression rates (Nowak *et al.*, 2011). This new valve consists of a movable thin steel needle connected to a manual rotating hand wheel and to an attached preloaded high-load piezo actuator (HVPZT) with sensor option (company: PI GmbH & Co. KG, model number: P-247.7S), referred to in the following as piezo ceramic for simplicity. The piezo ceramic is attached to an external energy recovery power amplifier. A schematic overview of the decompression valve can be found in Fig. 3.14.

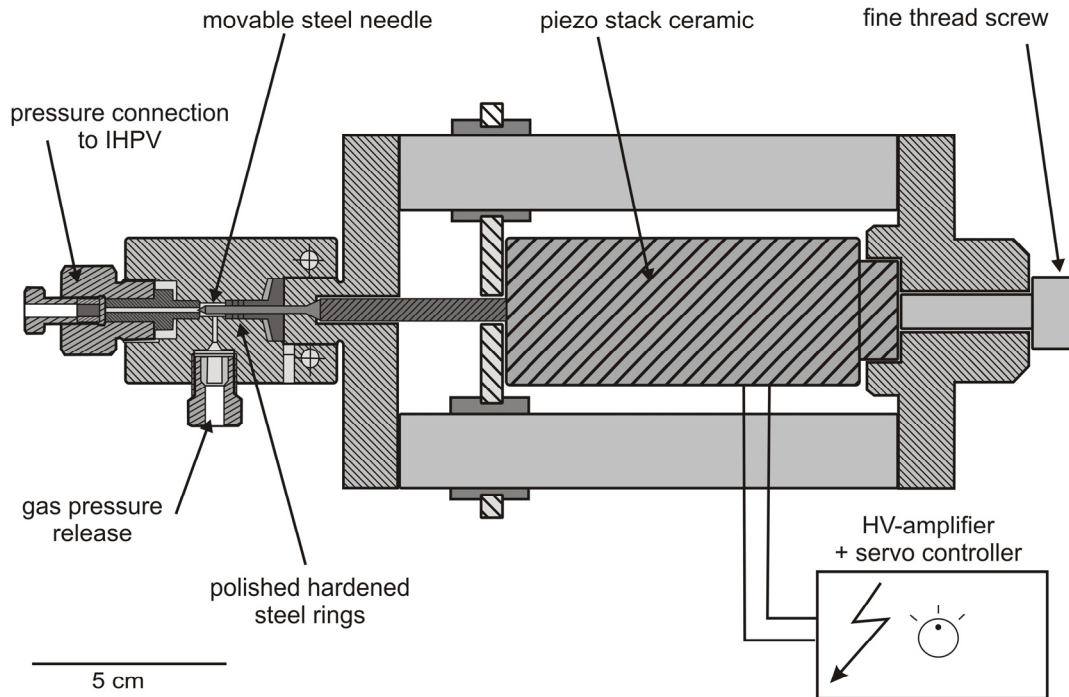


Fig. 3.14. Schematic illustration of the new decompression valve installed additionally to the IHPV. The center piece of this valve is the piezo ceramic that can move the steel needle due to mechanical strain induced by electrical voltage (source: Nowak *et al.*, 2011).

The piezo ceramic can be reversely expanded or contracted in one material-specific direction induced by electrical voltage (piezoelectric effect: a linear interaction between the mechanical and electrical state in the crystalline material). Therefore, the steel needle which is carefully connected directly to the piezo ceramic can be moved for few micrometers (max. 120 μm using max. 10 V), opening the gas pressure release valve. For visualization of the gas release, a flexible tube has been inserted into the pressure release valve, leading to a water filled container where gas escapes as bubbles, see Fig. 3.15. Adjusting the decompression rate has been proceeded by visual inspection as a combination of the rate of gas bubble release in the water container and the pressure display of the IHPVs logging unit.

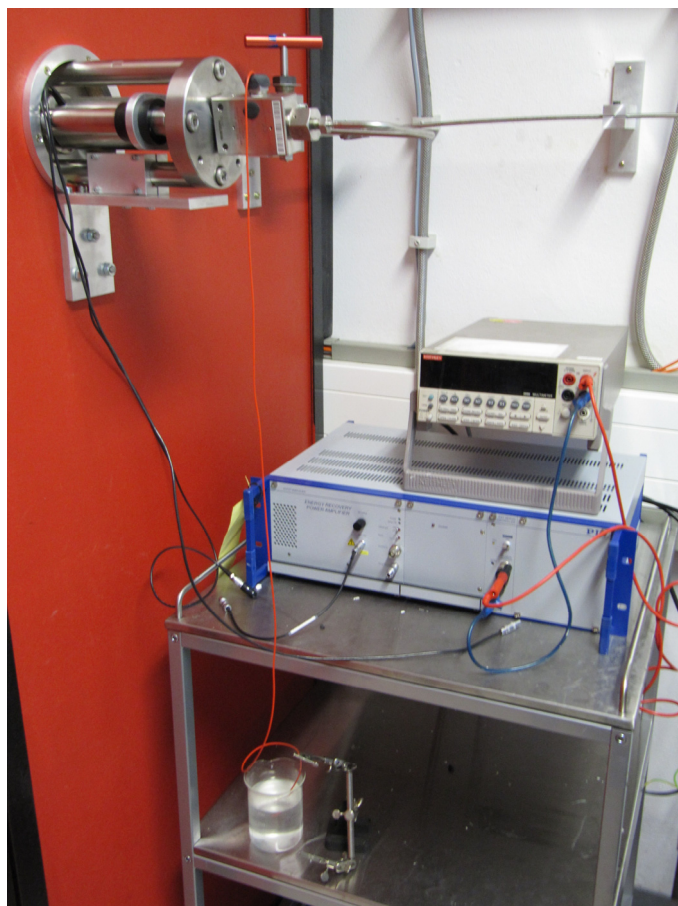


Fig. 3.15. Photo of the decompression valve at the high-pressure laboratory of the Institute for Mineralogy, Leibniz University Hannover, Germany. In the upper left corner the decompression valve is fixed to the wall. On the table the power amplifier and a voltage display are situated. The gas pressure release opening of the decompression valve is connected via a thin flexible tube to a filled water glass on the lower shelf of the table, where the release of single gas bubbles can be observed.

RESULTS

Phase assemblages and compositions of set-II HPD experiments

The experimental products of HPD set-II consist of glass, microlites and vesicles (Fig. 3.16). The solid experimental products obtained from both fluid-saturated (H_2O -bearing and the $\text{H}_2\text{O}+\text{CO}_2$ -bearing) starting assemblages at 930°C are composed of glass, oxides (Ox, mainly limenite), pyroxenes (Opx and Cpx). Amphibole (Amph) and plagioclase (Pl) microlites are not detected in any of the decompression experiments or in isobaric experiments at 300 MPa of both fluid-saturated systems. However, Pl is stable at the final pressure of 50 MPa in the H_2O -bearing and the $\text{H}_2\text{O}+\text{CO}_2$ -bearing system (UN103 and UN105, respectively), as already shown in our previously discussed phase stability experiments (see *chapter 2* and *Appendix Table A.3* for chemical composition of Pl microlites).

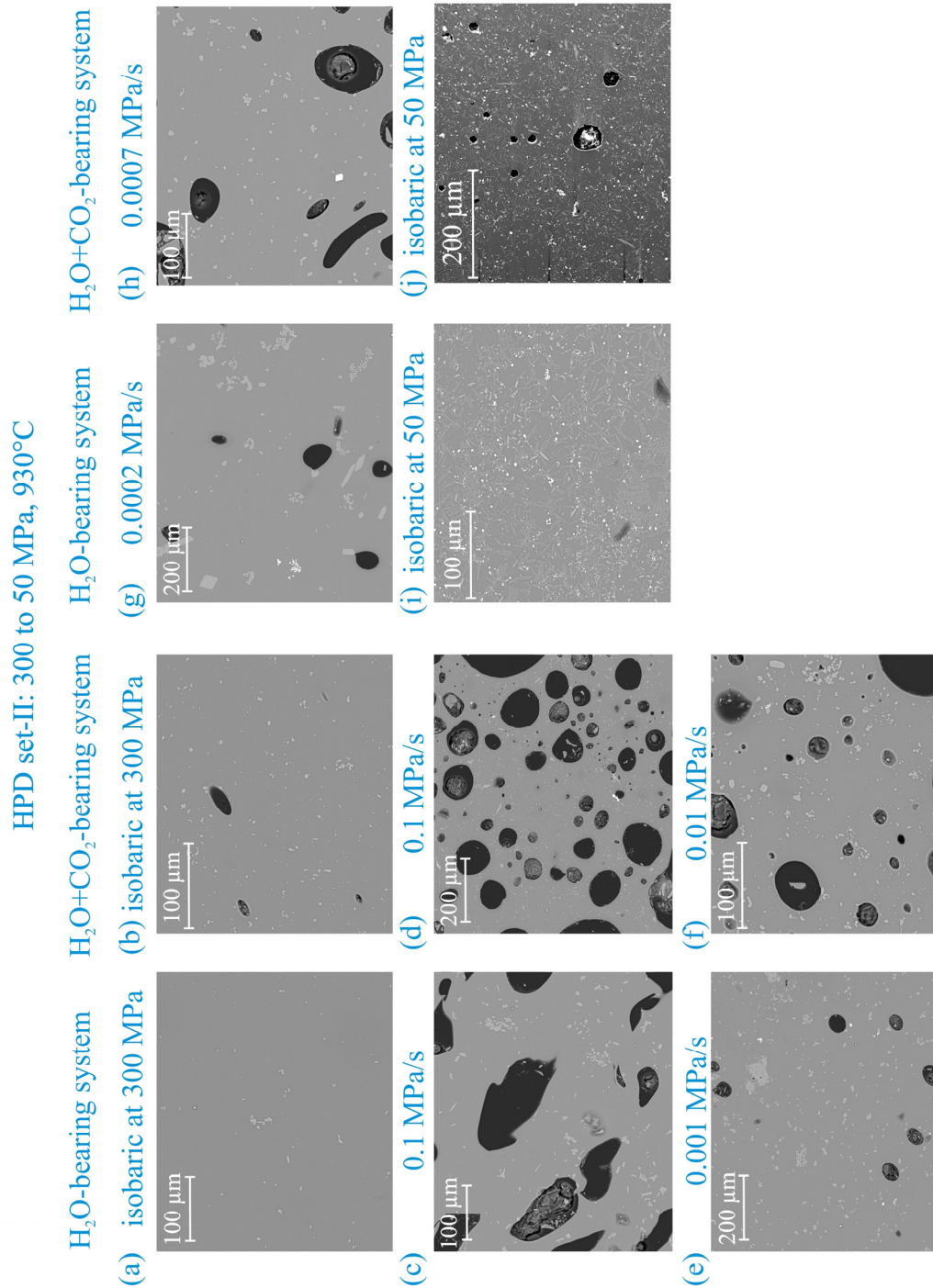


Fig. 3.16 a-j. BSE pictures of the products of isobaric and HPD experiments of set-II. Black bodies are bubbles; light grey particles represent microlites such as Cpx, Opx, Pl and oxides.

Melt compositions

The chemical analyses of the residual melts are listed in Table. 3.3 and plotted in Fig. 3.17. The chemical composition of the glasses in both fluid-saturated systems remains nearly constant with changing decompression rates and is in the same range as the composition of the isobaric starting glasses at 300 MPa. The experimental data are compared with the compositional range of natural Unzen dome and conduit groundmass glasses (grey fields in Fig. 3.17; Nakada & Motomura, 1999; Noguchi *et al.*, 200b). Except for the Na₂O contents

3. DECOMPRESSION EXPERIMENTS

(Fig. 3.17g), none of the major oxides of the decompression experiments overlap with the composition of the natural Unzen samples. On the other hand, the chemical compositions of the H₂O-bearing and H₂O+CO₂-bearing isobaric experiments at 50 MPa are similar to natural groundmass glasses for most major oxides.

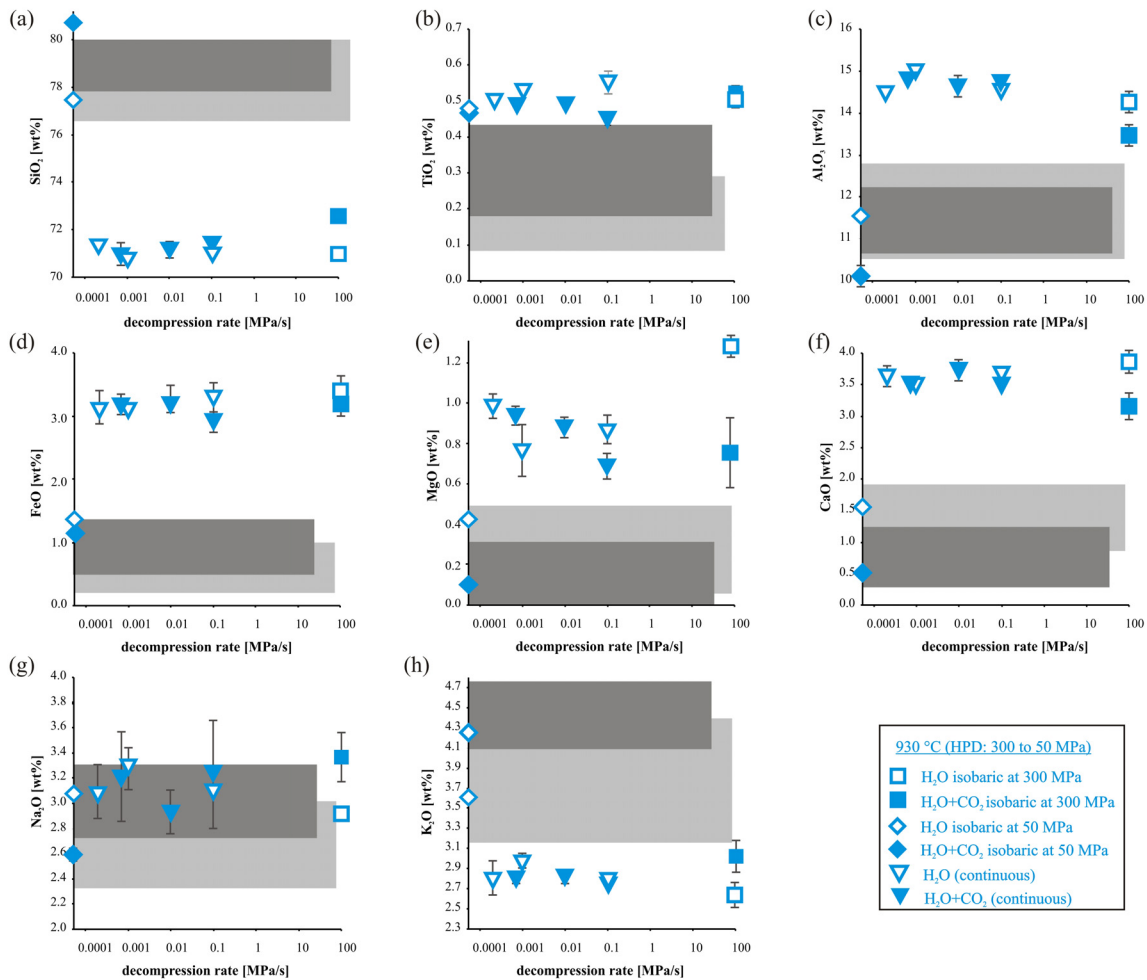


Fig. 3.17. Normalized chemical compositions of the experimental residual melts of set-II as a function of the decompression rate. The dark grey shaded areas show the chemical composition range of the erupted natural groundmass glass in erupted rocks (Nakada & Motomura, 1999) and the light grey shaded areas show the estimated chemical composition range of groundmass glass composition in the conduit rocks (Noguchi *et al.*, 2008b) of the 1991-1995 Unzen eruption. Error bars show standard deviation (1σ) of replicate analyses.

Table 3.3. Experimental condition and chemical composition of residual melts of set-II. Numbers in parentheses show the standard deviation (1σ) of replicated analyses.

sample	X H ₂ O	Decompression rate [MPa/s]	Na ₂ O	SiO ₂	Al ₂ O ₃	CaO	K ₂ O	TiO ₂	FeO	MgO	MnO	total [wt%]
DEC02+06	1.0	isobaric at 300 MPa	2.91 (0.20)	70.99 (0.37)	14.26 (0.29)	3.90 (0.16)	2.75 (0.11)	0.51 (0.04)	3.39 (0.22)	1.29 (0.06)	0.00 (0.00)	92.95 (0.81)
HPD05	1.0	0.1	3.11 (0.26)	71.05 (0.23)	14.58 (0.13)	3.71 (0.03)	2.82 (0.12)	0.55 (0.03)	3.31 (0.23)	0.86 (0.07)	0.00 (0.00)	95.73 (0.16)
HPD11	1.0	0.001	3.30 (0.14)	70.82 (0.18)	14.99 (0.16)	3.50 (0.12)	2.98 (0.13)	0.53 (0.02)	3.11 (0.08)	0.76 (0.13)	0.00 (0.00)	97.45 (1.00)
HPD01	1.0	0.0002	3.08 (0.20)	71.36 (0.19)	14.51 (0.26)	3.64 (0.19)	2.80 (0.18)	0.50 (0.01)	3.12 (0.28)	0.99 (0.07)	0.00 (0.00)	97.72 (1.00)
UN103	1.0	isobaric at 50 MPa	3.12 (0.14)	77.79 (0.18)	11.64 (0.22)	1.52 (0.09)	3.60 (0.14)	0.49 (0.06)	1.41 (0.09)	0.43 (0.09)	0.00 (0.00)	100.80 (0.55)
DEC05+10	0.6	isobaric at 300 MPa	3.35 (0.58)	72.47 (0.41)	13.50 (0.24)	3.13 (0.20)	3.08 (0.16)	0.52 (0.02)	3.19 (0.31)	0.76 (0.18)	0.00 (0.00)	96.72 (1.00)
HPD17	0.6	0.1	3.25 (0.19)	71.61 (0.16)	14.76 (0.32)	3.53 (0.14)	2.77 (0.08)	0.46 (0.05)	2.94 (0.19)	0.69 (0.06)	0.00 (0.00)	96.02 (0.65)
HPD18	0.6	0.01	2.94 (0.19)	71.23 (0.43)	14.68 (0.16)	3.73 (0.18)	2.84 (0.06)	0.49 (0.04)	3.20 (0.30)	0.88 (0.05)	0.00 (0.00)	96.41 (1.03)
HPD07	0.6	0.0007	3.21 (0.36)	71.00 (0.45)	14.83 (0.22)	3.53 (0.09)	2.81 (0.05)	0.49 (0.01)	3.18 (0.14)	0.93 (0.04)	0.00 (0.00)	98.37 (0.63)
UN105	0.6	isobaric at 50 MPa	2.59 (0.23)	80.93 (0.28)	10.04 (0.30)	0.53 (0.05)	4.18 (0.09)	0.47 (0.05)	1.12 (0.10)	0.14 (0.06)	0.00 (0.00)	98.78 (0.58)

Initial and final pressure of decompression experiments after 4 day of annealing at 930°C were 300 and 50 MPa, respectively.

Note: Numbers in parentheses show the standard deviation (1σ) of replicated analyses

X H₂O: mole fraction of water prior to decompression

Table 3.4. Textural and chemical results for HPD set-II. Numbers in parentheses show the standard deviation (1σ) of replicated analyses.

sample	X H ₂ O	Decompression rate [MPa/s]	log BND [mm ⁻³]	log MND _{op} [mm ⁻³]	H ₂ O [wt%] ⁺ (NIR)	CO ₂ [wt%] ⁺ (MIR)
DEC02+06	1.0	isobaric at 300 MPa	2.24 (0.01)	5.07 (0.13)	6.95 (0.33)	0.00
HPD05	1.0	0.1	2.58 (0.14)	5.01 (0.19)	1.77 (0.29)	0.00
HPD11	1.0	0.001	2.90 (0.14)	5.04 (0.27)	2.51 (0.28)	0.00
HPD01	1.0	0.0002	2.56 (0.01)	4.11 (0.12)	2.69 (0.27)	0.00
UN103*	1.0	isobaric at 50 MPa	3.25 (0.01)	6.31 (0.06)	1.97 (0.20)	0.00
DEC05+10	0.6	isobaric at 300 MPa	4.20 (0.10)	5.85 (0.15)	4.42 (0.30)	n.d.
HPD17	0.6	0.1	4.94 (0.03)	5.90 (0.15)	1.35 n.d.	0.18
HPD18	0.6	0.01	4.44 (0.07)	5.89 (0.14)	1.67 (0.31)	0.02
HPD07	0.6	0.0007	2.94 (0.04)	5.06 (0.10)	2.63 (0.27)	0.00
UN105*	0.6	isobaric at 50 MPa	n.d.	n.d.	2.11 (0.22)	0.00

MND_{op}: microlite number density calculated for other microlite phases incl. pyroxenes and oxides

n.d.: not detected / determined

X H₂O: mole fraction of water prior to decompression

+: errors in parentheses for FTIR derived H₂O and CO₂ contents are calculated by error propagation, but are likely to have relatively higher (~20%) uncertainties, e.g. due to the low sample thickness

**: in these isobaric experiments at 50 MPa and 930°C, Pt crystallized in the system (average An contents can be found in Appendix Table A.3.2)*

Water concentrations obtained from NIR spectroscopy (details see *chapter 2.1.*) in the fluid-saturated starting glasses at 300 MPa are 6.95 wt% and 4.42 wt% for the H₂O-bearing and for the H₂O+CO₂-bearing system, respectively. The residual melts of the decompression end products show water concentrations that are close to equilibrium concentrations at final pressure (isobaric at 50 MPa $\sim 2.0 \pm 0.2$ wt%) for both systems, see Table 3.3. The H₂O content of all decompression end products are similar within the error to that expected at isobaric 50 MPa. However, the quality of the NIR determination may have been negatively affected by larger microlite phases or bubbles.

Textures

Bubble and crystal size distributions (BND and CSD, respectively) as well as bubble and microlite number densities (BND and MND, respectively) have been determined following the methods already described in *chapter 3.1.1.*

Bubbles

The BSD in the samples show concave-up shaped size distributions, as illustrated in *Appendix* Figs. B.1 and B.2. In the H₂O+CO₂-bearing system, especially the population densities at smaller sizes (< 0.05 mm) are higher when compare to the H₂O-bearing system. There seems to be a systematic variation of the BSD as a function of the decompression rate: the population densities of smaller sized bubbles (< 0.05 mm) decrease with decreasing decompression rate. While at the lowest conducted decompression rate, two generations of bubbles were detectable in both fluid-saturated systems: one generation at bubble sizes < 0.01 mm and another bubble generation having sizes larger than 0.03 mm.

The BND values of the H₂O+CO₂-bearing system decrease with decreasing decompression rate from 0.1 to 0.0007 MPa/s, ranging from $10^{5.9}$ mm⁻³ to $10^{5.0}$ mm⁻³ (Fig. 3.18), respectively. The BND values of the H₂O-bearing system follow the same trend as that of the H₂O+CO₂-bearing system at very low decompression rates (≤ 0.001 MPa/s) and are slightly lower than in the equilibrium experiment at 50 MPa. While the BND value of the highest conducted decompression rate (0.1 MPa) in the H₂O-bearing system is ~ 2.5 log units lower than that of the H₂O+CO₂-bearing system and does not fit to the observed trend of decreasing BNDs with decreasing decompression rates.

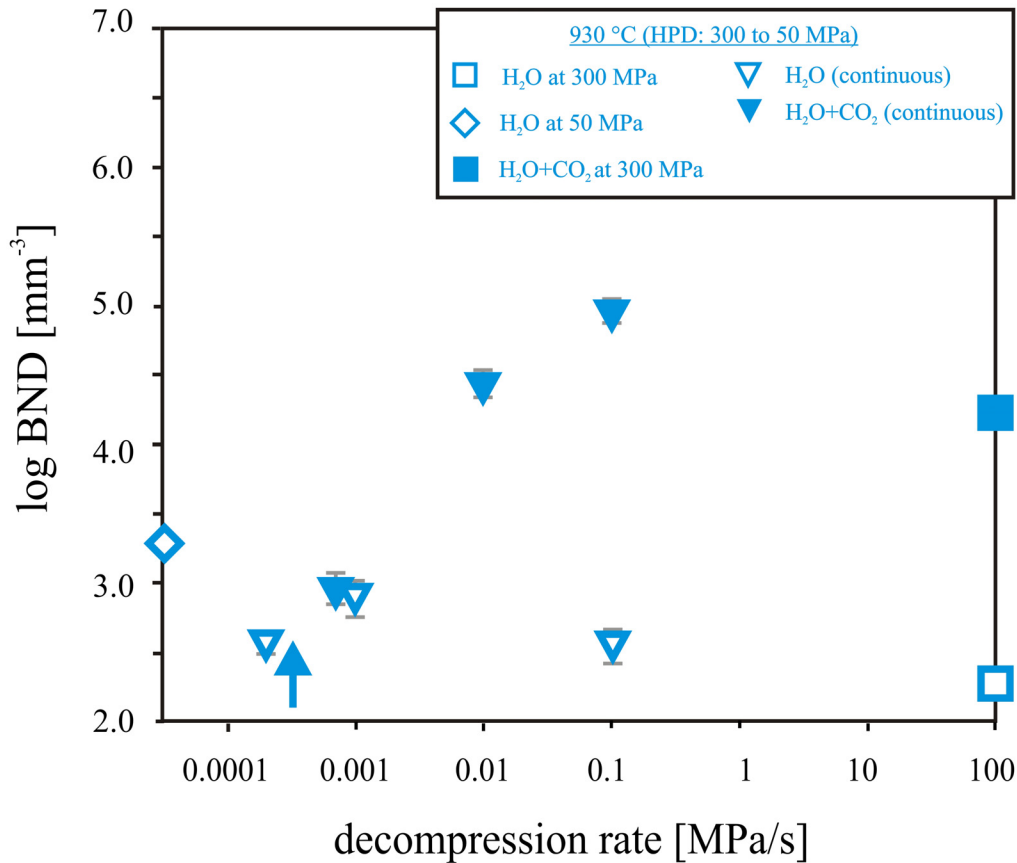


Fig. 3.18. Bubble number density (BND) as a function of the decompression rate for the H₂O-bearing system (empty symbols) and the H₂O+CO₂-bearing system (filled symbols). Triangles are continuous decompression experiments. The blue arrow indicates the onset of plagioclase crystallization in the H₂O-bearing system. Error bars show standard deviation (1σ) of replicate analyses.

Microlites

The average chemical composition of pyroxenes (Opx and Cpx) can be found in *Appendix Table A.6.1* and *A.6.2*. No MND_{Pl} or CSD values for plagioclase microlites were determined as Pl microlites did not crystallize in HPD experiments of the H₂O-bearing and H₂O+CO₂-bearing system at 930°C. Most CSD curves for other phases (OP) in the samples of both systems show concave-up shapes (*Appendix Figs. B.1* and *B.2*). There is a systematic variation in the H₂O-bearing samples: population densities with smaller microlite sizes (< 0.05 mm) decrease with decreasing decompression rate, while the maximum crystal sizes increase from 0.1 mm to 0.25 mm with increasing decompression rate from 0.1 to 0.0002 MPa/s, respectively. In the H₂O+CO₂-bearing system, only the population densities at smaller crystal sizes (< 0.05 mm) decrease with decreasing decompression rate, but there cannot be found any significant systematic variation in the maximum microlite size with changing decompression rates (*Appendix Fig. B.2*).

3. DECOMPRESSION EXPERIMENTS

The MNDs for other phases (MND_{OP}) in the H_2O+CO_2 -bearing system range from $10^{5.9} \text{ mm}^{-3}$ at decompression rates $\geq 0.01 \text{ MPa/s}$ to $10^{5.1} \text{ mm}^{-3}$ at the lowest decompression rate (0.0007 MPa/s), see Fig. 3.19. While the MND_{OP} values in the H_2O -bearing system range from $10^{5.0} \text{ mm}^{-3}$ at decompression rates $\geq 0.001 \text{ MPa/s}$ to $10^{4.1} \text{ mm}^{-3}$ at the lowest decompression rate (0.0002 MPa/s).

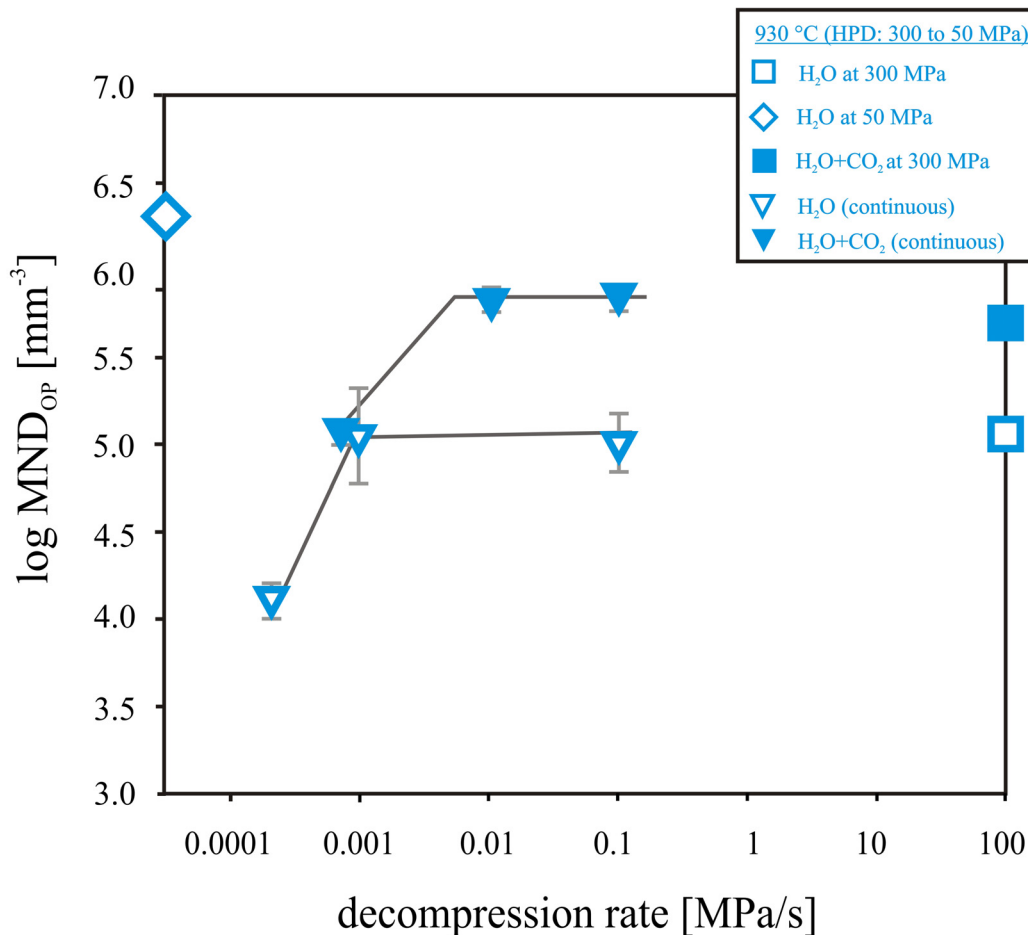


Fig. 3.19. Microlite number density for all other phases (MND_{OP}) such as pyroxenes and oxides as a function of the decompression rate for the H_2O -bearing system (empty triangles) and the H_2O+CO_2 -bearing system (filled triangles). Error bars show standard deviation (1σ) of replicate analyses.

3.2. Low pressure decompression (LPD)

The main focus concerning the low pressure decompression (LPD) experiments was the simulation of magma ascent from a starting pressure of 50 MPa to a final surface pressure of 0.1 MPa at both investigated temperatures of 850°C and 930°C (set-III and set-IV, respectively; *chapter 3.2.1.*), completing the data sets of our performed high pressure decompression (HPD) experiments presented in *chapter 3.1.* In our LPD experiments, only the water-bearing system was investigated as carbon dioxide is assumed to be totally exsolved from the melt at those low depths (e.g. Fogel & Rutherford, 1990; Behrens *et al.*, 2004; Liu *et al.*, 2005). Additionally, one LPD set was performed starting at a higher pressure of 200 MPa down to surface pressure at 850 °C (set-V; see *chapter 3.2.2.*). This experimental approach (starting at 200 MPa) is covering the lower pressure range estimated for the storage conditions of the mixed dacitic magma prior to the 1991-1995 Unzen eruption (minimum pressure of 160 MPa; Venezky & Rutherford, 1999), and was chosen as a result of our former presented phase stability experiment at these conditions (sample Un06), where plagioclase microlites were not yet crystallized. The decompression paths for our LPD experiments of set-III, set-IV and set-V are plotted schematically in Fig. 3.20.

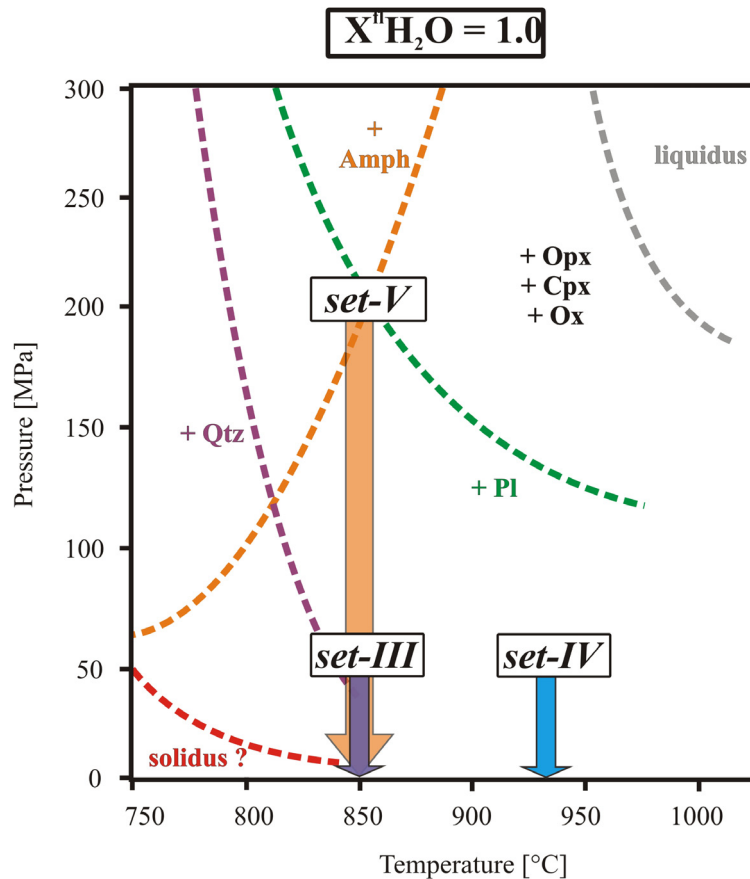


Fig. 3.20. Schematic phase diagram for water-saturated rhyodacitic magma, derived from this study *chapter 2* (phase stability experiments). The purple and blue arrows show the isothermal decompression paths of LPD set-III and set-IV, starting from 50 MPa down to final 0.1 MPa at temperatures of 850°C and 930°C, respectively. While the orange arrow indicates the isothermal decompression path of LPD set-V, starting from 200 MPa down to final 0.1 MPa at a temperature of 850°C.

3.2.1. LPD: from 50 to 0.1 MPa at high- and low-temperatures (set-III and set-IV)

Experimental strategy

For the capsule preparation, we followed the method described in *chapter 3.1.2* (HPD experiments), while starting pressure and annealing times were adjusted to the here corresponding experimental approaches: annealing time of 14 days at 50 MPa for the synthesis capsules. Decompression rates varied between 0.1 and 0.0001 MPa/s and decompression was performed as multi-step decrease in pressure at 850°C in CSPVs or as continuous pressure release at 930°C in the IHPVs, using the new developed valve described above (*chapter 3.1.2*). Experimental conditions of each LPD run are given in

Table 3.5. Chemical and textural data were determined by the analytical methods described already above in *chapter 2* and *chapter 3.1.1*.

RESULTS

Phase assemblage and compositions

The end products of water-saturated LPD experiments at 850°C and at 930°C consist of glass, microlites and vesicles (Fig. 3.21 and *Appendix* Figs. B.3 and B.4). Solid experimental products of the starting assemblage at 50 MPa are composed of glass, plagioclase and oxides as well as \pm pyroxenes at both temperatures. The mineral assemblage of all LPD end products is consistent with that of the starting materials at 50 MPa, while having additional quartz (Qtz) microlites crystallized in both LPD sets, usually in close contact to the bubbles. Chemical compositions of plagioclases and pyroxenes can be taken from *Appendix* Table A.7.1-3.

The average anorthite (An) contents of Pl microlites in LPD end products do not differ much from the starting composition at 50 MPa: 54 mol% at 930°C and 44 mol% at 850°C, see *Appendix* Table A.7.1. Plagioclases crystallized at 850°C (set-III) have slightly lower An contents (41-44 mol%) when compared to those of the high-temperature (set-IV; 930°C) LPD set (53-54 mol%). All anorthite contents are in the range of naturally crystallized Pl microlites from Unzen dome and conduit samples (Noguchi *et al.*, 2008a, b).

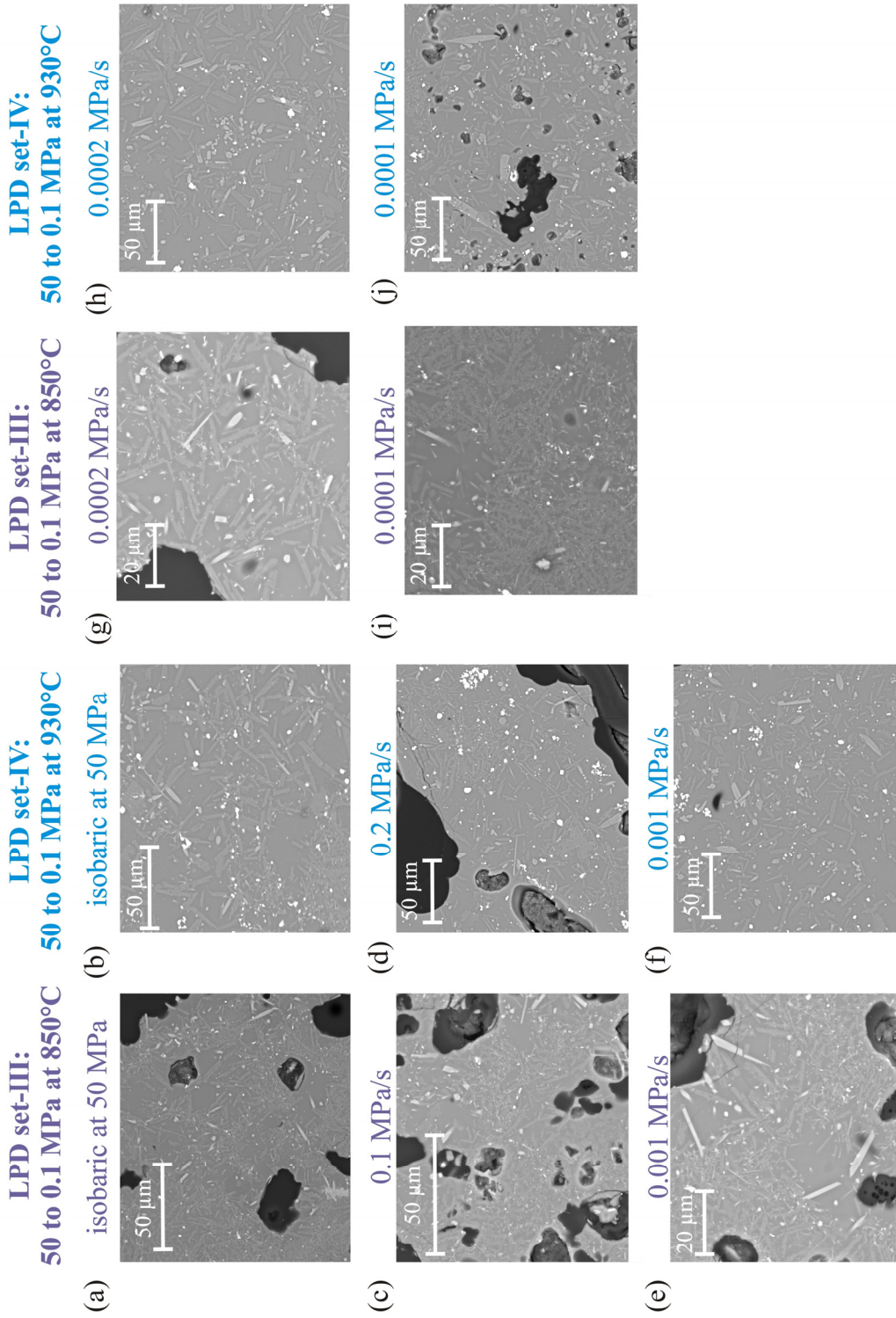


Fig. 3.21 a-j. BSE pictures of the products of isobaric and decompression experiments for LPD set-III (850°C, left side) and set-IV (930°C, right side). Black bodies are bubbles; light grey particles represent microlites such as Cpx, Opx, Pl and oxides.

Table 3.5. Experimental conditions and chemical compositions of residual glasses for the H₂O-bearing system (X^HH₂O=1.0) at 850 °C (set-III) and at 930 °C (set-IV).

sample set #	T [°C]	Decompression rate [MPa/s]	Na ₂ O	SiO ₂	Al ₂ O ₃	CaO	K ₂ O	TiO ₂	FeO	MgO	MnO	total [wt%]
Big01	850	isobaric at 50 MPa	2.72 (0.10)	78.94 (0.23)	11.00 (0.14)	1.16 (0.08)	4.13 (0.11)	0.30 (0.03)	1.52 (0.16)	0.21 (0.06)	0.00 (0.00)	98.49 (0.67)
LPD05	850	0.1	2.74 (0.07)	78.37 (0.36)	11.07 (0.34)	1.11 (0.02)	4.16 (0.32)	0.26 (0.03)	2.00 (0.71)	0.29 (0.35)	0.00 (0.00)	99.12 (1.35)
LPD04	850	0.01	2.89 (0.20)	78.51 (0.31)	11.32 (0.15)	1.07 (0.15)	4.49 (0.14)	0.27 (0.07)	1.34 (0.13)	0.10 (0.13)	0.00 (0.00)	100.12 (0.87)
LPD03	850	0.001	2.55 (0.12)	79.54 (0.48)	10.72 (0.60)	0.81 (0.13)	4.75 (0.07)	0.26 (0.05)	1.15 (0.26)	0.20 (0.18)	0.00 (0.00)	97.06 (0.77)
LPD02	850	0.0002	2.62 (0.16)	80.09 (0.40)	10.71 (0.20)	0.47 (0.07)	4.88 (0.06)	0.27 (0.04)	0.92 (0.20)	0.04 (0.05)	0.00 (0.00)	100.23 (0.50)
LPD01	850	0.0001	2.59 (0.17)	79.92 (0.58)	10.81 (0.35)	0.51 (0.22)	5.07 (0.18)	0.26 (0.01)	0.82 (0.17)	0.02 (0.04)	0.00 (0.00)	100.03 (0.52)
UN103	930	isobaric at 50 MPa	3.12 (0.14)	77.79 (0.18)	11.64 (0.22)	1.52 (0.09)	3.60 (0.14)	0.49 (0.06)	1.41 (0.09)	0.43 (0.09)	0.00 (0.00)	100.80 (0.55)
LPD21	930	0.02	3.15 (0.12)	75.84 (0.46)	12.22 (0.17)	1.80 (0.05)	3.82 (0.11)	0.44 (0.07)	2.33 (0.26)	0.40 (0.05)	0.00 (0.00)	99.33 (0.43)
LPD23	930	0.001	3.13 (0.27)	77.03 (0.34)	11.88 (0.33)	1.18 (0.08)	4.15 (0.11)	0.47 (0.07)	1.86 (0.29)	0.30 (0.02)	0.00 (0.00)	100.86 (0.71)
LPD22	930	0.0002	3.28 (0.31)	77.94 (0.62)	11.48 (0.31)	0.94 (0.10)	4.10 (0.13)	0.49 (0.03)	1.60 (0.12)	0.19 (0.03)	0.00 (0.00)	99.74 (0.59)
LPD26	930	0.0001	3.01 (0.26)	78.70 (0.33)	11.34 (0.20)	0.84 (0.06)	3.95 (0.10)	0.50 (0.03)	1.44 (0.16)	0.21 (0.04)	0.00 (0.00)	100.67 (0.52)

Initial and final pressure of decompression experiments after 14 day of annealing at temperatures of 850°C and 930°C were 50 and 0.1 MPa, respectively.

Note: Numbers in parentheses show the standard deviation (1σ) of replicated analyses

Table 3.6. Textural results of set-III (850°C) and set-IV (930°C). Numbers in parentheses show the standard deviation (1σ) of replicated analyses.

sample #	T [°C]	decompression rate [MPa/s]	log BND [mm ⁻³]	log MND _{op} [mm ⁻³]	log MND _{pr} [mm ⁻³]	Max. Pl length [μm]	Average An content [mol%]	H ₂ O [wt%] ⁺ (NIR)	CO ₂ [wt%] ⁺ (MIR)
Big01	850	isobaric at 50 MPa	4.01 (0.19)	6.16 (0.12)	6.25 (0.15)	17	44	n.d. n.d.	0.00
LPD05	850	0.1	4.73 (0.07)	6.13 (0.13)	6.36 (0.11)	22	41	n.d. n.d.	n.d.
LPD04	850	0.01	4.73 (0.10)	6.41 (0.16)	6.31 (0.14)	20	44	n.d. n.d.	n.d.
LPD03	850	0.001	4.40 (0.08)	6.43 (0.30)	6.36 (0.08)	11	41	n.d. n.d.	n.d.
LPD02	850	0.0002	4.11 (0.09)	6.42 (0.15)	6.14 (0.12)	17	44	n.d. n.d.	n.d.
LPD01	850	0.0001	4.33 (0.13)	6.40 (0.17)	6.18 (0.06)	18	42	0.48 n.d.	n.d.
UN103	930	isobaric at 50 MPa	3.25 (0.01)	6.31 (0.06)	6.00 (0.26)	40	54	1.97 (0.20)	0.00
LPD21	930	0.02	3.20 (0.18)	5.78 (0.14)	5.59 (0.13)	53	53	n.d. n.d.	n.d.
LPD23	930	0.001	3.59 (0.07)	5.97 (0.08)	6.12 (0.10)	42	53	n.d. n.d.	n.d.
LPD22	930	0.0002	4.07 (0.14)	6.05 (0.05)	6.01 (0.06)	44	54	n.d. n.d.	n.d.
LPD26	930	0.0001	5.31 (0.20)	5.96 (0.16)	5.95 (0.10)	50	54	n.d. n.d.	n.d.

MND_{op}: microlite number density calculated for other microlite phases incl. pyroxenes and oxides

n.d.: not detected / determined

+ : errors in parentheses for FTIR derived H₂O and CO₂ contents are calculated by error propagation, but are likely to have relatively higher (~20%) uncertainties, e.g. due to the low sample thickness

3. DECOMPRESSION EXPERIMENTS

Melt compositions

The chemical analyses of the residual melts of LPD sets III and IV are listed in Table 3.5 and plotted in Fig. 3.22. The chemical composition of the residual glasses obtained from LPD experiments at both temperatures change nearly constantly with decreasing decompression rate for most major element oxides. The SiO_2 and K_2O contents in residual glasses increase with decreasing decompression rates, while Al_2O_3 , FeO , MgO and CaO contents of glasses decrease with decreasing decompression rates. Over all, the chemical compositions of the low-temperature (850°C) LPD experiments at all performed decompression rates overlap with the compositional range of groundmass glasses of natural erupted Unzen rocks (grey fields in Fig. 3.22; Nakada & Motomura, 1999). While the chemical compositions of the high-temperature (930°C) LPD experiments are only close to natural Unzen dome samples at very low decompression rates (< 0.001 MPa/s).

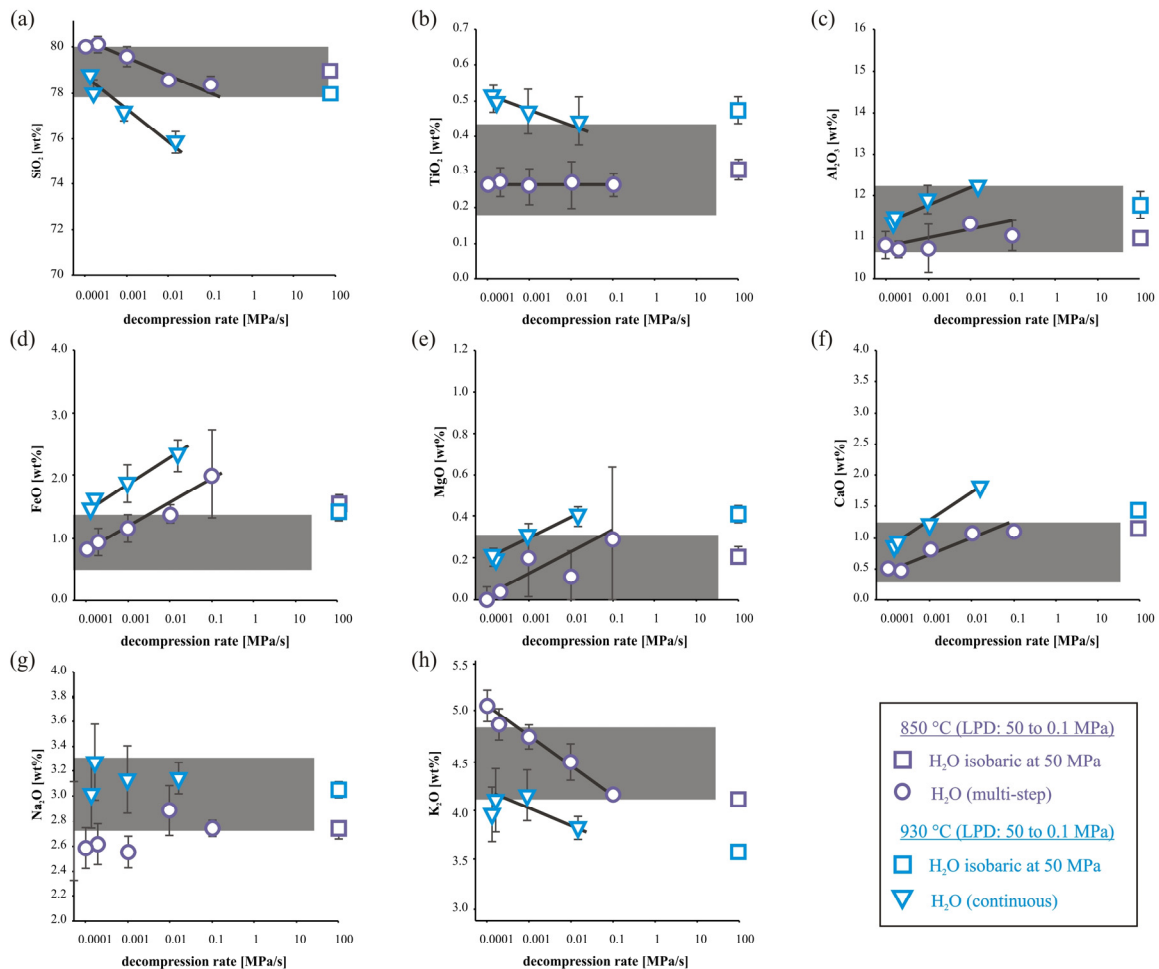


Fig. 3.22. Normalized chemical compositions of the experimental residual melts as a function of the decompression rate at 850°C (set-III; purple symbols) and at 930°C (set-IV; blue symbols). The grey shaded areas show the chemical composition range of the natural groundmass glass in erupted rocks (Nakada & Motomura, 1999) of the 1991-1995 Unzen eruption. Error bars show standard deviation (1σ) of replicate analyses.

The determination of water concentrations in the residual glasses by NIR spectroscopy was not practicable as all LPD end products were highly crystallized, providing not enough space for high quality analysis (without the influence of crystals or bubbles).

Textures

Bubbles

The BSD curves of the LPD samples show concave-up shapes for both temperatures, as illustrated in *Appendix* Figs. B.3 and B.4. A systematic variation of the BSD can be observed as a function of the decompression rate at 930°C: the maximum bubble size decreases from ~0.55 mm at 0.2 MPa/s to ~0.15 mm at 0.0001 MPa/s, while the population densities of small-sized bubbles increase at decompression rates < 0.001 MPa/s. Such distinct variations are not detectable in the low-temperature (850°C) LPD samples: maximum bubbles sizes range between ~0.35 and ~0.55 mm, while the population densities of all bubble size intervals are similar at all decompression rates. The determined BND values at 850°C are in the same order of magnitude for all decompression experiments, varying from $10^{4.1} \text{ mm}^{-3}$ to $10^{4.7} \text{ mm}^{-3}$, see Fig. 3.23. Whereas at 930°C there can be observed an (exponentially) increasing trend of BNDs with decreasing decompression rates, ranging from $10^{3.2} \text{ mm}^{-3}$ to $10^{5.1} \text{ mm}^{-3}$ at decompression rates of 0.02 to 0.0001 MPa/s, respectively.

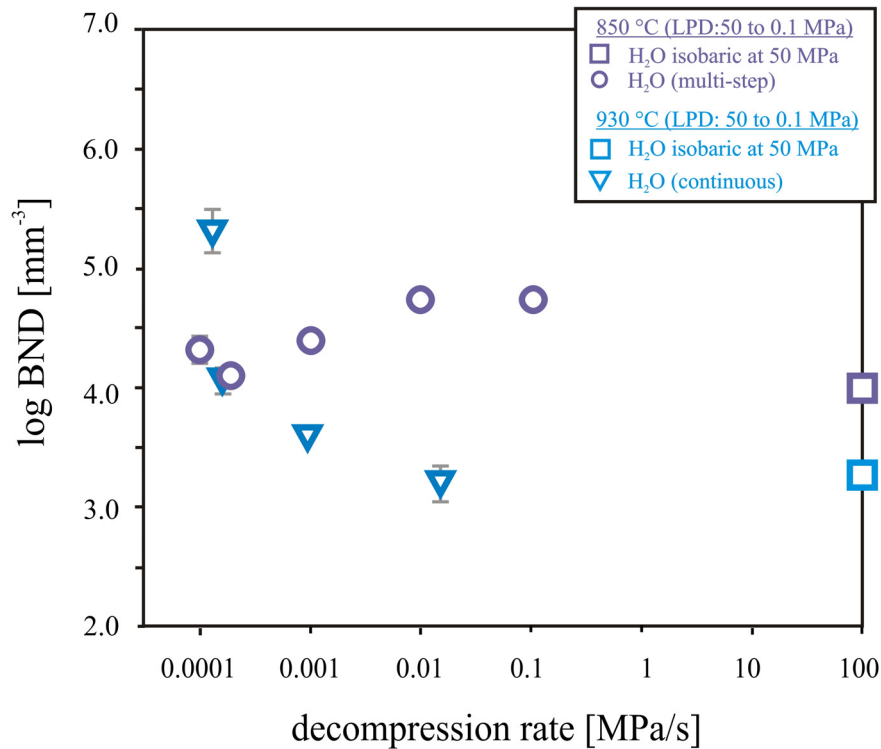


Fig. 3.23. Bubble number density (BND) as a function of the decomposition rate for the H_2O -bearing system at 850°C (set-III; purple symbols) and at 930°C (set-IV; blue symbols). Circles are multi-step decompression experiments and triangles represent continuous decompression experiments. Error bars show standard deviation (1σ) of replicate analyses.

Microlites

The CSDs in the LPD samples show concave-up curves for both temperatures, as illustrated in *Appendix* Figs. B.3 and B.4. A systematic variation of the CSDs with changing decompression rates can not be observed for both LPD sets. Population densities for plagioclase (Pl) microlites are slightly higher than for all other phases (OP) at sizes > 0.02 mm. When comparing CSD curves of set-III and set-IV at correlating decompression rates with each other then significant higher population densities at size intervals < 0.02 mm can be observed at 850°C , but generally higher maximum crystal sizes at 930°C . The CSD curves for set-III have steeper slopes at crystal sizes < 0.02 mm than compare to set-IV.

The determined MND_{Pl} values of both LPD sets at all decompression rates are in the same order of magnitude, ranging from $10^{6.0} \text{ mm}^{-3}$ to $10^{6.4} \text{ mm}^{-3}$, see Fig. 3.24a. Except for one decompression experiment at 930°C and 0.02 MPa/s , which is having a slightly lower MND_{Pl} value of $10^{5.6} \text{ mm}^{-3}$. Overall, the MND_{Pl} values stay nearly constant with changing decompression rates, while values of MND_{Pl} are ~ 0.1 - 0.3 log units higher at low temperatures. However, experimental MND_{Pl} values are ~ 0.3 - 0.5 log units higher than for

natural plagioclase microlites in natural Unzen dome samples (Noguchi *et al.*, 2008a). MND_{OP} values are in the same range as MND_{PI} values and do not change significantly with varying decompression rates (Fig. 3.24b). Again, values for high-temperature LPD experiments are ~ 0.4 - 0.5 log units lower than for LPD experiments at 850°C . While MND_{PI} and MND_{OP} values of decompression experiments are similar to the starting materials at 50 MPa (indicated by square symbols in Fig. 3.24 a-b).

Experimentally crystallized plagioclase microlites in all LPD runs show tabular appearances. The maximum length of Pl microlites are not significantly changing with decreasing decompression rates at both investigated temperatures, see Fig. 3.25. At 850°C , Pl microlites grew to a maximum of $\sim 20\ \mu\text{m}$, while at 930°C maximum lengths of $\sim 50\ \mu\text{m}$ were reached, which is in the lower range of Pl microlites found in Unzen conduit samples (Noguchi *et al.*, 2008 b; Goto *et al.*, 2008) but are too low for erupted Unzen dome samples (Noguchi *et al.*, 2008a).

3. DECOMPRESSION EXPERIMENTS

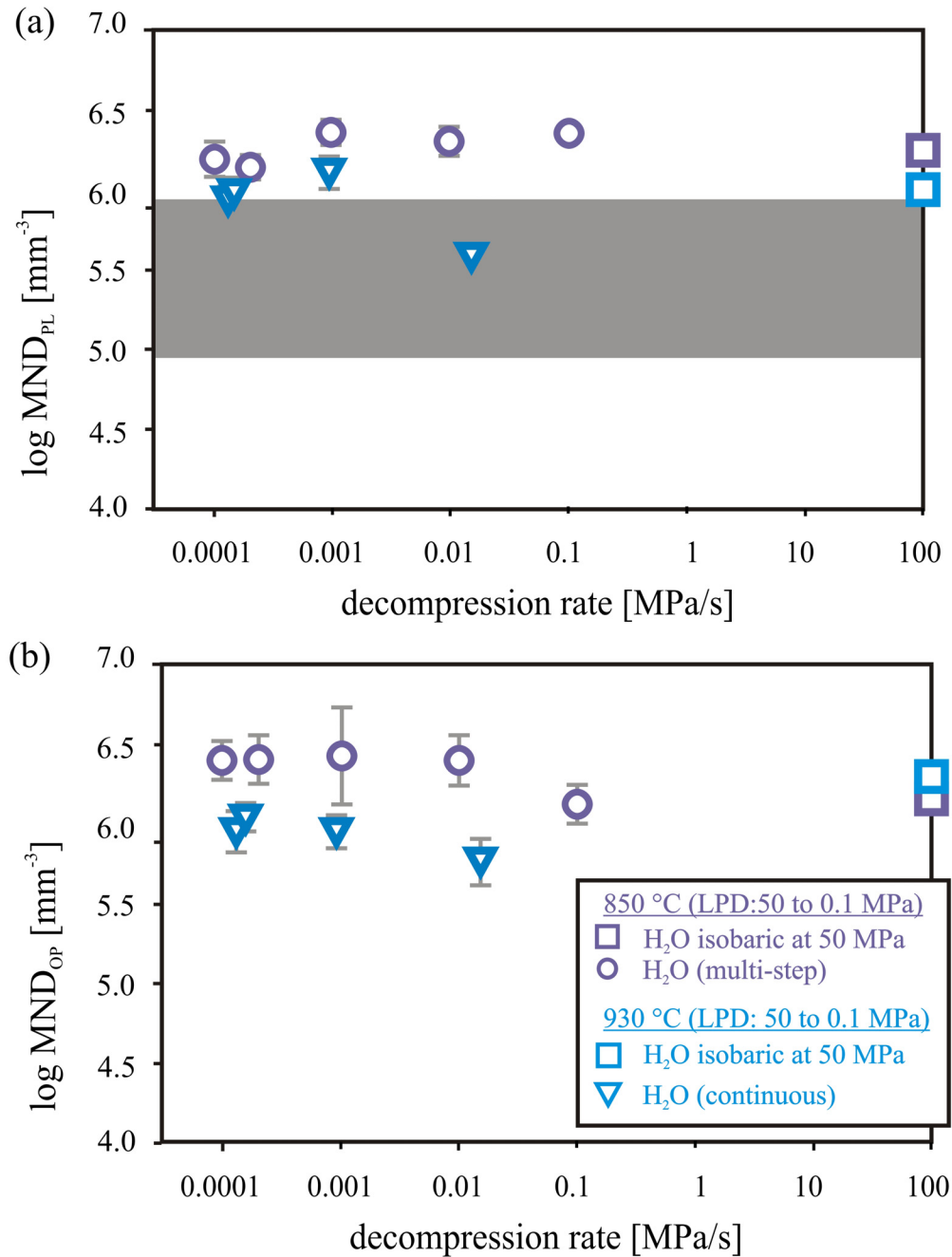


Fig. 3.24. Microlite number density (MND) as a function of the decompression rate for the H₂O-bearing system at 850°C (purple symbols) and at 930°C (blue symbols). (a) MND for plagioclases only (MND_{PL}) and (b) MND for all other phases (MND_{OP}) such as amphiboles, pyroxenes and oxides. The grey shaded area shows the MND_{PL} of natural dome samples (Noguchi *et al.*, 2008a). Error bars show standard deviation (1σ) of replicate analyses.

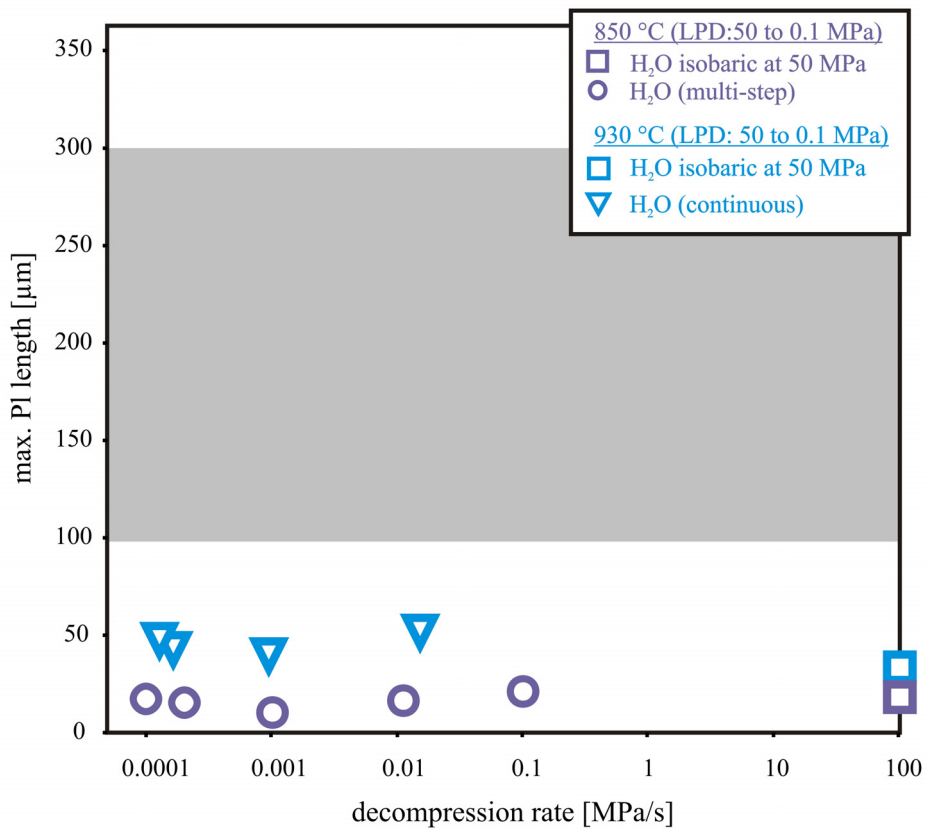


Fig. 3.25. Maximum Pl length as a function of the decompression rate. Dark grey shaded area represents the range of Pl microlite lengths of Unzen natural dome samples after Noguchi *et al.* (2008a).

3.2.2. LPD: from 200 to 0.1 MPa at low-temperature (set-V)

Experimental strategy

For the capsule preparation, we followed the method described in *chapter 3.1.2 (HPD experiments at 930°C)*, while the annealing time was 7 days at 200 MPa and 850°C for LPD set-V. Multi-step decompression experiments were conducted in CSPVs with decompression rates ranging from 0.01 to 0.0001 MPa/s, see Table 3.7. Chemical and textural data were determined by the analytical methods described already above in *chapters 2 and 3.1.1*.

RESULTS

Phase assemblage and compositions

The experimental products of LPD set-V at 850°C (sample Big03+04) consist of glass, microlites and vesicles (Fig. 3.26 and *Appendix Fig. B.5*). Solid experimental products of the starting assemblage at 200 MPa are composed of glass, plagioclase, amphibole, oxides and pyroxenes. Chemical composition of determined microlite phases are given in *Appendix Table A.8*. The mineral assemblage of all LPD end products is consistent with that of the starting materials at 200 MPa. Except at decompression rates ≤ 0.0002 MPa/s, Amph microlites are not present anymore in the LPD end products, which is in agreement with former studies on Amph stabilities in the 1991-1995 Unzen system (e.g. Sato *et al.*, 1999; Venezky & Rutherford, 1999; see also this study *chapter 2*).

The average anorthite contents of the analysed Pl microlites show no systematic variation with changing decompression rates and range from 65 to 50 mol%. The compositions and magnesium numbers [$Mg\# = Mg/(Fe_{tot} + Mg)$, moles] of detected Amph microlites were analyzed, see *Appendix Table. A.8.1*. At isobaric starting conditions, the average Mg# is 0.64, while Mg numbers of the two LPD experiments at 0.01 MPa/s and 0.001 MPa/s are 0.72 and 0.70, respectively.

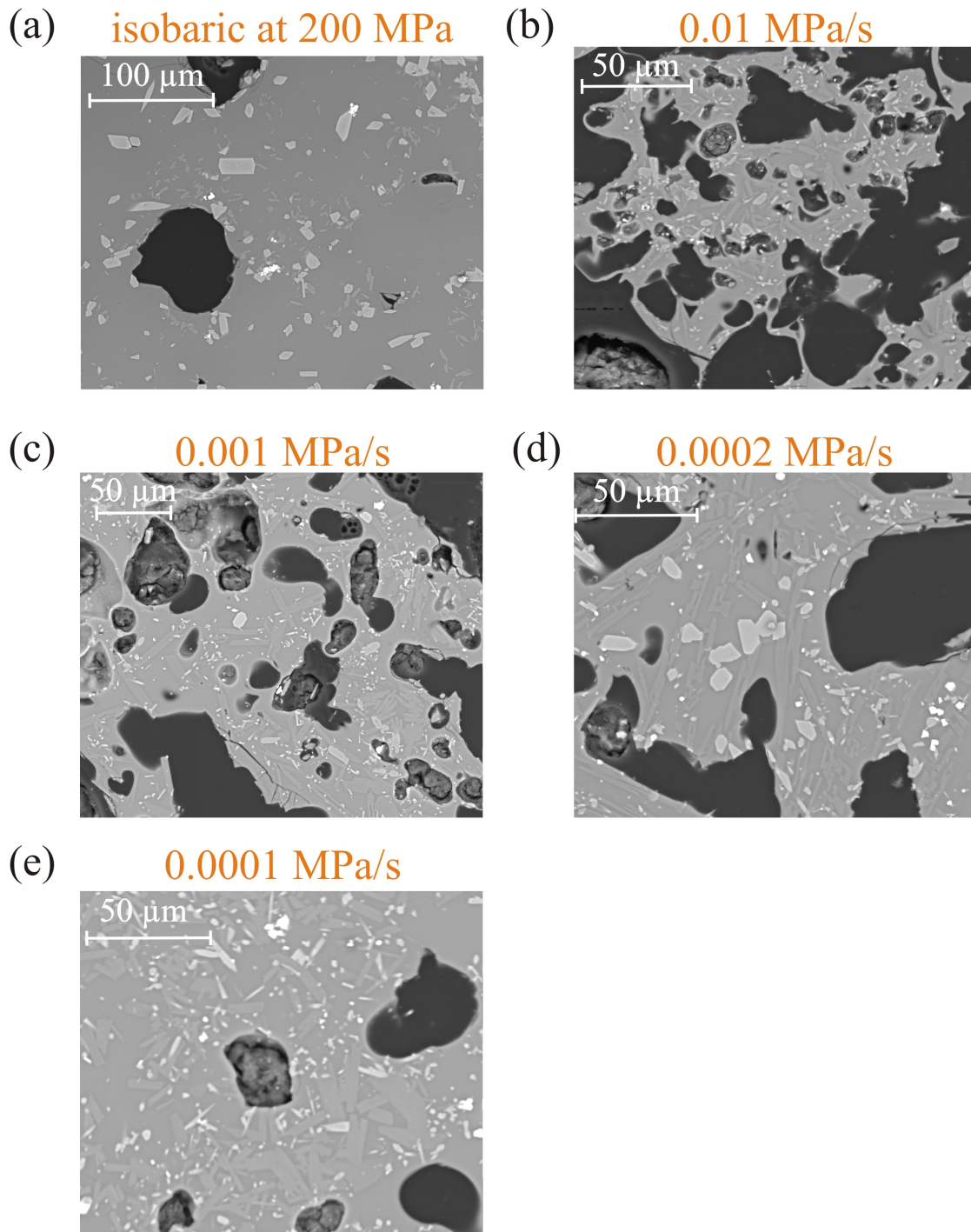
LPD set-V: 200 to 0.1 MPa at 850°C

Fig. 3.26 a-j. Images of the products of isobaric and decompression experiments for LPD set-V (850°C). Black bodies are bubbles; light grey particles represent microlites such as plagioclases, pyroxenes and oxides ± amphiboles.

Table 3.7. Experimental conditions and chemical compositions of residual glasses for the H₂O-bearing system (X^HH₂O=1.0) at 850 °C (set-V).

sample	set #	Decompression rate [MPa/s]	Na ₂ O	SiO ₂	Al ₂ O ₃	CaO	K ₂ O	TiO ₂	FeO	MgO	total [wt%]
Big03+04	set-V	isobaric at 200 MPa	3.31 (0.20)	72.25 (0.41)	14.46 (0.19)	3.31 (0.24)	2.91 (0.06)	0.43 (0.04)	2.73 (0.18)	0.59 (0.05)	94.29 (0.39)
LPD13	set-V	0.01	3.25 (0.03)	72.23 (0.20)	13.87 (0.86)	2.76 (0.40)	3.42 (0.28)	1.06 (1.01)	3.09 (0.17)	0.32 (0.03)	100.43 (1.10)
LPD12	set-V	0.001	3.15 (0.02)	77.14 (0.34)	12.45 (0.14)	1.40 (0.06)	4.09 (0.16)	0.33 (0.02)	1.44 (0.11)	0.00 (0.00)	100.87 (1.04)
LPD06	set-V	0.0002	3.27 (0.16)	77.29 (0.88)	11.74 (0.41)	0.95 (0.08)	4.43 (0.17)	0.47 (0.04)	1.74 (0.20)	0.11 (0.07)	99.77 (0.94)
LPD09	set-V	0.0001	3.12 (0.23)	78.91 (0.46)	11.43 (0.30)	0.64 (0.05)	4.44 (0.12)	0.27 (0.03)	1.15 (0.14)	0.02 (0.04)	99.34 (0.28)

Initial and final pressure of decompression experiments after 7 day of annealing at 850 °C were 200 and 0.1 MPa, respectively.

Note: Numbers in parentheses show the standard deviation (1σ) of replicated analyses

Table 3.8. Experimental results of set-V (LPD: 200 to 0.1 MPa).

sample #	set #	decompression rate [MPa/s]	log BND [nm ⁻³]	log MND _{op} [nm ⁻³]	log MND _{pl} [nm ⁻³]	Max. Pl length [μm]	Average An content [mol%]	H ₂ O [wt%] ⁺ (NIR)	CO ₂ [wt%] ⁺ (MIR)
Big03+04	set-V	isobaric at 200 MPa	3.45 (0.01)	6.05 (0.15)	6.12 (0.17)	18	65	5.75 (0.29)	0.00
LPD13	set-V	0.01	4.14 (0.14)	6.20 (0.20)	5.95 (0.18)	20	56	n.d.	n.d.
LPD12	set-V	0.001	4.13 (0.13)	6.19 (0.09)	5.74 (0.08)	49	60	n.d.	n.d.
LPD06	set-V	0.0002	4.17 (0.15)	6.12 (0.10)	5.99 (0.11)	58	50	n.d.	n.d.
LPD09	set-V	0.0001	3.52 (0.23)	6.30 (0.08)	6.10 (0.02)	76	65	n.d.	n.d.

MND_{op}: microtite number density calculated for other microtite phases incl. pyroxenes and oxides

Note: Numbers in parentheses show the standard deviation (1σ) of replicated analyses

n.d.: not detected / determined

+ : errors in parentheses for FTIR derived H₂O and CO₂ contents are calculated by error propagation, but are likely to have relatively higher (~20%) uncertainties, e.g. due to the low sample thickness

Melt compositions

The chemical analyses of the residual melts of LPD set-V are listed in Table 3.7 and plotted in Fig. 3.37. The SiO_2 and K_2O contents of the residual glasses increase with decreasing decompression, while Al_2O_3 , FeO , and CaO contents of the residual glasses decrease with decreasing decompression rate. The experimental LPD data of set-V are compared with the natural Unzen compositional range of dome groundmass glasses in Fig. 3.27 (grey fields; Nakada & Motomura, 1999). The concentrations of all major oxides overlap with natural compositions at low decompression rates only (< 0.0002 MPa/s).

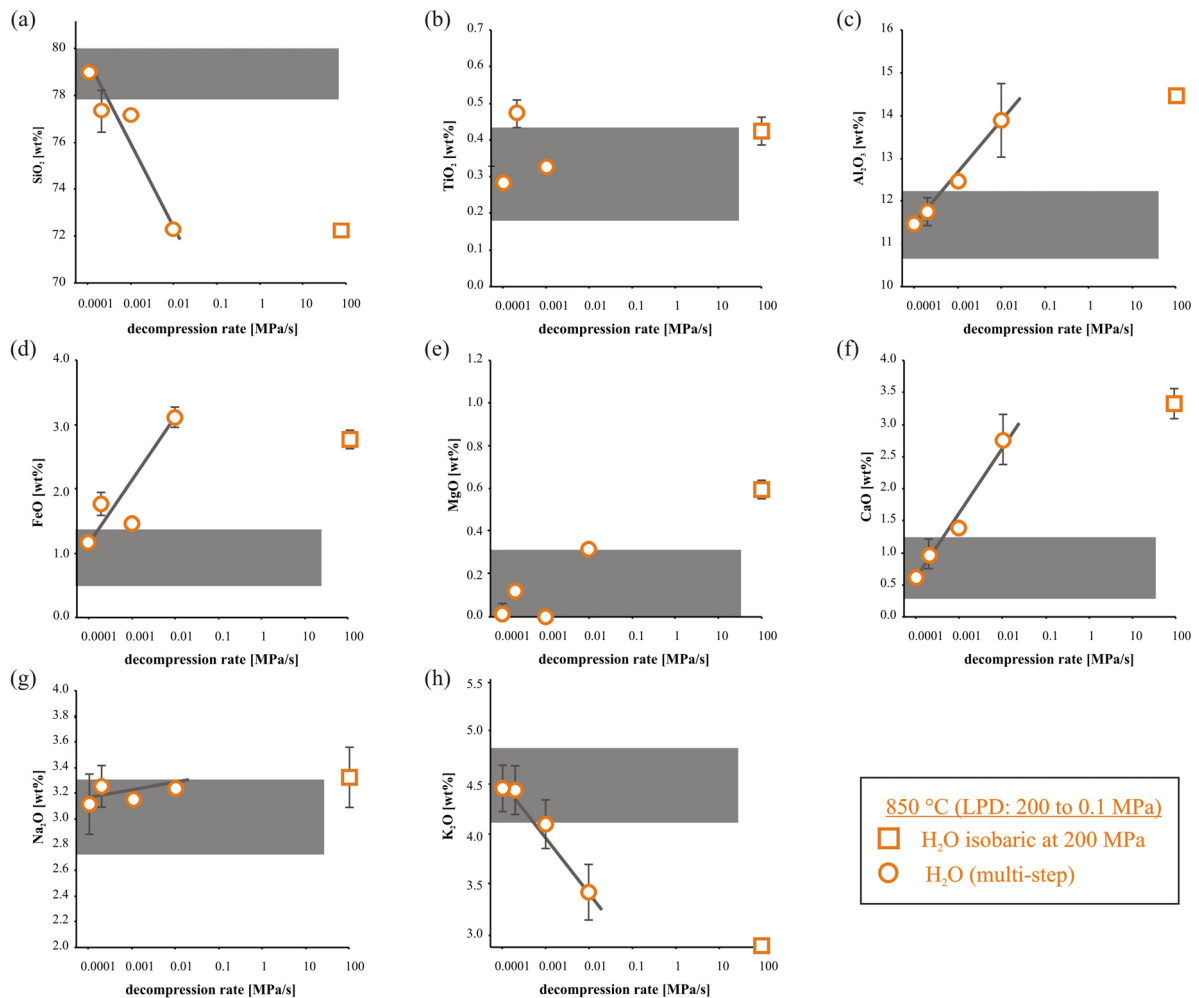


Fig. 3.27. Normalized chemical compositions of the experimental residual melts as a function of the decompression rate at 850°C of set-V (orange symbols). The grey shaded areas show the chemical composition range of the erupted natural groundmass glass in erupted rocks (Nakada & Motomura, 1999).

3. DECOMPRESSION EXPERIMENTS

Water concentrations of the residual glass determined by NIR spectroscopy at starting pressure (200 MPa) are in good agreement with each other and lie at 5.75 wt% and 5.71 wt%, respectively. Due to high crystallinity of the LPD experimental end products NIR and MIR analyses were not of good quality and therefore not determined.

Textures

Bubbles

The bubbles size distribution curves are concave-up shaped for all LPD end products, see *Appendix Fig. B.5*. The BSD curve of the starting material at isobaric conditions is characterized by a nearly straight line with a relatively flat slope, having rather high \ln population densities (7 to 15 mm^{-4}) for all bubble size intervals. The maximum bubble size and maximum \ln population densities (for the smallest analysed size interval) are similar in all four decompression samples, having values of ~ 0.85 mm and ~ 15 mm^{-4} , respectively. BSD curves at decompression rates ≤ 0.001 MPa/s show an even and continuous distribution of the size intervals, whereas at the fastest conducted decompression rate (0.01 MPa/s) there is a gap at size intervals of ~ 0.2 - 0.8 mm. Otherwise no significant systematic variation can be observed with changing decompression rate. BND values for decompression rates ≥ 0.0002 MPa/s are in the same range ($10^{4.1}$ to $10^{4.2}$ mm^{-3}), while being slightly higher than at isobaric starting conditions at 200 MPa and 850°C, see *Fig. 3.28*. For the lowest decompression rate (0.0001 MPa/s), the BND value is similar to that of the starting material ($\sim 10^{3.5}$ mm^{-3}), while their BSD curves show not the same trend, see above.

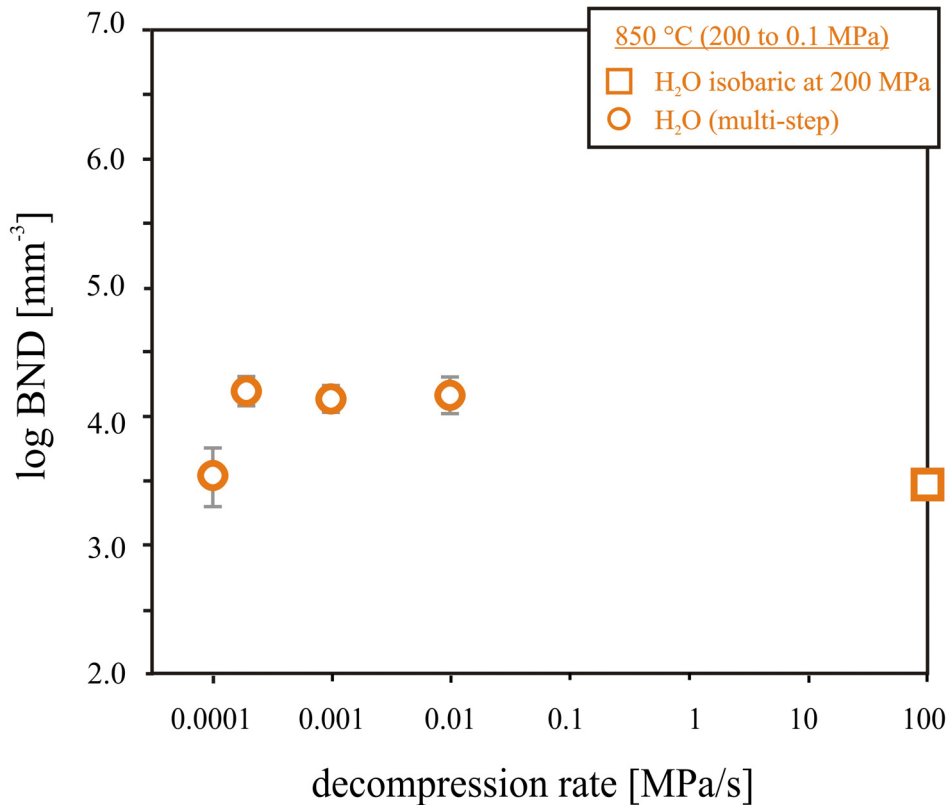


Fig. 3.28. Bubble number density (BND) as a function of the decompression rate for the H₂O-bearing system at 850 °C (orange symbols). Error bars show standard deviation (1σ) of replicate analyses.

Microlites

The crystal size distribution curves for plagioclase microlites (PI) and for other phases (OP) are concave-up shaped, shown in *Appendix* Fig. B.5. CSD curves for LPS experiments are characterized by a steeper slope at lower sizes intervals than the CSD curves of the isobaric experiment. The maximum microlites sizes of the other phases (OP; oxides, pyroxenes \pm amphiboles) are larger than for plagioclases at isobaric 200 MPa and at the fast decompression rate of 0.01 MPa/s. At slower decompression rates (≤ 0.001 MPa/s) PI sizes become similar to OP sizes with a maximum of ~ 0.05 mm. While at the lowest conducted decompression rate (0.0001 MPa/s) PI microlites reach even maximum size intervals of ~ 0.08 mm.

No distinct systematic variation of MND_{PI} values is observable with changing decompression rates, see Fig. 3.29a. MND_{PI} values for the isobaric sample and the LPD end products range from $10^{5.7}$ to $10^{6.1}$ mm⁻³. The MND_{OP} values for our LPD experiments are slightly higher than for isobaric conditions at 200 MPa, ranging from $10^{6.1}$ to $10^{6.3}$ mm⁻³, (Fig. 3.29b). An increasing trend of maximum PI lengths with decreasing decompression rate can be detected (Fig. 3.30), ranging from ~ 20 μ m at 0.01 MPa/s (equal to isobaric

3. DECOMPRESSION EXPERIMENTS

conditions at 200 MPa) to 76 μm at 0.0001 MPa/s. Plagioclase microlites of these LPD runs from 200 to 0.1 MPa show overall a tabular appearance.

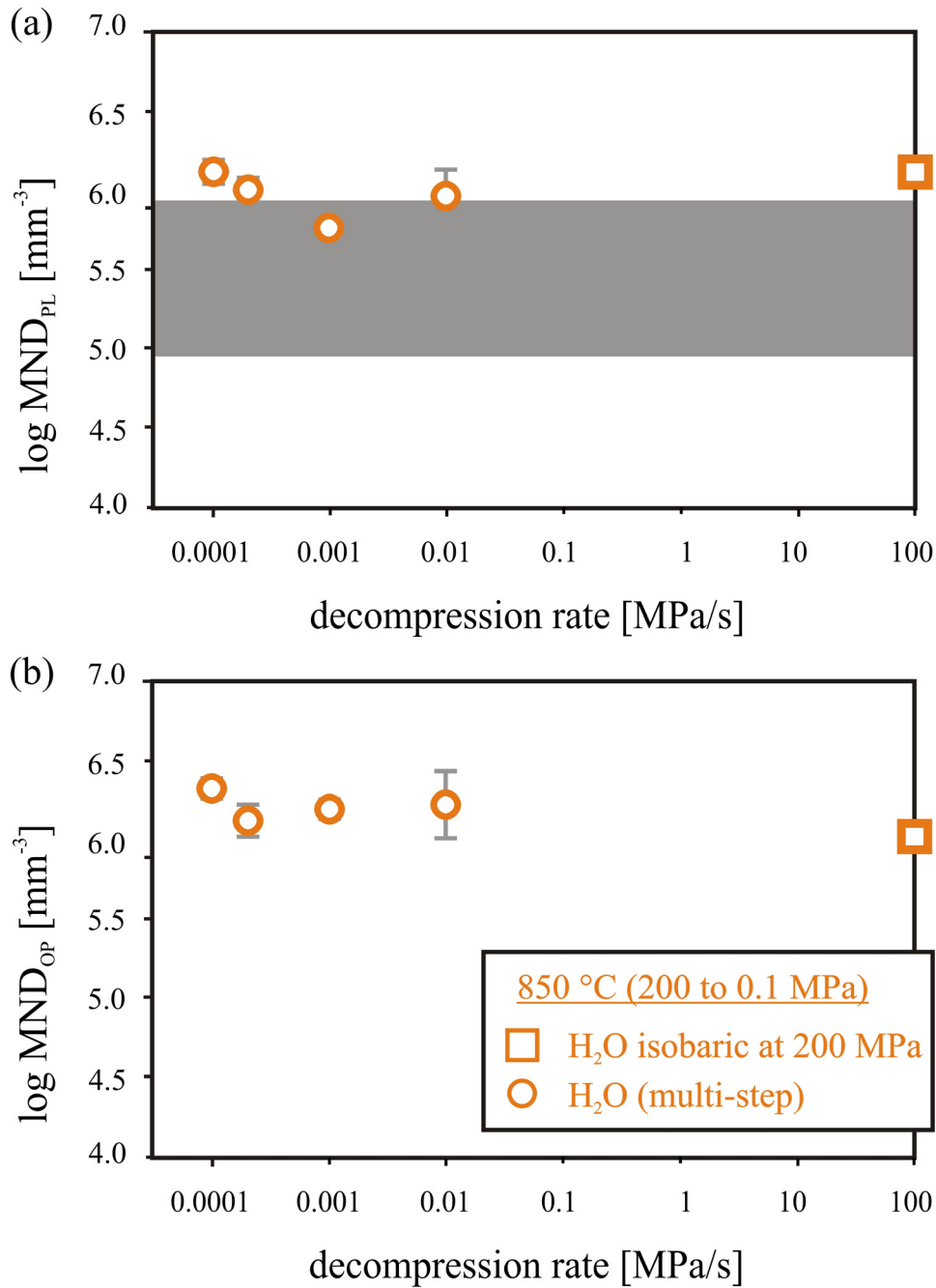


Fig. 3.29. Microlite number density (MND) as a function of the decompression rate for the-H₂O-bearing system at 850°C (orange symbols). (a) MND for plagioclases only (MND_{PL}) and (b) MND for all other phases (MND_{OP}) such as amphiboles, pyroxenes and oxides. The grey shaded area show the MND_{PL} of natural dome samples (Noguchi *et al.*, 2008a). Error bars show standard deviation (1σ) of replicate analyses.

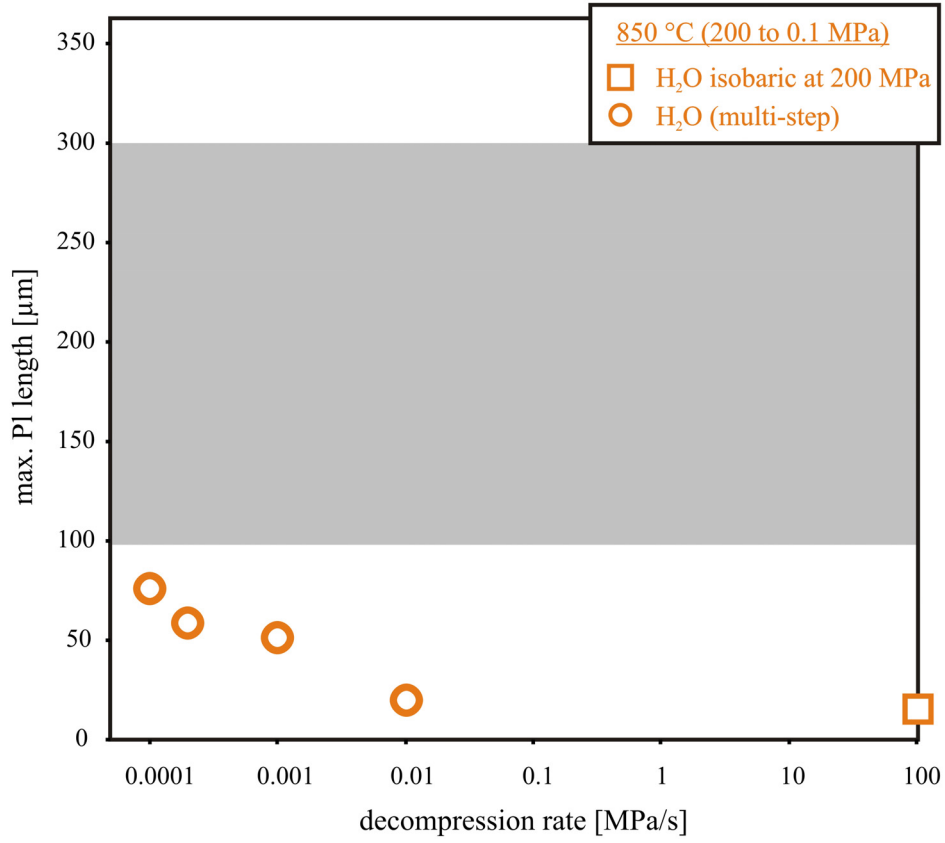


Fig. 3.30. Maximum plagioclase (Pl) length as a function of the decompression rate. Grey shaded area represents the range of Pl microlite lengths of Unzen natural dome samples after Noguchi *et al.* (2008a).

3.3. Comparison of three different decompression methods: continuous, multi-step and single-step decompression (set-VI)

Decompression experiments presented in this chapter have been originally performed to test the newly constructed continuous decompression valve described in chapter 3.1.2. Results and interpretations of the experimental products are conforming to a certain extent with sections of the paper of Nowak et al. (2011) to which I am the second author and therefore I was significantly involved in co-writing the paper.

INTRODUCTION

Over the decades of investigating in magma ascent-related vesiculation and crystallization processes, numerous experiments were conducted simulating the magma ascent at different stages: from great depth as deep as the storage conditions of magma chambers, to shallower depths and even to (near-) surface pressures. Therefore, different decompression methods were performed. For example, Hurwitz & Navon (1994), Gardner & Denis (2004) and Gardner (2007a) were using the single-step method where the entire pressure range, from starting to final pressure, is released by a sudden instantaneous drop (within few seconds) followed by a variable equilibration time (of seconds, minutes or days) at final pressure, changing the effective decompression rate. In other experimental studies (e.g. Mourtada-Bonnefoi & Laporte, 1999; Larsen & Gardner, 2004, Gardner, 2007b, 2009; Marziano *et al.*, 2007; Castro & Dingwell, 2009), especially investigating lower decompression rates, pressure was released stepwise (multi-step decompression), meaning that variable multiple smaller instantaneous pressure drops with subsequent dwell periods are performed. Actual continuous decompression experiments were usually only conducted at decompression rates higher than 0.1 MPa/s by manually bleeding-off the (gas) pressure from the vessel (e.g. Mangan & Sisson, 2000, 2005; Martel & Schmidt, 2003, Marziano *et al.*, 2007; Hamada *et al.*, 2010). There have been attempts to improve the method of continuous decompression working at lower rates. Mourtada-Bonnefoi & Laporte (2004) used an automatic computer-controlled decompression device, where the pressure vessel was connected to a set of air-operated valves allowing small-scale pressure steps of ~0.1-1.0 MPa (Laporte *et al.*, 2000), allowing decompression rates of 0.0003-0.03 MPa/s. While Brugger & Hammer (2010) performed continuous decompression experiments using a new hydraulically driven screw pump pressure variator with programmable controller, starting

at maximum pressures of 110-140 MPa and performing decompression rates of 0.0001-0.03 MPa/s.

Brugger & Hammer (2010) showed also that crystal textures (e.g. crystal shape, total crystallinity) are evidently influenced by the decompression path, comparing continuous and multi-step decompression experiments. Former experimental studies (e.g. Hurwitz & Navon, 1994) demonstrated that crystal textures can also affect the formation of bubbles, acting as nucleation sites. Therefore, the main attention in this *chapter* is drawn to the questions: Are bubble forming processes (in crystal-free systems) also influenced by the decompression path? And are their results (here mainly: BND values) comparable to each other?

From thermodynamics and kinetics we already understood that several parameters such as melt composition, viscosity and/or water saturation have an influence on the formation (i.e. nucleation, growth and coalescence) of bubbles. For example, the review of Sparks *et al.* (1994) showed that bubbles can either nucleate homogeneously or heterogeneously from a supersaturated melt. In the case of homogeneous bubble nucleation, small clusters of gas molecules form the so-called bubble embryos. Dependent on the free energy, associated with the formation of the separate gas phase, and on the interfacial energy, associated with the creation of the bubble surface, a bubble embryo can grow or can shrink (see review of Sparks *et al.*, 1994). An embryo can only grow when, by adding one extra molecule to the cluster, the critical radius (r_c) is overcome. r_c is given by:

$$r_c = 2\sigma/\Delta P \quad (4),$$

where σ is the interfacial tension (also referred to as melt-vapor surface tensions; e.g. Mangan & Sisson, 2005) and ΔP the supersaturation pressure (i.e. difference between gas pressure in the melt and the ambient pressure). Mangan & Sisson (2005) showed that as water exsolves from the melt and the melt evolves to more silicic compositions, the melt-vapor surface tensions (σ) increase, thus lowering the bubble nucleation rate and ultimately the number of bubbles produced. On the other hand, the higher the supersaturation pressure the lower the critical size of an embryo, facilitating nucleation.

Experimental strategy

To investigate the influence of the decompression method on the formation of bubbles in our experimental products, we performed a set (set-VI) of decompression experiments in IHPVs. Decompression was conducted at an average constant decompression rate of 0.28 MPa/s (equivalent to an ascent velocity of 34 km/h) from a starting pressure of 300 MPa

3. DECOMPRESSION EXPERIMENTS

down to a final pressure of 50 MPa in a fluid-saturated system, using three different decompression methods: single-step decompression, multi-step decompression and continuous pressure release (see Fig. 3.31). The experimental temperature was chosen above the liquidus (at 1050°C) to minimize the influence of crystals on the bubble nucleation (e.g. Hurwitz & Navon, 1994).

For single-step decompression (sample DEC11-8), the entire pressure of 250 MPa was instantaneously released from 300 MPa down to final 50 MPa within a few seconds (~20 sec), equivalent to 12.5 MPa/s, and then the capsule was hold at the final pressure for the next 15 minutes before quenching. For multi-step decompression (sample DEC11-6), pressure was released in five equal steps of 50 MPa with an interval of three minutes. During each step pressure was also released at a rate of 12.5 MPa/s. The continuous decompression from 300 MPa to 50 MPa (sample DEC11-5) was conducted for 15 minutes, using the novel decompression valve described in *chapter 3.1.2* (Nowak *et al.*, 2011). When pressure is released on gas, there will be significant cooling of the gas and the sample up to 35°C (Hamada *et al.*, 2010). However, during our decompression experiments the temperature fluctuation of the samples were kept constant within 10°C due to the fast response of the internal furnace. Furthermore, Hamada *et al.* (2010) demonstrate that temperature has an insignificant effect on BNDs in hydrous rhyolitic melt at a given decompression rate. Thus, our results are not affected by small temperature fluctuations within 10 °C.

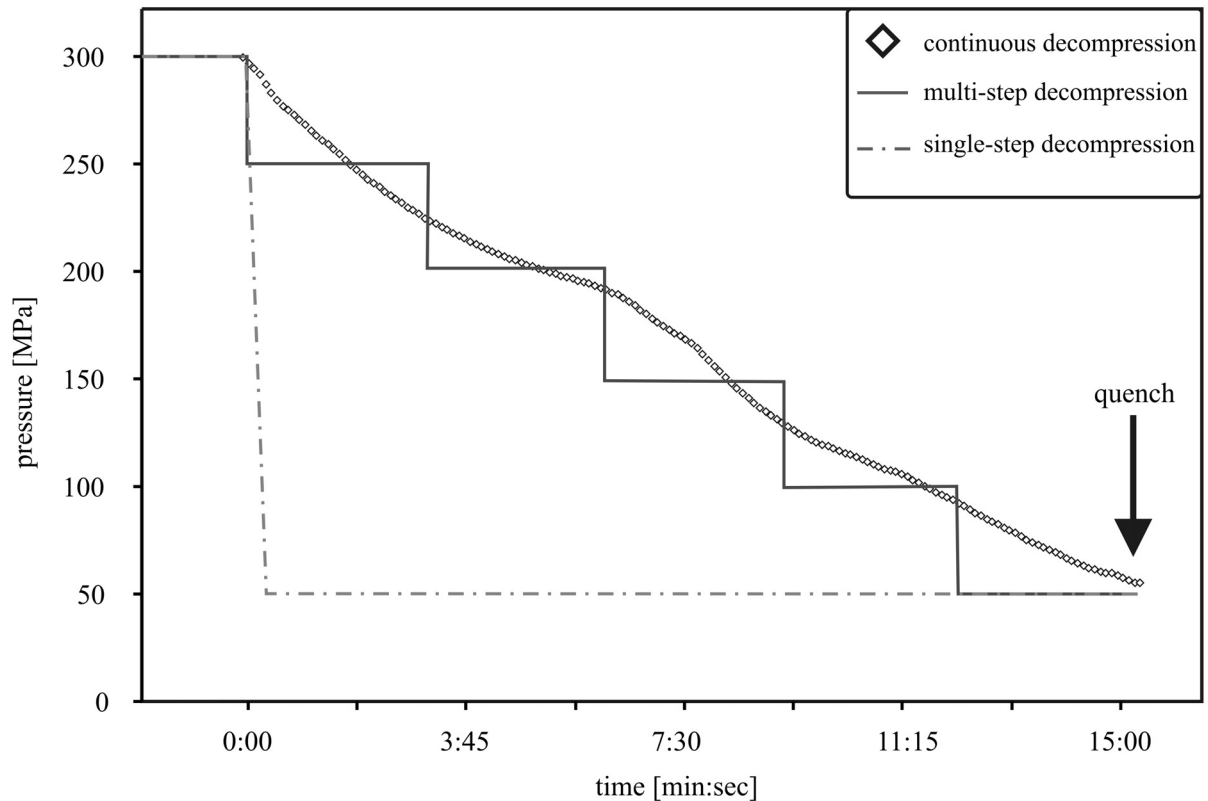


Fig. 3.31. Schematic diagram showing the differences of the P-t paths between continuous decomposition (diamond symbols), multi-step decomposition (solid line) and single-step decomposition (dashed line) at experimental conditions of 1050°C in the H₂O-saturated system.

Starting material and experimental method

Several cylinders of dry glass (details on glass preparation see *chapter 2*) were loaded with about 10 wt% H₂O into Au₈₀Pd₂₀ capsules (2.5 cm long and with inner diameter of 2.8 mm) and welded shut. The amount of water was chosen to be sufficient to saturate all melts at given 300 MPa and 1050°C. The capsule was placed in Ar-pressurized internally heated pressure vessel (IHPV) at oxygen fugacity corresponding to a range between QFM+1.0 to QFM+1.7 (which was achieved by addition of hydrogen gas to Ar). After annealing for four days at the P-T conditions of 300 MPa and 1050°C, the synthesis capsule (DEC11syn, Table 3.9) was rapidly quenched by dropping it into the cold zone of the sample holder. The quench rate was about 150 °C/second. This synthesized silica-rich starting glass (65.99 wt% SiO₂; DEC11syn) included only very few (total porosity < 0.5 vol%), isolated micro-bubbles (< 30 μm in diameter) and contained 7.46 wt% H₂O (see Table 3.9 and Fig. 3.32a), which is in agreement with former water solubility experiments on high-silicic melts (e.g. ~7.33 wt% H₂O, Holtz *et al.*, 1995; ~7.10 wt% H₂O, Jaupart & Tait, 1990).

3. DECOMPRESSION EXPERIMENTS

After quenching, the hydrated glass cylinder was cut to several small glass cylinders (~0.5 cm length each). Finally, these fluid-saturated (\pm bubbles) glass cylinders were individually inserted into Au₈₀Pd₂₀ capsules (~ 1.5 cm length), which were welded shut (star-shaped on top and bottom) and loaded into the IHPV. After a short annealing time of two hours at 300 MPa and 1050°C, an isothermal decompression to the final pressure of 50 MPa was initialized. After reaching the final P, the capsules were rapidly quenched. Cylindrical cores with a diameter of 2.0 mm were drilled out of the quenched experimental products. In addition, thin sections were prepared for electron microprobe and FTIR analyses (analytical details see *chapter 2*). For image and textural analysis we followed the methods of Higgins (BSD; 2000, 2002, 2006a,b) and that of Noguchi *et al.* (BND; 2008a), see also *chapter 3.1.1*.

Table 3.9. Results of chemical and textural analyses for dry starting glass, fluid-saturated starting material (DEC11syn) and experimental decompression end products of set- VI (DEC11-5, DEC11-6 and DEC11-8).

sample	synthetic rhyodacitic starting glass	DEC11syn	DEC11-5	DEC11-6	DEC11-8
starting pressure [MPa]	(dry)	300	300	300	300
final pressure [MPa]	--		50	50	50
decompression rate [MPa/s]	--		0.28	0.28	0.28
decompression method	--	isobaric	continuous	multi-step	single-step
number of decompression steps	--	--	--	5	1
pressure drop per decompression step [MPa]	--	--	--	50	250
<i>glass composition:</i>					
SiO ₂ [wt%]	69.95	65.99 (0.26)	68.71 (0.25)	69.02 (0.22)	69.80 (0.38)
TiO ₂ [wt%]	0.50	0.47 (0.04)	0.50 (0.04)	0.52 (0.05)	0.51 (0.05)
Al ₂ O ₃ [wt%]	14.21	13.17 (0.18)	13.89 (0.25)	13.96 (0.14)	13.88 (0.15)
FeO [wt%]	3.57	3.51 (0.24)	3.95 (0.16)	3.41 (0.24)	3.26 (0.36)
MnO [wt%]	0.12	-- (--)	-- (--)	-- (--)	-- (--)
MgO [wt%]	1.44	1.48 (0.13)	1.47 (0.10)	1.56 (0.07)	1.58 (0.15)
CaO [wt%]	4.05	3.86 (0.19)	3.96 (0.11)	4.18 (0.14)	4.08 (0.14)
Na ₂ O [wt%]	3.16	2.72 (0.12)	3.13 (0.15)	3.19 (0.12)	3.20 (0.16)
K ₂ O [wt%]	2.75	2.48 (0.11)	2.68 (0.12)	2.65 (0.12)	2.74 (0.14)
H ₂ Oglass [wt%] by NIR	--	7.46 (0.32)	3.01 (0.31)	2.76 (0.29)	2.32 (0.31)
<i>textural analyses:</i>					
vesicularity [vol%]	--	< 0.50	63.67	44.45	23.22
logBND [mm ⁻³] after Noguchi <i>et al.</i> (2008)	--	-- --	2.37 (0.17)	3.37 (0.13)	4.81 (0.10)
<i>Note: Numbers in parentheses show the standard deviation (1σ) of replicated analyses</i>					
<i>--: not determined (MnO contents of decompression products were under the detection limit)</i>					

RESULTS

The chemical melt compositions of the end products of all three different decompression methods are similar within the uncertainties for all element oxides. Although it seems that the water content of the residual melt decreases with changing decompression from a continuous (3.01 wt%) to a multi-step (2.76 wt%) and to a single-step (2.32 wt%) path (see Fig. 3.33). No significant H₂O gradient was detected from EMPA totals in the residual melts (between two neighboring bubbles).

The calculated BND values are shown in Fig. 3.33. The BND values obtained show a distinct trend: increasing from continuous to multi-step and to single-step decompression methods (Table 3.9, Fig. 3.33).

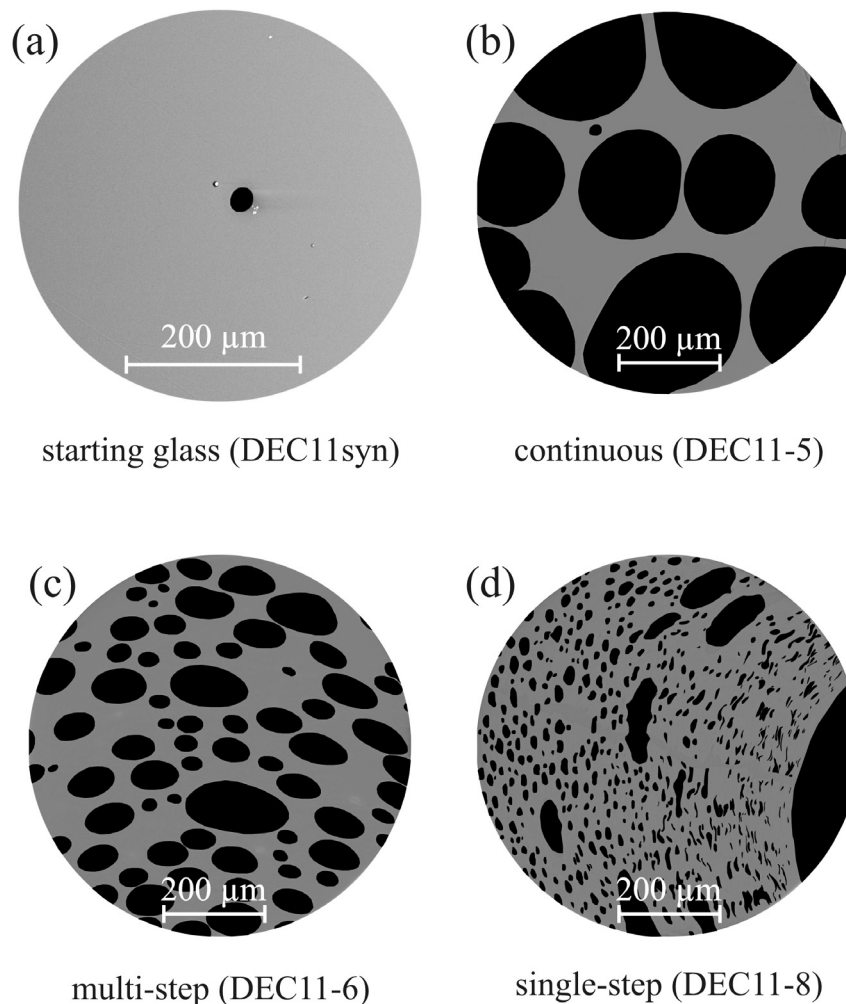


Fig. 3.32 a-d. Modified images of the (a) starting glass (DEC11syn) and of the experimental end products of (b) continuous decompression (DEC11-5), (c) multi-step decompression (DEC11-6) and (d) single-step decompression (DEC11-8). Black bodies are bubbles

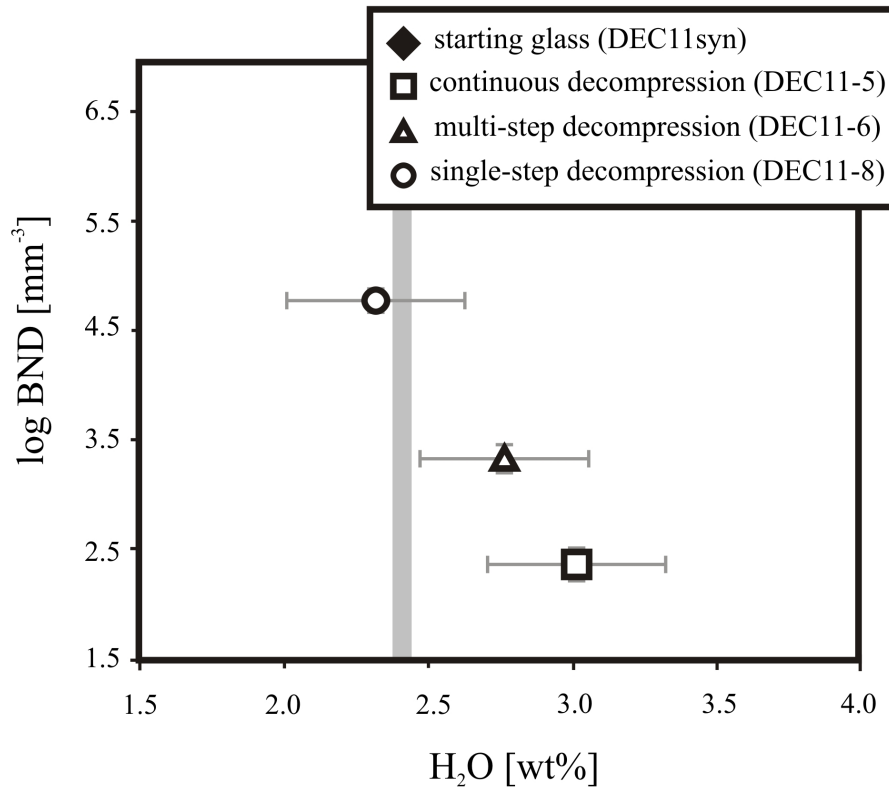


Fig. 3.33. H₂O-content of the residual melts determined by NIR vs. log BND, plotted for decompression experiments only. Gray line represents water solubility at 1050°C and final P 50 MPa given by experimental literature data (e.g. Holtz *et al.*, 1995 or Yamashita, 1999).

The bubble size distribution (BSD) curves of our experimental end products show three different trends as illustrated in Fig. 3.34. The BSD curve for the sample of the single-step decompression shows the largest variations both in the size of the bubbles and in the population number density when compared with the other two decompression methods. This single-step sample contains the largest proportion of small bubbles. The BSD trend for the sample of multi-step decompression shows the smallest variations between the size and the population density of bubbles, whereas the BSD of the continuously decompressed sample shows a very flat curve in Fig. 3.34, indicating similar proportions of bubbles with different size.

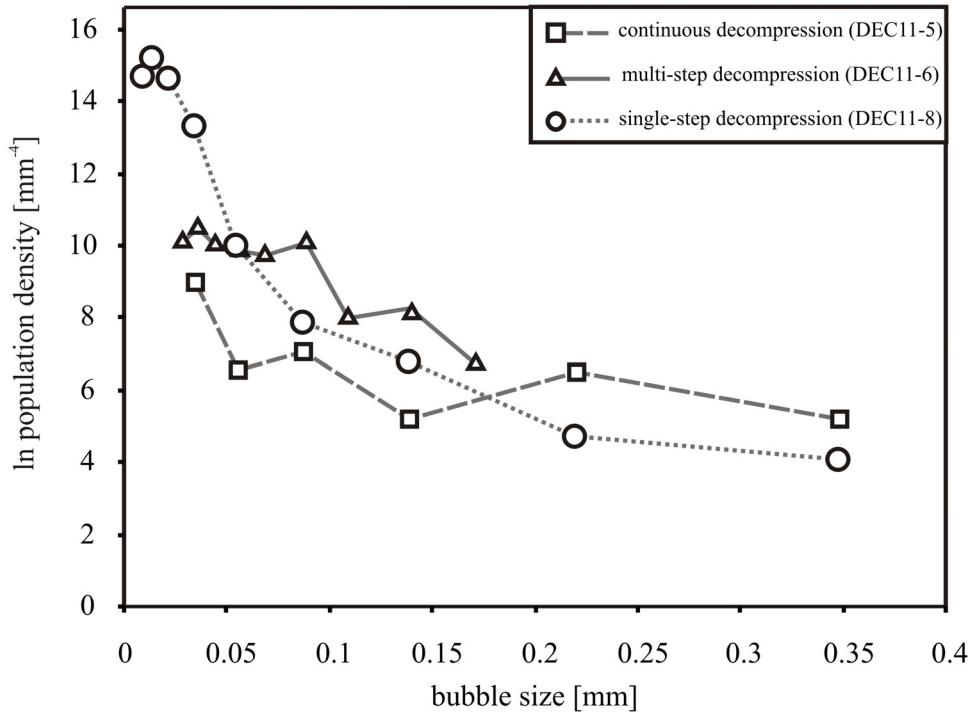


Fig. 3.34. Bubble size distribution, calculated following the method of Higgins (2000), in samples after decompression experiments.

DISCUSSION

Comparison of decompression methods

The observation that the BND values of the sample increase from continuous decompression to multi-step decompression and to single-step decompression provides important constraints on the mechanism of bubble formation. Changes in the BND values combined with BSD and porosity data give information on the processes of nucleation and growth of bubbles in the systems having different decompression histories. The BND value is representing the total number of bubbles per unit volume; hence, difference in BND reflects differences in bubble nucleation and growth.

Unfortunately, the nucleation pressure (P_n) was not directly determined for our experimental setup, for example by intermediate runs or in-situ observation techniques, which would provide further information on the origin of the bubble nucleation process: heterogeneous or homogeneous. P_n is influencing directly the nucleation process: pressure differences (ΔP) between the starting pressure and P_n as little as ~ 5 MPa may imply heterogeneous nucleation, while greater ΔP (i.e. lower P_n) would imply homogeneous nucleation (e.g. see review of Sparks *et al.*, 1994).

3. DECOMPRESSION EXPERIMENTS

In our single-step decompression experiment, the volatile oversaturation produced by instantaneous pressure drop to 50 MPa is definitely high enough for nucleation, resulting in high BNDs as the decompression rate is fast. In the continuous decompressions, water was not exsolved nor were bubbles nucleated until enough oversaturation pressure was reached (P_n : here unknown). During further continuous decompression the exsolved water would rather diffuse into already existing bubbles and let those grow due to favourable energetics than to accumulate into new clusters that could result in new nucleation (see review of Sparks *et al.*, 1994) explaining the low BND values. P_n in our multi-step decompressions experiments was probably higher than during continuous but lower than during single-step decompression as we decompress by 50 MPa (Fig. 3.31), resulting in intermediate bubble sizes.

As the fluid-saturated starting glass synthesized at 300 MPa and 1050°C was nearly crystal- and bubble-free (Fig. 3.32a), homogeneous bubble nucleation is expected to be the primary process in the decompression experiments. However, in the experimental product of the single-step experiment the influence of heterogeneous bubble growth may be observed, see large bubble at the right hand side of Fig. 3.32d. The secondary growth of a preexisting bubble, already contained in the starting glass, could lead to an elongation and bending of the primary homogeneously nucleated smaller bubbles.

Bubble growth can take place during decompression due to either diffusion of gas out of a supersaturated melt into the bubble or due to expansion of existing gas bubbles as pressure reduces (see review of Sparks *et al.*, 1994). The effects of surface tension, of melt viscosity and of inertia can hinder the growth of bubbles. Since the higher BND numbers are attributed to higher proportion of nuclei, we can suggest that the bubble nucleation was the dominant process during the single-step decompression experiment resulting in higher numbers of relatively small-sized bubbles (compare BND and BSD, Table 3.9 and Fig. 3.33 and 3.34). Due to the sudden drop in pressure (equal to) of 250 MPa within the first few seconds of the single-step decompression experiment, the melt became highly water-supersaturated at the final pressure of 50 MPa. At these conditions, the critical size of bubble embryo (see above: Sparks *et al.*, 1994) was dramatically reduced due to a high supersaturation pressure (ΔP) and relatively low initial melt-vapor surface tensions (σ ; Mangan & Sisson, 2005). Thus, enhanced volatile exsolution (Hurwitz & Navon 1994) led to major bubble nucleation in the system. In contrast, bubble growth was the dominant bubble forming process (Gardner 2007a, b) in the continuously decompressed system as indicated by the low BND value and the rather large average bubble size when compared

to multi-step or single-step decompression runs (see Fig. 3.33 and 3.34). At the beginning of the continuous decompression, bubble nucleation and therefore water exsolution can only start when P_n is overcome. During the ongoing continuous pressure release and therefore continuous water exsolution from the melt (starting at pressure $< P_n$), no significant oversaturation was reached again for a given time interval, precluding further nucleation of bubbles. Hence, water diffused rather into already existing bubbles, while probably only a few new bubbles nucleated, undergoing continuous growth and coalescence during decompression. Thus, the single-step and continuous decompression paths represent two extreme cases in which bubble nucleation and bubble growth are predominant processes, respectively. In this sense, the multi-step decompression method represents the intermediate case between rapid and slow release of pressure in magmatic system.

In comparison to the water solubility of high-silica melts at 1050°C and 50 MPa of ~2.4 wt% H₂O (e.g. Holtz *et al.*, 1995; Yamashita, 1999), it seems that the total loss of water is more effective in the course of single drop of pressure than in the other cases (Fig. 3.33), indicating that rapid magma ascent or quick pressure release with a subsequent long dwell time at low pressures will result in more efficient magma degassing. Although it has to be noted that these changes in the determined water contents of the residual melts (by NIR) are within the uncertainties (± 0.3 wt%) and may be used for qualitative discussion only. Therefore, the assumption that more bubbles per unit volume seem to be linked to more effective degassing should be taken with care. As no significant water gradients in the residual melts were detected (by EMPA totals) it can be assumed that the experimental products were in equilibrium at final P.

Implication for previous experimental decompression studies on bubble formation

We have clearly demonstrated that the bubble forming processes are influenced by the decompression path, indicated by great differences in vesicularity and BND values. Although water contents of the residual melts are slightly differing (but still within the uncertainties), it can be assumed that water exsolution in all three decompression scenarios are similar, resulting in (near-) equilibrium conditions in our here conducted experiments. When comparing results of former decompression experiments with each other, it should be taken in account that in single-step decompression experiments BNDs are usually higher due to the dominating nucleation process, while in continuous decompression experiments bubble growth is dominating resulting in lower BNDs. It has to be further

3. DECOMPRESSION EXPERIMENTS

investigated if these differences are within the same order of magnitude at all decompression rates (here: ~ 2 orders of magnitude for BND values between single-step and continuous). Additionally, the height of decompression steps is an important factor affecting the bubble forming process. Small decompression steps (e.g. ≤ 5 MPa; becoming similar to continuous decompression) are presumably negligible, as they are resulting in rather low oversaturation pressures inadequate for initiating bubble nucleation after each step. While, larger steps (> 20 MPa) are suggested to trigger further nucleation after each (sudden) decompression step, increasing the total bubble numbers per unit volume and becoming more similar to the single-step decompression method.

Implication for natural systems

During magma ascent in volcanic conduits, the magma can change its physical and chemical properties either continuously or step-wise due to changes in P-T conditions, water exsolution rate, bubble forming and crystallization processes (e.g. Hurwitz & Navon, 1994). These variations have a major impact on the rheological and dynamic behaviour of the magma and therefore also on the magma ascent paths and rates (e.g. Ida, 1996; Melnik & Sparks, 1999; Maeda, 2000). Thus, there is a self-sustaining feedback between the physicochemical and flow properties of the magma and P-T-time conditions. Another external parameter, potentially influencing magma ascent rate, can be the conduit diameter, which is probably not constant over the entire distance from magma chambers to the volcanic vent (e.g. Noguchi *et al.*, 2008). Therefore, we can expect a broad range of decompression rates from the onset of magma ascent at depth until the actual eruption at the surface, as well as changing ascent velocities with time due to variation in the magma supply from below. The data obtained in our study clearly show that the manner and efficiency of fluid exsolution are strongly dependent on the style of decompression. The most reactive system, in terms of bubble proportion and the amount of exsolved fluid, is expected to be developed in eruptions with very rapid pressure release, for instance, in plinian eruptions (Hamada *et al.*, 2010) or in catastrophic caldera-forming events.

3.4. 3D segmentation and visualization

The previously presented and discussed bubble and microlite number densities (BND, MND, respectively) have been obtained by the 3D correction method following Noguchi *et al.* (2008a) using the *CSDcorrection* software (Higgins 2006a,b), for details see *chapter 3.1.1*. Although truncation effects were minimized by analyzing more than one image per sample at different positions and different magnifications (e.g. Armienti, 2008), it can be assumed that the previously used determination method is still characterized by a relatively large error. This error may derive from the generalization of aspect ratios and circularities of the investigated objects (bubbles or microlites), as well as from the possible effect of object coalescence that is not totally resolved by the 2D images. Therefore, it was aimed to gain *true* 3D volume data from the segmentation and visualization of μ -tomographical scan datasets and to improve the BND and MND determination, using an enhanced version of the open-source software *YaDiV* (developed by Dr. K.-I. Friese, Welfenlab, Leibniz University Hannover, Germany; Friese *et al.*, 2011).

Synchrotron-based X-ray μ -tomography

We analyzed our cylindrical experimental run products at the Synchrotron Light Source (*SLS*) of the Paul-Scherrer-Institute in Villigen, Switzerland. The beamline for **T**OMographic **M**icroscopy and **C**oherent **r**Adiology experimen**T**s (*TOMCAT*) receives photons from a 2.9 T superbending magnet with a critical energy of 11.1 keV and produces a monochromatic beam, see Fig. 3.35.

This non-destructive synchrotron-based X-ray μ -tomography was used to record a series of 2048 digitalized 2D projection images (having 256 grey levels). A typical 2D image has a resolution of 2048 x 2048 pixel with a pixel size of 0.74 μm at 10x magnification or of 0.37 μm at 20x magnification. The distance between two neighboring images and the projection depth are defined by only one pixel. Grey values of the images depend on the chemical composition and density of minerals and glasses as well as on the presence of bubbles. Due to infiltration of noise by physical properties of this analytical method, a filter (*Parzen*) was used for reconstruction and smoothing of the images. Unfortunately, the images provided by *TOMCAT* cannot be used to investigate in plagioclases statistics, as this mineral phase was poorly resolved by this analytical method showing hardly any clear crystal boundaries.

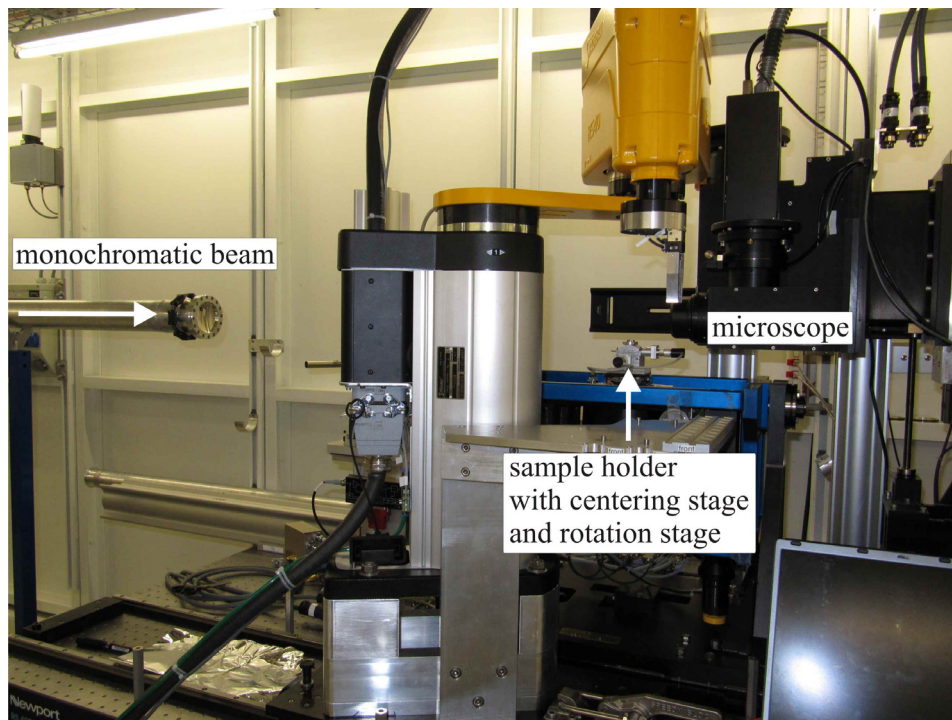


Fig. 3.35. Photo of μ -tomography operation table of *TOMCAT* beamline at *SLS*, Villigen, Switzerland. A sample is fixed on a centering and rotation stage in front of a microscope that detects the monochromatic X-ray beam.

YaDiV software and further enhancements

For 3D segmentation and visualization of our *TOMCAT*-derived scans, we used the Java-based open-source software *YaDiV* (“Yet another **D**icom **V**iewer”: <http://www.welfenlab.de/yadiv/>) provided by the Welfenlab of the Leibniz University Hannover, Germany. Major advantages of the *YaDiV* software are its independence from hardware and operating systems as well as its low electronic storage requirements. Originally this software was developed to handle medical data (Frieze *et al.*, 2011), which are usually processed in the relatively low-volume *DICOM* file format, which already includes patient-related as well as size-related information (e.g. spacing in x-, y- or z-direction). Therefore, this 3D software had to be modified to suit our demand which was carried out in close cooperation by the software programmer Dr. Karl-Ingo Frieze of the Welfenlab, Leibniz University Hannover. Special focus was given to the processing of large volume datasets (as *Tiff* or *Jpeg* file format) with total volume sizes of up to 1.2 GB per scan compressed or 32 GB uncompressed. The second task was to obtain the true volume value of single objects (here: bubble or microlite) within one sample.

First of all, the scan pictures were cropped and the pixel size of each picture was reduced from 2048 x 2048 pixel to 1024 x 1048 pixel reducing the total file size of one

scan. As the original pixel resolution of the single 2D projection images was high (e.g. 1 pixel = 0.74 μm at 10x magnification or 1 pixel = 0.37 μm at 20x magnification) and particles < 3 μm in diameter were not considered, changing the resolution to 1 pixel = 1.48 μm (at 10x magnification or 1 pixel = 0.74 μm at 20 magnification) is still accurate enough for our purposes, which was confirmed by statistical analysis of different image resolutions (2048, 1024 and 512 voxel).

Segmentation in terms of image analysis techniques is defined as the identification of regions that are pixel-based or voxel-based forming a specific structure which does not necessarily need to be geometrically connected. In general, two segments were created for each scan: one for bubbles and one for mineral phases (excluding plagioclases because of their poor resolution by this tomographical method), \pm one for oxides only. Due to the differences in chemical composition and the related specific grey values in the scan images, these phases were easily distinguished from the surrounding melt (intermediate grey values). The object-related grey values were marked throughout the total length of the scan (usually 1500 single images) and extracted into their individual segment using the *YaDiV* software. Additional software features such as erosion and dilatation functions (shrink and grow, respectively; for details see latter text and Fig. 3.40 a-d) and free-draw functions facilitated and upgraded the image evaluation to create these segments. Finally, the information of each segment is converted into 3D volume datasets (three dimensions; x,y,z) by calculating the connectivity, allowing the 3D visualization of the bubbles and minerals, see e.g. Fig. 3.36. Images and videos of the 3D visualized objects can be obtained by desktop snapshots or by desktop session recorder (here: *Istanbul*), respectively.

3. DECOMPRESSION EXPERIMENTS

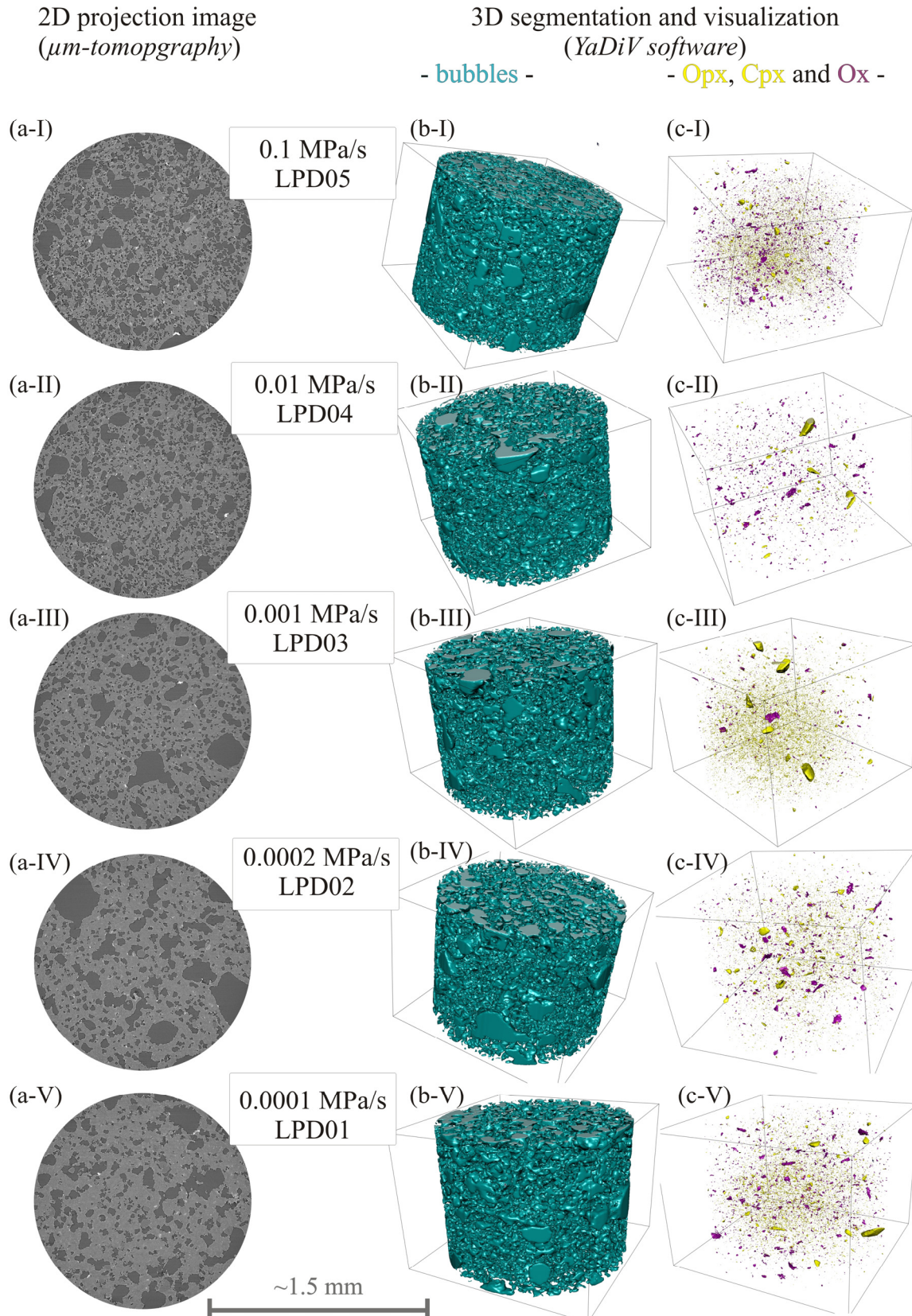


Fig. 3.36. Comparison of 2D images and 3D segment visualization of set-III samples (LPD: 50 to 0.1 MPa, at 850°C). 2D projection images obtained by μm -tomography are shown in a-I to a-V, where dark grey areas represent bubbles. 3D visualization of the segments bubbles (blue/turquoise color) and minerals (Opx + Cpx in yellow and Ox in pink color) are shown in b-I to b-V and in c-I to c-V, respectively. The diameter of the samples in the images is approximately 1.5 mm, not to be mistaken with size of the boxes indicated in the 3D images.

Additionally, a statistical software feature was newly designed to determine and extract volume characteristics of each individual (connected) object in one segment as a text file. Hence, this statistical information can be used for the BND and MND determination resulting in nearly true 3D volume data which errors are negligible. Therefore, we followed the original BND calculation method of Gardner *et al.* (1999, 2007):

$$BND = \frac{\phi_m}{\sum \frac{n_i}{N_T} V_i} \quad (5),$$

where n_i and V_i are the number and true volume of bubbles of diameter i , respectively, N_T is the total number of bubbles measured, and ϕ_m is the measured volume fraction of the vesicles. The same procedure has been used to determine the MND_{OP} values for microlite phases excluding plagioclase (i.e. oxides, amphiboles and pyroxenes).

Table 3.10. Experimental run conditions and results of 2D and 3D textural analyses for the two low-temperature (850°C) LPD sets: set-III (50 to 0.1 MPa) and set-V (200 to 0.1 MPa).

sample #	set #	decompression rate [MPa/s]	2D		3D		2D		3D	
			log BND [mm ⁻³]	error [mm ⁻³]	log BND [mm ⁻³]	volume fraction Φ [%]	log MND_{OP} [mm ⁻³]	error [mm ⁻³]	log MND_{OP} [mm ⁻³]	volume fraction Φ [%]
LPD 01	set-III	0.0001	4.33	(0.13)	2.96	11.24	6.40	(0.17)	4.33	1.13
LPD 02	set-III	0.0002	4.11	(0.09)	2.98	11.20	6.42	(0.15)	4.35	0.99
LPD 03	set-III	0.001	4.40	(0.08)	3.59	12.02	6.43	(0.30)	4.33	1.11
LPD 04	set-III	0.01	4.73	(0.10)	3.69	12.88	6.41	(0.16)	4.02	0.28
LPD 05	set-III	0.1	4.73	(0.07)	3.62	15.47	6.13	(0.13)	4.47	1.17
LPD 09	set-V	0.0001	3.52	(0.23)	2.01	11.98	6.30	(0.08)	3.69	0.17
LDP 06	set-V	0.0002	4.17	(0.15)	3.88	46.34	6.12	(0.10)	4.43	2.58
LPD 12	set-V	0.001	4.13	(0.13)	3.41	18.83	6.19	(0.09)	3.72	0.13
LPD 13	set-V	0.01	4.14	(0.14)	3.24	22.34	6.20	(0.20)	3.93	1.66

Note: Numbers in parentheses show the standard deviation (1σ) of replicated 2D analyses
2D: following the method after Noguchi *et al.* (2008a) including a 3D correction described in chapter 3.1.1.
3D: obtained using YaDiV software described in this chapter

Comparison of 2D or 3D generated BND and MND values

The BND and MND_{OP} values of set-III and set-V obtained by the two different calculation methods, (1) from simple 2D images following the method of Noguchi *et al.* (2008a) using Higgins *CSDcorrection* software (2000, 2002, 2006a) or (2) from the 3D segmentation and visualization of tomographical scans using *YaDiV* software, are directly compared to each other in Table 3.10 and Fig. 3.37 a-b. Values obtained by using method (1) will be referred to as “2D” values and values that were determined using the *YaDiV* software will be referred to as “3D” values in the following text. 2D values are in general higher than for 3D values. In detail, the log BND values obtained from 2D are ~0.5-1.5 log units higher than the 3D values, while the log MND_{OP} values of 3D are even 2.0-2.5 log units lower than for 2D values.

An explanation for the differences in BND and MND_{OP} values obtained by the two calculation methods 2D and 3D can be found in the basic understanding of number densities (ND). In principle, the number densities are defined as the number of objects per unit volume (of the magma). The number density values do not provide direct information on the sizes of the investigated objects, only on the total number of objects. Therefore an increase in BND or MND is correlated to higher numbers of bubbles or microlites, respectively, whereas a decrease in BND and MND is correlated to lower bubbles or microlites numbers, respectively (e.g. Gardner, 2007). A parameter influencing the total number, for example of bubbles, is the process of coalescence: when two (small-sized) single bubbles are connected with each other in order to form one single bubble of a bigger volume, the total number of bubbles is reduced. The process of bubble coalescence may occur either (1) static or (2) dynamic (e.g. Cashman & Mangan, 1994). In case (1), the neighboring bubble walls are thinning and/or rupturing and in case (2), bubbles collide due to variable buoyancies of different-sized bubbles. On the other hand, mineral grains can coalescent too by simply growing together. As these processes of bubble and crystal coalescence are not restricted to one direction only, it is difficult to determine the degree of connectivity of objects throughout a 3-dimensional volume from only looking at a 2-dimensional image. For example, two bubbles that are separated from each other in a 2D image (see Fig. 3.38 looking onto the x- and y-axes, white numbers 1 and 2), may actually be connected in the third dimension (following the development along the z-axis in Fig. 3.38, yellow number 1), also see review by Armienti (2008).

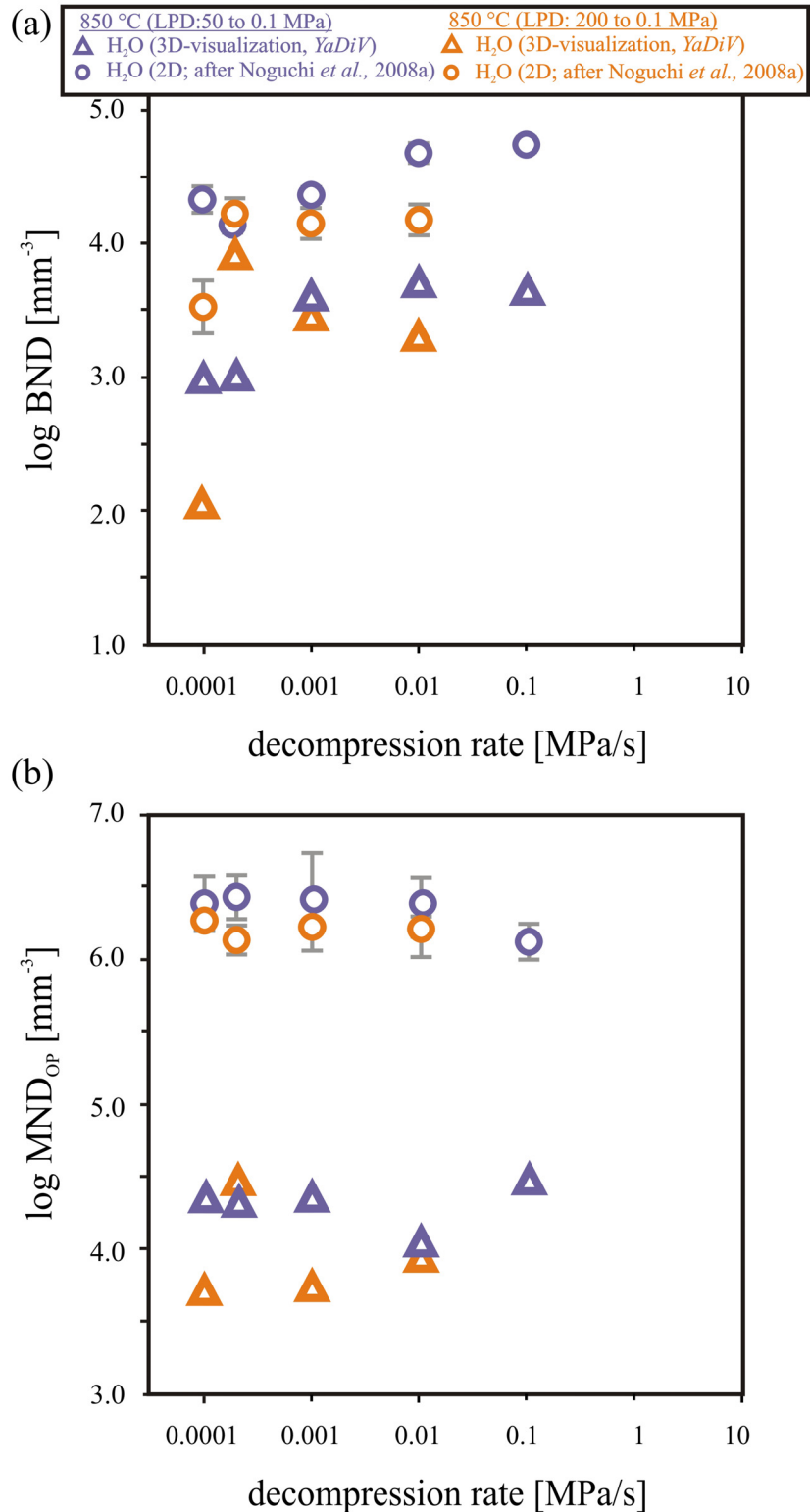


Fig. 3.37. Comparison of 2D and 3D data of low-temperature (850°C) LPD experiments. (a) Bubble number density (BND) and (b) microlite number density for all other phases (MND_{OP}) as a function of the decompression rate for the H₂O-bearing system. Circles represent 2D data obtained following the method of Noguchi *et al.* (2008a) and triangles represent 3D data obtained using *YaDiV* software. Purple symbols show LPD experimental results from 50 to 0.1 MPa and orange symbols show LPD results from 200 to 0.1 MPa. Error bars show standard deviation (1σ) of replicate 2D analyses. Errors for 3D analyses are negligible.

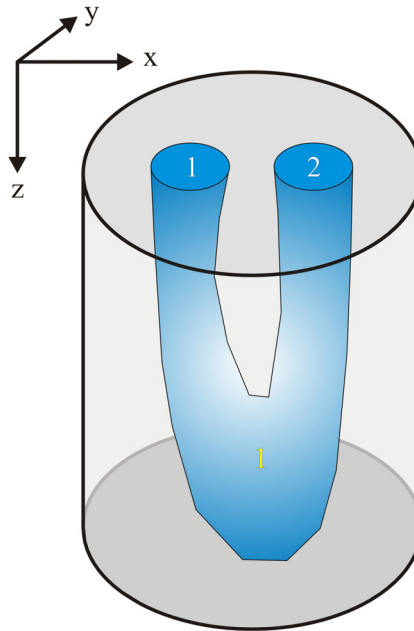


Fig. 3.38. Schematic example of the phenomenon of bubble coalescence influencing the accuracy of stereological reconstruction methods. When looking onto the 2-dimensional plane of x- and y-axes we can identify two separate bubbles indicated by the white numbers. While following their development along the z-axis, we see that in reality these two bubbles are connected and have to be counted as only one, indicated by the yellow number.

Additionally, it has to be noted that parameters concerning the image generation (e.g. optical magnification of the microscope, pixel resolution of the digitalized image) can influence the information if two bubbles are projected to be connected or separated. Thus, this crucial information on coalescence of objects within a 3-dimensional volume may be lacking or may get lost during the calculation method using the *CSDcorrection* software to convert data obtained from 2D images into 3D volumes. Furthermore, the *CSDcorrection* software requests the input of object-related data such as the roundness factor and the shape (short:intermediate:long) which have to be generalized for all investigated single objects throughout one image or sample (Higgins, 2000). This may be practical for samples containing only perfectly and uniformly shaped bubbles or crystals (i.e. formed without disturbances), but this is usually not the case in natural or experimental systems. Therefore, it can be assumed that the here introduced 3D method, obtaining (true) volume data by 3D segmentation and visualization using *YaDiV* software, is up to this date the most adequate way to reduce analytical-related errors. Furthermore, results of former stereological studies on size distributions and number densities containing 3D reconstruction (and/or 3D manipulation) methods have to be taken with care and a direct comparison with true 3D data from tomographical scan analysis might not be favorable or should include a detailed discussion on the data accuracy of both methods.

Outlook: Other *YaDiV* software applications related to rock textures*Orientation of objects within space*

One advantage of 3D segmentation and visualization of tomographical scan data using the *YaDiV* software is the spatial presentation of structures that may not be clear from looking on 2D images only. Especially flow dynamics such as preferred orientation of bubbles (Fig. 3.39 a) or orientated crystallization of minerals (Fig. 3.39c), as well as single shape phenomenon (e.g. hollow crystals in Fig. 3.39b) can be understood more easily when presented to the human eye in three dimensions, especially in moving pictures.

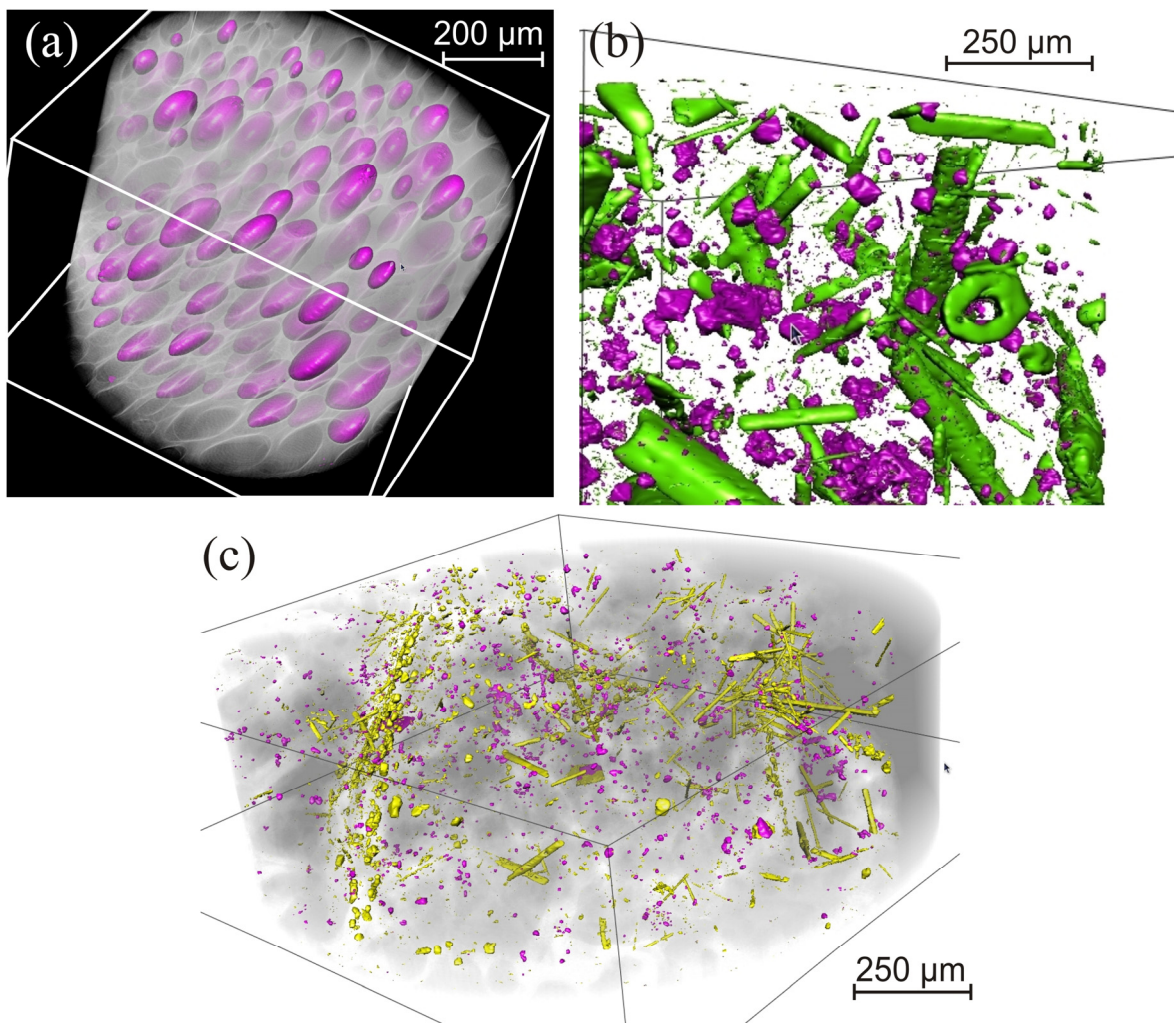


Fig. 3.39 a-c. Screenshots of *YaDiV* 3D visualization of different segments. (a) Sample DEC11-6 shows spatial orientation elongated bubbles [pink]. The main focus in (b) is concentrated on the hollow shape of an amphibole mineral (green) right hand side of the natural Unzen dome sample DAC_4. (c) Visualization of minerals (pyroxenes in yellow, oxides in purple color), grey background represents *Texture2d Volume Rendering* (pixel cloud) of bubbles of sample LPD07. Interesting here is the orientated crystallization of yellow pyroxene minerals along a bubble-free crack zone on the left hand side.

In a next step, we are working on developing and programming a software algorithm that is able to identify the preferred direction of orientated objects within a single segment.

3. DECOMPRESSION EXPERIMENTS

In case of Fig. 3.39 a, this would concern the orientation of bubbles or vesicles in our samples, which could give implications on degassing processes (such as bubble coalescence or on bubble segregation from the melt (e.g. relevant to the determination of the eruption style: effusive vs. explosive)).

Surface recognition algorithm

Another planned *YaDiV* software tool to edit and to simplify the 3D segmentation process of mineralogical samples is a surface recognition algorithm (a so called model-based segmentation method). Therefore, object specific shape characteristics (surface tension of bubbles as spheres or ellipsoids; crystal systems or class, etc.) have to be determined and taught to the software, which will then be automatically recognized and marked throughout the entire scan (in all three dimensions) by using this special algorithm. Additionally, the surface recognition algorithm could be integrated into the region shrinking and growing process. Therefore, we have to go into detail on this particular shrinking and growing process: when pixel of a certain range of grey values are marked and segmented, the tool “shrink” or “grow” can delete or add pixel, respectively, to the segmented pixels if a certain (user defined) grey value variance is respected, see Fig. 3.40 a-d. The variance determines the maximum difference between the grey value of the seed pixel and its surrounding pixel that are acceptable to be summarized in a marked segment.

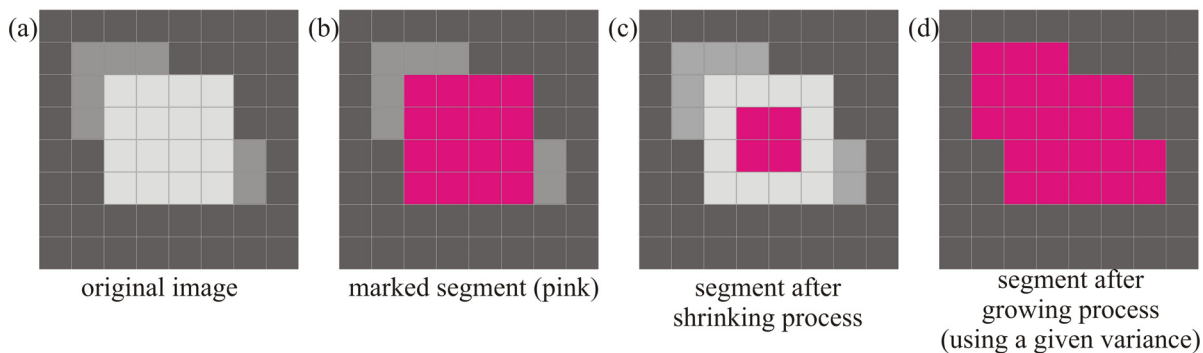


Fig. 3.40 a-d. Schematic presentation of segmentation and the tools (algorithms) shrinking and growing using a given variance of grey values: (a) the original pixel image with different gray values (light, intermediate and dark), (b) pixel having light grey values are marked in pink color and saved as one segment, (c) resulting segment (pink) after a region shrinking process and (d) resulting segment after a region grow function respecting a certain given grey value variance of image (b).

Thus, integrating the surface recognition algorithm to e.g. a grow function would only allow the addition of a neighboring pixel to the segment if (1) it correlates to the given grey value variance and if (2) the object characteristic (e.g. crystal shape or a,b,c-

axes ratio) are not violated by the growth function. This algorithm would be especially useful when the quality of tomographical projection images are affected by beam dispersion or by preparation-related cracks, see Fig. 3.41 a-b respectively.

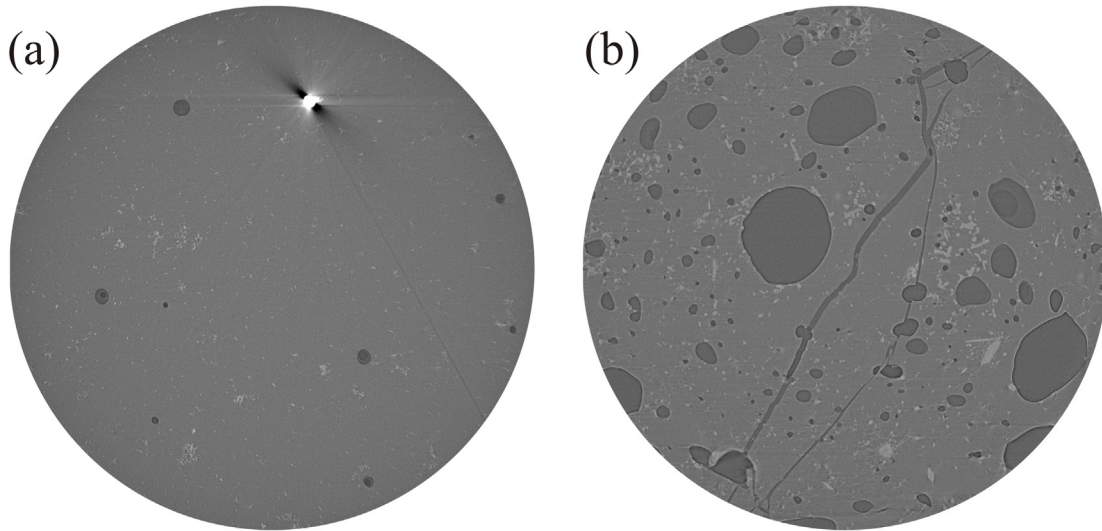


Fig. 3.41. Tomographical 2D projection images showing (a) beam dispersion caused by high-density oxide mineral (white color) and (b) cracks caused by the sample preparation.

Additional information preserved by μ -tomography

Due to the non-destructive method of synchrotron-based X-ray μ -tomography some additional information are preserved on the projection images that would have been destroyed through normal thin section preparation (cutting, polishing, etc). In our decompression samples we were able to observe two distinct phenomena that were not detectable by image analysis of simple 2D BSE pictures taken from microprobe thin sections: (1) mineral phases that crystallized inside bubbles and (2) liquids trapped inside intact bubbles, see Fig. 3.42 a and b respectively.

One possible explanation for the crystallization of minerals inside bubbles could derive from the chemical composition of the bubble fluids. It can be expected that not only pure H_2O or a pure mixture of $\text{H}_2\text{O}+\text{CO}_2$ is forming the decompression-induced vesicles but to some extent other element oxides may have also diffused from the melt into the gas bubbles, e.g. here: SiO_2 . When these volatile gases become oversaturated in respect to SiO_2 or temperatures are decreased, these oxides can precipitate and lead to crystallization of quartz minerals inside the vesicles (e.g. Newton & Manning, 2000, 2008).

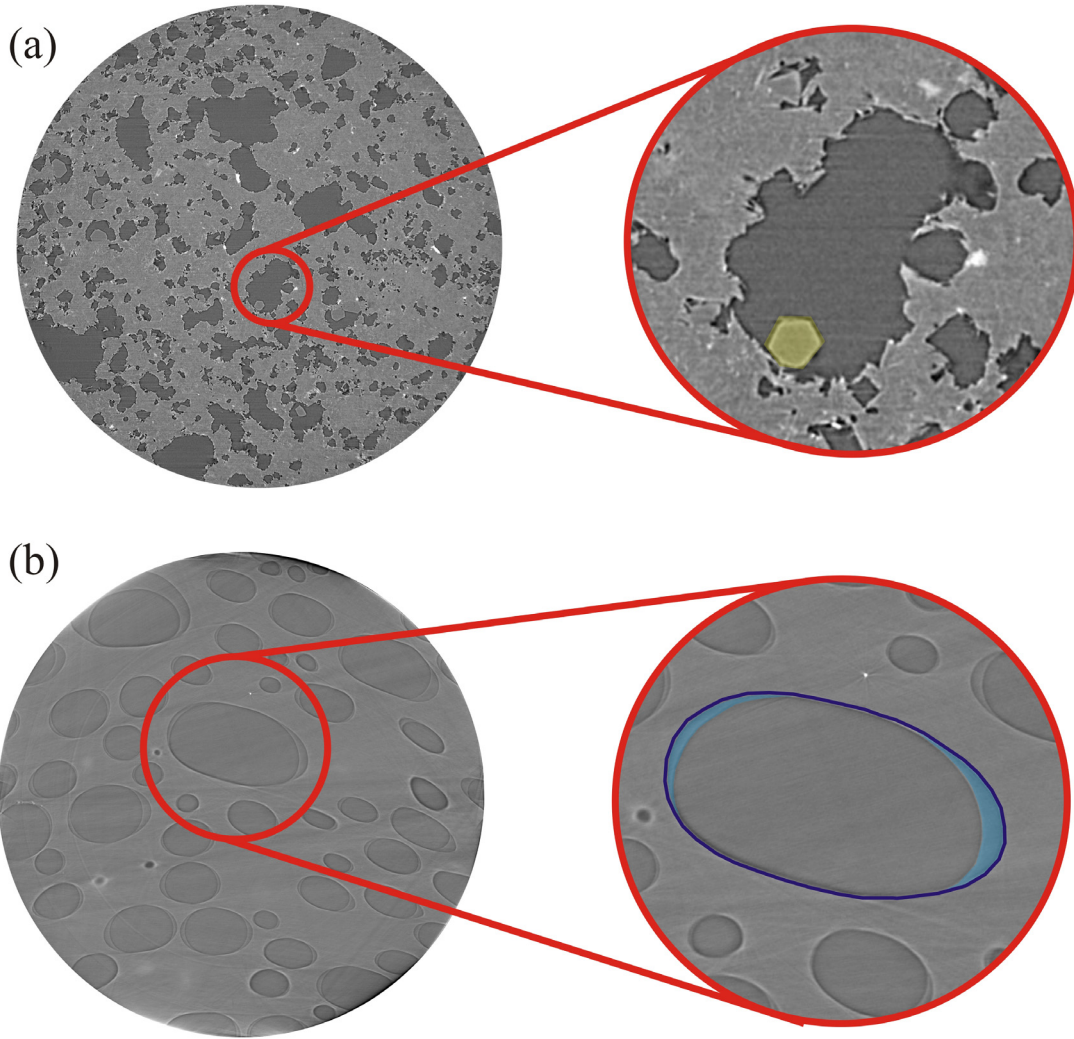


Fig. 3.42. Additional information preserved in 2D projection images from μ -tomography. On the left, original full-size image with red marked area of interest that is enlarged on the right. (a) mineral phase (here maybe quartz) that crystallized inside a bubble (highlighted in yellow on the right) and (b) quenched liquids (light blue shaded area on the right) trapped inside an intact bubble (dark blue contour indicating size of bubble when fluid was still gaseous).

In samples without the influence of crystals, bubbles were preserved in perfect shape (as spheres or ellipsoids), see Fig. 3.42b. Due to the image-given procedure of X-ray μ -tomography differences in chemical composition and/or density are indicated by different grey values in the 2D projection images. Taking a closer look at undamaged bubbles (not influenced by cylinder preparation), two areas within one single bubble can be observed: (1) a major dark area in the middle and (2) minor light area on the bubble wall (highlighted in light blue color in Fig. 3.42b). A very light frame (marked in dark blue in Fig. 3.42b) is surrounding these two areas as a whole, which is interpreted as the original gas bubble volume (before experimental quenching), while area (2) is representing the liquidized volatile after quenching. As liquids have higher densities as air or gas, area (1) is meant to be the air-filled cavity of the preserved gas bubble volume. Thus, from determination of

the chemical composition and the volume of the volatile fluids, one could then recalculate the dominating gas pressure inside bubbles at given (experimental) pressure and temperature conditions. The volume can be easily determined by *YaDiV* segmentation and statistical option, while the chemical composition could be analyzed for instance by laser ablation.

At this point, we have to emphasize the limitations of μ -tomography: due to the high resolution and restriction of voxel sizes, not our entire sample can be recorded at once. At the highest resolution (20 x magnification leading to 0.37 μm per pixel), a maximum sample diameter of 757.76 μm can be investigated, which in our case of experimental cylinders of 1.9-2.0 mm is only a third of one sample. Increasing the image diameter can only be achieved by reducing the resolution, which might result in loss of existing micro-structures. But especially in our nucleation experiments it is important to have a global view of one experimental sample. For example, are there any heterogeneous nucleation events at the interface capsule wall and melt due to reduced theoretical supersaturation pressure (e.g. Martel & Bureau, 2001)? Thus, is there a difference in bubble distribution within one sample: outer-inner part, bottom-top? Answers to these questions are essential to understand the processes occurring not only in our small-scaled experiments but are also applicable to large-scaled natural systems, e.g. magma chambers, conduits, etc. A solution to this problem can be the method of Pamukcu & Gualda (2010): combining information at various resolutions.

CONCLUSION

Here we demonstrated successfully that the processing of non-destructive μ -tomography images using *YaDiV* software can provide useful (visual) insights and (nearly) true volume data of mineralogical objects (here: bubbles and crystals). Although the quality and quantity of obtained volume data are of course dependent on the tomographical scan resolution as well as to some degree on the users' accuracy, the ongoing development of this originally medical-based software can lead to an important contribution to the geoscientific field. Furthermore, *YaDiV* is an open-source freeware and can be adapted by anyone with programming skills at all times, exhibiting advantages compared to other commonly used and expensive 3D computer software programs (e.g. *MATLAB*, *AVIZO* etc.) which properties are restricted by the software developing company and which usually require high-capacity hardware (internal storage, graphic boards, etc.).

4. DISCUSSION

Dynamics of vesiculation

In general, it is difficult to compare our experimental BND data to natural erupted Unzen samples, especially as the 1991-1995 eruption was more of the effusive, dome-forming Merapi-type. Thus, progressing (complete) degassing of the magma close to the surface did not preserve major vesicle structures in the erupted Unzen rocks (e.g. Nakada & Motomura, 1999). Therefore, we will only discuss here qualitatively the results of degassing (water exsolution and evolution of bubble number densities) along our experimental decompression paths and will try to compare our experimental BND data to natural explosive Plinian eruptions (see discussion section: *comparison to natural BND data*) that have preserved vesicle structures in their erupted rocks due to fast magma ascent and incomplete magma degassing.

Equilibrium distribution of volatiles in melt and fluid

The analyses of the chemical composition and the water content of the residual glasses of HPD set-I showed that the process of water exsolution from the melt is decoupled from the onset of crystallization in the decompression system. At high decompression rates, no significant amount of water was exsolved resulting in fairly high water contents of the residual glasses at final pressures of 50 MPa. While at lower decompression rate (< 0.1 MPa/s, equilibrium conditions were reached in the H₂O-bearing system and < 1.0 MPa/s in the H₂O+CO₂-bearing system). These observations are in agreement with former experimental studies on rhyolites compiled in a review of Rutherford (2008), showing the transition from non- to near-equilibrium degassing at decompression rates of 0.025 to 0.25 MPa/s. As our other decompression sets II-V have been conducted using decompression rates ≤ 0.1 MPa/s, we can assume near-equilibrium conditions for those experiments, which is also supported by the observation of similar water contents within each set being close to equilibrium conditions (isobaric runs at final pressures).

Bubble nucleation vs. bubble growth

The process of bubble nucleation can either occur homogeneously from the melt or heterogeneously along the surface of nucleation sites such as crystals (e.g. Hurwith & Navon, 1994). The review of Sparks *et al.* (1994) explains that small clusters of gas

molecules form due to local concentration fluctuations requiring energy to form the bubble embryo interface. The bubble embryo will grow if the free energy associated with the formation of the separate gas phase is greater than the interfacial energy. Therefore, a critical bubble radius (r_c) has to be overcome, which is dependent on the ratio between the interfacial tension (σ) and the supersaturation pressure (ΔP). In case of homogeneous bubble nucleation, the required ΔP is greater than necessary for heterogeneous nucleation, where the gas phase can wet the surface of crystals lowering the required supersaturation pressure (e.g. Sparks *et al.*, 1994). Anyway, at low saturation pressures it is more favorable for gas molecules to diffuse into pre-existing bubbles, resulting in bubble growth, than clustering to nucleate a new bubble.

A compilation of decompression-induced bubble nucleation studies performing homogeneous nucleation (Mourtada-Bonnefoi & Laporte, 1999, 2002; Mangan & Sisson, 2000 and Gonde *et al.*, 2011) and heterogeneous nucleation experiments (Gardner & Denis, 2004 and Gardner, 2007) in rhyolitic systems are plotted in Fig. 4.1a, showing that in general bubble number densities (BNDs) are decreasing with decreasing decompression rates, while the homogeneous nucleation trend is having a steeper slope than the heterogeneous nucleation trend (see also inset in Fig. 4.1a). The dependence of the BND values on the decompression rate can be explained by supersaturation kinetics (see review of Sparks *et al.*, 1994). At fast decompression, the melt becomes highly supersaturated because the pressure release is faster than the ability of the system to react with volatile exsolution. This leads to a low nucleation pressure (P_n) resulting in intensive bubble nucleation. At low decompression, P_n is shifted to higher pressures. Here, lower degrees of supersaturation are reached due to relatively more time for the system to relax after decompression. Thus, the melt-vapor surface tension and the critical bubble radius are increasing (e.g. Mangan & Sisson, 2005), lowering the bubble nucleation rate and hence the bubble number density. However, a decrease in BND is not attributed to lower nucleation only; it simply gives information about the number of bubbles per unit volume but not on their sizes. If the total number of bubbles (N_T) remains constant while their individual volume increases, the BND values will remain constant too. On the other hand, a lower nucleation rate or bubble coalescence would result in lower BND values (e.g. Gardner, 2007a,b).

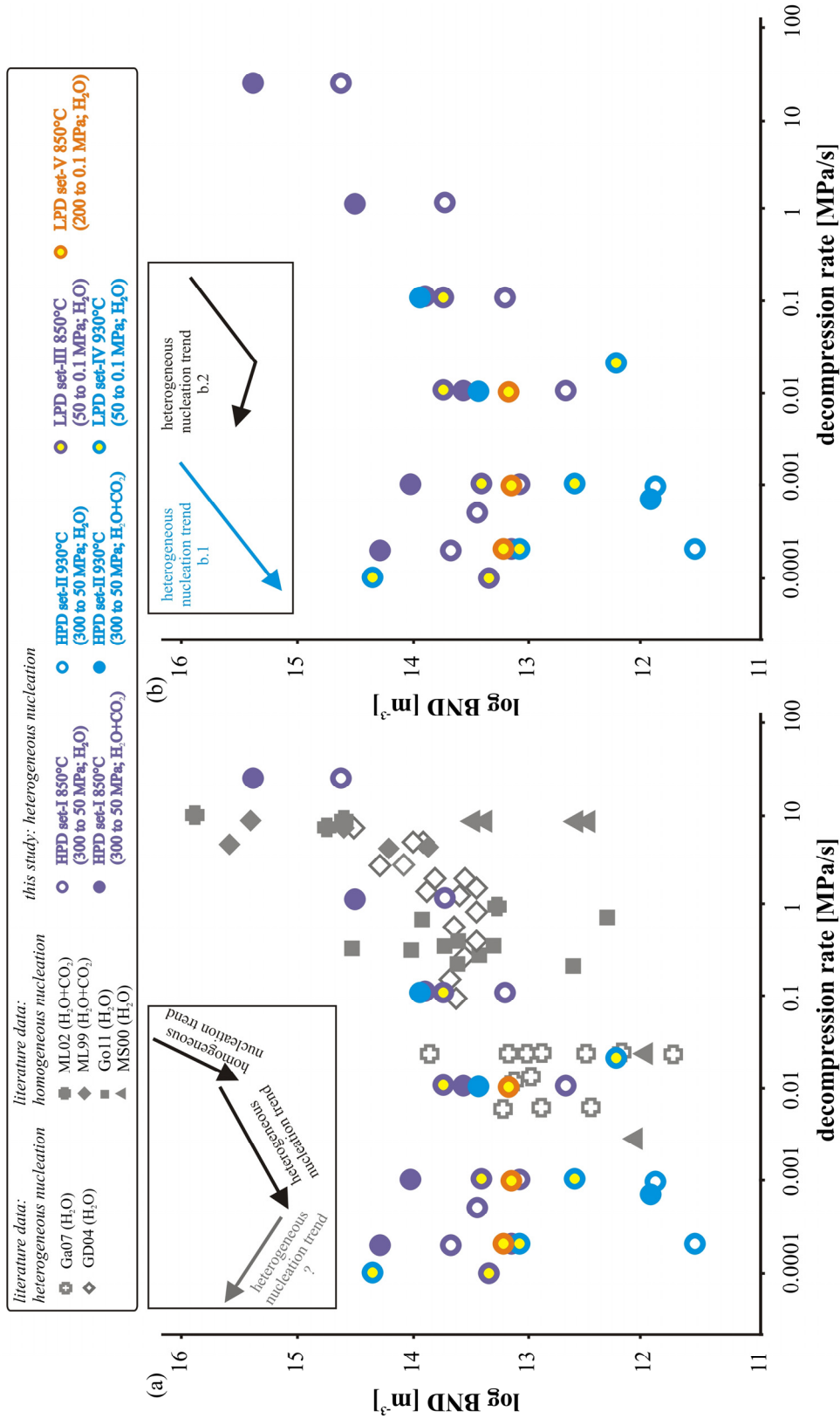


Fig. 4.1. Compiled experimental data of the BND as a function of the decompression rate (a) including literature data and (b) this study only. In the legend, open symbols refer to homogeneous bubble nucleation from Mourtada-Bonnefoi & Laporte (1999; ML99), Gardner (2007b; Ga07) and from Gardner & Denis (2004; GD04), while filled symbols refer to homogeneous nucleation data from Mourtada-Bonnefoi & Laporte (1999 and 2002; ML99 and ML02, respectively), Gonde *et al.* (2011; Go11) and from Mangan & Sisson (2000; MS00). Starting and final pressures of the decompression experiments are given in brackets. Low pressure data sets (final pressure: 0.1 MPa) from our study are additionally marked by yellow filled symbols. Error bars are not shown again for simplicity.

Our experimental decompression experiments of set-I to set-V are following the same trend as indicated for heterogeneous bubble nucleation in Fig. 4.1a at decompression rates ≥ 0.01 MPa/s, while BND values for the H₂O+CO₂-bearing system of set-I and set-II

are usually higher when compare to their H₂O-bearing counterparts. But at low decompression rates and especially for LPD experiments (set-III to set-V), BND values are higher than expected from the suggested heterogeneous nucleation trend. In general, two heterogeneous nucleation trends can be extracted from our experimental BND data, see inlet in Fig. 4.1b. The first trend (*b.1*) is identical to the suggested heterogeneous nucleation trend derived from literature data in Fig. 4.1a of decreasing BNDs with decreasing decompression rates, which is valid for HPD experiments of set-II (930°C) even at low decompression rates (< 0.0 MPa/s). While the second trend (*b.2*) is similar to trend *b.1* at decompression rates ≥ 0.01 MPa/s, whereas at decompression rates < 0.01 MPa the BND values slightly increase again with decreasing decompression rates as seen in experiments of HPD set-I and for LPD sets III-V. This difference in bubble number densities at low decompression rates (< 0.01 MPa/s) can be explained by differences in microlite number densities. MND_{OP} values of HPD set-II are approximately 0.5-1.0 log units lower (see Fig. 4.4b) than MND_{OP} values of the other decompression sets, resulting in fewer bubble nucleation sites (see Hurwith & Navon (1994) and thus lower BNDs.

Lautze *et al.* (2010) have demonstrated the effect of Ostwald ripening on BND in starting materials with increasing annealing time. BND values decrease by one order of magnitude from one day annealing time to one month. In this case, the bubble fraction nearly remained constant while the mean bubble radius more than doubled (*series 3*) indicating dominating bubble coalescence with time. Additionally, the BND values of the starting material are also dependent on the sample preparation. For sets I to V, we used glass powder having two size fractions which could have lead to initial heterogeneities, acting as nucleation sites. In our decompression set-VI, we investigated only bubble forming processes above the liquidus, while we used homogeneously hydrated glass cylinders as a starting material, avoiding the influence of crystals and of grain boundaries of the glass powder fractions on bubble nucleation. Although our conducted annealing periods of 4 to 14 days at starting P-T-conditions can not be directly transferred to interpret natural residence times in the magma chamber prior to an eruption, our datasets are adequate to predict qualitatively the evolution of BND as a function of the decompression rate. Furthermore, we were able to show a clear dependence of BND on the decompression path (see *chapter 3.3*), which should be taking in account when comparing decompression results of different studies with each other.

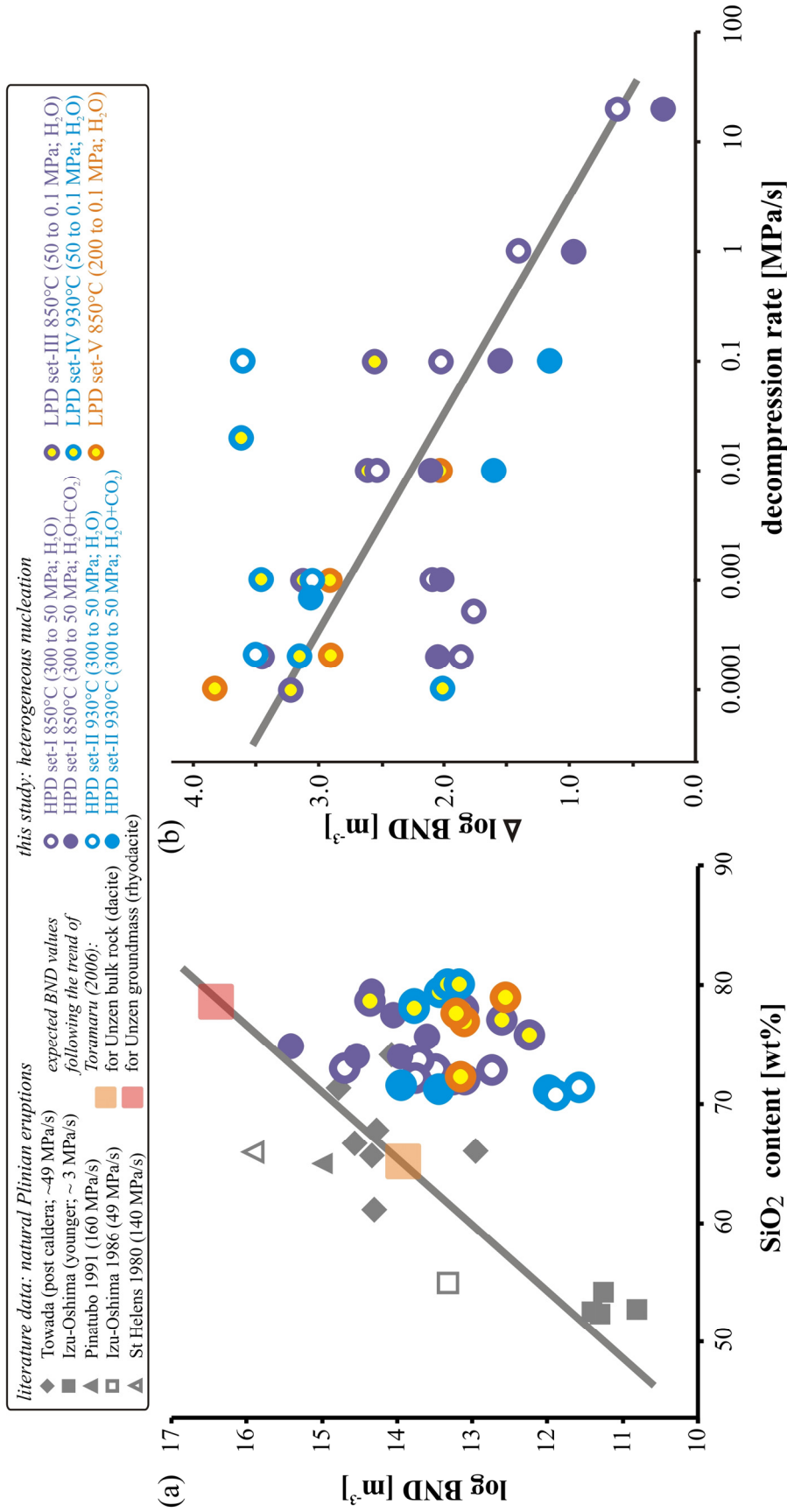


Fig. 4.1. Compiled experimental data of the BND as a function of the decompression rate (a) including literature data and (b) this study only. In the legend, open symbols refer to heterogeneous bubble nucleation from Mourtada-Bonnefoi & Laporte (1999; ML99), Gardner (2007b; Ga07) and from Gardner & Denis (2004; GD04), while filled symbols refer to homogeneous nucleation data from Mourtada-Bonnefoi & Laporte (1999 and 2002; ML99 and ML02, respectively), Gonde *et al.* (2011; Go11; T= 900°C, P_{start}= 361-331 MPa, P_{final}= 4 MPa) and from Mangan & Sisson (2000; MS00; T= 900°C, P_{start}= 200 MPa, P_{final}= 100-25 MPa). Details on experimental conditions for literature studies (ML99, ML02, Ga07 and GD04) see caption of Fig. 3.12. Starting and final pressures of our decompression experiments are given in brackets. Low pressure data sets (final pressure: 0.1 MPa) from our study are additionally marked by yellow filled symbols. Error bars are not shown again for simplicity.

Comparison to natural BND data

Unfortunately, natural Unzen BND values are not given by literature yet and therefore our experimental data can not be directly applied to the case of the 1991-1995 Unzen eruption (see also beginning of the discussion section: *dynamics of vesiculation*). But we can try to compare our BND results to a range of natural plinian eruptions compiled by Toramaru (2006), see Fig. 4.2a. A trendline can be drawn from those natural data, showing a clear dependence of logBND on the silica content of bulk rocks. Furthermore, it seems that there is also a positive dependence of the estimated decompression rates for those plinian eruptions following the vesicularity trend. When following this trend, using the chemical composition of natural Unzen bulk rock (Nakada & Motomura, 1999), BND values of $\sim 10^{13.5} \text{ m}^{-3}$ and approximately $\sim 50 \text{ MPa/s}$ are can be expected (see orange square in Fig. 4.2a). On the other hand, Unzen groundmass composition is more silica-rich and the vesicularity trend would therefore predict higher BNDs and presumably also faster decompression rates (see red square in Fig. 4.2a). But this dependence of the decompression rate following the logBND-SiO₂ trend should be taken with care as estimated decompression rates can already vary greatly for the one eruption (here e.g. Towada: 6.3 to 91 MPa/s) although having similar vesicularities and chemical compositions.

Our experimental BND data are all located below the trendline. LPD experiments have higher SiO₂ contents (closer to natural Unzen groundmass composition; Nakada & Motomura, 1999) and also larger deviations from the observed trend when compared to HPD experiments, which is shown more clearly in Fig. 4.2b plotting the deviation from the trend, derived from compiled data given by Toramaru (2006), in dependence of the decompression rate. Here in Fig. 4.2b another trend can be observed from our experimental data: increasing deviation from the natural vesicularity trend (see Fig. 4.2a) with decreasing decompression rates, which is understandable as the 1991-1995 Unzen eruption was not of an explosive character like plinian eruptions, having rather magma ascent rates.

Dynamics of magma crystallization

Crystallization processes occurring during our decompression experiments can be best detected by shifting chemical compositions of residual glasses. The onset of crystallization (delay of decompression-induced nucleation and growth of microlites) was only detected in experimental runs of both fluid-saturated systems of HPD set-I (Fig. 3.4). In HPD set-II (at 930°C) no change of the chemical composition with decreasing decompression rate was

observed (see Fig. 3.17). While LPD sets III to V experiments were only performed using decompression rates ≤ 0.1 MPa/s, showing an immediate change in chemical composition with decreasing decompression rate (see Figs. 3.22 and 3.27). A decrease of MgO, FeO, CaO and/or Al₂O₃ contents and the simultaneous increase of SiO₂ and K₂O content were clearly related to the crystallization of plagioclases and pyroxenes. Especially the observed systematic decrease of CaO in the residual melt and the simultaneous increase of CaO in the Pl microlites (*Appendix* Tables A.3, A.5.1, A.7.1 and A.8.1) with decreasing decompression rate are characteristic for Pl crystallization.

Plagioclase microlite crystallization

From our decompression experiments three distinct models of plagioclase crystallization can be distinguished: (1) Pl is part of the starting mineral assemblage (at low pressures) and do not grow significant larger in size during further decompression, (2) Pl is part of the starting mineral assemblage (at relatively high pressures) while their maximum lengths increase with decreasing decompression rate and (3) Pl is not part of the starting assemblage (at high pressures) and is only nucleating as well as growing during further decompression, becoming continuously larger in size with decreasing decompression rates.

The first case (1) is referring to our LPD experiments starting at 50 MPa (sets III-IV), where due to low water contents (~ 2.0 wt%) the crystallization kinetics are relatively slow and do not significant dependence of the maximal lengths with decreasing decompression rate (Fig. 4.3). LPD experiments of set-V starting from higher pressures (200 MPa) represent the second case (2) where higher initial water contents (~ 5.8 wt%) result in faster kinetics, leading to crystal growth and increasing microlites sizes with decreasing decompression rates. The shapes of plagioclase microlites formed by model (1) and (2) remain tabular, resulting from relatively low degrees of undercooling (oversaturation of the melt with respect to a mineral phase; e.g. Lofgren, 1974; Muncill & Lasaga, 1987, 1988). While in case of model (3), equivalent to two HPD experiments of set-I (H₂O-bearing, ≤ 0.0005 MPa/s), we have relatively high water contents (~ 6.5 wt%) at starting conditions (here: 300 MPa, 850°C) and therefore fast crystallization kinetics. Pl microlites nucleation during the decompression process and due to relatively high degrees of undercooling ($\sim 100^\circ\text{C}$ or less of undercooling) rapid and non-equilibrium growth of Pl microlites occurs, resulting in skeletal in mineral shapes. These large Pl microlites are similar in length to natural Unzen dome samples (~ 250 μm ; Noguchi *et al.*, 2008a; dark grey shaded area in Fig. 4.3).

No plagioclase microlites were crystallized in HPD set-II (300 to 50 MPa), indicating that the experimental temperature of 930°C was presumably too high and performed decompression rates (0.1 to 0.0002 MPa/s) were still too fast to result in appropriate high degrees of undercooling leading to the (skeletal) crystallization of Pl microlites.

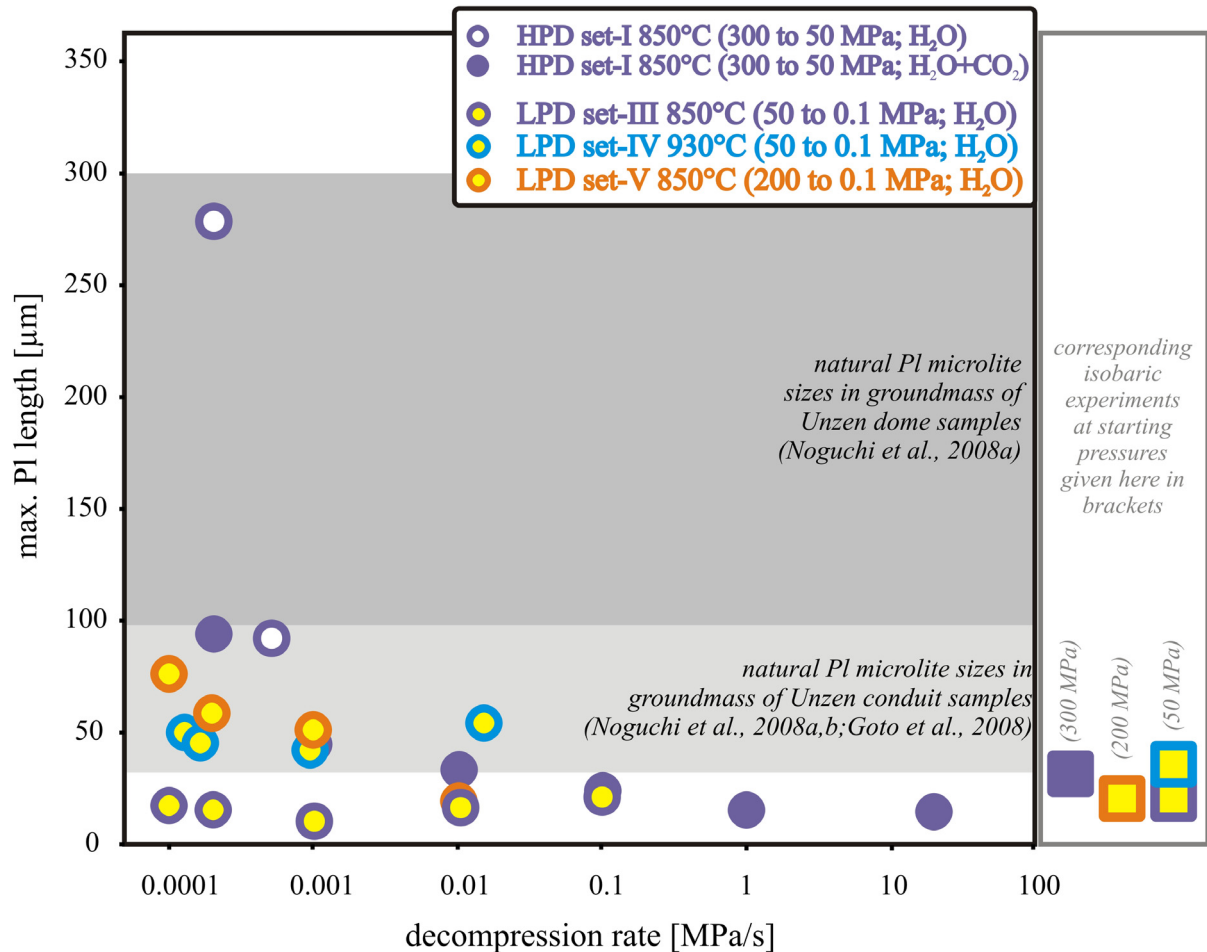


Fig. 4.3. Maximum Pl length as a function of the decompression rate. Dark grey shaded area represents the range of Pl microlite lengths of Unzen natural dome samples after Noguchi *et al.* (2008a). Pl microlites in core samples are smaller (<100 μm) (indicated by the light grey shaded area), except one sample (C14-1-1) where Pl microlites reach up to 300 μm in length (see Noguchi *et al.*, 2008a,b; Goto *et al.*, 2008). Maximum Pl lengths for isobaric starting conditions are plotted in the right box, given the corresponding starting pressures in brackets.

Microlite number densities (MND)

First of all, it has to be noted that the MND values for both plagioclases-only (MND_{Pl}) and for all other phases (MND_{OP}) of our decompression experiments seem to be dependent on the initial isobaric starting conditions. Thus, this makes the direct comparison of our decompression-derived experimental MND_{Pl} data with the MND_{Pl} range of natural erupted Unzen dome rocks ($10^{5.9}$ to $10^{6.1}$ mm^{-3} , e.g. Noguchi *et al.*, 2008a; indicated by grey

shaded area in Fig. 4.4a) rather invalid and allows only a qualitatively discussion of our experimental MND data.

In general, the MND values remain constant within the analytical uncertainties with decreasing decompression rates (Fig. 4.4), indicating rather dominant microlite growth during decompression if there is a simultaneously shift in chemical concentration of the residual glasses. The pre-existence of particular mineral phases at starting P-T conditions favors the growth of those crystals than the nucleation of new crystals, which would require higher degrees of supersaturation. Two exceptions have to be made here for HPD experiments at low decompression rates: (1) the above mentioned and discussed nucleation of plagioclase minerals in water-bearing set-I at decompression rates ≤ 0.0005 MPa/s and (2) the decrease of MND_{OP} values in the H₂O-bearing and H₂O+CO₂-bearing system of set-II at decompression rates < 0.001 MPa/s and < 0.01 MPa/s, respectively. This second observation can be explained by Ostwald ripening, where the numbers of crystals are reduced due to the effect of coalescence or dissolution, which can be supported by observations of our corresponding crystal size distributions (see *Appendix* Figs. B.1 and B.2).

Furthermore, the determined MND_{PI} values of HPD experiments (set-I) are approximately 0.5-1.0 log units lower than those of LPD experiments (set III-V, symbols marked with yellow filling in Fig. 4.4), ranging from $10^{5.4}$ to $10^{5.7}$ mm⁻³ and from $10^{5.7}$ to $10^{6.4}$ mm⁻³, respectively, which is presumably also an artefact of the initial microlite number densities at isobaric starting conditions. From chemical changes of the residual glasses and of the Pl microlites themselves as well as from overgrowth rims, we know that crystallization processes take place even at shallower depths (~50 MPa) to surface pressures, here preferably mineral growth. Therefore, our experimental study can not confirm the observation of Martel & Schmidt (2003) from experimental decompression experiments with pre-existing Pl minerals at isobaric starting conditions, showing that mineral growth is dominating at pressures > 50 MPa and that at lower pressure (< 50 MPa) microlite nucleation is dominating. On the other hand, such a distinct trend of dominating crystallization processes was also not observed in the experimental study of Brugger & Hammer (2010), where the investigated plagioclase microlites nucleated during decompression, not being part of the starting assemblage at isobaric conditions. Here the number densities of Pl microlites, taken from snapshot experiments at different pressures along the decompression path, showed diverse developments of microlite number densities at different decompression rates, allowing no clear statements of either dominating mineral

growth or nucleation at certain pressure ranges. Unfortunately, the number densities of Pl microlites given by Martel & Schmidt (2003) as well as by Brugger & Hammer (2010) are referring only to 2-dimensional areas (N_A in mm^{-2}) excluding 3D correction (e.g. Higgins, 2000, 2002, 2006), which does not allow the direct comparison of their data with our experimental MND_{Pl} values.

Toramaru *et al.* (2008) plotted $\log \text{MND}_{\text{Pl}}$ versus the silica content of bulk rock compositions of various eruption styles, including the 1991-1995 Unzen eruption, Fig. 4.5a. Our experimental decompression datasets have similar MND_{Pl} values compare to the natural Unzen rocks, but our experimental values are shifted to higher SiO_2 contents as we used the 1991-1995 erupted groundmass composition for our experimental study excluding phenocrysts. Therefore, we have plotted additionally the data for Unzen groundmass composition (Nakada & Motomura), see red framed and grey shaded area in Fig. 4.5. The diagram scale-up in Fig. 4.5b shows that only two decompression experiments match the red framed field for 1991-1995 erupted Unzen groundmass: $\text{H}_2\text{O}+\text{CO}_2$ -bearing sample DA29 (0.0002 MPa/s; HPD set-I) and H_2O -bearing sample LPD22 (0.0002 MPa/s, LPD set-IV). Unfortunately, Pl microlites of these two runs are of tabular shape and reach only maximum microlite sizes of $\sim 50\text{-}100 \mu\text{m}$, which is in the range of natural Unzen conduit samples (Noguchi *et al.*, 2008a,b; Goto *et al.*, 2008) but not in the range of erupted dome samples. The only experimental run reproducing the skeletal and $300 \mu\text{m}$ large Pl microlites of Unzen dome rocks (e.g. Noguchi *et al.*, 2008a) was the H_2O -bearing sample DA28 (HPD at 850°C) at 0.0002 MPa/s. Although at these conditions the residual melt is having only $\sim 74 \text{ wt}\% \text{SiO}_2$.

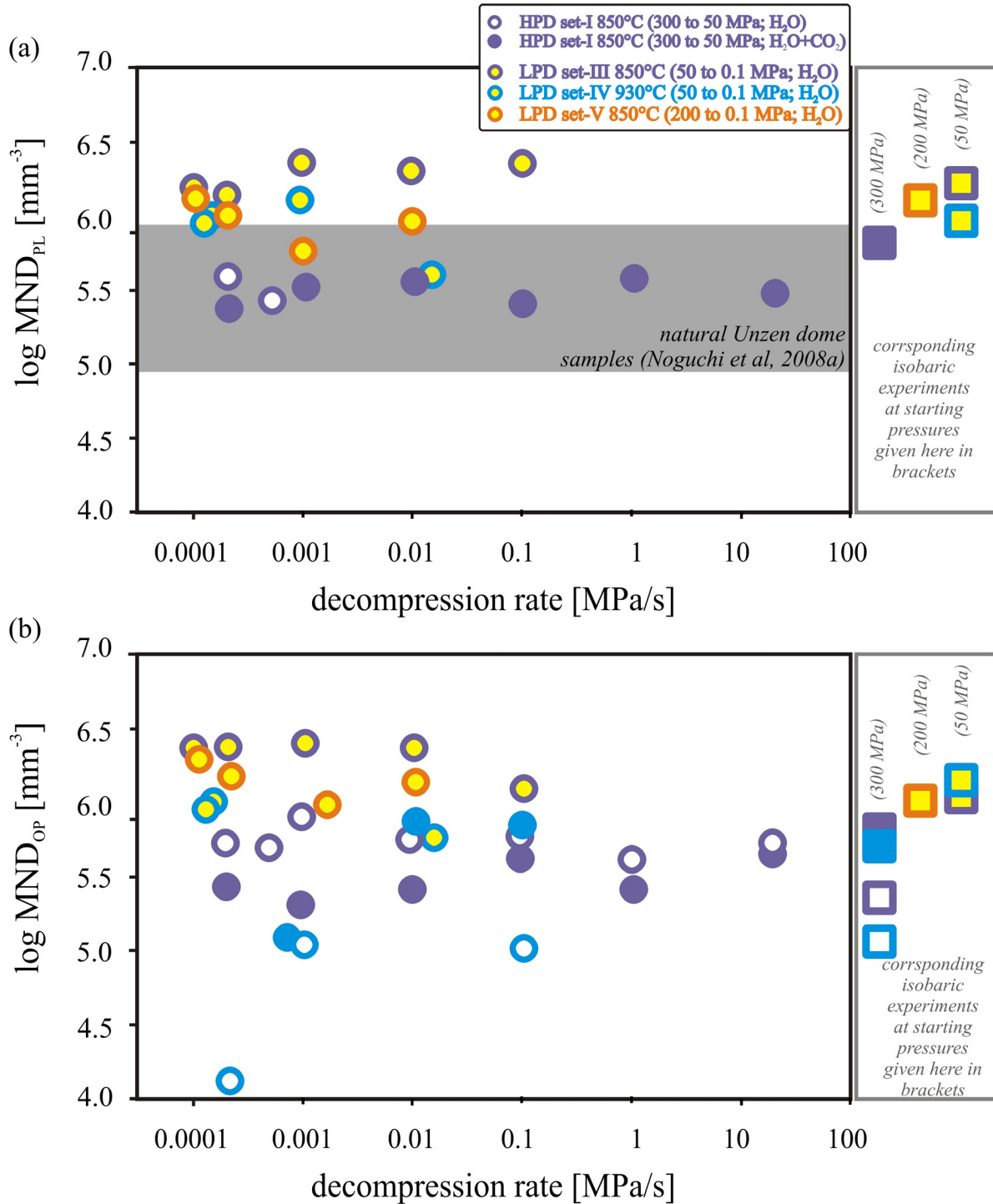


Fig. 4.4. Compiled HPD and LPD experimental data of the log MND for (a) plagioclases and for (b) all other phases as a function of the decompression rate. Grey shaded area represents the range of microlite number density of natural Unzen dome samples after Noguchi *et al.* (2008a). Low pressure data sets (final pressure = 0.1 MPa) are additionally marked by yellow color filling empty symbols in Fig. (a). Log MND values for isobaric starting conditions are plotted in the right box, given the corresponding starting pressures in brackets. Error bars are not shown again for simplicity.

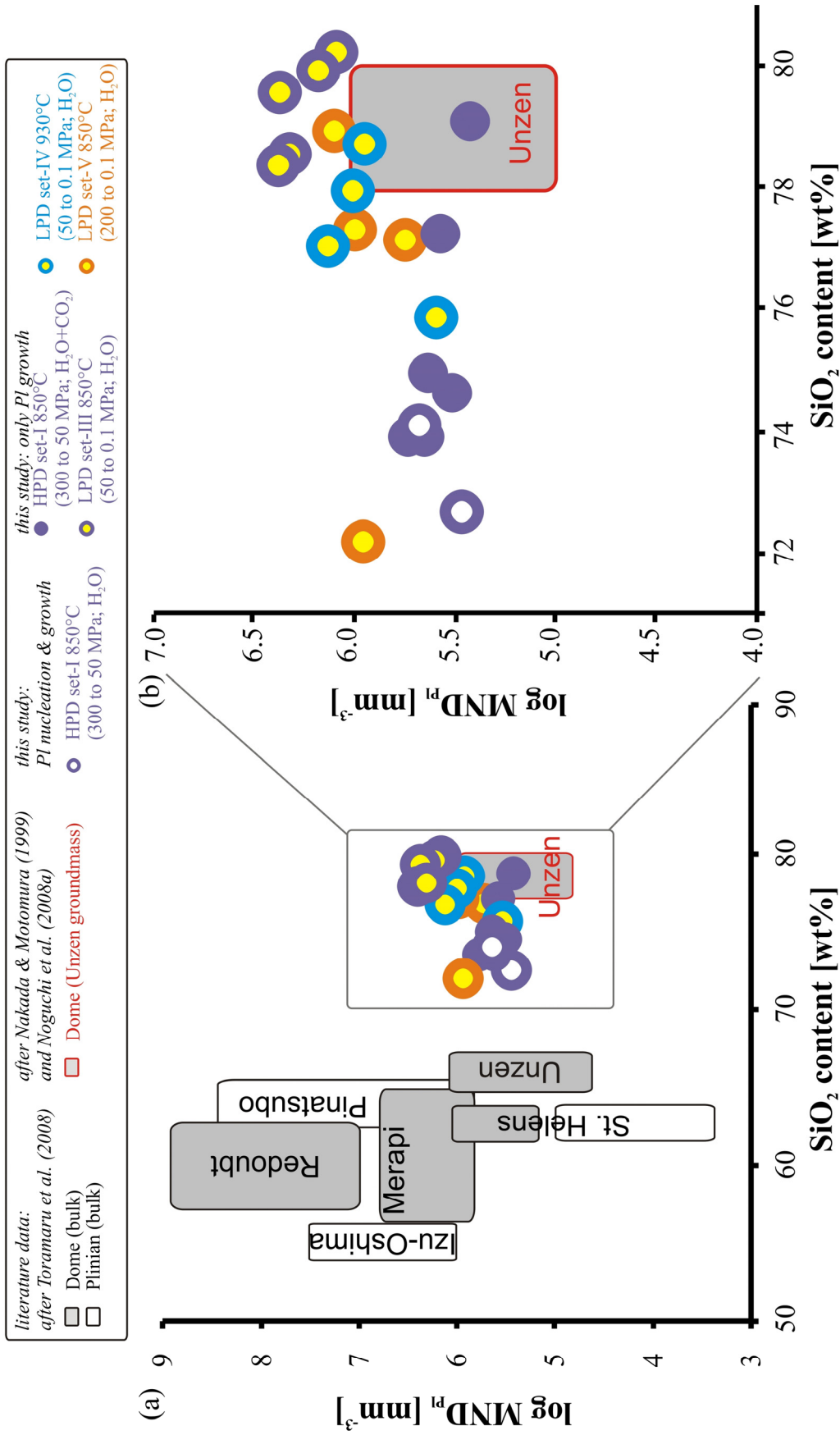


Fig. 4.5. Log MND_{PI} vs. SiO₂-content of bulk rock for dome and plinian eruptions, modified after Toramaru *et al.* (2008). Our HPD experimental datasets are plotted as empty purple or blue circles (at 850°C and 930°C, respectively). Our LPD experiments are given by yellow filled circles. The data for 1991–1995 natural Unzen groundmass is indicated by the red framed square (Nakada & Motomura, 1999; Noguchi *et al.*, 2008a).

Effect of sample preparation and experimental setup on vesiculation and crystallization processes

It has to be noted that there might have been parameters already during the capsule preparation influencing our degassing and crystallization processes during our experimental decompression runs already. For once, we have used a glass powder as a starting material, whose grain size boundaries could have acted as nucleation sites for bubbles as well as for microlites (e.g. Marziano et al., 2007), lowering the required supersaturation pressure and favouring early heterogeneous nucleation processes (e.g. Mangan & Sisson, 2005). This might explain why our MND values of the decompression experiments are in the same range as the ones of the starting material for all experimental sets. It seems that the MNDs of our decompression experiments were already given by the MNDs at isobaric starting conditions. It might have been a better approach to use homogeneous dry glass cylinders as a starting material instead of glass powder, and then synthesizing the fluid-saturated samples at above-liquidus conditions prior to the decompression process.

Secondly, the preparation of big synthesis capsules for the $\text{H}_2\text{O}+\text{CO}_2$ -bearing system ($X^{\text{fl}}\text{H}_2\text{O} \sim 0.6$) of the high-pressure decompression set at 930°C (HPD set-II, see *chapter 3.1.2.*), was probably followed by the loosing of important amounts of volatile components during the opening of the big synthesis capsule to cut the glass cylinder into smaller samples for further decompression experiments. Thus, a lowering of the concentration of carbon dioxide in the fluid phase resulted prior to the decompression, increasing the mole fraction of water and becoming close to 1.0 and therefore similar to the conditions of the initial H_2O -bearing system. This might also explain the similarities in the chemical compositions and texture, as well as the lack of crystallized Pl microlites in the assumed $\text{H}_2\text{O}+\text{CO}_2$ -bearing system of both fluid-saturated systems at 930°C .

Several decompression experiments needed to be repeated as capsule walls showed holes or cracks, which are probably related to the high gas pressure inside the capsule. One weak link were of course the welding seams on which capsules bursted open. The capsule length (15 to 20 mm) was intentionally chosen to be large enough to allow the growing gas pressure to expand, with increasing water exsolution from the melt, without destroying the wholeness of the capsule. But anyway, deformed or inflated (intact) capsules also allow the melt to flow, influencing the mass transport and for example the bubble formation processes, which should be taken care off when discussing experimental results.

Furthermore, there might have been differences in the P-T-paths of decompression experiments conducted in CSPVs and IHPVs. The inertia of the rather slow external furnace in CSPV experimental setups might have lead to high coolings ($\sim 30^{\circ}\text{C}$) at rather high decompression rates and to even several cooling events related to each pressure release in multi-decompression experiments. On the other hand, such thermal fluctuations are not expected in IHPVs as the thermocouples are directly positioned next to the sample inside the furnace, which therefore can react faster on changes in temperatures.

Effect of degassing and crystallization: Implications for magma ascent dynamics at Unzen

Similar groundmass compositions for most major elements and similar MND_{Pl} values of natural Unzen dome (e.g. Nakada & Momomura, 1999) and conduit samples (e.g. Noguchi *et al.*, 2008a,b) could indicate no significant crystallization process occurring during Unzen magma ascent from shallow depths to the surface. This stands in contrast to our chemical and textural analyses of HPD and LPD experiments, showing continuous dominant crystal growth at high and low pressures. However, the sampled Unzen conduit rocks have probably undergone a different thermal history after the eruption and therefore their textural and chemical data should be used with caution.

The two main observations which are useful for the estimation of the magma ascent rate from our experimental run products are the reproduction of (1) the chemical composition of natural matrix glasses and (2) the occurrence and characteristics of the natural Unzen mineral assemblage; especially the preservation of Amph microlites as well as the shapes and lengths of Pl microlites. The chemical composition of natural Unzen groundmass glass was best reproduced by our H_2O -bearing LPD experiments (set III to V) and by our $\text{H}_2\text{O}+\text{CO}_2$ -bearing HPD experiments of set-I (850°C) at the lowest conducted decompression rates ($0.0002 - 0.0001 \text{ MPa/s}$), see Figs. 3.4, 3.22 and 3.27, corresponding to ascent velocities of $\sim 12\text{-}24 \text{ m/h}$. On the other hand, natural Pl microlites with skeletal shapes and lengths of $\sim 300 \mu\text{m}$ (e.g. Noguchi *et al.*, 2008a) are only observed when Pl is nucleating and growing during decompression, which was only the case in our H_2O -bearing HPD set-I (850°C) at decompression rates $< 0.0005 \text{ MPa}$ (corresponding to $\sim 50 \text{ m/h}$), although the chemical composition of the residual glasses did not match natural dome samples yet. The phase relation experiments of our study have showed that the major Unzen groundmass minerals (plagioclase, pargasite, pyroxenes and Fe-Ti-oxides; e.g. Venezky & Rutherford, 1999) are only stable in a relatively narrow P-T- $X^{\text{fl}}\text{H}_2\text{O}$ range (see

checkered areas in Fig. 2.3 to Fig. 2.6). Although our stability experiments have showed that amphiboles only crystallize at pressures above 100 MPa and at temperatures of less than $\sim 860^\circ\text{C}$ in fluid-saturated systems having high mole fractions of water (> 0.6), pargasite microlites were preserved in natural erupted dome samples, indicating that the magma ascent had to be fast enough at lower pressure (< 100 MPa) to hinder the total dissolution of former stable pargasite crystals. This effect can be seen in LPD experiments of set-V, starting at 200 MPa with pressure release down to surface pressures (0.1 MPa). Here amphiboles (having Al_2O_3 contents of 8-9 wt% and being $\sim 20\text{-}25$ μm long) were part of the starting assemblage at 200 MPa and 850°C . But after the decompression runs, Amph microlites were only detected in samples of LPD experiments with decompression rates ≥ 0.001 MPa/s. Groundmass pargasites observed in natural erupted Unzen dome samples are still having lengths of 100-300 μm , which is nearly ten times larger than our experimentally grown amphibole microlites. Thus it can be suggested that natural pargasite microlites were large enough in size at depth to be not totally dissolved during magma ascent at decompression rates even as low as 0.0001 MPa/s (correlating to 12 m/h).

The exact determination of the water activity in the ascending magmas to the surface is difficult. Considering that the estimated ascent rates are lower than 50 m/h, volatile exsolution must have occurred at conditions close-to-equilibrium in the pressure range 300-0.1 MPa, which is typical for effusive non-violent eruptions (e.g. Hurwitz & Navon, 1994), as observed at Unzen. Assuming that the released volatiles are, at least in part, escaping from the magmatic system (open system degassing; e.g., Turner *et al.*, 1983; Gerlach, 1986) melts would be almost free of CO_2 at low pressures (< 50 MPa). On the other hand, the model of Ohba *et al.* (2008) assumes that $\text{CO}_2\text{-H}_2\text{O}$ -bearing fluids were continuously ascending in the Unzen conduit, which would maintain a relatively low water activity in the ascending magmas (the water activity would be mainly controlled by the percolation of $\text{CO}_2\text{-H}_2\text{O}$ -bearing fluids). Thus, if the percolation of such fluids were “buffering” the water activity in the conduit, an ascent rate of ~ 50 m/h is more realistic than a value of ~ 10 m/h. In any case, these values are in general agreement with estimations from petrology by Nakada & Motomura (1999; 12-30 m/hour), from textural analysis by Noguchi *et al.* (2008a; 29-274 m/h in the pressure range 70-100 MPa) and by the MND decompression rate meter of Toramaru *et al.* (2008; 29-132 m/h) as well as from water exsolution rates by Toramaru *et al.* (2008; 50-245 m/h), while data from electrical resistivity structure measurements by Kagiya *et al.* (1999) lead to lower estimated ascent rates (~ 0.8 m/h).

5. CONCLUSION

Isothermal decompression experiments using a rhyodacitic composition show that the large size ($\sim 300 \mu\text{m}$; Noguchi *et al.*, 2008a) and the skeletal shape of natural plagioclase microlites can be only reproduced experimentally if the nucleation and growth occurs along the decompression path; here in our study only in water-bearing decompression experiments from 300 to 50 MPa at decompression rate $< 0.0005 \text{ MPa/s}$. Once Pl nucleation has proceeded, the degree of undercooling (as well as diffusivity of cations in the melts), which is dependent on the decompression rate, is expected to be the main parameter influencing mineral growth kinetics (mineral size). Thus, the size and shape of Pl microlites can be used to constrain ascent rates. Furthermore, phase relation experiments indicate a narrow stability field for the mineral assemblage observed in natural erupted Unzen rocks, including pargasite. Amphibole microlites were only preserved under certain conditions in our decompression experiments which leads to the general conclusion that (1) the ascending magma must have crossed P-T- $X^{\text{fl}}\text{H}_2\text{O}$ conditions that allow the crystallization of Amph microlites (and the overgrowth of Amph phenocrysts), (2) the decompression rate of the rising magma from shallow depths to surface pressures has to be fast enough so that Amph crystals do not dissolve entirely during the magma ascending process, dependent on the initial maximum Amph microlite sizes at depth, and (3) Pl microlites were not part of the mineral starting assemblage prior to the magma ascent, nucleating and growing only during decompression. In the case of Unzen magmas, we can therefore assume water activities close to 1.0 and magma ascent rates of $\sim 30\text{-}50 \text{ m/h}$ (probably not constant; Noguchi *et al.*, 2008a). Furthermore, we also suggest a non-isothermal decompression path in the lower temperature range estimated for Unzen mixed dacite prior to the eruption ($870\text{-}930^\circ\text{C}$; e.g. Venezky & Rutherford, 1999).

In our decompression experiments, using a partially crystallized starting material containing bubbles, a transition from non-equilibrium to near-equilibrium water release from the Unzen rhyolitic melt is observed at decompression rates between 1 and 0.1 MPa/s (at water-saturated conditions from 300 to 50 MPa, 850°C). Furthermore, a major influence of bubble forming processes on the decompression path was detected, performing continuous, multi-step and single-step decompression. Efforts in further development of a 3D segmentation and visualization software (*YaDiV*) were successful in providing true volume data from tomography scans for bubbles and microlites.

6. REFERENCES

- Aranovich, L.Y. & Newton, R.C. (1999). Experimental determination of CO₂-H₂O activity concentration relations at 600–1000 °C and 6–14 kbar by reversed decarbonation and dehydration reactions. *American Mineralogist* **84**, 1319-1332.
- Armienti, P. (2008). Decryption of igneous rock textures: crystal size distribution tools. *Reviews in Mineralogy and Geochemistry* **69**, 623-649.
- Baker, D.R., Freda, C., Brooker, R. A. & Scarlato, P. (2005). Volatile diffusion in silicate melts and its effects on melt inclusions. *Annals of Geophysics* **48**, N. 4/5.
- Baker, D.R., Lang, P., Robert, G., Bergevin, J.-F., Allard, E. & Bai, L. (2006). Bubble growth in slightly supersaturated albite melt at constant pressure. *Geochimica et Cosmochimica Acta* **70**, 1821-1838.
- Behrens, H. & Zhang, Y. (2001). Ar diffusion in hydrous silicic melts: implications for volatile diffusion mechanisms and fractionation. *Earth and Planetary Science Letters* **192**, 363-376.
- Behrens, H., Ohlhorst, S., Holtz, F. & Champenois, M. (2004). CO₂ solubility in dacitic melts equilibrated with H₂O-CO₂ fluids: Implications for modelling the solubility of CO₂ in silicic melts. *Geochimica et Cosmochimica Acta* **68**, 4687-4703.
- Berndt, J., Liebske, C., Holtz, F., Freise, M., Nowak, M., Ziegenbein, D., Hurkuck, W. & Koepke, J. (2002). A combined rapid-quench and H₂-membrane setup for internally heated pressure vessels: Description and application for water solubility in basaltic melts. *American Mineralogist* **87**, 1717-1726.
- Botcharnikov, R.E., Behrens, H., Holtz, F., Koepke, J. & Sato, H. (2004). Sulfur and chlorine solubility in Mt. Unzen rhyodacitic melt at 850°C and 200 MPa. *Chemical Geology* **213**, 207-225.
- Botcharnikov, R.E, Koepke, J., Almeev, R.R. & Holtz, F. (2008). Experimental phase relations, mineral-melt equilibria and liquid lines of descent in a hydrous ferrobasalt - Implications for the Skaergaard intrusion and Columbia River flood basalts. *Journal of Petrology* **49** (9), 1687-1727.
- Browne, B.L. & Gardner, J.E. (2006). The influence of magma ascent path on the texture, mineralogy, and formation of hornblende reaction rims. *Earth and Planetary Science Letters* **246**, 161-176.

- Browne, B.L., Eichelberger, J.C., Patino, L.C., Vogel, T.A., Dehn, J., Uto, K. & Hoshizumi, H. (2006). Generation of porphyric and equigranular mafic enclaves during magma recharge events at Unzen Volcano, Japan. *Journal of Petrology* **47**, 301-328.
- Cashman, K.V. & Mangan, M.T. (1994). (1994). Physical aspects of magma degassing II. Constraints on vesiculation processes from textural studies of eruptive products. *Reviews in Mineralogy* **30**, 447-478.
- Castro, J.M. & Dingwell, D.B. (2009). Rapid ascent of rhyolitic magma at Chaitén volcano, Chile. *Nature Letters* **461**, 780-783.
- Chevychelov, V.Y., Botcharnikov, R.E. & Holtz, F. (2008). Partitioning of Cl and F between fluid and hydrous phonolitic melt of Mt. Vesuvius at ~850–1000 °C and 200 MPa. *Chemical Geology* **256**, 172-184.
- Cichy, S.B., Botcharnikov, R.E., Holtz, F. & Behrens, H. (2010). Vesiculation and Microlite Crystallization Induced by Decompression: A Case Study of the 1991-95 Mt Unzen Eruption (Japan). *Journal of Petrology* **52**, 1469-1492, doi: 10.1093/petrology/egq072.
- Cluzel, N., Laporte, D., Provost, A. & Kannevischer, I. (2008). Kinetics of heterogeneous bubble nucleation in rhyolitic melts: implications for the number density of bubbles in volcanic conduits and for pumice textures. *Contributions to Mineralogy and Petrology* **156**, 745-763.
- Couch, S., Sparks, R.S.J. & Carroll, M.R. (2003). The kinetics of degassing-induced crystallization at Soufriere Hills volcano, Montserrat. *Journal of Petrology* **44**, 1477-1502.
- Devine, J.D., Gardener, J.E., Brack, H.P., Layne, G.D., & Rutherford, M.J. (1995). Comparison of microanalytical methods for estimating H₂O contents of silicic volcanic glasses. *American Mineralogist* **80**, 319-328.
- Ebadi, A. & Johannes, W. (1991) Beginning of melting and composition of first melts in the system Qz-Ab-Or-H₂O-CO₂. *Contributions to Mineralogy and Petrology* **106**, 286–295.
- Freise, M., Holtz, F., Nowak, M., Strauß, H., & Scoates, J.S. (2009). Differentiation and crystallization conditions of basalts from the Kerguelen large igneous province: an experimental study. *Contributions to Mineralogy and Petrology* **158**, 505-527.
- Friese, K.I., Blanke, P. & Wolter, F.E. (2011). Yadviv - an open platform for 3d visualization and 3d segmentation of medical data. *The Visual Computer* **27**, 129-139.

-
- Fogel, R.A. & Rutherford, M.J. (1990). The solubility of carbon dioxide in rhyolitic melts: A quantitative FTIR study. *American Mineralogy* **75**, 1311-1326.
- Gardner, J.E. (2007a). Bubble coalescence in rhyolitic melts during decompression from high pressure. *Journal of Volcanology and Geothermal Research* **166**, 161-176.
- Gardner, J.E. (2007b). Heterogeneous bubble nucleation in highly viscous silicate melts during instantaneous decompression from high pressure. *Chemical Geology* **236**, 1-12.
- Gardner, J.E. (2009). The impact of pre-existing gas on the ascent of explosively erupted magma. *Bulletin of Volcanology* **71**, 835-844.
- Gardner, J.E., Hilton, M. & Carroll, M.R. (1999). Experimental constraints on degassing of magma: isothermal bubble growth during continuous decompression from high pressure. *Earth and Planetary Science Letters* **168**, 201-218.
- Gardner, J.E. & Denis, M.-H. (2004). Heterogeneous bubble nucleation on Fe-Ti oxide crystals in high-silica rhyolitic melts. *Geochimica et Cosmochimica Acta* **68**, 3587-3597.
- Gerlach, T. M. (1986). Exsolution of H₂O, CO₂ and S during eruptive episodes at Kilauea Volcano, Hawaii. *Journal of Volcanology and Geothermal Research* **91**, 177-182.
- Geschwind, C.-H. & Rutherford, M.J. (1995). Crystallization of microlites during magma ascent: the fluid mechanics of 1980-1986 at Mount St Helens. *Bulletin of Volcanology* **57**, 356-370.
- Gonde, C., Martel, C., Pichavant, M. & Bureau H. (2011). In situ bubble vesiculation in silicic magmas. *American Mineralogist* **96**, 111-124.
- Goto, Y., Nakada, S., Kurokawa, M., Shimano, T., Sugimoto, T., Sakuma, S., Hoshizumi, H., Yoshimoto, M. & Uto, K. (2008). Character and origin of lithofacies in the conduit of Unzen volcano, Japan. *Journal of Volcanology and Geothermal Research* **175**, 45-59.
- Hamada, M., Laporte, D., Cluzel, N., Koga, K.T. & Kawamoto, T. (2010). Simulating bubble number density of rhyolitic pumices from Plinian eruptions: constraints from fast decompression experiments. *Bulletin of Volcanology* **72**, 735-746.
- Hammer, J.E. (2008). Experimental studies of the kinetics and energetics of magma crystallization. In: Putrika, K. D. & Tepley, F. J., III (eds) *Minerals, Inclusions and Volcanic Processes. Mineralogical Society of America and Geochemical Society, Reviews in Mineralogy and Geochemistry* **69**, 9-59.
- Hammer, J.E. & Rutherford, M.J. (2002). An experimental study of the kinetics of decompression-induced crystallization in silicic melt. *Journal of Geophysical Research* **107**, 1-23.

- Hess, K.-U. & Dingwell, D.B. (1996). Viscosities of hydrous leucogranitic melts: a non-Arrhenian model. *American Mineralogist* **81**, 1297-1300.
- Higgins, M. (2000). Measurement of crystal size distribution. *American Mineralogist* **85**, 1105-1116.
- Higgins, M. (2002). Closure in crystal size distributions (CSD), verification of CSD calculations, and the significance of CSD fans. *American Mineralogist* **87**, 171-175.
- Higgins, M. (2006a). Verification of ideal semi-logarithmic, lognormal or fractal crystal size distributions from 2D datasets. *Journal of Volcanology and Geothermal Research* **154**, 8-16.
- Higgins, M. (2006b). *Quantitative textural measurements in igneous and metamorphic petrology*. Cambridge University Press
- Holtz, F., Behrens, H., Dingwell, D.B. & Johannes, W. (1995). Water solubility in haplogranitic melts. Compositional, pressure and temperature dependence. *American Mineralogist* **80**, 94-108.
- Holtz, F., Sato, H., Lewis, J., Behrens, H. & Nakada, S. (2005). Experimental petrology of the 1991-1995 Unzen Dacite, Japan. Part I: phase relations, phase composition and preeruptive conditions. *Journal of Petrology* **46**, 319-337.
- Holloway, J.R. (1971) *Internally heated pressure vessels*. In G.C. Ulmer, Ed. *Research techniques for high temperature and pressure*. Springer Verlag, New York, p. 217-258.
- Hoshizumi, H., Uto, K. & Watanabe, K. (1999). Geology and eruptive history of Unzen volcano, Shimabara Peninsula, Kyushu, SW Japan. *Journal of Volcanology and Geothermal Research* **89**, 81-94.
- Hoshizumi, H., Matsumoto, A. & Kurihara, A. (2005). Growth history of Unzen volcano, Kyushu, Japan – Results of two flank drillings of the Unzen Scientific Drilling Project. *Extended Abstract Volume of “Unzen Workshop 2005”*, O-19.
- Hurwitz, S. & Navon, O. (1994). Bubble nucleation in rhyolitic melts: experiments at high pressure, temperature and water content. *Earth and Planetary Science Letters* **122**, 267-280.
- Ida, Y. (1996). Cyclic fluid effusion accompanied by pressure change: implication for volcanic eruptions and tremor. *Geophysical Research Letters* **23**, 1457-1460.
- Jaupart, C. & Tait, S. (1990). Dynamics of eruptive phenomena. *Reviews in Mineralogy and Geochemistry* **24**, 213-238.
- Johannes, W. & Holtz, F. (1996). *Petrogenesis and experimental petrology of granitic rocks*. Minerals and Rocks, Series Vol. 22. xiii + 335 pp. Berlin: Springer-Verlag.

-
- Kagiyama, T., Utada, H. & Yamamoto, T. (1999). Magma ascent beneath Unzen Volcano, SW Japan, deduced from the electrical resistivity structure. *Journal of Volcanology and Geothermal Research* **89**, 35–42.
- Larsen, J.F. (2005). Experimental study of plagioclase rim growth around anorthite seed crystals in rhyodacitic melt. *American Mineralogist* **90**, 417-427.
- Larsen, J.F. & Gardner, J.E. (2004). Experimental study of water degassing from phonolite melts: implications for volatile oversaturation during magmatic ascent. *Journal of Volcanology and Geothermal Research* **134**, 109-124.,
- Laporte, D., Mourtada-Bonnefoi, C. & Cacault, Ph. (2000). Homogeneous bubble nucleation in a rhyolitic liquid: the effect of magma ascent rate, *Journal of Conference Abstracts* **5**, 62.
- Lautze, N.C., Sisson, T.W., Mangan, M.T. & Grove T.L. (2010). Segregating gas from melt: an experimental study of the Ostwald ripening of vapor bubbles in magmas. *Contributions to Mineralogy and Petrology*, doi: 10.1007/s00410-010-0535-x
- Liu, Y., Zhang, Y. & Behrens, H. (2005). Solubility of H₂O in rhyolitic melts at low pressures and a new empirical model for mixed H₂O-CO₂ solubility in rhyolitic melts. *Journal of Volcanology and Geothermal Research* **143**, 219-235.
- Lofgren, G.E. (1974). An experimental study of plagioclase crystal morphology: isothermal crystallization. *American Journal of Science* **274**, 243-273.
- Maeda, I. (2000). Nonlinear visco-elastic volcanic model and its application to the recent eruption of Mt. Unzen. *Journal of Volcanology and Geothermal Research* **95**, 35-47.
- Mangan, M. & Sisson, T. (2000). Delayed disequilibrium degassing in rhyolite magma: decompression experiments and implications for explosive volcanism. *Earth and Planetary Science Letters* **183**, 441-455.
- Mangan, M. & Sisson, T. (2005). Evolution of melt-vapor surface tension in silicic volcanic systems: experiments with hydrous melts. *Journal of Geophysical Research* **110**, B01202, doi: 10.1029/2004JB003215.
- Marsh, B.D. (1988). Crystal size distribution (CSD) in rocks and the kinetics and dynamics of crystallization. I. Theory. *Contribution to Mineralogy and Petrology* **99**, 277-291.
- Martel, C. & Bureau, H. (2001). In situ high-pressure and high-temperature bubble growth in silicic melts. *Earth and Planetary Science Letters* **191**, 115-127.
- Martel, C. & Schmidt, B.C. (2003). Decompression experiments as an insight into ascent rates of silicic magmas. *Contribution to Mineralogy and Petrology* **144**, 397-415.

- Marziano, G.I., Schmidt, B.C. & Dolfi, D. (2007). Equilibrium and disequilibrium degassing of a phonolitic melt (Vesuvius AD 79 „white pumic“) simulated by decompression experiments. *Journal of Volcanology and Geothermal Research* **161**, 151-164.
- Melnik, O. & Sparks, R.S.J. (1999). Nonlinear dynamics of lava dome extrusion. *Nature* **402**, 37-41.
- Mourtada-Bonnefoi, C.C. & Laporte, D. (1999). Experimental study on homogeneous bubble nucleation in rhyolitic magmas. *Geophysical Research Letters* **26**, 3505-3508.
- Mourtada-Bonnefoi, C.C. & Laporte, D. (2002). Homogeneous bubble nucleation in rhyolitic magmas: an experimental study of the effect of H₂O and CO₂. *Journal of Geophysical Research* **107**, B4, doi: 10.1029/2001JB00290.
- Mourtada-Bonnefoi, C. C., Laporte, D. (2004). Kinetics of bubble nucleation in a rhyolitic melt: an experimental study of the effect of ascent rate. *Earth and Planetary Science Letters* **218**, 521-537.
- Muncill, G.E. & Lasaga, A.C. (1987). Crystal-growth kinetics of plagioclase in igneous systems: One-atmosphere experiments and application of a simplified growth model. *American Mineralogist* **72**, 299-311.
- Muncill, G.E. & Lasaga, A.C. (1988). Crystal-growth kinetics of plagioclase in igneous systems: Isothermal H₂O-saturated experiments and extension of a growth model to complex silicate melts. *American Mineralogist* **73**, 982-992.
- Nakada, S. & Fuji, T. (1993). Preliminary report on the activity at Unzen Volcano (Japan), November 1990-November 1991: Dacite lava domes and pyroclastic flows. *Journal of Volcanology and Geothermal Research* **54**, 319-333.
- Nakada, S. & Motomura, Y. (1999). Petrology of the 1991-95 eruption at Unzen: effusion pulsation and groundmass crystallization. *Journal of Volcanology and Geothermal Research* **89**, 173-196.
- Nakada, S., Shimizu, H. & Ohta K. (1999). Overview of the 1990-1995 eruption at Unzen Volcano. *Journal of Volcanology and Geothermal Research* **89**, 1-22.
- Nakada, S. & Eichelberger, J.C. (2004). Looking into a volcano drilling Unzen. *Geotimes* **49**, 14-17.
- Nakada, S., Uto, K., Sakuma, S., Eichelberger, J.C. & Shimizu, H. (2005). Scientific results of conduit drilling in the Unzen Scientific Drilling Project (USDP). *Scientific Drilling* **1**, 18-22, doi: 10.2204/iodp.sd.1.03.2005.

-
- Newton, R.C. & Manning, C.E. (2000). Quartz solubility in H₂O-NaCl and H₂O-CO₂ solutions at deep crust-upper mantle pressures and temperatures: 2-25 kbar and 500-900°C. *Geochimica et Cosmochimica Acta* **64**, 2993-3005.
- Newton, R.C. & Manning, C.E. (2008). Thermodynamics of SiO₂-H₂O fluid near the upper critical and point from quartz solubility measurements at 10 kbar. *Earth and Planetary Science Letters* **274**, 241-249.
- Nishi, K., Ishihara, K., Kamo, K., Ono, H. & Mori, H. (1995). Positioning of magma reservoir at Unzen volcano by GPS survey. *Bulletin of Volcanology Society of Japan* **40**, 43-51, in Japanese with English abstract.
- Nishi, K., Ono, H. & Mori, H. (1999). Global positioning system measurements of ground deformation caused by magma intrusion and lava discharge: the 1990-1995 eruption at unzendake volcano, Kyushu, Japan. *Journal of Volcanology and Geothermal Research* **89**, 23-34.
- Nishimura, K., Kawamoto, T., Kobayashi, T., Sugimoto, T. & Yamashita, S. (2005). Melt inclusion analysis of the Unzen 1991–1995 dacite: implications for crystallization processes of dacite magma. *Bulletin of Volcanology* **67**, 648–662.
- Noguchi, S., Toramaru, A. & Nakada, S. (2008a). Relation between microlite textures and discharge rate during the 1991-1995 eruptions at Unzen, Japan. *Journal of Volcanology and Geothermal Research* **175**, 141-155.
- Noguchi, S., Toramaru, A. & Nakada, S. (2008b). Groundmass crystallization in dacite dykes taken in Unzen Scientific Drilling Project (USDP-4). *Journal of Volcanology and Geothermal Research* **175**, 71-81.
- Nowak, M., Cichy, S.B., Botcharnikov, R.E., Walker, N. & Hurkuck, W. (2011). A new type of high pressure low-flow metering valve for experiments at continuous decompression: First experimental results for magmatic systems. *American Mineralogist* **96**, 1373-1380.
- Ohba, T., Hirabayashi, J.-I., Nogami, K., Kusakabe, M. & Yoshida, M. (2008). Magma degassing process during the eruption of Mt. Unzen, Japan in 1991 to 1995: modeling with the chemical composition of volcanic gas. *Journal of Volcanology and Geothermal Research* **175**, 120-132.
- Ohlhorst, S., Behrens, H. & Holtz, F. (2001). Compositional dependence of molar absorptivities of near-infrared OH- and H₂O bands in rhyolitic to basaltic glasses. *Chemical Geology* **174**, 5-20.

- O'Neill, H.S. (1987). Free energies of formation of NiO, CoO, Ni₂SiO₄, and Co₂SiO₄. *American Mineralogist* **72**, 280-291.
- Pitzer, K.S. & Sterner, S.M. (1994). Equation of state valid continuously from zero to extreme pressures for H₂O and CO₂. *Journal of Chemistry and Physics* **102**, 3111-3116.
- Pamukcu, A.S. & Gualda, G.A.R. (2010). Quantitative 3D petrography using X-ray tomography 2: Combining information at various resolutions. *Geosphere* **6**, 775-781.
- Rollinson, H. (1993). *Using geochemical data: evaluation, presentation, interpretation*. Longman Scientific & Technical. New York. 352 p.
- Rutherford, M.J. (2008). Magma ascent rates. *Reviews in Mineralogy and Geochemistry* **69**, 241-271.
- Rutherford, M.J. & Hill, P.M. (1993). Magma ascent rates from amphibole breakdown: an experimental study applied to the 1980-1986 Mount St. Helens eruption. *Journal of Geophysical Research* **98**, 19667-19685.
- Sato, H., Nakada, S., Fujii, T., Nakamura, M. & Suzuki-Kamata, K. (1999). Groundmass pargasite in the 1991-1995 dacite of Unzen volcano: phase stability experiments and volcanological implications. *Journal of Volcanology and Geothermal Research* **89**, 197-212.
- Sato, H., Holtz, F., Behrens, H., Botcharnikov, R.E. & Nakada, S. (2005). Experimental petrology of the 1991-1995 dacite of Unzen volcano. Part II: Cl/OH partitioning between hornblende and melt and its implications for the origin of oscillatory zoning of hornblende phenocryst. *Journal of Petrology* **46**, 339-354.
- Seno, T. (1977). The instantaneous rotation vector of the Philippine Sea plate relative to the Eurasian plate. *Tectonophysics* **42**, 209-266.
- Shaw, H.R. (1963) Hydrogen-Water Vapor Mixtures: Control of Hydrothermal Atmospheres by Hydrogen Osmosis. *Science* **139**, 1220-1222.
- Simakin, A.G., Armienti, P. & Epel'baum, M.B. (1999). Coupled degassing and crystallization: experimental study at continuous pressure drop, with application to volcanic bombs. *Bulletin of Volcanology* **61**, 275-287.
- Simakin, A.G., Armienti, P. & Salova, T.P. (2000). Joint degassing and crystallization: experimental study with a gradual pressure release. *Geochemistry International* **38**, 523-534.
- Sparks, R.S.J. (1978). The dynamics of bubble formation and growth in magmas: a review and analysis. *Journal of Volcanology and Geothermal Research* **3**, 1-37.

-
- Sparks, R.S.J., Barclay, J., Jaupart, C., Mader, H.M. & Phillips, J.C. (1994). Physical aspects of magma degassing I. Experimental and theoretical constraints on vesiculation. *Reviews in Mineralogy and Geochemistry* **30**, 412-445.
- Tamic, N., Behrens, H. & Holtz, F. (2001). The solubility of H₂O and CO₂ in rhyolitic melts in equilibrium with a mixed CO₂-H₂O fluid phase. *Chemical Geology* **174**, 333-347.
- Toramaru, A. (1995). Numerical study of nucleation and growth of bubbles in viscous magma. *Journal of Geophysical Research* **100**, 1913-1931.
- Toramaru, A. (2006). BND (bubble number density) decompression rate meter for explosive volcanic eruptions. *Journal of Volcanology and Geothermal Research* **154**, 303-316.
- Toramaru, A., Tsune, A. & Noguchi, S. (2008). Microlite number density (MND) water-exsolution rate meter. *Journal of Volcanology and Geothermal Research* **175**, 141-155.
- Turner, J.S., Huppert, H.E. & Sparks, R.S.J. (1983). An experimental investigation of volatile exsolution in evolving magma chambers. *Journal of Volcanology and Geothermal Research* **16**, 263-277.
- Venezky, D.Y. & Rutherford, M.J. (1999). Petrology and Fe-Ti oxide reequilibration of the 1991 Mount Unzen mixed magma. *Journal of Volcanology and Geothermal Research* **89**, 212-230.
- Vetere, F., Behrens, H., Schuessler, J.A., Holtz, F., Misiti, V. & Borchers, L. (2008). Viscosity of andesite melts and its implication for magma mixing prior to Unzen 1991-1995 eruption. *Journal of Volcanology and Geothermal Research* **175**, 208-217.
- Withers, A.C. & Behrens, H. (1999). Temperature-induced changes in the NIR spectra of hydrous albitic and rhyolitic glasses between 300 and 100 K. *Physics and Chemistry of Minerals* **27**, 119-132.
- Yamashita, S. (1999). Experimental study of the effect of temperature on water solubility in natural rhyolite melt to 100 MPa. *Journal of Petrology* **40**, 1497-1507.

7. APPENDIX A.1 – TABLES INDEX

Table	Title	Page
2.1	Chemical composition of used and investigated Unzen glasses: this study and literature	8
3.1	Experimental conditions and composition of residual melts (HPD set-I)	33
3.2	Experimental conditions and results of textural analysis (HPD set-I)	34
3.3	Experimental conditions and composition of residual melts (HPD set-II)	65
3.4	Experimental conditions and results of textural analysis (HPD set-II)	65
3.5	Experimental conditions and composition of residual melts (LPD set-III and set-IV)	73
3.6	Experimental conditions and results of textural analysis (LPD set-III and set-IV)	73
3.7	Experimental conditions and composition of residual melts (LPD set-V)	82
3.8	Experimental conditions and results of textural analysis (LPD set-V)	82
3.9	Experimental conditions, results of textural and chemical analyses (LPD set-VI)	92
3.10	Textural results of 2D and 3D image analyses	103
A.1	Experimental conditions of phase stability experiments.	138-139
A.2	Normalized chemical composition of residual glasses for phase stability experiments.	140-143
A.3	Chemical composition of plagioclase (Pl) cores for phase stability experiments [wt%].	144-145
A.4	Chemical composition of amphibole (Amph) for phase stability experiments [wt%].	146
A.5.1	Average plagioclase core compositions (HPD set-I)	147
A.5.2	Average amphibole compositions (HPD set-I)	147
A.5.3	Average clinopyroxene compositions (HPD set-I)	148
A.5.4	Average orthopyroxene compositions (HPD set-I)	148
A.6.1	Average clinopyroxene compositions (HPD set-II)	149
A.6.2	Average orthopyroxene compositions (HPD set-II)	149
A.7.1	Average plagioclase core compositions (LPD set-III and set-IV)	150
A.7.2	Average clinopyroxene compositions (LPD set-III and set-IV)	150
A.7.3	Average orthopyroxene compositions (LPD set-III and set-IV)	151
A.8.1	Average plagioclase core compositions (LPD set-V)	151
A.8.2	Average amphibole compositions (LPD set-V)	152
A.8.3	Average orthopyroxene compositions (LPD set-V)	152

7. APPENDIX A.2 – TABLES

Table A.1.1. Experimental conditions of phase stability experiments.

sample #	vessel	P [MPa]	T [°C]	run duration [days]	X ^{fl} H ₂ O	f _{O2} (correlated after O'Neill, 1987)	Amph	Pl	Cpx	Opx	Qtz	Ox	melt
DA11	CSPV	300	850	7	1.00	NNO	x	--	x	x	--	x	x
DA12	CSPV	300	850	7	0.63	NNO	--	x	x	x	--	x	x
DA44	CSPV	50	850	7	1.00	NNO	--	x	x	x	--	x	x
DA46	CSPV	50	850	7	0.45	NNO	--	x	x	x	(x)	x	x
Big_01	CSPV	50	850	7	1.00	NNO	--	x	(x)	(x)	--	x	x
Big_03+04	CSPV	200	850	7	1.00	NNO	x	--	(x)	(x)	--	x	x
DEC02+06	IHPV	300	930	4	1.00	NNO -0.95	--	--	x	x	--	x	x
DEC05+10	IHPV	300	930	4	0.84	NNO -1.75	--	--	x	x	--	x	x
UN06	CSPV	200	850	7	0.99	NNO	--	--	(x)	x	--	x	x
UN07	CSPV	200	850	7	0.87	NNO	--	x	--	x	--	x	x
UN10	CSPV	200	850	7	0.35	NNO	--	--	x	(x)	x	(x)	x
UN11	CSPV	200	800	7	0.95	NNO	x	x	(x)	(x)	--	x	x
UN16	CSPV	100	800	7	0.92	NNO	--	x	(x)	x	--	x	x
UN17	CSPV	100	800	7	0.83	NNO	--	x	(x)	x	--	x	x
UN18	CSPV	100	800	7	0.45	NNO	--	x	x	x	x	x	x
UN21	CSPV	100	800	7	0.98	NNO	(x)	x	x	x	(x)	x	x
UN22	CSPV	100	800	7	0.79	NNO	--	x	(x)	x	(x)	x	x
UN23	CSPV	100	800	7	0.65	NNO	--	x	(x)	x	x	(x)	x
UN26	CSPV	100	850	7	1.00	NNO	--	x	x	x	--	(x)	x
UN27	CSPV	100	850	7	0.79	NNO	--	x	x	(x)	--	(x)	x
UN31	CSPV	200	800	7	0.68	NNO	x	x	x	x	x	(x)	x
UN32	CSPV	200	800	7	0.56	NNO	x	x	x	x	x	(x)	x
UN33	CSPV	200	850	7	0.57	NNO	--	x	x	(x)	--	(x)	x
UN34	CSPV	200	850	7	0.55	NNO	--	x	x	(x)	x	(x)	x
UN35	CSPV	100	850	14	0.59	NNO	--	x	(x)	(x)	x	x	x
UN36	CSPV	100	850	14	0.33	NNO	--	(x)	(x)	(x)	x	x	x
UN37	CSPV	100	850	14	0.84	NNO	--	x	(x)	(x)	--	x	x
UN40	CSPV	100	825	14	0.68	NNO	--	x	(x)	(x)	x	(x)	x
UN41	CSPV	100	825	14	0.54	NNO	--	x	(x)	(x)	x	(x)	x
UN42	CSPV	100	825	14	0.38	NNO	--	x	(x)	(x)	x	(x)	x
UN44	CSPV	300	850	14	0.88	NNO	x	--	(x)	x	--	x	x
UN45	CSPV	300	850	14	0.46	NNO	--	x	(x)	(x)	x	(x)	(x)
UN47	CSPV	300	800	14	0.97	NNO	x	--	(x)	(x)	--	x	x
UN48	CSPV	300	800	14	0.82	NNO	x	x	(x)	x	--	x	x
UN51	IHPV	300	1000	5	0.99	NNO-0.50	--	--	--	--	--	--	x
UN52	IHPV	300	1000	5	0.81	NNO-1.38	--	--	x	(x)	--	x	x
UN53	IHPV	300	1000	5	0.54	NNO -0.99	--	--	x	(x)	--	x	x
UN54	IHPV	300	1000	5	0.30	NNO -1.99	--	x	(x)	x	--	(x)	x
UN55	IHPV	300	1000	5	0.49	NNO -10.26	--	x	x	(x)	--	x	x
UN56	IHPV	300	900	7	0.93	NNO -0.34	--	--	(x)	x	--	x	x
UN57	IHPV	300	900	7	0.95	NNO -0.67	--	--	(x)	x	--	x	x
UN58	IHPV	300	900	7	0.50	NNO -0.60	--	x	(x)	x	--	x	x
UN59	IHPV	300	900	7	0.20	NNO -1.71	--	(x)	x	(x)	x	x	x

x: positive mineral phase occurrence; (x): positive occurrence but no chemical analysis
 --: negative mineral phase occurrence
 CSPV: cold seal pressure vessel. IHPV: internally heated pressure vessel
 X^{fl}H₂O: mole fraction of H₂O in the fluid after the run
 NNO: Ni/NiO-buffer
 Amph=amphibole; Pl=plagioclase; Cpx=clinopyroxene; Opx=orthopyroxene; Qtz=quartz; Ox=oxide (mainly ilmenite)

Table A.1.2. Experimental conditions of phase stability experiments.

sample #	vessel	P [MPa]	T [°C]	run duration [days]	$X^{\text{fl}}\text{H}_2\text{O}$	f_{O_2} (correlated after O'Neill, 1987)	Amph	Pl	Cpx	Opx	Qtz	Ox	melt
UN60	IHPV	300	900	7	0.14	NNO -10.38	--	(x)	(x)	(x)	x	(x)	x
UN61	IHPV	200	900	8	0.80	NNO +0.60	--	--	x	x	--	x	x
UN62	IHPV	200	900	8	0.65	NNO +0.59	--	(x)	(x)	x	--	x	x
UN63	IHPV	200	900	8	0.74	NNO +0.17	--	x	x	x	--	x	x
UN64	IHPV	200	900	8	0.94	NNO -0.34	--	--	(x)	x	--	x	x
UN65	IHPV	200	900	8	1.00	NNO -9.25	--	--	(x)	(x)	--	(x)	(x)
UN66	IHPV	200	1000	6	0.78	NNO +1.08	--	--	--	--	--	(x)	x
UN67	IHPV	200	1000	6	0.95	NNO +0.68	--	--	--	--	--	--	x
UN68	IHPV	200	1000	6	0.66	NNO +0.87	--	--	--	--	--	x	x
UN70	IHPV	200	1000	6	0.35	NNO -9.02	--	--	(x)	x	--	x	x
UN71	CSPV	50	850	14	0.76	NNO	--	x	x	x	(x)	x	x
UN72	CSPV	50	850	14	0.85	NNO	--	x	(x)	x	--	x	x
UN73	CSPV	50	800	14	0.68	NNO	--	x	(x)	(x)	x	x	(x)
UN76	IHPV	100	900	8	0.67	n.d.	--	x	(x)	x	--	x	x
UN77	IHPV	100	900	8	0.28	n.d.	--	x	(x)	x	(x)	x	x
UN78	IHPV	100	900	8	0.84	n.d.	--	x	x	(x)	--	x	x
UN79	IHPV	100	900	8	1.00	n.d.	--	x	x	x	--	x	x
UN82	IHPV	300	930	6	0.47	n.d.	--	x	x	x	--	x	x
UN83	IHPV	300	930	6	0.63	n.d.	--	--	x	x	--	x	x
UN84	IHPV	200	930	7	0.95	NNO +2.63	--	--	x	(x)	--	x	x
UN85	IHPV	200	930	7	0.71	NNO +2.46	--	--	x	(x)	--	x	x
UN86	IHPV	200	930	7	0.62	NNO +2.04	--	x	x	(x)	--	x	x
UN87	IHPV	200	930	7	0.42	NNO +1.29	--	x	(x)	x	--	x	x
UN89	IHPV	100	930	10	1.0 ^(*)	NNO +1.60	--	x	(x)	x	--	x	x
UN90	IHPV	100	930	10	0.8 ^(*)	NNO +1.32	--	x	(x)	x	--	x	x
UN91	IHPV	100	930	10	0.6 ^(*)	NNO +1.42	--	x	(x)	x	--	x	x
UN92	IHPV	100	930	10	0.3 ^(*)	NNO +0.52	--	x	x	x	--	x	x
UN94	CSPV	250	850	9	1.0 ^(*)	NNO	x	--	(x)	(x)	--	x	x
UN95	CSPV	250	850	9	0.8 ^(*)	NNO	--	x	(x)	x	--	x	x
UN96	CSPV	250	850	9	0.6 ^(*)	NNO	--	x	(x)	x	--	x	x
UN98	IHPV	50	950	12	1.0 ^(*)	NNO +2.12	--	x	(x)	(x)	--	x	x
UN99	IHPV	50	950	12	0.8 ^(*)	NNO +1.48	--	x	(x)	x	--	x	x
UN100	IHPV	50	950	12	0.1 ^(*)	NNO +0.16	--	x	x	x	(x)	x	x
UN101	IHPV	50	950	12	0.3 ^(*)	NNO -0.38	--	x	(x)	(x)	--	x	x
UN102	IHPV	50	950	12	0.6 ^(*)	NNO -7.00	--	(x)	(x)	(x)	--	(x)	x
UN103	IHPV	50	930	14	1.0 ^(*)	NNO -7.11	--	x	x	(x)	--	x	x
UN104	IHPV	50	930	14	0.8 ^(*)	NNO +1.39	--	x	(x)	x	--	x	x
UN105	IHPV	50	930	14	0.6 ^(*)	NNO +0.96	--	x	(x)	x	--	x	x
UN106	IHPV	50	930	14	0.3 ^(*)	NNO -6.48	--	x	x	(x)	(x)	x	x
UN108	IHPV	50	900	14	0.1 ^(*)	NNO +1.32	--	x	(x)	x	(x)	x	x
UN109	IHPV	50	900	14	0.8 ^(*)	NNO +1.47	--	x	x	(x)	--	x	x
UN110	IHPV	50	900	14	0.6 ^(*)	NNO +1.65	--	x	x	(x)	--	x	x
UN111	IHPV	50	900	14	0.3 ^(*)	NNO +0.01	--	x	x	(x)	x	x	x
UN112	IHPV	50	900	14	1.0 ^(*)	NNO -7.05	--	(x)	x	(x)	x	x	(x)

x: positive mineral phase occurrence; (x): positive occurrence but no chemical analysis

--: negative mineral phase occurrence

CSPV: cold seal pressure vessel. IHPV: internally heated pressure vessel

$X^{\text{fl}}\text{H}_2\text{O}$: mole fraction of H_2O in the fluid after the run; (*): approx. mole fraction of H_2O in the fluid prior to the run

NNO: Ni/NiO-buffer

Amph=amphibole; Pl=plagioclase; Cpx=clinopyroxene; Opx=orthopyroxene; Qtz=quartz; Ox=oxide (mainly ilmenite)

Table A.2.1. Normalized chemical composition of residual glasses for phase stability experiments.

sample #	P [MPa]	T [°C]	X ^H H ₂ O	normalized to 100 [wt%]											NIR		MIR CO ₂ + [wt%]							
				Na ₂ O	SiO ₂	Al ₂ O ₃	CaO	K ₂ O	TiO ₂	FeO	MgO	MnO	H ₂ O+	CO ₂ +										
DA11	300	850	1.00	2.80	(0.19)	71.67	(0.36)	15.23	(0.04)	3.46	(0.18)	2.85	(0.12)	0.38	(0.06)	2.88	(0.27)	0.62	(0.10)	0.10	(0.12)	6.45	(0.32)	--
DA12	300	850	0.63	3.05	(0.03)	74.03	(0.35)	14.11	(0.28)	2.53	(0.38)	3.23	(0.15)	0.38	(0.02)	2.09	(0.12)	0.47	(0.10)	0.11	(0.03)	3.86	(0.41)	--
DA44	50	850	1.00	2.81	(0.05)	78.84	(0.12)	10.93	(0.06)	1.20	(0.05)	4.20	(0.11)	0.33	(0.07)	1.45	(0.14)	0.19	(0.04)	0.03	(0.09)	1.25	(0.20)	--
DA46	50	850	0.45	2.72	(0.40)	79.07	(0.28)	10.94	(0.04)	0.88	(0.02)	4.63	(0.06)	0.27	(0.04)	1.30	(0.12)	0.13	(0.00)	0.04	(0.08)	1.1	(0.13)	--
Big01	50	850	1.00	2.72	(0.10)	78.94	(0.23)	11.00	(0.14)	1.16	(0.08)	4.13	(0.11)	0.30	(0.03)	1.52	(0.16)	0.21	(0.06)	0.00	(0.00)	--	--	0.00
Big03+04	200	850	1.00	3.31	(0.20)	72.25	(0.41)	14.46	(0.19)	3.31	(0.24)	2.91	(0.06)	0.43	(0.04)	2.73	(0.18)	0.59	(0.05)	0.00	(0.00)	5.75	(0.29)	0.00
DEC02+06	300	930	1.00	2.91	(0.20)	70.99	(0.37)	14.26	(0.29)	3.90	(0.16)	2.75	(0.11)	0.51	(0.04)	3.39	(0.22)	1.29	(0.06)	0.00	(0.00)	6.95	(0.33)	0.00
DEC05+10	300	930	0.84	3.35	(0.58)	72.47	(0.41)	13.50	(0.24)	3.13	(0.20)	3.08	(0.16)	0.52	(0.02)	3.19	(0.31)	0.76	(0.18)	0.00	(0.00)	4.42	(0.30)	0.02
UN06	200	850	0.99	2.24	(0.83)	73.25	(0.73)	15.07	(0.26)	3.04	(0.12)	2.78	(0.28)	0.43	(0.02)	2.66	(0.29)	0.53	(0.08)	0.00	(0.00)	6.72	(0.31)	0.03
UN07	200	850	0.87	2.33	(0.79)	74.09	(0.56)	14.51	(0.37)	2.89	(0.20)	2.74	(0.28)	0.40	(0.03)	2.56	(0.14)	0.48	(0.07)	0.00	(0.00)	5.99	(0.28)	0.04
UN10	200	850	0.35	2.27	(1.18)	80.79	(9.60)	10.32	(4.91)	2.42	(1.78)	2.32	(2.11)	0.27	(0.19)	1.26	(1.05)	0.35	(0.45)	0.00	(0.00)	--	--	0.00
UN11	200	800	0.95	3.07	(0.17)	75.34	(0.26)	13.68	(0.09)	2.48	(0.23)	3.18	(0.06)	0.19	(0.05)	1.84	(0.12)	0.22	(0.00)	0.00	(0.00)	5.08	(0.25)	0.04
UN16	100	800	0.92	2.82	(0.15)	78.25	(0.29)	11.93	(0.16)	1.49	(0.03)	3.65	(0.13)	0.21	(0.03)	1.46	(0.16)	0.19	(0.05)	0.00	(0.00)	4.12	(0.28)	0.01
UN17	100	800	0.83	2.83	(0.15)	78.33	(0.41)	11.94	(0.28)	1.50	(0.03)	3.56	(0.04)	0.19	(0.02)	1.42	(0.12)	0.24	(0.05)	0.00	(0.00)	3.64	(0.28)	0.00
UN18	100	800	0.45	2.28	(0.14)	77.55	(1.61)	11.64	(0.32)	1.02	(0.32)	5.25	(0.30)	0.26	(0.11)	1.71	(0.75)	0.29	(0.27)	0.00	(0.00)	1.74	(0.28)	0.03
UN21	100	800	0.98	2.77	(0.20)	77.45	(0.55)	11.97	(0.36)	1.56	(0.12)	3.76	(0.14)	0.26	(0.08)	1.92	(0.69)	0.31	(0.17)	0.00	(0.00)	4.01	(0.26)	0.00
UN22	100	800	0.79	2.67	(0.21)	78.79	(0.17)	11.69	(0.19)	1.23	(0.08)	3.77	(0.06)	0.19	(0.01)	1.41	(0.17)	0.24	(0.11)	0.00	(0.00)	3.47	(0.24)	0.00
UN23	100	800	0.65	2.64	(0.01)	76.06	(0.01)	13.53	(0.01)	1.68	(0.01)	4.71	(0.01)	0.17	(0.01)	1.09	(0.01)	0.12	(0.01)	0.00	(0.00)	2.27	(0.24)	0.00
UN26	100	850	1.00	2.62	(0.25)	76.77	(0.21)	12.84	(0.11)	2.15	(0.18)	2.94	(0.14)	0.31	(0.02)	2.00	(0.25)	0.37	(0.04)	0.00	(0.00)	--	--	--
UN27	100	850	0.79	2.95	(0.31)	77.30	(0.35)	12.19	(0.11)	1.68	(0.08)	3.24	(0.12)	0.31	(0.01)	2.03	(0.26)	0.30	(0.04)	0.00	(0.00)	--	--	--
UN31	200	800	0.68	1.60	(1.01)	83.58	(1.23)	8.96	(5.46)	0.83	(0.26)	3.62	(2.68)	0.32	(0.33)	0.96	(0.57)	0.14	(0.10)	0.00	(0.00)	1.74	(0.21)	0.09
UN32	200	800	0.56	2.66	(0.19)	77.41	(0.05)	12.73	(0.07)	1.90	(0.09)	3.30	(0.02)	0.18	(0.01)	1.59	(0.20)	0.25	(0.02)	0.00	(0.00)	5.25	(0.26)	0.02
UN33	200	850	0.57	2.68	(0.06)	78.01	(0.20)	11.84	(0.12)	1.34	(0.08)	4.08	(0.17)	0.27	(0.05)	1.53	(0.02)	0.24	(0.08)	0.00	(0.00)	2.27	(0.24)	0.11
UN34	200	850	0.55	2.33	(0.38)	81.38	(4.30)	10.70	(2.73)	2.49	(0.28)	2.08	(1.54)	0.18	(0.03)	0.77	(0.01)	0.08	(0.11)	0.00	(0.00)	1.60	(0.20)	0.11
UN35	100	850	0.59	2.84	(0.28)	77.78	(0.80)	11.76	(0.21)	1.12	(0.25)	4.62	(0.10)	0.30	(0.05)	1.44	(0.05)	0.14	(0.00)	0.00	(0.00)	--	--	0.04
UN36	100	850	0.33	2.34	(0.12)	77.80	(0.37)	11.35	(0.10)	0.84	(0.15)	5.74	(0.23)	0.33	(0.08)	1.39	(0.09)	0.21	(0.07)	0.00	(0.00)	--	--	0.06
UN37	100	850	0.84	3.02	(0.06)	75.94	(0.16)	12.70	(0.17)	1.96	(0.09)	3.59	(0.08)	0.36	(0.02)	2.12	(0.08)	0.32	(0.04)	0.00	(0.00)	3.83	(0.25)	0.01
UN40	100	825	0.68	2.61	(0.08)	77.65	(0.56)	11.92	(0.29)	1.60	(0.16)	3.78	(0.15)	0.28	(0.01)	1.88	(0.16)	0.29	(0.14)	0.00	(0.00)	3.91	(0.25)	0.01

Note: Numbers in parentheses show the standard deviation (1σ) of replicated analyses
X^HH₂O: mole fraction of H₂O in the fluid after the run
+: errors in parentheses for FTIR derived H₂O contents are calculated by error propagation, but are likely to have relatively higher (~20%) uncertainties, e.g. due to the low sample thickness
--: not detected / not present
--: values were not (successfully) determined by FTIR spectroscopy

Table A.2.2. Normalized chemical composition of residual glasses for phase stability experiments.

sample #	P [MPa]	T [°C]	X ^H H ₂ O	Na ₂ O	SiO ₂	Al ₂ O ₃	CaO	K ₂ O	TiO ₂	FeO	MgO	MnO	MIR											
													H ₂ O+ [wt%]	CO ₂ + [wt%]										
normalized to 100 [wt%]																								
UN41	100	825	0.54	2.71	(0.28)	77.38	(1.32)	12.01	(1.00)	1.23	(0.43)	4.84	(0.27)	0.28	(0.06)	1.33	(0.18)	0.22	(0.16)	0.00	(0.00)	1.61	(0.25)	0.03
UN42	100	825	0.38	3.07	(0.70)	75.13	(3.35)	12.47	(2.18)	3.30	(1.14)	2.90	(1.45)	0.29	(0.06)	2.18	(1.24)	0.66	(0.59)	0.00	(0.00)	--	--	0.03
UN44	300	850	0.88	2.93	(0.06)	73.30	(0.24)	14.40	(0.12)	2.95	(0.10)	2.83	(0.11)	0.42	(0.04)	2.62	(0.39)	0.54	(0.04)	0.00	(0.00)	6.89	(0.33)	0.02
UN45	300	850	0.46	2.54	(0.39)	77.17	(0.18)	12.31	(0.17)	0.93	(0.01)	5.58	(0.03)	0.26	(0.01)	1.08	(0.03)	0.12	(0.06)	0.00	(0.00)	--	--	0.13
UN47	300	800	0.97	2.96	(0.26)	73.91	(0.54)	14.30	(0.12)	3.16	(0.12)	2.98	(0.10)	0.25	(0.02)	2.12	(0.20)	0.32	(0.04)	0.00	(0.00)	8.65	(0.32)	0.00
UN48	300	800	0.82	2.87	(0.25)	76.84	(0.31)	12.76	(0.18)	1.98	(0.09)	3.49	(0.11)	0.20	(0.04)	1.62	(0.23)	0.25	(0.03)	0.00	(0.00)	4.72	(0.24)	0.08
UN51	300	1000	0.99	3.25	(0.07)	70.25	(0.17)	13.99	(0.20)	4.17	(0.14)	2.72	(0.09)	0.48	(0.03)	3.61	(0.18)	1.52	(0.06)	0.00	(0.00)	6.72	(0.32)	0.03
UN52	300	1000	0.81	3.19	(0.17)	70.32	(0.37)	14.28	(0.27)	3.85	(0.23)	2.79	(0.13)	0.54	(0.03)	3.67	(0.31)	1.36	(0.11)	0.00	(0.00)	4.01	(0.29)	0.05
UN53	300	1000	0.54	3.32	(0.24)	69.95	(0.37)	14.34	(0.19)	4.05	(0.23)	2.83	(0.04)	0.51	(0.06)	3.60	(0.16)	1.35	(0.09)	0.04	(0.09)	3.97	(0.29)	0.05
UN54	300	1000	0.30	3.47	(0.10)	72.46	(0.46)	13.45	(0.22)	3.10	(0.21)	3.05	(0.10)	0.58	(0.02)	3.14	(0.22)	0.77	(0.16)	0.00	(0.00)	2.48	(0.26)	0.12
UN55	300	1000	0.49	2.88	(0.25)	75.42	(0.28)	12.07	(0.32)	1.55	(0.49)	4.92	(0.11)	0.75	(0.08)	1.91	(0.48)	0.51	(0.44)	0.00	(0.00)	--	--	0.14
UN56	300	900	0.93	3.20	(0.17)	71.33	(0.26)	14.82	(0.29)	3.42	(0.25)	2.82	(0.11)	0.50	(0.02)	3.22	(0.59)	0.69	(0.08)	0.00	(0.00)	7.61	(0.32)	0.05
UN57	300	900	0.95	3.31	(0.19)	71.64	(0.35)	14.74	(0.15)	3.44	(0.18)	2.88	(0.09)	0.48	(0.06)	2.86	(0.21)	0.65	(0.06)	0.00	(0.00)	5.68	(0.30)	0.07
UN58	300	900	0.50	3.42	(0.22)	73.88	(0.16)	13.63	(0.14)	2.62	(0.08)	3.25	(0.04)	0.39	(0.02)	2.32	(0.28)	0.48	(0.03)	0.00	(0.00)	4.03	(0.24)	0.04
UN59	300	900	0.20	2.81	(0.21)	77.05	(0.18)	12.07	(0.16)	1.43	(0.11)	4.30	(0.11)	0.31	(0.05)	1.80	(0.10)	0.23	(0.05)	0.00	(0.00)	2.00	(0.21)	0.10
UN60	300	900	0.14	3.13	(0.55)	75.54	(0.68)	13.93	(0.60)	2.84	(0.91)	3.60	(1.55)	0.30	(0.10)	0.59	(0.24)	0.08	(0.14)	0.00	(0.00)	--	--	0.13
UN61	200	900	0.80	3.15	(0.37)	70.86	(0.55)	14.78	(0.13)	3.57	(0.05)	2.88	(0.16)	0.50	(0.03)	3.34	(0.23)	0.93	(0.06)	0.00	(0.00)	6.18	(0.28)	0.00
UN62	200	900	0.65	3.19	(0.27)	71.04	(0.32)	14.78	(0.23)	3.68	(0.16)	2.88	(0.11)	0.54	(0.05)	3.12	(0.15)	0.77	(0.05)	0.00	(0.00)	5.26	(0.28)	0.00
UN63	200	900	0.74	3.46	(0.26)	71.78	(0.21)	14.12	(0.11)	3.22	(0.11)	3.09	(0.04)	0.51	(0.03)	3.12	(0.23)	0.71	(0.07)	0.00	(0.00)	3.35	(0.26)	0.03
UN64	200	900	0.94	3.08	(0.15)	74.92	(0.27)	12.93	(0.10)	2.31	(0.19)	3.46	(0.09)	0.39	(0.05)	2.46	(0.16)	0.44	(0.04)	0.00	(0.00)	--	--	0.00
UN65	200	900	1.00	2.41	(0.19)	76.30	(0.55)	12.27	(0.02)	1.04	(0.49)	6.38	(0.82)	0.58	(0.02)	1.03	(0.42)	0.00	(0.00)	0.00	(0.00)	--	--	0.00
UN67	200	1000	0.78	3.21	(0.15)	70.07	(0.62)	14.02	(0.18)	4.06	(0.08)	2.75	(0.09)	0.50	(0.03)	3.88	(0.57)	1.51	(0.10)	0.00	(0.00)	4.83	(0.31)	0.00
UN66	200	1000	0.95	3.28	(0.14)	70.45	(0.20)	14.00	(0.29)	3.85	(0.09)	2.75	(0.07)	0.56	(0.03)	3.62	(0.12)	1.50	(0.09)	0.00	(0.00)	5.65	(0.32)	0.00
UN68	200	1000	0.66	3.19	(0.16)	70.38	(0.40)	13.76	(0.26)	4.12	(0.13)	2.77	(0.11)	0.49	(0.05)	3.80	(0.29)	1.49	(0.05)	0.00	(0.00)	4.58	(0.32)	0.00
UN70	200	1000	0.35	3.17	(0.40)	76.11	(1.15)	11.83	(0.41)	1.45	(0.24)	4.32	(0.15)	0.60	(0.06)	2.21	(1.06)	0.31	(0.04)	0.00	(0.00)	--	--	0.08
UN71	50	850	0.76	2.69	(0.32)	77.22	(0.53)	12.00	(0.26)	1.70	(0.06)	3.61	(0.10)	0.46	(0.05)	2.07	(0.31)	0.25	(0.15)	0.00	(0.00)	2.05	(0.29)	0.07
UN72	50	850	0.85	2.58	(0.65)	77.89	(0.33)	11.76	(0.20)	1.47	(0.12)	3.71	(0.12)	0.44	(0.05)	1.89	(0.29)	0.25	(0.02)	0.00	(0.00)	1.71	(0.27)	0.01
UN73	50	800	0.68	2.09	(0.25)	79.19	(0.94)	11.41	(0.69)	0.73	(0.11)	5.39	(0.27)	0.20	(0.05)	0.83	(0.14)	0.15	(0.12)	0.00	(0.00)	--	--	0.01
UN76	100	900	0.67	3.21	(0.12)	73.77	(0.43)	13.60	(0.23)	2.69	(0.08)	3.07	(0.06)	0.46	(0.06)	2.65	(0.15)	0.52	(0.06)	0.03	(0.04)	4.28	(0.27)	0.04

Note: Numbers in parentheses show the standard deviation (1σ) of replicated analyses
X^HH₂O: mole fraction of H₂O in the fluid after the run
+ : errors in parentheses for FTIR derived H₂O contents are calculated by error propagation, but are likely to have relatively higher (~20%) uncertainties, e.g. due to the low sample thickness
--: not detected / not present
--: values were not (successfully) determined by FTIR spectroscopy

Table A.2.3. Normalized chemical composition of residual glasses for phase stability experiments.

sample #	P [MPa]	T [°C]	X ^H H ₂ O	normalized to 100 [wt%]													NIR		MIR					
				Na ₂ O	SiO ₂	Al ₂ O ₃	CaO	K ₂ O	TiO ₂	FeO	MgO	MnO	H ₂ O ⁺ [wt%]	CO ₂ ⁺ [wt%]										
UN7	100	900	0.28	3.17	(0.21)	74.95	(0.18)	12.98	(0.12)	2.32	(0.06)	3.26	(0.12)	0.47	(0.04)	2.42	(0.10)	0.42	(0.03)	0.02	(0.03)	2.92	(0.27)	0.03
UN78	100	900	0.84	3.06	(0.21)	76.55	(0.37)	12.21	(0.13)	1.75	(0.13)	3.55	(0.13)	0.39	(0.06)	2.15	(0.12)	0.29	(0.06)	0.03	(0.03)	2.60	(0.24)	0.04
UN79	100	900	1.00	2.99	(0.38)	77.13	(0.89)	11.87	(0.14)	1.68	(0.19)	3.59	(0.13)	0.38	(0.02)	2.05	(0.28)	0.31	(0.11)	0.00	(0.00)	--	--	0.04
UN82	300	930	0.47	3.20	(0.62)	73.87	(0.59)	13.27	(0.16)	2.56	(0.16)	3.18	(0.05)	0.56	(0.03)	2.83	(0.20)	0.52	(0.03)	0.00	(0.00)	2.39	(0.33)	0.11
UN83	300	930	0.63	2.21	(1.05)	71.59	(0.91)	14.45	(0.15)	3.87	(0.21)	2.75	(0.06)	0.51	(0.06)	3.39	(0.13)	1.22	(0.09)	0.01	(0.02)	5.89	(0.31)	0.05
UN84	200	930	0.95	2.99	(0.84)	72.11	(0.73)	14.31	(0.23)	3.72	(0.23)	2.72	(0.06)	0.47	(0.03)	2.61	(0.18)	1.04	(0.05)	0.03	(0.07)	6.01	(0.31)	0.01
UN85	200	930	0.71	2.95	(0.41)	72.08	(0.57)	14.60	(0.27)	3.60	(0.11)	2.80	(0.10)	0.48	(0.03)	2.49	(0.48)	0.97	(0.07)	0.03	(0.04)	4.67	(0.30)	0.00
UN86	200	930	0.62	3.61	(0.32)	71.91	(0.36)	14.51	(0.09)	3.30	(0.14)	2.79	(0.14)	0.45	(0.03)	2.37	(0.10)	1.02	(0.13)	0.03	(0.03)	4.45	(0.28)	0.01
UN87	200	930	0.42	2.51	(0.38)	77.05	(0.55)	12.41	(0.16)	1.96	(0.12)	3.41	(0.22)	0.43	(0.02)	1.82	(0.10)	0.38	(0.11)	0.02	(0.03)	2.21	(0.23)	0.05
UN89	100	930	1.0 ^(*)	3.02	(0.59)	71.12	(0.46)	14.46	(0.22)	3.55	(0.15)	2.87	(0.10)	0.51	(0.02)	3.51	(0.19)	0.95	(0.08)	0.00	(0.01)	4.01	(0.29)	0.00
UN90	100	930	0.8 ^(*)	2.85	(0.75)	72.89	(0.60)	13.81	(0.16)	3.09	(0.18)	2.90	(0.05)	0.51	(0.05)	3.18	(0.31)	0.71	(0.07)	0.05	(0.05)	3.98	(0.29)	0.00
UN91	100	930	0.6 ^(*)	2.15	(0.55)	73.99	(0.47)	13.42	(0.09)	2.90	(0.17)	3.10	(0.09)	0.52	(0.03)	3.23	(0.22)	0.66	(0.07)	0.03	(0.06)	3.39	(0.29)	0.00
UN92	100	930	0.3 ^(*)	2.92	(0.72)	75.75	(0.58)	12.51	(0.18)	2.05	(0.08)	3.39	(0.15)	0.50	(0.03)	2.43	(0.36)	0.40	(0.06)	0.04	(0.04)	2.40	(0.25)	0.01
UN94	250	850	1.0 ^(*)	3.20	(0.16)	71.95	(0.34)	14.71	(0.25)	3.60	(0.21)	2.88	(0.15)	0.34	(0.04)	2.79	(0.20)	0.53	(0.05)	0.00	(0.00)	6.96	(0.35)	0.00
UN95	250	850	0.8 ^(*)	3.09	(0.31)	74.03	(0.56)	13.89	(0.17)	2.75	(0.13)	3.11	(0.10)	0.31	(0.03)	2.40	(0.23)	0.42	(0.05)	0.00	(0.00)	5.71	(0.31)	0.02
UN96	250	850	0.6 ^(*)	3.09	(0.08)	74.40	(0.27)	13.72	(0.35)	2.51	(0.21)	3.31	(0.14)	0.35	(0.02)	2.26	(0.28)	0.35	(0.05)	0.00	(0.00)	4.97	(0.30)	0.03
UN98	50	950	1.0 ^(*)	3.14	(0.15)	73.23	(0.59)	13.14	(0.29)	2.89	(0.13)	3.20	(0.06)	0.54	(0.04)	3.08	(0.25)	0.78	(0.08)	0.00	(0.00)	2.86	(0.30)	0.01
UN99	50	950	0.8 ^(*)	3.19	(0.25)	74.69	(0.23)	12.69	(0.26)	2.26	(0.12)	3.29	(0.15)	0.57	(0.03)	2.72	(0.20)	0.60	(0.09)	0.00	(0.00)	--	--	0.02
UN100	50	950	0.1 ^(*)	3.27	(0.29)	73.92	(0.24)	12.78	(0.09)	2.50	(0.05)	3.31	(0.13)	0.52	(0.05)	3.05	(0.26)	0.64	(0.04)	0.00	(0.00)	2.14	(0.26)	0.04
UN101	50	950	0.3 ^(*)	3.15	(0.27)	76.07	(0.44)	11.81	(0.20)	1.81	(0.13)	3.66	(0.06)	0.61	(0.06)	2.48	(0.25)	0.41	(0.04)	0.00	(0.00)	--	--	0.04
UN102	50	950	0.6 ^(*)	2.45	(0.07)	78.24	(0.30)	10.93	(0.32)	0.88	(0.06)	5.06	(0.06)	0.61	(0.08)	1.65	(0.15)	0.18	(0.03)	0.00	(0.00)	--	--	0.04
UN103	50	930	1.0 ^(*)	3.12	(0.14)	77.79	(0.18)	11.64	(0.22)	1.52	(0.09)	3.60	(0.14)	0.49	(0.06)	1.41	(0.09)	0.43	(0.09)	0.00	(0.00)	2.11	(0.22)	0.00
UN104	50	930	0.8 ^(*)	3.00	(0.19)	77.52	(0.39)	11.83	(0.08)	1.58	(0.15)	3.59	(0.07)	0.50	(0.05)	1.42	(0.17)	0.51	(0.05)	0.04	(0.08)	2.15	(0.22)	0.00
UN105	50	930	0.6 ^(*)	2.59	(0.23)	80.93	(0.28)	10.04	(0.30)	0.53	(0.05)	4.18	(0.09)	0.47	(0.05)	1.12	(0.10)	0.14	(0.06)	0.00	(0.00)	1.97	(0.20)	0.00
UN106	50	930	0.3 ^(*)	2.89	(0.28)	79.22	(0.20)	10.86	(0.21)	1.09	(0.08)	3.89	(0.09)	0.51	(0.07)	1.19	(0.08)	0.34	(0.02)	0.00	(0.00)	--	--	0.00
UN108	50	900	0.1 ^(*)	3.14	(0.24)	76.25	(0.66)	12.04	(0.19)	1.68	(0.06)	3.78	(0.07)	0.48	(0.07)	2.24	(0.67)	0.39	(0.03)	0.00	(0.00)	2.44	(0.25)	0.00
UN109	50	900	0.8 ^(*)	2.97	(0.19)	77.58	(0.33)	11.73	(0.11)	1.48	(0.10)	3.79	(0.09)	0.43	(0.03)	1.70	(0.24)	0.33	(0.03)	0.00	(0.00)	2.28	(0.24)	0.00

Note: Numbers in parentheses show the standard deviation (1σ) of replicated analyses

X^HH₂O: mole fraction of H₂O in the fluid after the run: (*): approx. mole fraction of H₂O in the fluid prior to the experimental run

+: errors in parentheses for FTIR derived H₂O contents are calculated by error propagation, but are likely to have relatively higher (~20%) uncertainties, e.g. due to the low sample thickness

--: not detected / not present

---: values were not (successfully) determined by FTIR spectroscopy

Table A.2.4. Normalized chemical composition of residual glasses for phase stability experiments.

sample #	P [MPa]	T [°C]	$X^H H_2O$	normalized to 100 [wt%]											NIR		MIR
				Na ₂ O	SiO ₂	Al ₂ O ₃	CaO	K ₂ O	TiO ₂	FeO	MgO	MnO	H ₂ O ⁺ [wt%]	CO ₂ ⁺ [wt%]			
UN110	50	900	0.6 ^(*)	2.95 (0.21)	77.80 (0.49)	11.57 (0.15)	1.36 (0.11)	3.82 (0.11)	0.46 (0.03)	1.76 (0.20)	0.28 (0.04)	0.00 (0.00)	0.00 (0.00)	0.00 (0.00)	--	--	0.01
UN111	50	900	0.3 ^(*)	2.65 (0.20)	79.01 (0.51)	10.82 (0.18)	1.07 (0.07)	4.12 (0.10)	0.39 (0.04)	1.71 (0.28)	0.23 (0.16)	0.00 (0.00)	0.00 (0.00)	0.00 (0.00)	--	--	0.01
UN112	50	900	1.0 ^(*)	2.30 (0.15)	76.77 (0.80)	11.95 (0.12)	0.60 (0.11)	6.61 (0.09)	0.46 (0.04)	1.16 (0.40)	0.15 (0.05)	0.00 (0.00)	0.00 (0.00)	0.00 (0.00)	--	--	0.01

Note: Numbers in parentheses show the standard deviation (1σ) of replicated analyses

$X^H H_2O$: mole fraction of H_2O in the fluid after the run; (): approx. mole fraction of H_2O in the fluid prior to the experimental run*

+ : errors in parentheses for FTIR derived H_2O contents are calculated by error propagation, but are likely to have relatively higher (~20%) uncertainties, e.g. due to the low sample thickness

--: not detected / not present

---: values were not (successfully) determined by FTIR spectroscopy

Table A.3.1. Chemical composition of plagioclase (Pl) cores for phase stability experiments [wt%].

Sample #	P [MPa]	T [°C]	X ^H H ₂ O	chemical composition of plagioclase (Pl) cores [wt%]													total	An [mol%]	Ab [mol%]	Or [mol%]	N
				Na ₂ O	SiO ₂	Al ₂ O ₃	CaO	K ₂ O	TiO ₂	FeO	MgO	MnO	total	An	Ab	Or					
UN07	200	850	5.10 (0.09)	56.86 (1.00)	25.88 (1.11)	10.47 (0.37)	0.51 (0.08)	0.19 (0.09)	1.19 (0.30)	0.29 (0.21)	0.00 (0.00)	100.50	52	45	3	3					
UN10	200	850	3.94 (0.18)	63.17 (1.19)	16.90 (0.69)	6.47 (0.30)	2.19 (0.10)	0.46 (0.19)	4.46 (0.54)	2.05 (0.02)	0.00 (0.00)	99.64	40	44	16	3					
UN11	200	800	4.53 (0.58)	56.52 (2.35)	26.47 (2.32)	10.64 (1.23)	0.52 (0.29)	0.20 (0.28)	1.07 (0.80)	0.14 (0.18)	0.00 (0.00)	100.07	55	42	3	3					
UN16	100	800	4.89 (0.20)	58.64 (0.44)	24.32 (0.51)	8.78 (0.35)	0.77 (0.04)	0.13 (0.01)	1.53 (0.46)	0.33 (0.23)	0.00 (0.00)	99.39	47	48	5	3					
UN17	100	800	5.02 (0.15)	56.10 (1.46)	25.38 (0.44)	10.37 (0.83)	0.47 (0.14)	0.10 (0.03)	1.49 (0.23)	0.64 (0.39)	0.00 (0.00)	99.57	52	45	3	3					
UN18	100	800	3.36 (n.d.)	74.51 (n.d.)	13.19 (n.d.)	4.04 (n.d.)	1.05 (n.d.)	0.16 (n.d.)	0.64 (n.d.)	0.11 (n.d.)	0.00 (n.d.)	97.07	36	53	11	1					
UN21	100	800	4.47 (0.78)	59.82 (3.73)	23.62 (1.39)	8.42 (1.15)	0.86 (0.37)	0.13 (0.01)	1.81 (0.54)	0.48 (0.34)	0.00 (0.00)	99.62	48	46	6	3					
UN22	100	800	4.94 (0.31)	59.74 (2.90)	23.25 (1.78)	8.46 (1.19)	0.85 (0.35)	0.14 (0.06)	1.70 (0.14)	0.56 (0.18)	0.00 (0.00)	99.64	46	49	6	4					
UN23	100	800	5.22 (n.d.)	59.04 (n.d.)	24.24 (n.d.)	8.74 (n.d.)	0.69 (n.d.)	0.10 (n.d.)	1.69 (n.d.)	0.71 (n.d.)	0.00 (n.d.)	100.44	46	50	4	1					
UN26	100	850	4.78 (0.04)	55.36 (1.32)	26.39 (1.03)	10.81 (0.45)	0.40 (0.13)	0.11 (0.05)	1.47 (0.48)	0.28 (0.15)	0.00 (0.00)	99.61	54	43	2	3					
UN27	100	850	4.33 (0.27)	58.08 (2.04)	23.31 (1.22)	9.08 (0.76)	0.85 (0.28)	0.13 (0.02)	1.76 (0.20)	0.56 (0.25)	0.00 (0.00)	98.10	51	44	6	3					
UN31	200	800	4.90 (n.d.)	63.70 (n.d.)	21.20 (n.d.)	5.90 (n.d.)	2.06 (n.d.)	0.15 (n.d.)	0.94 (n.d.)	0.21 (n.d.)	0.00 (n.d.)	99.06	34	51	14	1					
UN32	200	800	4.74 (0.89)	59.02 (4.25)	24.10 (2.31)	8.98 (1.36)	0.69 (0.43)	0.22 (0.27)	1.09 (0.21)	0.27 (0.23)	0.00 (0.00)	99.12	49	46	5	3					
UN33	200	850	4.91 (0.28)	61.99 (2.62)	23.06 (1.86)	7.99 (0.97)	0.94 (0.21)	0.23 (0.24)	1.11 (0.25)	0.23 (0.07)	0.00 (0.00)	100.46	44	49	6	4					
UN34	200	850	4.91 (n.d.)	62.47 (n.d.)	19.37 (n.d.)	5.91 (n.d.)	1.96 (n.d.)	0.57 (n.d.)	2.52 (n.d.)	0.97 (n.d.)	0.00 (n.d.)	98.68	35	52	14	1					
UN35	100	850	4.10 (0.24)	65.23 (1.46)	18.82 (0.63)	5.30 (0.51)	2.19 (0.24)	0.57 (0.60)	1.83 (0.36)	0.40 (0.02)	0.00 (0.00)	98.44	35	48	17	3					
UN36	100	850	4.76 (0.60)	64.16 (0.44)	20.04 (1.92)	6.15 (0.21)	2.01 (0.14)	0.14 (0.06)	1.81 (1.61)	0.79 (0.87)	0.00 (0.00)	99.86	36	50	14	3					
UN37	100	850	4.39 (0.15)	55.92 (2.68)	25.81 (1.72)	10.52 (1.16)	0.55 (0.27)	0.09 (0.05)	1.49 (0.21)	0.33 (0.13)	0.00 (0.00)	99.10	55	42	3	3					
UN40	100	825	4.42 (0.67)	59.14 (2.84)	23.06 (1.52)	8.93 (1.15)	0.90 (0.42)	0.20 (0.19)	1.46 (0.34)	0.65 (0.13)	0.00 (0.00)	98.76	50	44	6	3					
UN41	100	825	5.27 (0.23)	61.53 (1.87)	22.54 (1.66)	7.43 (1.08)	1.21 (0.45)	0.45 (0.59)	1.09 (0.44)	0.25 (0.17)	0.00 (0.00)	99.78	40	52	8	3					
UN42	100	825	3.65 (0.68)	65.65 (4.66)	16.00 (0.16)	5.47 (2.01)	2.60 (0.96)	0.21 (0.04)	4.00 (1.70)	1.90 (1.02)	0.00 (0.00)	99.48	35	43	21	2					
UN45	300	850	4.01 (0.74)	67.90 (6.48)	17.03 (2.64)	4.70 (0.51)	2.09 (0.27)	0.44 (0.23)	2.15 (1.60)	0.71 (0.50)	0.00 (0.00)	99.02	33	50	17	2					
UN48	300	800	5.42 (0.59)	57.63 (1.94)	24.77 (1.60)	8.96 (0.85)	0.62 (0.24)	0.18 (0.18)	1.51 (0.51)	0.27 (0.27)	0.00 (0.00)	99.36	46	50	4	9					
UN51	300	1000	5.03 (0.48)	58.95 (0.84)	23.34 (2.56)	8.58 (0.79)	0.96 (0.17)	0.11 (0.04)	1.83 (1.84)	0.78 (1.02)	0.00 (0.00)	99.58	46	48	6	4					
UN54	300	1000	4.20 (0.35)	57.01 (2.81)	24.93 (1.97)	10.32 (1.19)	0.80 (0.42)	0.15 (0.08)	1.14 (0.32)	0.53 (0.35)	0.00 (0.00)	99.08	55	40	5	4					
UN55	300	1000	4.84 (0.23)	63.52 (1.02)	21.88 (1.05)	6.85 (0.44)	1.93 (0.20)	0.23 (0.03)	0.94 (0.18)	0.16 (0.02)	0.00 (0.00)	100.36	38	49	13	3					
UN58	300	900	4.67 (0.20)	56.82 (2.16)	25.54 (1.43)	10.14 (1.13)	0.65 (0.24)	0.11 (0.05)	0.93 (0.31)	0.18 (0.08)	0.00 (0.00)	99.05	52	44	4	5					

N: number of analyses

Note: Numbers in parentheses show the standard deviation (1σ) of replicated analyses

n.d.: not detected/not determined

Table A.3.2. Chemical composition of plagioclase (Pl) cores for phase stability experiments [wt%].

Sample #	P [MPa]	T [°C]	chemical composition of plagioclase (Pl) cores [wt%]														total	An [mol%]	Ab [mol%]	Or [mol%]	N
			X ^H H ₂ O	Na ₂ O	SiO ₂	Al ₂ O ₃	CaO	K ₂ O	TiO ₂	FeO	MgO	MnO									
UN63	200	900	3.46 (0.65)	54.15 (2.67)	27.04 (2.04)	12.37 (1.07)	0.56 (0.37)	0.12 (0.08)	1.30 (0.57)	0.45 (0.56)	0.00 (0.00)	99.45	64	32	4	4					
UN71	50	850	4.00 (0.27)	62.40 (3.09)	20.59 (1.50)	7.30 (1.00)	1.41 (0.42)	0.20 (0.05)	1.87 (1.87)	0.67 (1.28)	0.00 (0.00)	98.43	45	45	10	6					
UN72	50	850	4.59 (0.42)	56.01 (2.05)	25.60 (2.71)	10.46 (1.08)	0.51 (0.24)	0.09 (0.05)	1.61 (1.88)	0.68 (1.28)	0.00 (0.00)	99.54	54	43	3	5					
UN73	50	800	3.88 (0.19)	64.21 (0.86)	16.98 (0.18)	5.64 (0.41)	2.43 (0.16)	0.23 (0.04)	3.19 (0.12)	1.41 (0.09)	0.00 (0.00)	97.97	36	45	19	2					
UN77	100	900	4.53 (0.33)	54.63 (1.07)	26.85 (0.46)	11.22 (0.11)	0.43 (0.14)	0.12 (0.05)	1.62 (0.46)	0.19 (0.06)	0.00 (0.00)	99.60	56	41	3	4					
UN78	100	900	4.55 (0.28)	56.54 (2.53)	25.02 (1.32)	10.29 (1.06)	0.64 (0.39)	0.14 (0.07)	1.85 (0.56)	0.64 (0.51)	0.00 (0.00)	99.67	53	43	4	4					
UN79	100	900	4.53 (0.16)	58.92 (1.88)	22.94 (1.34)	9.08 (0.90)	0.93 (0.27)	0.14 (0.05)	1.79 (0.81)	0.68 (0.63)	0.00 (0.00)	99.01	49	45	6	5					
UN82	300	930	4.27 (0.49)	58.76 (4.12)	23.41 (2.74)	8.93 (1.78)	0.99 (0.56)	0.19 (0.11)	1.34 (0.26)	0.36 (0.22)	0.00 (0.00)	98.25	50	43	7	5					
UN86	200	930	3.57 (0.29)	51.78 (0.66)	29.63 (0.69)	13.63 (0.57)	0.25 (0.04)	0.05 (0.04)	1.03 (0.32)	0.08 (0.02)	0.00 (0.00)	100.01	67	32	1	4					
UN87	200	930	4.53 (0.23)	59.41 (1.83)	23.05 (1.13)	8.56 (0.78)	1.02 (0.23)	0.18 (0.04)	1.47 (0.14)	0.24 (0.13)	0.00 (0.00)	98.45	48	46	7	5					
UN89	100	930	2.50 (0.12)	50.37 (1.28)	30.08 (1.37)	15.01 (0.64)	0.30 (0.12)	0.06 (0.03)	0.94 (0.18)	0.24 (0.33)	0.00 (0.00)	99.50	75	23	2	5					
UN90	100	930	3.41 (0.46)	53.06 (2.72)	27.79 (1.81)	12.78 (1.22)	0.36 (0.25)	0.10 (0.04)	1.42 (0.48)	0.33 (0.23)	0.00 (0.00)	99.26	66	32	2	4					
UN91	100	930	3.67 (0.33)	55.19 (2.14)	26.66 (1.35)	11.68 (0.96)	0.59 (0.28)	0.11 (0.03)	1.21 (0.22)	0.17 (0.05)	0.00 (0.00)	99.28	61	35	4	5					
UN92	100	930	4.40 (0.31)	57.55 (1.87)	23.82 (3.02)	10.24 (0.60)	0.76 (0.26)	0.17 (0.10)	2.05 (0.87)	0.77 (0.83)	0.00 (0.00)	99.77	54	42	5	3					
UN95	250	850	4.49 (0.11)	55.13 (0.51)	27.46 (0.68)	11.26 (0.43)	0.38 (0.05)	0.08 (0.07)	1.25 (0.83)	0.15 (0.14)	0.00 (0.00)	100.20	57	41	2	5					
UN96	250	850	4.37 (0.30)	56.13 (1.45)	26.81 (1.27)	10.90 (0.64)	0.48 (0.18)	0.12 (0.07)	1.12 (0.60)	0.19 (0.26)	0.00 (0.00)	100.12	56	41	3	6					
UN98	50	950	3.59 (0.25)	56.15 (2.43)	26.03 (1.68)	11.11 (1.22)	0.74 (0.32)	0.11 (0.04)	1.27 (0.32)	0.25 (0.10)	0.00 (0.00)	99.25	60	35	5	6					
UN99	50	950	4.12 (0.11)	55.43 (1.39)	26.92 (0.64)	11.53 (0.62)	0.47 (0.15)	0.10 (0.03)	1.55 (0.60)	0.23 (0.13)	0.00 (0.00)	100.35	59	38	3	5					
UN101	50	950	4.31 (0.19)	55.74 (1.44)	25.71 (1.62)	10.61 (0.77)	0.47 (0.27)	0.08 (0.04)	1.73 (1.36)	0.94 (1.40)	0.00 (0.00)	99.59	56	41	3	3					
UN100	50	950	3.87 (0.05)	57.99 (0.89)	24.18 (0.38)	9.72 (0.39)	0.93 (0.09)	0.19 (0.02)	1.68 (0.31)	0.28 (0.06)	0.00 (0.00)	98.84	55	39	6	3					
UN103	50	930	4.49 (0.12)	56.22 (1.59)	25.93 (1.30)	10.41 (0.73)	0.65 (0.23)	0.14 (0.06)	1.83 (0.62)	0.28 (0.32)	0.00 (0.00)	99.96	54	42	4	4					
UN104	50	930	4.39 (0.35)	55.89 (1.57)	27.00 (1.08)	11.16 (0.59)	0.51 (0.23)	0.06 (0.05)	0.84 (0.09)	0.14 (0.11)	0.00 (0.00)	99.98	57	40	3	5					
UN105	50	930	4.09 (0.26)	59.26 (2.99)	24.07 (2.03)	9.29 (1.43)	1.00 (0.44)	0.14 (0.07)	1.08 (0.14)	0.19 (0.06)	0.00 (0.00)	99.13	52	41	7	6					
UN106	50	930	4.64 (0.21)	58.70 (0.50)	24.65 (2.11)	9.78 (0.20)	0.72 (0.12)	0.10 (0.07)	1.14 (0.61)	0.79 (1.39)	0.02 (0.04)	100.54	51	44	5	4					
UN108	50	900	4.00 (0.13)	61.03 (0.62)	21.86 (0.61)	7.96 (0.35)	1.30 (0.09)	0.19 (0.04)	1.44 (0.43)	0.31 (0.22)	0.00 (0.00)	98.09	48	43	9	4					
UN109	50	900	4.11 (0.66)	60.58 (5.00)	22.40 (2.59)	8.68 (2.11)	1.13 (0.66)	0.19 (0.09)	1.70 (0.63)	0.60 (0.53)	0.00 (0.00)	99.39	49	42	8	5					
UN110	50	900	4.27 (0.25)	58.95 (2.26)	23.94 (1.70)	9.33 (1.05)	0.88 (0.31)	0.14 (0.07)	1.39 (0.73)	0.50 (0.45)	0.00 (0.00)	99.40	51	43	6	5					
UN111	50	900	4.54 (0.32)	61.95 (1.41)	22.06 (1.62)	7.93 (0.57)	1.28 (0.25)	0.18 (0.08)	1.26 (0.55)	0.34 (0.30)	0.00 (0.00)	99.54	45	46	9	3					
Big01	50	850	5.03 (0.34)	60.24 (1.24)	22.39 (1.08)	8.19 (0.32)	1.07 (0.20)	0.19 (0.04)	1.95 (0.34)	0.50 (0.14)	0.00 (0.00)	99.56	44	49	7	4					

N: number of analyses

Note: Numbers in parentheses show the standard deviation (1σ) of replicated analyses

n.d.: not detected/not determined

Table A.4. Chemical composition of amphibole (Amph) for phase stability experiments [wt%].

sample #	P [MPa]	T [°C]	X ^H H ₂ O	chemical composition of amphiboles (Amph) [wt%]											total	Mg#	N
				Na ₂ O	SiO ₂	Al ₂ O ₃	CaO	K ₂ O	TiO ₂	FeO	MgO	MnO					
UN11	200	800	0.9	1.25 (0.15)	46.44 (1.12)	9.04 (0.84)	10.74 (0.52)	0.38 (0.06)	1.39 (0.13)	14.09 (1.72)	14.14 (1.06)	0.00 (0.00)	97.47	0.66	5		
UN31	200	800	0.7	n.d.	n.d.	n.d.	n.d.	n.d.	n.d.	n.d.	n.d.	n.d.	n.d.	n.d.	n.d.		
UN32	200	800	0.6	1.40 (n.d.)	47.26 (n.d.)	7.84 (n.d.)	9.08 (n.d.)	0.35 (n.d.)	1.37 (n.d.)	16.83 (n.d.)	13.08 (n.d.)	0.00 (n.d.)	97.21	0.60	1		
UN44	300	850	0.9	1.14 (0.05)	45.59 (0.57)	7.25 (0.55)	10.47 (0.22)	0.29 (0.04)	1.75 (0.13)	12.74 (0.40)	11.19 (0.43)	0.00 (0.00)	90.42	0.64	5		
UN47	300	800	1.0	1.39 (0.17)	45.75 (1.63)	8.78 (0.73)	11.43 (1.08)	0.40 (0.07)	1.36 (0.60)	13.93 (2.57)	14.43 (1.45)	0.00 (0.00)	97.47	0.67	14		
UN48	300	800	0.8	n.d.	n.d.	n.d.	n.d.	n.d.	n.d.	n.d.	n.d.	n.d.	n.d.	n.d.	n.d.		
UN94	250	850	1.0	1.44 (0.09)	46.27 (0.81)	8.53 (0.82)	10.66 (0.47)	0.40 (0.04)	1.87 (0.09)	14.20 (1.17)	13.49 (0.43)	0.00 (0.00)	96.87	0.66	7		
DA11	300	850	1.0	1.38 (0.07)	45.92 (0.31)	8.32 (0.22)	10.88 (0.49)	0.38 (0.03)	1.83 (0.16)	12.39 (0.22)	14.19 (0.28)	0.35 (0.03)	95.64	0.73	4		
Big03+04	200	850	1.0	1.40 (0.18)	46.00 (0.80)	8.24 (0.85)	11.43 (1.54)	0.37 (0.05)	2.02 (0.19)	14.36 (0.83)	12.69 (0.64)	0.00 (0.00)	96.50	0.64	5		

N: number of analyses
Note: Numbers in parentheses show the standard deviation (1σ) of replicated analyses
n.d.: not detected/not determined

Table A.5.1. Average plagioclase core compositions (numbers in parentheses show the standard deviation 1σ from replicate measurements).

sample	X H ₂ O	Decompression rate [MPa/s]	chemical composition of plagioclase (Pl) cores [wt%]													
			SiO ₂	TiO ₂	Al ₂ O ₃	FeO	MnO	MgO	CaO	Na ₂ O	K ₂ O	Total	An	Ab	Or	N
DA54*	1	0.0005	56.77 (0.83)	0.03 (0.01)	26.86 (0.67)	0.53 (0.07)	0.00 (0.04)	0.05 (0.02)	10.21 (0.43)	5.44 (0.24)	0.34 (0.04)	100.23	49.9	48.1	2.0	6
DA28**	1	0.0002	55.91 (4.56)	0.04 (0.05)	27.11 (2.72)	0.55 (0.22)	0.01 (0.04)	0.06 (0.06)	10.60 (1.82)	4.71 (0.85)	0.31 (0.20)	99.31	54.2	43.4	2.4	42
DA44	1	isobaric at 50 MPa	62.31 (1.78)	0.23 (0.15)	20.24 (1.26)	1.63 (0.21)	0.00 (0.02)	0.66 (0.23)	7.32 (0.74)	4.26 (0.47)	1.49 (0.33)	98.31	43.5	45.8	10.7	3
DA12	0.6	isobaric at 300 MPa	54.13 (2.62)	0.05 (0.02)	28.10 (1.80)	0.47 (0.11)	0.00 (0.02)	0.05 (0.04)	11.43 (1.01)	4.24 (0.35)	0.37 (0.34)	98.85	58.4	39.2	2.4	5
DA20	0.6	20	55.70 (1.46)	0.07 (0.06)	26.36 (1.30)	0.98 (0.47)	0.01 (0.02)	0.20 (0.23)	10.50 (1.12)	4.82 (0.36)	0.40 (0.09)	99.02	53.3	44.3	2.4	4
DA23	0.6	1	55.19 (2.13)	0.06 (0.05)	26.97 (1.46)	0.68 (0.26)	0.00 (0.02)	0.11 (0.06)	11.06 (1.15)	4.58 (0.39)	0.45 (0.24)	99.11	55.5	41.7	2.7	9
DA14*	0.6	0.1	54.54 (2.80)	0.10 (0.03)	27.93 (1.75)	0.70 (0.06)	0.00 (0.02)	0.14 (0.04)	11.77 (1.37)	4.33 (0.10)	0.35 (0.25)	99.86	58.8	39.1	2.1	10
DA65*	0.6	0.01	54.62 (2.38)	0.07 (0.03)	28.07 (1.65)	0.60 (0.21)	0.01 (0.02)	0.07 (0.05)	11.82 (1.33)	4.24 (0.43)	0.44 (0.23)	99.93	59.0	38.4	2.6	10
DA51	0.6	0.001	54.84 (1.30)	0.10 (0.07)	27.99 (1.15)	0.79 (0.53)	0.01 (0.03)	0.16 (0.20)	11.85 (0.85)	4.63 (0.42)	0.33 (0.05)	100.70	57.5	40.6	1.9	8
DA29	0.6	0.0002	54.07 (2.05)	0.04 (0.02)	28.11 (1.34)	0.54 (0.13)	0.00 (0.04)	0.07 (0.05)	11.58 (0.96)	4.26 (0.37)	0.35 (0.17)	99.01	58.7	39.1	2.2	20
DA46	0.6	isobaric at 50 MPa	64.87 (2.95)	0.51 (0.33)	18.77 (0.93)	2.54 (1.54)	0.00 (0.04)	0.80 (0.79)	6.15 (0.59)	3.35 (0.75)	1.51 (0.35)	98.51	44.2	43.8	13.0	9

N: number of analyses

*: the experiment was duplicated at the same condition, analyses of water content and glass are average values

***: 3 experiments were conducted at the same condition. In all experiments large Pl microclitics were observed. The glass analysis was determined for 1 experiment

Table A.5.2. Average amphibole compositions (numbers in parentheses show the standard deviation 1σ from replicate measurements).

sample	X H ₂ O	Decompression rate [MPa/s]	chemical composition of amphiboles (Amph) [wt%]													
			SiO ₂	TiO ₂	Al ₂ O ₃	FeO	MnO	MgO	CaO	Na ₂ O	K ₂ O	Total	Mg#	N		
DA11	1	isobaric at 300 MPa	45.92 (0.31)	1.83 (0.16)	8.32 (0.22)	12.39 (0.22)	0.35 (0.03)	14.19 (0.28)	10.88 (0.49)	1.38 (0.07)	0.38 (0.03)	95.64	0.73	4		
DA19	1	20	46.12 (0.72)	1.64 (0.16)	6.78 (0.53)	12.42 (0.27)	0.00 (0.05)	12.04 (0.85)	10.48 (0.40)	1.04 (0.09)	0.33 (0.02)	90.85	0.64	3		
DA13*	1	0.1	45.87 (0.36)	1.93 (0.11)	8.38 (0.11)	13.02 (0.32)	0.34 (0.09)	14.07 (0.39)	10.36 (0.22)	1.39 (0.10)	0.38 (0.04)	95.74	0.70	4		
DA64*	1	0.01	46.20 (1.00)	1.79 (0.13)	6.92 (0.76)	13.31 (0.21)	0.00 (0.05)	11.98 (0.22)	10.47 (0.32)	1.20 (0.11)	0.34 (0.04)	92.19	0.63	8		
DA54*	1	0.0005	45.83 (0.00)	1.73 (0.00)	7.08 (0.00)	11.91 (0.00)	0.02 (0.00)	11.20 (0.00)	10.71 (0.00)	1.16 (0.00)	0.31 (0.00)	89.95	0.63	1		
DA28**	1	0.0002	44.74 (0.81)	1.76 (0.14)	7.75 (0.81)	12.65 (0.31)	0.01 (0.05)	10.41 (0.69)	10.69 (0.24)	1.20 (0.10)	0.33 (0.03)	89.54	0.59	22		
DA65*	0.6	0.01	45.90 (0.21)	1.77 (0.05)	7.67 (0.10)	13.23 (0.15)	0.02 (0.03)	11.39 (0.13)	10.55 (0.22)	1.19 (0.04)	0.37 (0.02)	92.08	0.61	1		

N: number of analyses

*: the experiment was duplicated at the same condition, analyses of water content and glass are average values

***: 3 experiments were conducted at the same condition. In all experiments large Pl microclitics were observed. The glass analysis was determined for 1 experiment

Table A.5.3. Average clinopyroxene compositions (numbers in parentheses show the standard deviation 1σ from replicate measurements).

sample	X H ₂ O [MPa/s]	Decompression rate	chemical composition of clinopyroxene (Cpx) [wt%]													Total	Mg#	N
			SiO ₂	TiO ₂	Al ₂ O ₃	FeO	MnO	MgO	CaO	Na ₂ O	K ₂ O	Na ₂ O	K ₂ O	Total				
DA22	1	1	55.70 (5.94)	0.68 (0.42)	6.89 (2.19)	9.73 (2.40)	0.01 (0.06)	8.66 (2.19)	16.23 (4.23)	0.76 (0.30)	0.83 (0.68)	98.49	0.61	6				
DA13*	1	0.1	52.15 (4.17)	0.79 (0.05)	5.59 (2.24)	11.26 (1.41)	0.05 (0.02)	11.19 (2.42)	17.53 (3.49)	0.64 (0.31)	0.40 (0.47)	99.62	0.65	6				
DA64*	1	0.01	54.01 (2.29)	0.39 (0.03)	3.57 (1.64)	10.45 (0.61)	0.00 (0.06)	11.36 (1.52)	18.38 (2.28)	0.44 (0.12)	0.37 (0.29)	98.96	0.66	8				
DA28**	1	0.0002	50.03 (1.19)	0.65 (0.36)	3.74 (0.58)	11.13 (1.98)	0.00 (0.02)	11.99 (1.16)	20.22 (0.51)	0.43 (0.27)	0.08 (0.02)	98.28	0.67	5				
DA44	1	isobaric at 50 MPa	55.10 (1.85)	0.48 (0.29)	3.27 (0.80)	22.29 (2.71)	0.00 (0.07)	13.06 (1.04)	6.92 (2.68)	0.58 (0.15)	0.52 (0.25)	102.21	0.51	4				
DA12	0.6	isobaric at 300 MPa	55.41 (5.57)	0.56 (0.24)	6.50 (3.61)	12.55 (6.32)	0.55 (0.18)	9.66 (5.12)	11.60 (5.82)	0.54 (0.33)	0.75 (0.62)	98.14	0.58	3				
DA23	0.6	1	52.20 (0.00)	0.33 (0.00)	2.37 (0.00)	17.93 (0.00)	0.03 (0.00)	13.63 (0.00)	11.62 (0.00)	0.26 (0.00)	0.29 (0.00)	98.67	0.58	1				
DA14*	0.6	0.1	54.07 (3.39)	0.49 (0.09)	3.18 (1.85)	13.20 (1.40)	0.00 (0.04)	12.76 (2.06)	15.74 (2.73)	0.36 (0.22)	0.39 (0.46)	100.18	0.64	8				
DA65*	0.6	0.01	53.99 (2.22)	0.39 (0.15)	4.20 (1.16)	11.52 (0.71)	0.01 (0.01)	11.36 (1.02)	17.46 (2.29)	0.57 (0.31)	0.41 (0.23)	99.90	0.64	7				
DA51	0.6	0.001	52.26 (0.34)	0.33 (0.13)	1.74 (1.09)	15.50 (1.84)	0.00 (0.04)	13.01 (0.97)	16.26 (1.64)	0.23 (0.16)	0.18 (0.13)	99.51	0.60	3				
DA29	0.6	0.0002	51.98 (0.94)	0.46 (0.19)	2.11 (0.74)	15.68 (1.78)	0.02 (0.04)	13.25 (1.14)	15.12 (1.74)	0.27 (0.14)	0.16 (0.14)	99.05	0.60	10				
DA46	0.6	isobaric at 50 MPa	55.66 (0.14)	0.31 (0.06)	3.40 (0.86)	20.42 (1.72)	0.04 (0.04)	12.48 (1.33)	8.37 (1.77)	0.53 (0.18)	0.75 (0.03)	101.96	0.52	3				

N: number of analyses

*: the experiment was duplicated at the same condition, analyses of water content and glass are average values

***: 3 experiments were conducted at the same condition. In all experiments large Pl microclites were observed. The glass analysis was determined for 1 experiment

Table A.5.4. Average orthopyroxene compositions (numbers in parentheses show the standard deviation 1σ from replicate measurements).

sample	X H ₂ O [MPa/s]	Decompression rate	chemical composition of orthopyroxene (Opx) [wt%]													Total	Mg#	N
			SiO ₂	TiO ₂	Al ₂ O ₃	FeO	MnO	MgO	CaO	Na ₂ O	K ₂ O	Na ₂ O	K ₂ O	Total				
DA19	1	20	51.30 (0.21)	0.25 (0.03)	1.23 (0.16)	24.07 (0.25)	0.01 (0.04)	19.74 (0.21)	1.68 (0.16)	0.02 (0.03)	0.02 (0.02)	98.33	0.60	3				
DA13*	1	0.1	52.69 (1.19)	0.24 (0.07)	1.21 (0.71)	22.56 (0.99)	0.01 (0.03)	21.45 (1.20)	1.69 (0.23)	0.03 (0.02)	0.04 (0.11)	99.91	0.64	22				
DA64*	1	0.01	52.95 (0.82)	0.22 (0.03)	0.98 (0.36)	21.47 (0.56)	0.02 (0.05)	22.91 (0.42)	1.60 (0.28)	0.01 (0.01)	0.01 (0.00)	100.19	0.67	4				
DA50	1	0.001	51.99 (0.27)	0.26 (0.02)	1.41 (0.18)	24.53 (0.50)	0.00 (0.03)	20.20 (0.29)	1.65 (0.20)	0.02 (0.01)	0.03 (0.01)	100.09	0.60	7				
DA54*	1	0.0005	52.13 (0.25)	0.18 (0.05)	1.09 (0.31)	23.42 (0.41)	0.02 (0.02)	20.30 (0.67)	1.64 (0.15)	0.02 (0.02)	0.03 (0.01)	98.84	0.61	6				
DA28**	1	0.0002	51.55 (0.55)	0.21 (0.08)	1.10 (0.41)	24.00 (1.08)	0.00 (0.01)	19.66 (1.36)	1.81 (0.45)	0.02 (0.02)	0.03 (0.01)	98.39	0.60	9				
DA12	0.6	isobaric at 300 MPa	50.79 (0.06)	0.25 (0.09)	1.45 (0.25)	24.82 (0.13)	1.03 (0.04)	17.96 (0.08)	1.76 (0.33)	0.02 (0.02)	0.05 (0.02)	98.13	0.56	2				
DA20	0.6	20	50.90 (0.27)	0.30 (0.22)	1.25 (0.39)	26.22 (0.58)	0.01 (0.02)	17.85 (0.32)	1.91 (0.21)	0.02 (0.03)	0.02 (0.02)	98.50	0.55	7				
DA23	0.6	1	50.91 (0.68)	0.29 (0.13)	1.37 (0.48)	25.61 (2.53)	0.02 (0.04)	17.76 (1.39)	2.64 (2.89)	0.05 (0.07)	0.05 (0.08)	98.71	0.56	12				
DA14*	0.6	0.1	51.13 (0.30)	0.26 (0.15)	1.66 (0.45)	24.63 (0.18)	0.38 (0.01)	18.85 (0.25)	1.87 (0.12)	0.06 (0.02)	0.02 (0.01)	98.86	0.58	12				
DA65*	0.6	0.01	51.64 (0.55)	0.25 (0.05)	1.50 (0.47)	25.02 (0.67)	0.02 (0.04)	19.28 (0.51)	1.75 (0.21)	0.03 (0.06)	0.05 (0.04)	99.54	0.58	16				
DA51	0.6	0.001	51.21 (0.49)	0.36 (0.27)	1.43 (0.19)	26.83 (0.46)	0.00 (0.02)	18.26 (0.34)	1.85 (0.22)	0.03 (0.03)	0.02 (0.02)	99.99	0.55	7				

N: number of analyses

*: the experiment was duplicated at the same condition, analyses of water content and glass are average values

***: 3 experiments were conducted at the same condition. In all experiments large Pl microclites were observed. The glass analysis was determined for 1 experiment

Table A.6.1. Average clinopyroxene compositions in wt% (numbers in parentheses show the standard deviation 1σ from replicate measurements).

sample	X H ₂ O	Decompression rate [MPa/s]	chemical composition of clinopyroxene (Cpx) [wt%]													Total	Mg#	N
			SiO ₂	TiO ₂	Al ₂ O ₃	FeO	MnO	MgO	CaO	Na ₂ O	K ₂ O	MgO	CaO	Na ₂ O	K ₂ O			
DEC02+06	1.0	isobaric at 300 MPa	52.81 (0.56)	0.32 (0.07)	1.65 (0.46)	8.53 (0.51)	0.00 (0.00)	15.75 (0.71)	20.32 (1.02)	0.29 (0.13)	0.06 (0.04)	99.71	0.79	15				
HPD05	1.0	0.1	52.08 (0.40)	0.27 (0.07)	1.19 (0.37)	8.25 (0.88)	0.00 (0.00)	15.35 (0.34)	20.63 (0.62)	0.20 (0.04)	0.02 (0.02)	97.98	0.78	6				
HPD11	1.0	0.001	51.98 (0.86)	0.31 (0.13)	1.30 (0.94)	9.37 (2.77)	0.00 (0.00)	15.48 (1.46)	19.10 (4.12)	0.17 (0.09)	0.04 (0.01)	97.74	0.76	4				
HPD01	1.0	0.0002	52.85 (0.26)	0.27 (0.05)	1.15 (0.25)	8.57 (0.23)	0.00 (0.00)	15.57 (0.26)	20.54 (0.06)	0.19 (0.01)	0.04 (0.02)	99.18	0.77	3				
UNI103*	1.0	isobaric at 50 MPa	52.51 (1.59)	0.41 (0.21)	2.23 (1.05)	14.05 (2.50)	0.00 (0.00)	17.79 (2.96)	12.28 (5.80)	0.22 (0.08)	0.10 (0.02)	99.59	0.70	4				
DEC05+10	0.6	isobaric at 300 MPa	n.d.	n.d.	n.d.	n.d.	n.d.	n.d.	n.d.	n.d.	n.d.	n.d.	n.d.	n.d.				
HPD17	0.6	0.1	n.d.	n.d.	n.d.	n.d.	n.d.	n.d.	n.d.	n.d.	n.d.	n.d.	n.d.	n.d.				
HPD18	0.6	0.01	51.49 (0.14)	0.39 (0.03)	1.59 (0.18)	11.82 (0.65)	0.00 (0.00)	13.91 (0.32)	18.28 (0.87)	0.19 (0.07)	0.07 (0.03)	97.75	0.68	3				
HPD07	0.6	0.0007	52.10 (0.88)	0.40 (0.24)	1.75 (0.77)	9.00 (0.78)	0.00 (0.00)	14.66 (1.02)	20.21 (0.88)	0.24 (0.05)	0.06 (0.03)	98.41	0.75	5				
UNI105*	0.6	isobaric at 50 MPa	n.d.	n.d.	n.d.	n.d.	n.d.	n.d.	n.d.	n.d.	n.d.	n.d.	n.d.	n.d.				

N: number of analyses
n.d.: not detected/ not determined

Table A.6.2. Average orthopyroxene compositions in wt% (numbers in parentheses show the standard deviation 1σ from replicate measurements).

sample	X H ₂ O	Decompression rate [MPa/s]	chemical composition of orthopyroxene (Opx) [wt%]													Total	Mg#	N
			SiO ₂	TiO ₂	Al ₂ O ₃	FeO	MnO	MgO	CaO	Na ₂ O	K ₂ O	MgO	CaO	Na ₂ O	K ₂ O			
DEC02+06	1.0	isobaric at 300 MPa	n.d.	n.d.	n.d.	n.d.	n.d.	n.d.	n.d.	n.d.	n.d.	n.d.	n.d.	n.d.	n.d.	n.d.	n.d.	
HPD05	1.0	0.1	n.d.	n.d.	n.d.	n.d.	n.d.	n.d.	n.d.	n.d.	n.d.	n.d.	n.d.	n.d.	n.d.	n.d.	n.d.	
HPD11	1.0	0.001	51.64 (1.03)	0.27 (0.10)	1.49 (0.96)	20.64 (0.07)	0.00 (0.00)	20.58 (0.39)	1.76 (0.28)	0.00 (0.00)	0.03 (0.01)	96.41	0.64	2				
HPD01	1.0	0.0002	53.20 (0.06)	0.20 (0.03)	1.18 (0.22)	17.48 (0.25)	0.00 (0.00)	24.10 (0.32)	1.72 (0.23)	0.00 (0.01)	0.00 (0.00)	97.88	0.71	13				
UNI103*	1.0	isobaric at 50 MPa	n.d.	n.d.	n.d.	n.d.	n.d.	n.d.	n.d.	n.d.	n.d.	n.d.	n.d.	n.d.	n.d.	n.d.	n.d.	
DEC05+10	0.6	isobaric at 300 MPa	52.27 (0.47)	0.25 (0.06)	1.25 (0.42)	22.40 (0.30)	0.00 (0.00)	20.75 (0.22)	1.73 (0.05)	0.28 (0.21)	0.02 (0.02)	98.94	0.63	9				
HPD17	0.6	0.1	51.91 (0.23)	0.22 (0.02)	1.18 (0.26)	19.21 (1.28)	0.00 (0.00)	21.26 (0.77)	1.99 (0.05)	0.01 (0.02)	0.02 (0.01)	95.81	0.66	5				
HPD18	0.6	0.01	52.29 (0.19)	0.24 (0.02)	1.41 (0.20)	18.97 (0.56)	0.00 (0.00)	21.85 (0.41)	1.85 (0.36)	0.00 (0.00)	0.02 (0.02)	96.63	0.67	3				
HPD07	0.6	0.0007	n.d.	n.d.	n.d.	n.d.	n.d.	n.d.	n.d.	n.d.	n.d.	n.d.	n.d.	n.d.				
UNI105*	0.6	isobaric at 50 MPa	55.56 (1.34)	0.28 (0.04)	1.70 (0.63)	12.58 (1.18)	0.02 (0.04)	28.81 (1.21)	1.30 (0.19)	0.06 (0.10)	0.13 (0.21)	100.43	0.82	5				

N: number of analyses
n.d.: not detected/ not determined

Table A.7.1. Average plagioclase core compositions in wt% (numbers in parentheses show the standard deviation 1σ from replicate measurements).

sample	X H ₂ O [MPa/s]	Decompression rate	chemical composition of plagioclase (Pl) cores [wt%]														Total	An	Ab	Or	N
			SiO ₂	TiO ₂	Al ₂ O ₃	FeO	MnO	MgO	CaO	Na ₂ O	K ₂ O	Na ₂ O	K ₂ O	CaO	Na ₂ O	K ₂ O					
Big01	1.0	isobaric at 50 MPa	60.24 (1.24)	0.19 (0.04)	22.39 (1.08)	1.95 (0.34)	0.00 (0.00)	0.50 (0.14)	8.19 (0.32)	5.03 (0.34)	1.07 (0.20)	99.56	44	49	7	4					
LPD05	1.0	0.1	63.57 (2.41)	0.20 (0.02)	20.14 (1.36)	1.88 (0.67)	0.00 (0.00)	0.55 (0.42)	6.89 (0.77)	4.37 (0.47)	1.61 (0.32)	99.19	41	47	12	5					
LPD04	1.0	0.01	62.30 (1.37)	0.19 (0.04)	21.62 (0.71)	2.02 (0.58)	0.00 (0.00)	0.54 (0.32)	7.87 (0.55)	4.76 (0.15)	1.30 (0.21)	100.60	44	48	9	5					
LPD03	1.0	0.001	61.70 (1.67)	0.17 (0.05)	20.59 (1.10)	2.48 (0.89)	0.00 (0.00)	0.83 (0.68)	7.24 (0.56)	4.82 (0.26)	1.44 (0.29)	99.26	41	49	10	4					
LPD02	1.0	0.0002	59.93 (2.73)	0.25 (0.19)	21.48 (2.23)	2.39 (1.23)	0.00 (0.00)	0.54 (0.54)	7.84 (0.78)	4.76 (0.66)	1.23 (0.42)	98.41	44	48	8	5					
LPD01	1.0	0.0001	61.95 (4.15)	0.21 (0.06)	22.49 (2.79)	2.12 (0.32)	0.00 (0.00)	0.48 (0.21)	7.74 (1.68)	4.98 (0.77)	1.33 (0.69)	101.31	42	49	9	4					
UN103	1.0	isobaric at 50 MPa	56.22 (1.59)	0.14 (0.06)	25.93 (1.30)	1.83 (0.62)	0.00 (0.00)	0.28 (0.32)	10.41 (0.73)	4.49 (0.12)	0.65 (0.23)	99.96	54	42	4	4					
LPD21	1.0	0.02	57.35 (3.02)	0.18 (0.03)	24.13 (1.55)	1.84 (0.48)	0.00 (0.00)	0.34 (0.12)	9.59 (1.13)	4.06 (0.54)	0.90 (0.43)	98.39	53	41	6	5					
LPD23	1.0	0.001	56.74 (3.63)	0.14 (0.06)	25.29 (2.36)	1.54 (0.41)	0.00 (0.00)	0.33 (0.17)	10.18 (1.56)	4.36 (0.25)	0.77 (0.59)	99.35	53	42	5	5					
LPD22	1.0	0.0002	57.91 (4.18)	0.13 (0.06)	24.55 (2.43)	1.49 (0.34)	0.00 (0.00)	0.36 (0.25)	10.04 (1.74)	4.14 (0.27)	0.86 (0.52)	99.48	54	40	6	5					
LPD26	1.0	0.0001	57.90 (3.93)	0.16 (0.06)	24.40 (2.42)	1.42 (0.38)	0.00 (0.00)	0.41 (0.31)	9.97 (1.57)	4.06 (0.50)	0.88 (0.51)	99.20	54	40	6	5					

N: number of analyses

Table A.7.2. Average clinopyroxene compositions in wt% (numbers in parentheses show the standard deviation 1σ from replicate measurements).

sample	X H ₂ O [MPa/s]	Decompression rate	chemical composition of clinopyroxene (Cpx) [wt%]														Total	Mg#	N
			SiO ₂	TiO ₂	Al ₂ O ₃	FeO	MnO	MgO	CaO	Na ₂ O	K ₂ O	Na ₂ O	K ₂ O	CaO	Na ₂ O	K ₂ O			
Big01	1.0	isobaric at 50 MPa	52.04 (2.29)	1.77 (2.44)	1.47 (0.25)	24.67 (0.92)	0.00 (0.00)	14.30 (0.97)	6.36 (0.81)	0.18 (0.05)	0.26 (0.06)	101.06	0.51	3					
LPD05	1.0	0.1	56.09 (1.09)	0.44 (0.23)	2.57 (3.25)	20.24 (1.12)	0.00 (0.00)	12.41 (2.09)	7.97 (2.79)	0.44 (0.20)	0.62 (0.48)	100.78	0.52	3					
LPD04	1.0	0.01	55.53 (1.94)	0.25 (0.06)	2.77 (5.23)	22.64 (4.19)	0.00 (0.00)	12.81 (3.40)	4.41 (0.85)	0.50 (0.43)	0.71 (0.92)	99.62	0.50	3					
LPD03	1.0	0.001	54.91 (1.14)	0.97 (0.96)	3.25 (4.64)	21.55 (3.35)	0.00 (0.00)	12.29 (1.91)	6.90 (1.37)	0.57 (0.24)	0.68 (0.65)	101.12	0.50	4					
LPD02	1.0	0.0002	54.44 (1.61)	0.22 (0.03)	2.15 (1.27)	24.40 (1.68)	0.00 (0.00)	13.92 (1.60)	4.86 (0.91)	0.39 (0.27)	0.44 (0.26)	100.83	0.50	4					
LPD01	1.0	0.0001	55.78 (1.20)	0.28 (0.09)	2.56 (3.04)	20.53 (1.78)	0.00 (0.00)	12.77 (2.29)	8.36 (2.22)	0.45 (0.25)	0.55 (0.40)	101.28	0.53	6					
UN103	1.0	isobaric at 50 MPa	52.51 (1.59)	0.41 (0.21)	2.23 (1.05)	14.05 (2.50)	0.00 (0.00)	17.79 (2.96)	12.28 (5.80)	0.22 (0.08)	0.10 (0.02)	99.59	0.70	4					
LPD21	1.0	0.02	n.d.	n.d.	n.d.	n.d.	n.d.	n.d.	n.d.	n.d.	n.d.	n.d.	n.d.	n.d.	n.d.	n.d.	n.d.	n.d.	
LPD23	1.0	0.001	n.d.	n.d.	n.d.	n.d.	n.d.	n.d.	n.d.	n.d.	n.d.	n.d.	n.d.	n.d.	n.d.	n.d.	n.d.	n.d.	
LPD22	1.0	0.0002	n.d.	n.d.	n.d.	n.d.	n.d.	n.d.	n.d.	n.d.	n.d.	n.d.	n.d.	n.d.	n.d.	n.d.	n.d.	n.d.	
LPD26	1.0	0.0001	n.d.	n.d.	n.d.	n.d.	n.d.	n.d.	n.d.	n.d.	n.d.	n.d.	n.d.	n.d.	n.d.	n.d.	n.d.	n.d.	

N: number of analyses

n.d.: not detected/ not determined

Table A.7.3. Average orthopyroxene compositions in wt% (numbers in parentheses show the standard deviation 1σ from replicate measurements).

sample	X H ₂ O [MPa/s]	Decompression rate	chemical composition of orthopyroxene (Opx) [wt%]														
			SiO ₂	TiO ₂	Al ₂ O ₃	FeO	MnO	MgO	CaO	Na ₂ O	K ₂ O	Total	Mg#	N			
Big01	1.0	n.d.	n.d.	n.d.	n.d.	n.d.	n.d.	n.d.	n.d.	n.d.	n.d.	n.d.	n.d.	n.d.	n.d.	n.d.	n.d.
LPD05	1.0	0.1	60.18 (n.d.)	0.20 (n.d.)	4.99 (n.d.)	18.93 (n.d.)	0.00 (n.d.)	9.63 (n.d.)	2.66 (n.d.)	0.89 (n.d.)	1.50 (n.d.)	98.99	0.48	1			
LPD04	1.0	0.01	n.d.	n.d.	n.d.	n.d.	n.d.	n.d.	n.d.	n.d.	n.d.	n.d.	n.d.	n.d.	n.d.	n.d.	n.d.
LPD03	1.0	0.001	n.d.	n.d.	n.d.	n.d.	n.d.	n.d.	n.d.	n.d.	n.d.	n.d.	n.d.	n.d.	n.d.	n.d.	n.d.
LPD02	1.0	0.0002	n.d.	n.d.	n.d.	n.d.	n.d.	n.d.	n.d.	n.d.	n.d.	n.d.	n.d.	n.d.	n.d.	n.d.	n.d.
LPD01	1.0	0.0001	n.d.	n.d.	n.d.	n.d.	n.d.	n.d.	n.d.	n.d.	n.d.	n.d.	n.d.	n.d.	n.d.	n.d.	n.d.
UNI03	1.0	isobaric at 50 Mpa	n.d.	n.d.	n.d.	n.d.	n.d.	n.d.	n.d.	n.d.	n.d.	n.d.	n.d.	n.d.	n.d.	n.d.	n.d.
LPD21	1.0	0.02	55.91 (1.76)	0.29 (0.04)	2.40 (3.12)	10.61 (1.40)	0.00 (0.00)	26.58 (4.38)	1.48 (0.209)	0.13 (0.21)	0.36 (0.60)	97.78	0.82	5			
LPD23	1.0	0.001	54.58 (0.70)	0.38 (0.22)	1.93 (0.55)	13.01 (1.65)	0.00 (0.00)	27.17 (2.14)	1.25 (0.16)	0.09 (0.18)	0.10 (0.15)	98.52	0.79	5			
LPD22	1.0	0.0002	54.96 (0.43)	0.25 (0.05)	1.36 (0.79)	11.83 (1.31)	0.00 (0.00)	28.25 (1.23)	1.43 (0.20)	0.00 (0.00)	0.04 (0.01)	98.12	0.81	5			
LPD26	1.0	0.0001	54.27 (0.15)	0.26 (0.02)	1.43 (0.26)	14.63 (0.98)	0.00 (0.00)	26.57 (1.09)	1.57 (0.37)	0.00 (0.00)	0.03 (0.02)	98.85	0.76	5			

N: number of analyses
n.d.: not detected/ not determined

Table A.8.1. Average plagioclase core compositions in wt% (numbers in parentheses show the standard deviation 1σ from replicate measurements).

sample	X H ₂ O [MPa/s]	Decompression rate	chemical composition of plagioclase (Pl) cores [wt%]													
			SiO ₂	TiO ₂	Al ₂ O ₃	FeO	MnO	MgO	CaO	Na ₂ O	K ₂ O	An	Ab	Or	N	
Big03+04	1.0	isobaric at 200 MPa	52.60 (1.82)	0.08 (0.04)	28.78 (1.16)	0.98 (0.38)	0.00 (0.00)	0.09 (0.03)	12.86 (1.06)	3.67 (0.58)	0.35 (0.18)	65	33	2	5	
LPD13	1.0	0.01	55.84 (2.64)	0.06 (0.06)	27.34 (1.88)	0.63 (0.11)	0.00 (0.00)	0.01 (0.03)	11.50 (1.45)	4.69 (0.89)	0.46 (0.31)	56	41	3	4	
LPD12	1.0	0.001	53.14 (1.08)	0.02 (0.03)	29.34 (0.79)	0.51 (0.07)	0.00 (0.00)	0.00 (0.00)	12.91 (0.94)	4.72 (0.86)	0.21 (0.02)	60	39	1	5	
LPD06	1.0	0.0002	56.15 (2.29)	0.06 (0.03)	26.53 (1.62)	0.70 (0.12)	0.00 (0.00)	0.09 (0.04)	10.27 (1.03)	5.28 (0.20)	0.50 (0.36)	50	47	3	5	
LPD09	1.0	0.0001	50.75 (1.29)	0.01 (0.01)	30.25 (0.88)	0.49 (0.04)	0.00 (0.00)	0.01 (0.02)	13.73 (1.11)	3.90 (0.68)	0.18 (0.03)	65	34	1	5	

N: number of analyses

Table A.8.2. Average amphibole core compositions in wt% (numbers in parentheses show the standard deviation 1σ from replicate measurements).

sample	X H ₂ O	Decompression rate [MPa/s]	chemical composition of amphiboles (Amph) [wt%]											Total	Mg#	N
			SiO ₂	TiO ₂	Al ₂ O ₃	FeO	MnO	MgO	CaO	Na ₂ O	K ₂ O					
Big03+04	1.0	isobaric at 200 MPa	46.00 (0.80)	2.02 (0.19)	8.24 (0.85)	14.36 (0.83)	0.00 (0.00)	12.69 (0.64)	11.43 (1.54)	1.40 (0.18)	0.37 (0.05)	96.50	0.64	5		
LPD13	1.0	0.01	46.38 (1.29)	1.65 (0.27)	8.90 (1.62)	11.79 (0.69)	0.00 (0.00)	15.24 (0.92)	10.97 (0.43)	1.91 (0.13)	0.36 (0.09)	97.20	0.72	4		
LPD12	1.0	0.001	46.72 (0.32)	1.68 (0.11)	9.43 (1.41)	12.08 (1.16)	0.00 (0.00)	13.74 (2.07)	10.84 (0.78)	1.79 (0.18)	0.52 (0.19)	96.80	0.70	5		
LPD06	1.0	0.0002	n.c.	n.c.	n.c.	n.c.	n.c.	n.c.	n.c.	n.c.	n.c.	n.c.	n.c.	n.c.		
LPD09	1.0	0.0001	n.c.	n.c.	n.c.	n.c.	n.c.	n.c.	n.c.	n.c.	n.c.	n.c.	n.c.	n.c.		

N: number of analyses
n.c.: not crystallized

Table A.8.3. Average orthopyroxene compositions in wt% (numbers in parentheses show the standard deviation 1σ from replicate measurements).

sample	X H ₂ O	Decompression rate [MPa/s]	chemical composition of orthopyroxene (Opx) [wt%]											Total	Mg#	N
			SiO ₂	TiO ₂	Al ₂ O ₃	FeO	MnO	MgO	CaO	Na ₂ O	K ₂ O					
Big03+04	1.0	isobaric at 200 MPa	52.90 (0.46)	0.23 (0.06)	1.08 (0.21)	21.53 (0.50)	0.00 (0.00)	22.39 (0.32)	1.76 (0.14)	0.00 (0.00)	0.03 (0.00)	99.92	0.65	5		
LPD13	1.0	0.01	n.d.	n.d.	n.d.	n.d.	n.d.	n.d.	n.d.	n.d.	n.d.	n.d.	n.d.	n.d.		
LPD12	1.0	0.001	51.66 (0.22)	0.22 (0.01)	1.44 (0.26)	24.79 (0.22)	0.00 (0.00)	18.80 (0.09)	1.57 (0.15)	0.36 (0.44)	0.03 (0.01)	98.89	0.58	3		
LPD06	1.0	0.0002	51.81 (0.25)	0.24 (0.05)	1.17 (0.39)	21.78 (0.30)	0.00 (0.00)	20.94 (0.23)	1.71 (0.22)	0.02 (0.03)	0.04 (0.03)	97.70	0.63	7		
LPD09	1.0	0.0001	50.58 (0.28)	0.23 (0.6)	1.13 (0.40)	26.33 (0.46)	0.00 (0.00)	16.82 (0.64)	2.00 (0.82)	0.03 (0.07)	0.04 (0.05)	97.16	0.53	5		

N: number of analyses
n.d.: not detected/ not determined

7. APPENDIX B.1 – FIGURE INDEX

Figure	Title	Page
1.1	Location map of Kyushu Island and Unzen volcano, Japan	1
1.2	Vertical section through the USDP-4 well	3
1.3	Three-dimensional image of conduit drilling	3
1.4	Illustration of pre-eruptive Unzen conditions	4
1.5	Schematic phase diagram for water-saturated rhyodacitic magma	5
2.1	Externally heated pressure vessels (CSPV)	10
2.2	Internally heated pressure vessel (IHPV)	12
2.3 a-d	Phase stability diagrams at constant pressures	16-17
2.4 a-c	Phase stability diagrams at constant temperatures	19-20
2.5 a-b	Phase stability diagrams at water-saturated conditions: comparison of (a) our experimental results and (b) literature data	22
2.6 a-b	Phase stability diagrams at (a) $X^{\text{H}_2\text{O}}=0.6$ and at (b) $X^{\text{H}_2\text{O}}=0.8$	23
2.7	Al_2O_3 vs. Mg# of natural and experimental amphiboles	25
3.1	Schematic phase diagrams (a) $X^{\text{H}_2\text{O}}=1.0$ and at (b) $X^{\text{H}_2\text{O}}=0.6$, showing the HPD experimental isothermal decompression paths	27
3.2	Schematic phase diagram for water-saturated rhyodacitic magma, indicating decompression paths of HPD set-I	31
3.3 a-j	BSE pictures of experimental end products of HPD set-I	41
3.4 a-h	Chemical composition of experimental residual melts as a function of the decompression rate for HPD set-I	44
3.5	H_2O -content of residual glasses for HPD set-I	45
3.6 a-f	BSD curves for experimental end products of HPD set-I	46
3.7	logBND vs. decompression rate for of experimental end products of HPD set-I	47
3.8 a-f	CSD curves for experimental end products of HPD set-I	48
3.9 a-b	logMND vs. decompression rate for of experimental end products of HPD set-I	49
3.10	Maximum Pl length as a function of the decompression rate for HPD set-I	50
3.11	Dissolved H_2O contents of glasses obtained from decompression experiments	52
3.12	Compiled experimental data of the BND as a function of the decompression rate	54
3.13	Log BND vs. SiO_2 -content of bulk rock for Plinian eruptions	55
3.14	Sketch of new decompression valve for the IHPV	61
3.15	Photo of experimental setup using the IHPV	62
3.16	BSE pictures of experimental end products of HPD set-II	63
3.17	Chemical composition of experimental residual melts as a function of the decompression rate for HPD set-II	64

7. APPENDIX

Figure	Title	Page
3.18	logBND vs. decompression rate for of experimental end products of HPD set-II	67
3.19	logMND vs. decompression rate for of experimental end products of HPD set-II	68
3.20	Schematic phase diagram for water-saturated rhyodacitic magma, indicating decompression paths of LPD set-III, set-IV and set-V	70
3.21	Images of experimental end products of LPD set-III and set-IV	72
3.22	Chemical composition of experimental residual melts as a function of the decompression rate for LPD set-III and set-IV	74
3.23	logBND vs. decompression rate for of experimental end products of LPD set-III and set-IV	76
3.24 a-b	logMND vs. decompression rate for of experimental end products of LPD set-III and set-IV	78
3.25	Maximum Pl length as a function of the decompression rate for LPD set-III and set-IV	79
3.26 a-j	Images of experimental end products of LPD set-V	81
3.27	Chemical composition of experimental residual melts as a function of the decompression rate for LPD set-V	83
3.28	logBND vs. decompression rate for of experimental end products of LPD set-V	85
3.29 a-b	logMND vs. decompression rate for of experimental end products of LPD set-V	86
3.30	Maximum Pl length as a function of the decompression rate for LPD set-V	87
3.31	Schematic diagram showing the three performed decompression methods	91
3.32 a-d	Modified images of experimental end products of LPD set-VI	93
3.33	H ₂ O-content of the residual melts determined by NIR vs. log BND for set-VI	94
3.34	BSD curves for experimental end products of set-VI	95
3.35	Photo of μ -tomography operation table of <i>TOMCAT</i> beamline at <i>SLS</i> , Villigen, Switzerland	100
3.36	Comparison of 2D images and 3D segment visualization of set-III samples	102
3.37 a-b	Comparison of log BND and log MND _{OP} values determined from 2D and 3D analyses	105
3.38	Schematic example of the phenomenon of bubble coalescence influencing the accuracy of stereological reconstruction methods	106
3.39 a-c	Screenshots of <i>YaDiV</i> 3D visualization of different segments	107
3.40 a-d	Schematic presentation of segmentation and the tools (algorithms) shrinking and growing	108
3.41 a-b	Tomographical 2D projection images showing (a) beam dispersion caused by high-density oxide mineral (white color) and (b) cracks caused by the sample preparation	109
3.42	Additional information preserved in 2D projection images from μ m-tomography	110

Figure	Title	Page
4.1 a-b	Compiled experimental data of the BND as a function of the decompression rate	114
4.2 a-b	(a) Log BND vs. SiO ₂ -content of bulk rock for Plinian eruptions, (b) Δ log BND as a function of the decompression rate	116
4.3	Maximum Pl length as a function of the decompression rate for HPD and LPD experiments	119
4.4	logMND vs. decompression rate for of experimental end products of HPD and of LPD	122
4.5 a-b	Log MND _{pl} vs. SiO ₂ -content of bulk rock for dome and plinian eruptions, modified after Toramaru <i>et al.</i> (2008) in comparison with our experimental data.	123
B.1 a-d	BSE images, BSD and CSD curves of H ₂ O-bearing HPD set-II (930°C)	156
B.2 a-d	BSE images, BSD and CSD curves of H ₂ O+CO ₂ -bearing HPD set-II (930°C)	157
B.3 a-e	BSE images, BSD and CSD curves of H ₂ O-bearing LPD set-III (850°C)	158
B.4 a-e	BSE images, BSD and CSD curves of H ₂ O-bearing LPD set-IV (930°C)	159
B.5 a-e	BSE images, BSD and CSD curves of H ₂ O-bearing LPD set-V (850°C)	160

7. APPENDIX B.2 – FIGURES

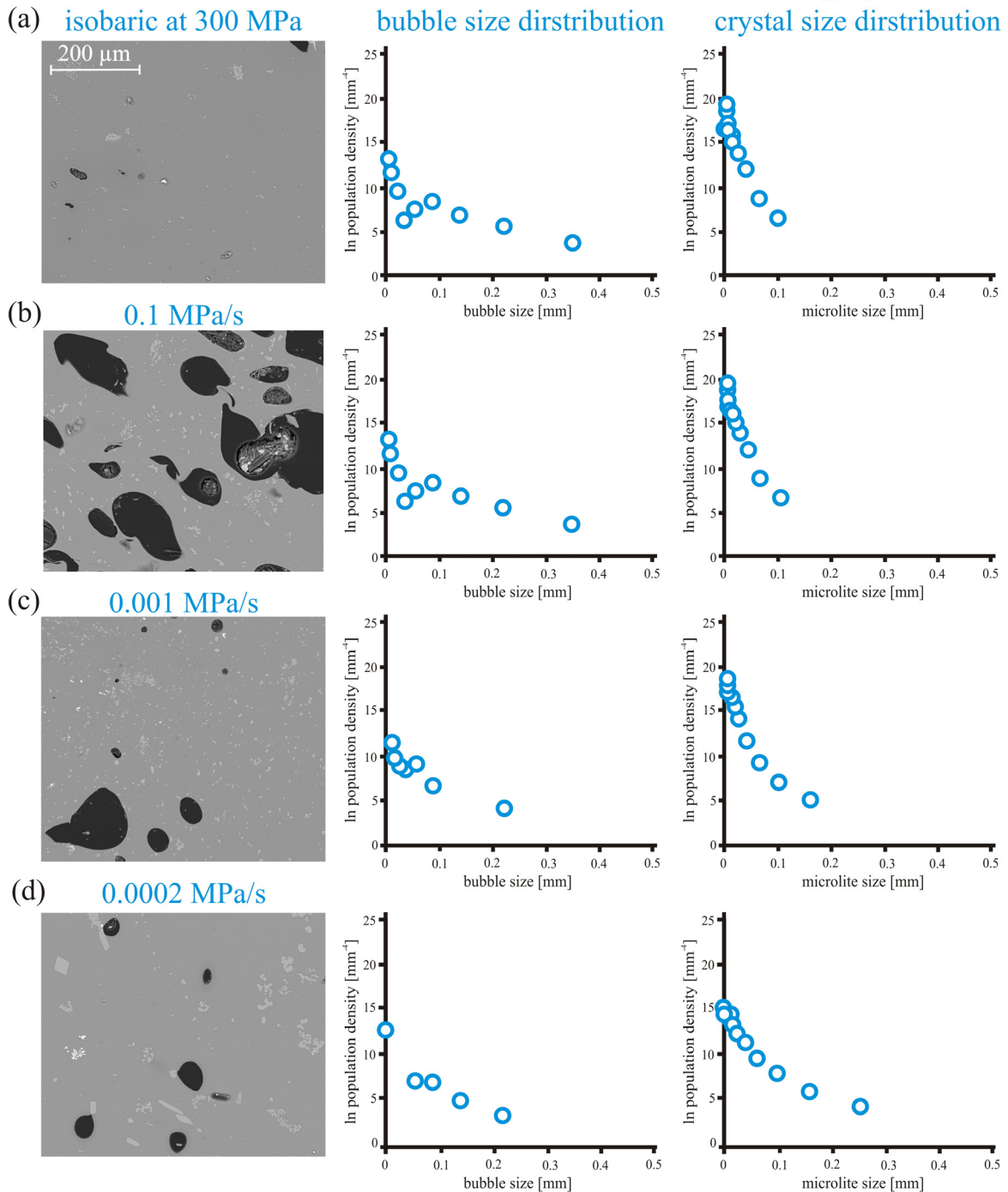
HPD set-II: 300 to 50 MPa at 930°C, H₂O-bearing system

Fig. B.1 a-d. BSE pictures of the H₂O-bearing products of isobaric and HPD experiments of set-II (right column). Black bodies are bubbles; light grey particles represent microlites such as Cpx, Opx and oxides. Bubble size distribution (middle column) and crystal size distribution (left column) of set-II, calculated following the method of Higgins (2000), for other phases (OP) only.

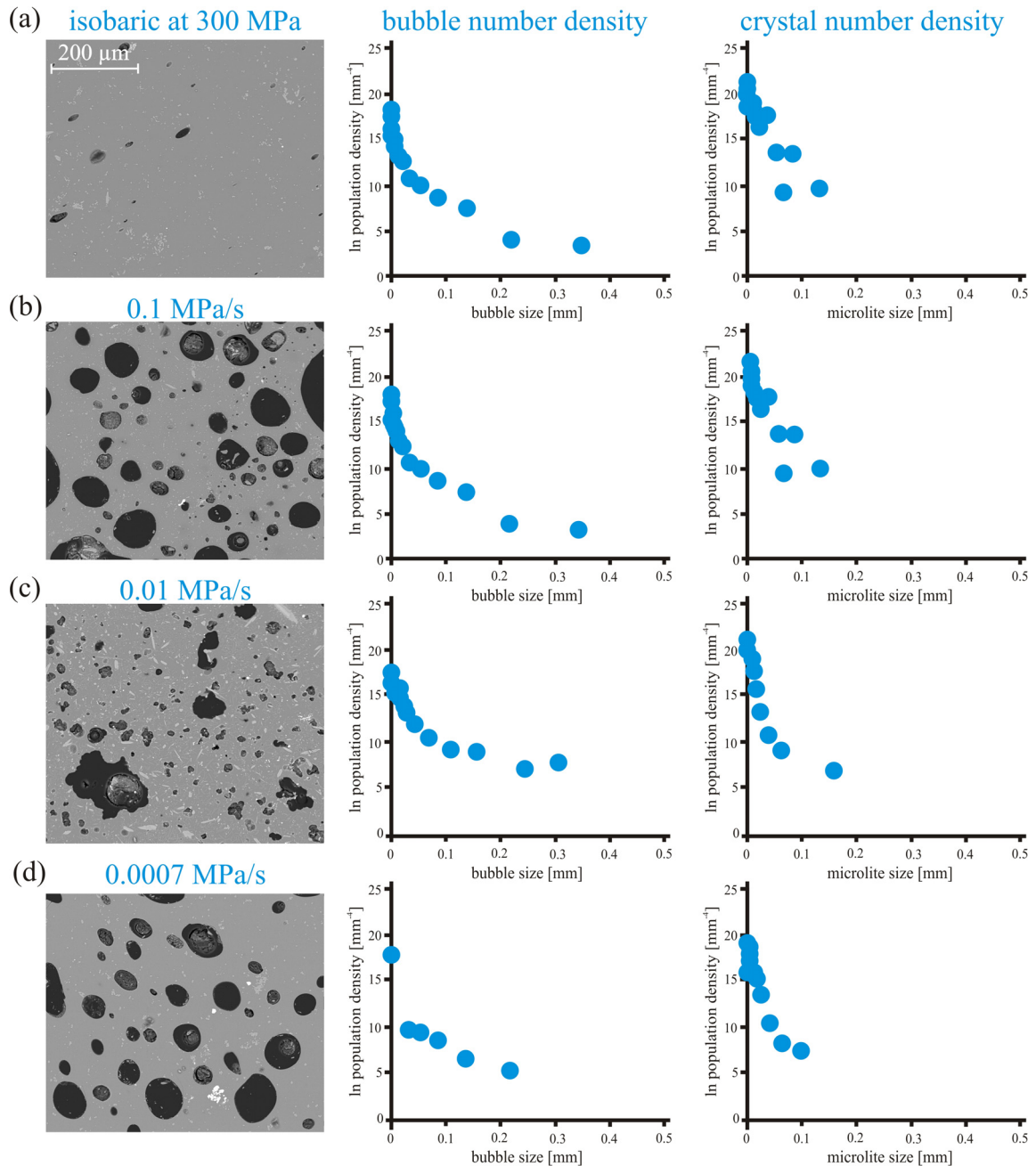
HPD set-II: 300 to 50 MPa at 930°C, H₂O+CO₂-bearing system

Fig. B.2 a-d. BSE pictures of the H₂O+CO₂-bearing products of isobaric and HPD experiments of set-II (right column). Black bodies are bubbles; light grey particles represent microlites such as Cpx, Opx oxides. Bubble size distribution (middle column) and crystal size distribution (left column) of set-II, calculated following the method of Higgins (2000), for other phases (OP) only.

LPD set-III: 50 to 0.1 MPa at 850°C

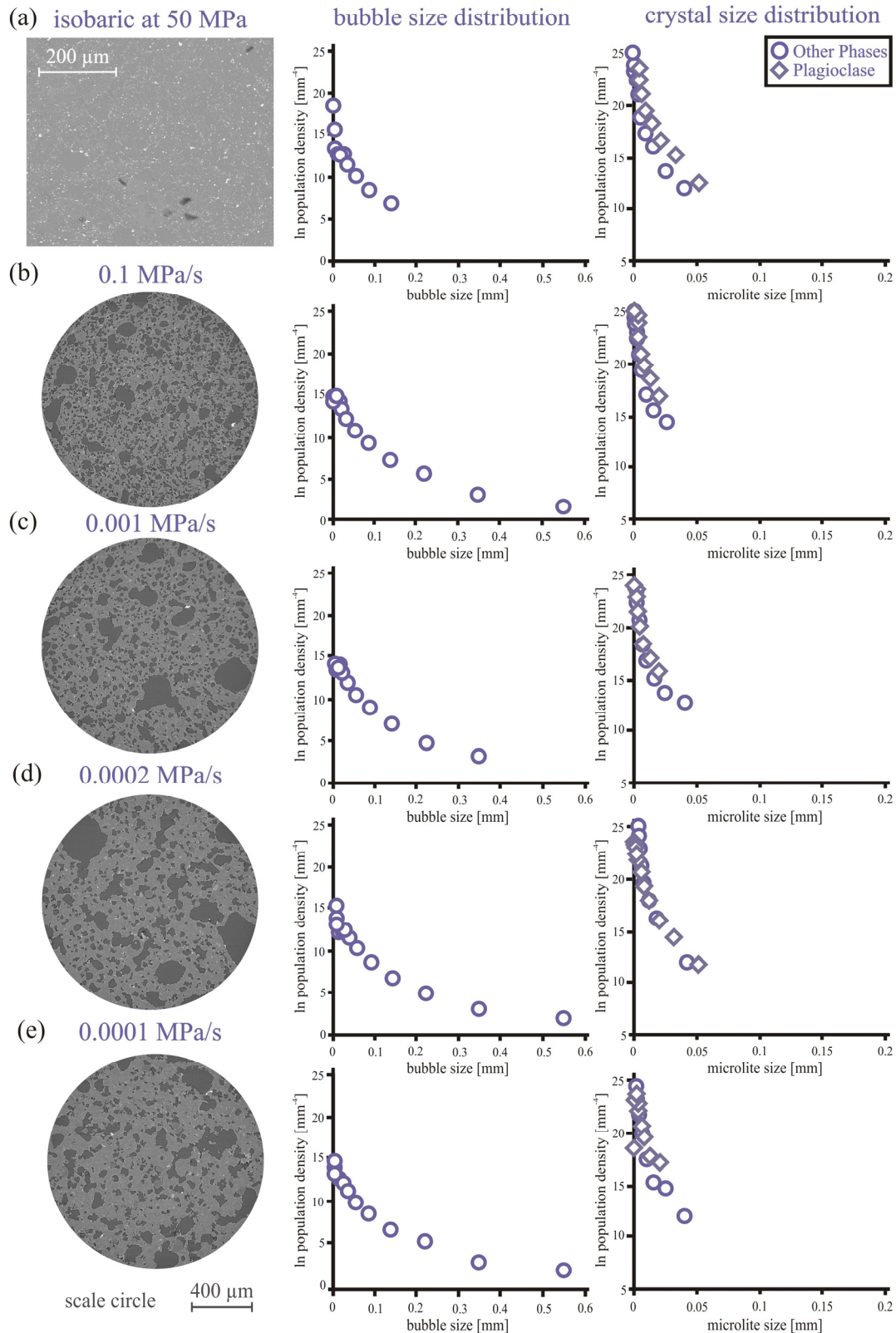


Fig. B.3 a-e. BSE pictures of the products of isobaric and LPD experiments of set-III (right column). Black bodies are bubbles; light grey particles represent microlites such as Cpx, Opx, Pl and oxides. Bubble size distribution (middle column) and crystal size distribution (left column) of set-III, calculated following the method of Higgins (2000), for other phases (OP) and for plagioclase (Pl) microlites.

LPD set-IV: 50 to 0.1 MPa at 930°C

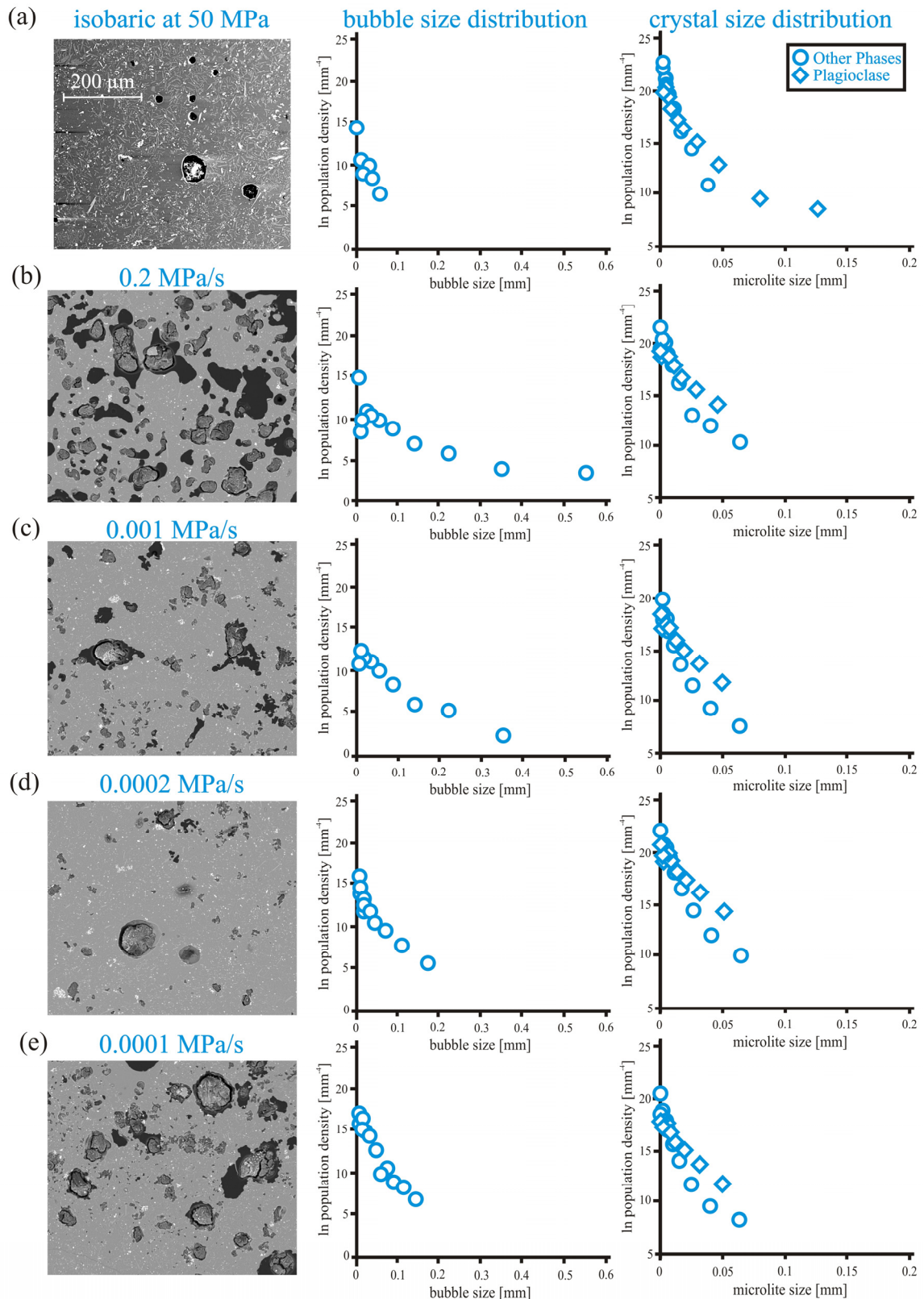


Fig. B.4 a-e. BSE pictures of the products of isobaric and LPD experiments of set-IV (right column). Black bodies are bubbles; light grey particles represent microlites such as Cpx, Opx, Pl and oxides. Bubble size distribution (middle column) and crystal size distribution (left column) of set-IV, calculated following the method of Higgins (2000), for other phases (OP) and for plagioclase (Pl) microlites.

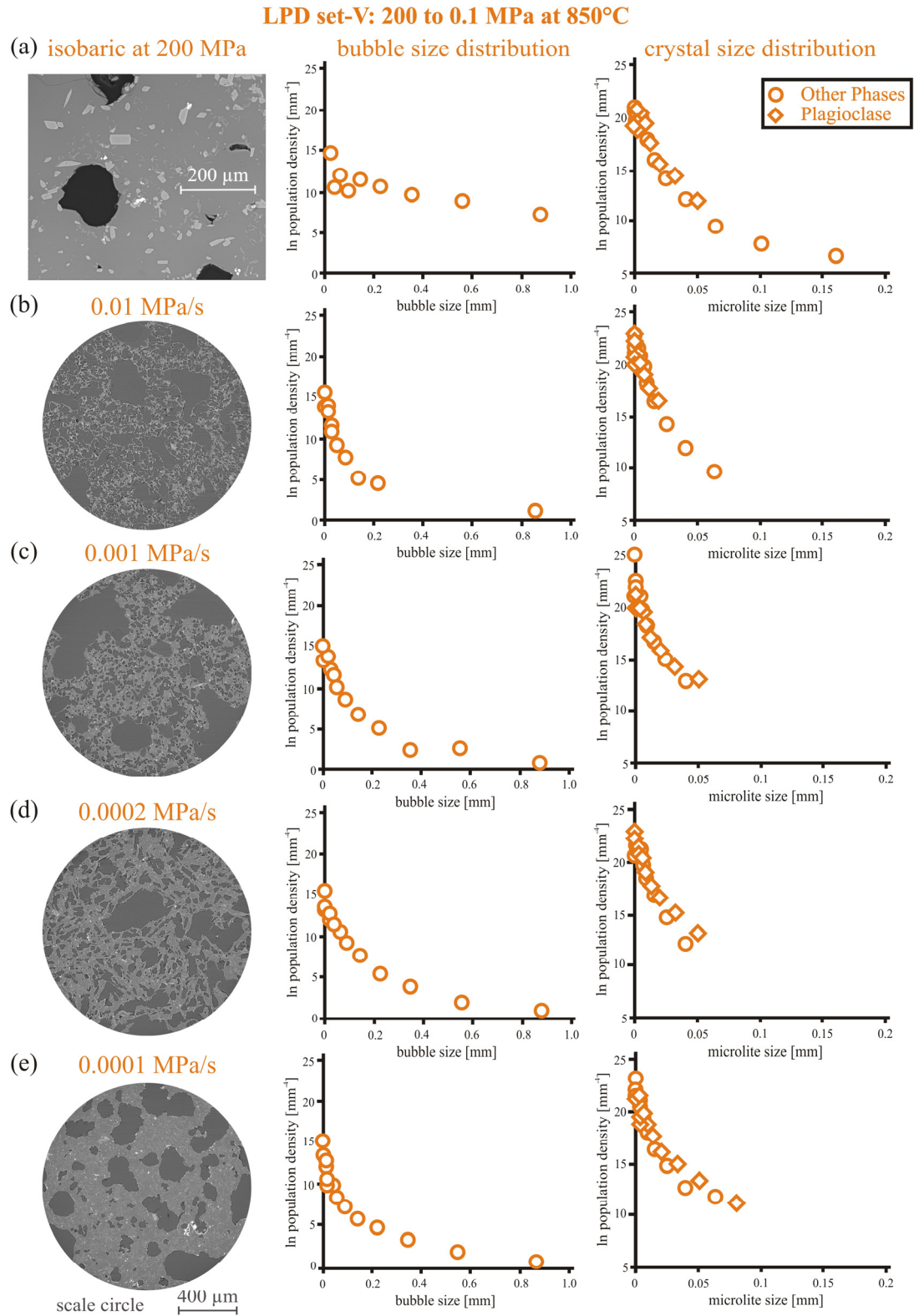


Fig. B.5 a-e. BSE pictures of the products of isobaric and LPD experiments of set-V (right column). Black bodies are bubbles; light grey particles represent microlites such as Cpx, Opx, Pl and oxides. Bubble size distribution (middle column) and crystal size distribution (left column) of set-V, calculated following the method of Higgins (2000), for other phases (OP) and for plagioclase (Pl) microlites.



Lebenslauf - Curriculum Vitae

Persönliche Daten

Name: Cichy
Vorname: Sarah Bettina
Anschrift: Lettow-Vorbeck-Allee 77 G
D-30455 Hannover
Geboren am: 08. August 1981 in Hannover
Nationalität: Deutsch



Schulbildung

1987-1988 Vorschule der Eichendorff-Grundschule, Hannover
1988-1992 Eichendorff-Grundschule, Hannover
1992-1994 Orientierungsstufe OS-Birkenstraße, Hannover
1994-2001 Gymnasium der Wilhelm-Raabe-Schule, Hannover
Abschluss: bilinguales Abitur (allgemeine Hochschulreife)

Hochschulausbildung

2001-2007 Leibniz Universität Hannover
Studiengang: Geowissenschaften
Abschluss: Diplom-Geowissenschaften (Dipl.-Geow.)

Beruflicher Werdegang

02/2005-03/2006 Studentische Hilfskraft am Zentrum für Materialkunde von Kulturgut e.V.
06/2006-05/2007 Studentische Hilfskraft am Institut für Mineralogie, Leibniz Universität Hannover
06/2007-03/2011 Wissenschaftliche Mitarbeiterin am Institut für Mineralogie, Leibniz Universität Hannover
04/2011-05/2011, Wissenschaftliche Hilfskraft am Institut für Bodenkunde, Leibniz Universität Hannover